Preparation and Characterization of Cathode Materials for Lithium-Oxygen Batteries

Storm, Mie Møller

Publication date:
2016

Document Version
Publisher's PDF, also known as Version of record

Mie Møller Storm

Preparation and Characterization of Cathode Materials for Lithium-Oxygen Batteries

---

Ph.D. THESIS
Submitted in candidacy for the degree Doctor of Philosophy

June 2016
Technical University of Denmark
Department of Energy Conversion and Storage

Preparation and Characterization of Cathode Materials for Lithium-Oxygen Batteries

Author

Mie Møller Storm
E-mail: mmst@dtu.dk

Supervisors

Senior Scientist Poul Norby
Section for Atomic Scale Modeling and Materials
Department of Energy Conversion and Storage
Technical University of Denmark
E-mail: pnor@dtu.dk

Consulting Professor Alan C. Luntz
Suncat Center for Interface Science and Catalysis
Nørskov group
Stanford University
E-mail: acluntz@stanford.edu

Technical University of Denmark

Section for Atomic Scale Modeling and Materials
Department of Energy Conversion and Storage
Frederiksborgvej 399
4000 Roskilde
Denmark

www.energy.dtu.dk
Tel: +45 46 77 58 00
E-mail: info@ecs.dtu.dk

June 2016

Keep your eyes on the stars
And your feet on the ground
Theodore Roosevelt

Preface

This thesis is submitted in candidacy for the Ph.D. degree from the Technical University of Denmark (DTU) and is based on the work carried out at Atomic Scale Modelling and Materials, DTU Energy, in the period from August 2012 to June 2016. The project was supervised by Senior Scientist Poul Norby and co-supervised by Alan Luntz. The work was funded by the Reliable project (project no 11-116792) funded by the Danish Council for strategic Research Program Commission on Sustainable Energy and Environment. Financially support for several synchrotron visits were received from The Danish Research Council for the financial support of synchrotron measurements (DANSCATT). During my project I had an external stay at the Korean Advanced Institute of Science and Technology (KAIST) in South Korea at the battery group led by Prof. Jang Wook Choi.

Acknowledgements

First and foremost I would like to thank my supervisor Poul Norby. It is amazing to have supervisor who lets me do everything I want and keeps coming up with more interesting “fun science” possibilities to investigate. You always had the time for helpful discussion, complicated and less complicated explanations, and new experiments. It is nice to have a patient and calm supervisor, especially during all the synchrotron experiments. I am still impressed with the amount of beam time you have gotten for the experiments.

I would like to thank the head of my group Tejs Vegge. You are always very busy, yet when I’ve managed to get a hold on you, you always have time to show a lot of interest in whatever was on my mind. I was very happy for your creation of the “running club” and your enthusiasm in all aspects of the group.

“If you know the chemistry, how come you have not made a product yet?” is a very common question to get when you are in science. However to “solve” a problem like commercialization of Li-air, is like feeding a hungry monster. You just keep stuffing knowledge and papers into the mouth of the monster hoping that one day your monster will feel full and explode to form a product. I would like to thank all my colleagues, Ane, Mathias, Jonathan, Kristian, Rune, Reza, Andreas, Supti, Jette, and many others. Many of you have been sorely missed the last couple of months and I had a wonderful time as “monster keepers” working with you. I would especially like to thank Marc for a good and fun collaboration during my first year as a Ph.D. student.

I would like to thank all the lab technicians at Risø, especially Annelise, Pernille and Agnes, you have made a trip to the lab a good time every day, and I would particularly like to thank you for the help and care during my pregnancy. I would like to thank Mike, you found a solution no matter what problem and device I needed constructed. I would also like to thank Kristina at Uppsala University and Ulla at University of Southern Denmark. I was very happy to visit and borrow your equipment and time.

I would like to thank all the people who helped during my time at Korean Advanced Institute of Science and Technology: I would like to thank Professor Jang Wook Choi and Professor Do-Kyung Kim for letting me visit your research groups. I would also like to thank Ji Hoon, Buyng Gon and Young Hwa. It was very interesting to collaborate with you and I would like to thank you for taking very good care of me during my stay in South Korea. I enjoyed visiting your country, learning about both your research but also your culture. I find myself missing kimchi rather often and I still practice my skill with metal chopsticks, so I, as I learned, can enhance my intellect.

I would like to thank all my friends and family for the care and interest you have taken in my work. It is always the time for more ice cream, more cake, more champagne, many more good times, and I look forward to many good times in the future. I would like to thank for all the help babysitting so that the last year of the Ph.D. went as smoothly as the first two.

I would like to thank Thor for not caring a bit about his mothers work but always greeting me with cubby hugs, many smiles, and wet kisses whenever I got home. At last I would like to thank Thomas.

Abstract

A possible future battery type is the Li-air battery which theoretically has the potential of reaching gravimetric energy densities close to those of gasoline. The Li-air battery is discharged by the reaction of Li-ions and oxygen, drawn from the air, reacting at the battery cathode to form Li_2O_2. The type of cathode material affects the battery discharge capacity and charging potential and with a carbon based cathode many questions are still unanswered. The focus of this Ph.D. project has been the synthesis of reduced graphene oxide as well as the investigation of the effect of reduced graphene oxide as a cathode material, combined with *in situ* investigations of the formation of decomposition products in and on the cathode. The reduced graphene oxide was synthesized by the modified Hummers method followed by thermal reduction of graphene oxide, while both were investigated by *in situ* X-ray diffraction. This study revealed an early formation of graphene oxide, new graphene oxide diffraction peaks and an unidentified crystal phase along with a disordered stage of the thermal reduction of graphene oxide. The oxidation time effect on graphene oxide, synthesized by the modified Hummers method, and the following chemically and thermal reduced graphene oxide was investigated. This revealed that trends introduced by changes in oxidation time were observed not only for the graphene oxide but also transcended to both types of reduced graphene oxide. Furthermore the change in oxidation time affected the discharge capacity of the battery as well as the charging potential. *In situ* X-ray diffraction studies on carbon black cathodes in a capillary battery showed the formation of crystalline Li_2O_2 on the first discharge cycle, the intensity of Li_2O_2 on the second discharge cycle was however diminished. The study furthermore showed how X-rays may affect the Li-O_2 battery, displaying how *in situ* studies may be invasive. An *in situ* X-ray diffraction study of a reduced graphene oxide cathode showed formation of both LiOH and Li_2O_2 which also was observed in cells with and without addition of water by XPS. The addition of water to the electrolyte gave indications of additional reactions taking place in the cell

The information provided in this study is useful for a better understanding of reduced graphene oxide both in regards to synthesis and as cathode material in Li-air batteries. The thesis illuminates the importance of considering the synthesis of reduced graphene oxide as this seems to be couple to the abilities as cathode materials in Li-air batteries. It furthermore introduces two types of capillary battery designs optimized for Li-air and *in situ* X-ray diffraction, but with possibilities within metal-air batteries in general, and it opens up for a discussion of how invasive *in situ* methods may be.

Dansk Resumé

En mulig fremtidig batteritype er Li-luft batteriet, som har potentiale til at nå en gravimetriske energitæthed lignende benzin. Li-luft batteriet aflader ved en reaktion mellem Li-ioner og ilt fra luften, der kombineres på katoden i batteriet til ideelt at danne Li_2O_2. Katodematerialet påvirker batteriets afladningskapacitet og opladningspotentiale, og for den karbon baseret katode er stadig mange spørgsmål ubesvaret. Dette har været motivationen for dette Ph.D.-projekt, med det hovedformål at undersøge syntesen af reduceret grafenoxid, effekten af reduceret grafenoxid som katode materiale og *in situ* dannelsen af afladningsprodukter på katoden. Syntesen af reduceret grafenoxid, igennem den indledende syntese af grafenoxid via den modificerede Hummers metode og efterfølgende termisk reduktion af grafenoxid, blev undersøgt ved *in situ* røntgendiffraktion: Denne undersøgelse viste en tidlig dannelse af grafenoxid, nye grafenoxid diffraktioner, og en uidentificeret fase samt en uordentlig fase observeret i løbet af den termiske reduktion af grafenoxid. Oxidationstidens indvirkning på grafenoxid, syntetiseret ved den modificerede Hummers metode, og følgende kemisk og termisk reduktion af grafenoxid blev undersøgt: Dette studie viste at tendenserne indført ved ændringer i oxidationtiden ikke blot påvirkede grafenoxid, men også havde indvirkning på begge type af reduceret grafenoxid. Endvidere påvirkede ændringen i oxidationstid afladningskapaciten i batteriet samt opladningspotentialet. *In situ* røntgendiffraktion undersøgelsen af en karbon katode i et kapillærbatteri designet til *in situ* studiet, viste dannelsen af krystallinsk Li_2O_2 under den første afladning. Allerede på anden afladning var denne intensitet dog aftagende. Undersøgelsen viste desuden, hvordan røntgenstrålerne kan påvirke Li-O_2 batteriet, og illustrerede hvordan *in situ* undersøgelser kan være invaderende på kemien. En *in situ* røntgendiffraktion undersøgelse af en reduced grafenoxid katode viste dannelsen af både LiOH og Li_2O_2 hvilke også blev observeret i celler med og uden tilsat vand i elektrolytten. Tilsætningen af vand til elektrolytten gav indikationer om yderlige reaktioner i batterierne.
Oplysningerne i dette studie er nyttige for en bedre forståelse af reduceret grafenoxid både i forhold til syntese og som katode materiale. Afhandlingen belyser betydningen af syntesemetoden for reduceret grafenoxid, da denne lader til at påvirke essentielle egenskaber i Li-luft batterierne med reduceret grafenoxid som katodemateriale. Der introduceres to typer af kapillærbatteri design der er optimeret til Li-luft og *in situ* røntgendiffraktion, men med muligheder inden for andre metal-luft batterier. Desuden åbnes op for en diskussion af, hvor invasiv *in situ* metoder kan være.

Abbreviations

Frequently used abbreviations in the thesis:

BET	Brunauer, Emmett, and Teller surface area
CNT	Carbon nanotubes
DEMS	Differential electrochemical mass spectrometer
DFT	Density Functional Theory
DME	1,2-Dimethoxyethane
DMSO	Dimethyl sulfoxide
GO	Graphene oxide
hr(s)	Hour(s)
HyrGO	Hydrazine reduced graphene oxide
I	Intensity
LiTFSI	Lithium bis(trifluoromethylsulfonyl)imide
NMR	Nuclear magnetic resonance
NMP	N-methyl-2-pyrrolidone
OCV	Open circuit voltage
PTFE	Polytetrafluoroethylene
PVDF	Polyvinylidene difluoride
rGO	Reduced graphene oxide
RPM	Rotations per minute
SEI	Solid electrolyte interface
SS	Stainless steel
SS NMR	Solid state nuclear magnetic resonance
TEGDME	Tetraethyle glycon dimethyl ether
TGA-MS	Thermogravimetry mass spectrometry
TrGO	Thermally reduced graphene oxide
XPS	X-ray photoelectron spectroscopy
XRD	X-ray diffraction

Contents

Preface i

Acknowledgements iii

Abstract v

Dansk Resumé vii

Abbreviations ix

Contents xi

1. Introduction 1

1.1. Energy 1
1.2. Electric Vehicles 2
1.3. Batteries 3
1.4. A brief history of the Li-air battery 5
1.5. Thesis scope and overview 6
1.6. Articles 7

2. Theory 9

2.1. The Li-air battery 9
2.1.1. Reaction mechanism 10
2.1.2. Anode 12
2.1.3. Electrolyte 12
2.1.4. Cathode 13
2.2. Battery test 13
2.2.1. Normalization of current and capacity 14
2.3. Cathode material 15
2.3.1. Carbon black 15

2.3.2. Graphene and other advanced carbon based structures 16
2.3.3. Additives: Catalyst and redox mediator 17

3. Experimental Techniques 19
3.1. X-ray diffraction 19
3.1.1. Synchrotron XRD 21
3.2. X-ray photoelectron spectroscopy 21
3.3. Solid state nuclear magnetic resonance 23
3.4. Scanning electron microscopy 24
3.5. Raman spectroscopy 25
3.6. Galvanostatic discharge and charge 26
3.7. Differential electrochemical mass spectrometry 26
3.7.1. Calculation of e^-/O_2 27
3.8. Battery designs 29
3.8.1. Swagelok batteries 29
3.8.2. Capillary batteries 31

4. GO and rGO syntheses 34
4.1. Graphene oxide 34
4.2. Reduced graphene oxide 36
4.2.1. Chemical reduction of GO 37
4.2.2. Thermal reduction of GO 37

5. *In situ* XRD of GO and rGO syntheses 39
5.1. *In situ* XRD of the modified Hummers synthesis 39
5.2. *In situ* XRD on thermal reduction of GO 43
5.2.1. In situ Raman spectroscopy on the thermal reduction of GO 46
5.3. Sub-conclusion 47

6. Oxidation time effects on GO and rGO 48
6.1. GO oxidation time effect 48
6.2. TGA-MS, SEM and BET 48
6.3. XRD 49
6.4. Raman spectroscopy 50
6.5. XPS 51
6.6. Solid state ^{13}C-MAS NMR 53
6.7. Electrochemical evaluation 54
6.7.1. Specific discharge capacity 55
6.7.2. Cycling 56
6.8. Sub-conclusion 56

7. *In situ* analysis of Li-O_2 cathodes 58
7.1. Battery designs 58
7.2. Li_2O_2 on a Super C65 cathode 60
7.3. Li_2O_2 and LiOH on a TrGO cathode 62
7.3.1. DEMS on a TrGO cathode 64
7.4. Sub-Conclusion 65

8. Conclusion and Outlook 67
8.1. Conclusion 67
8.2. Outlook 68

Bibliography 69

Appendix 79

Paper I
Paper II
Paper III
Paper IV

Chapter 1

1. Introduction

1.1. Energy

Ideally energy production should be both cheap as well as environmentally sustainable. The population of the world is increasing and along with an increase in living standard this means that a higher power production is in demand [1,2]. Simultaneously there is a growing awareness of how humans affect the environment and a focus on the limited resources on earth, thus the needed increase in energy production should ideally be less polluting as well as more sustainable. This is not only to leave a "cleaner world" for the generations to come, but also to avoid, if possible, the climate change predicted to be caused by the exhaustion of greenhouse gasses [3] as well as to reduce the problems with smog formation over large cities and industrial areas [4]. The current power production is mainly based on burning limited carbon based resources such as natural gas, oil, and coal as seen from Figure 1.1 showing the total worldwide energy production in 2013 [5].

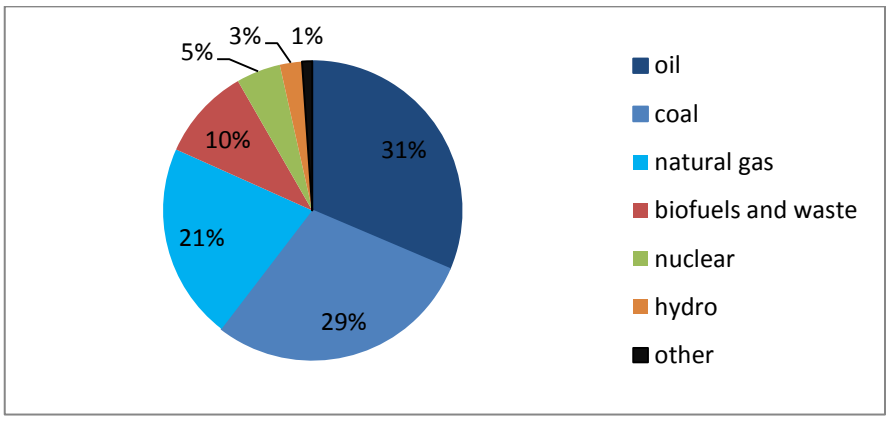

Figure 1.1: The sources of the total energy production of the world in 2013, inspired from ref. [6].

The sustainable energy sources such as tidal, wind, geothermal, and solar power are an alternative to the conventional current production methods. However geothermal energy has very specific requirements for location, and it has been well established that the sun does not shine (sufficiently for energy production) every day and the wind is just as unreliable. This means that an energy demand alone covered by sustainable methods may not meet the consumers demand for an ongoing, continuous, and unlimited supply of energy. Coal, fuel, and gas have the advantage that they are easy to transport and store as well as cheap, thus they have the possibility to produce energy when and where it is needed. For the sustainable energies to be implemented further similar flexibility is needed, and the development of flexible storage is therefore crucial [7].

1.2. Electric Vehicles

The oil consumption alone is a challenge to the world both in regards to political power, exhaustion of greenhouse gasses, and possible oil depletion. The transport sector is the main consumer of the oil (63.8 % in 2013 [5]), but the necessities of the transport sector is in reality cheap, light, and portable energy. These problems could be solved by electric vehicles (EV). EVs may either be fuel cell, capacitor, and/or battery powered, but focus on battery electric vehicles has increased recently [8]. The electrical cars for passenger transport may drive between 120-480 km on a single charge [9], but as the EVs, and especially the battery pack are expensive compared to the gasoline driven car this may hinder worldwide market expansion. In 2011 it was reported that the driving range of EVs should reach 480 km before being recharged to gain the attention of more than 44% of the American consumers. In UK an average range above 320 km is needed to get the interest of 53 % of the consumers [10]. These estimates are despite the fact that the normal day-to-day driving demand of a standard person (approx. 80 km [10]) may be covered by the current cheaper EV's such as the Nissan leaf, ~33,600 €, 135 km per charge (price in Denmark from feb-2016) [11]. The Tesla Model S has a driving range of ~480 km and therefore matches the driving requirements of the general consumer. However, the cost is at least ~140,000 € for a demonstration car (mileage: 16.000 km, price in Denmark from April-2016) [12], whereas more common family gasoline cars cost in the range of 27,000-40,000 €. Furthermore, as the gasoline car is more common on the roads additional infrastructure installations aimed at EVs has to be introduced to make EVs more attractive, whether it being an EV type with the need of a charger or an EV with the additional possibility of an exchangeable battery pack.

Other areas of the transportation sector also have a need for EVs such as transportation of goods by truck, garbage collection, and public transportation. These tasks require heavier vehicles and thus have a demand for even more stored energy. Some of these problems can be solved with capacitors instead of batteries, due to the predictability of the requirements [13,14]; however these are not discussed in this thesis.

It is important to keep in mind that the use of EVs alone does not equal a more sustainable transportation method, as the source of the charging power is essential.

1.3. Batteries

A battery is a device converting chemical energy to electric energy. The chemical energy is primarily stored inside the device in the electrodes, however some components for the chemical reactions may be added externally as in metal-air batteries.

The specific energy of a battery (Wh/kg) is defined by the specific capacity (Ah/kg) and the nominal voltage (V) of the battery multiplied. This provides two parameters that have an influence on the specific energy of a battery. An increase in the voltage of the battery, which is determined by the battery chemistry, will lead to an increase in specific energy. The specific energy can also be increased by an increase of the specific capacity, created either by drawing more current to the cathode or/and by the use of lighter materials. This means that the mass and type of active material determines the theoretical energy of the battery [15]. The energy density (Wh/l) of a battery is defined by the volume of the active components. This is an important measure for space limited applications and is certainly also relevant in the EV industry.

A large range of batteries are commercially available. The primary batteries are single use only with one available discharge, whereas secondary batteries are rechargeable with a reversible chemistry restoring the electrodes by the addition of current. The type of battery employed in a device is dependent on the requirements of the product and the price. Today's EVs utilize Li-ion batteries as the power source, similar to the batteries used in tablets, laptops, and mobile phone. The Li-ion battery has since its commercialization by Sony been the power supply for many new portable electronic devices. Other batteries such as Ni-MH batteries, which have replaced the Ni-Cd batteries, are often used for high power devices such as power tools and are cheaper than the Li-ion battery. Hearing aids use primary Zn-air batteries, with a non-rechargeable chemistry, and the lead-acid batteries are common as car batteries (not used for propulsion). Alkaline batteries are primary batteries and are used for powering

things such as toys, fire alarms, and doorbells. Figure 1.2 shows the specific energy of some of the current commercial batteries.

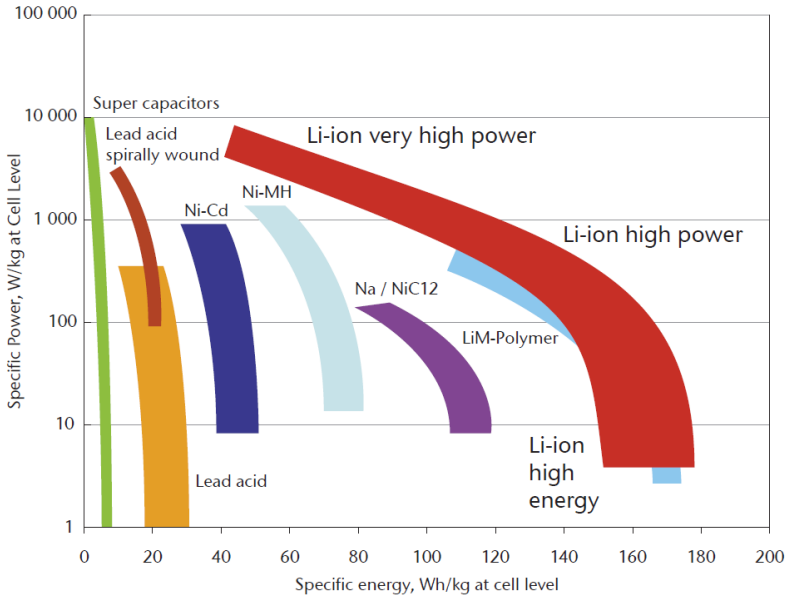

Figure 1.2: Specific energy and specific power from different battery technologies. Reprinted from [16].

The Li-ion battery has the highest specific energy (above 200 Wh/kg) of the commercial batteries [17], but it is not remotely close to matching the energy density of gasoline (13000 Wh/kg [18]). The chemistry of the Li-ion battery is based on movement of Li^+ inside the battery, with intercalation of ions in the negative electrode (often graphite) upon charge and reaction with Li^+ upon discharge at the positive electrode *e.g.* $LiNi_xMn_yCo_zO_2$, $LiMn_2O_4$, or $LiFePO_4$ [15,19]. The specific energy of the Li-ion battery is limited by: The mass of the battery often controlled by the heavy cathodes containing transition metals, the limited amount of Li^+ which may be intercalated in the electrode, and the voltage sensitivity of the components.

New battery technologies are needed to develop batteries with higher specific energy. Figure 1.3 shows the theoretical specific energy of current and future possible battery technologies.

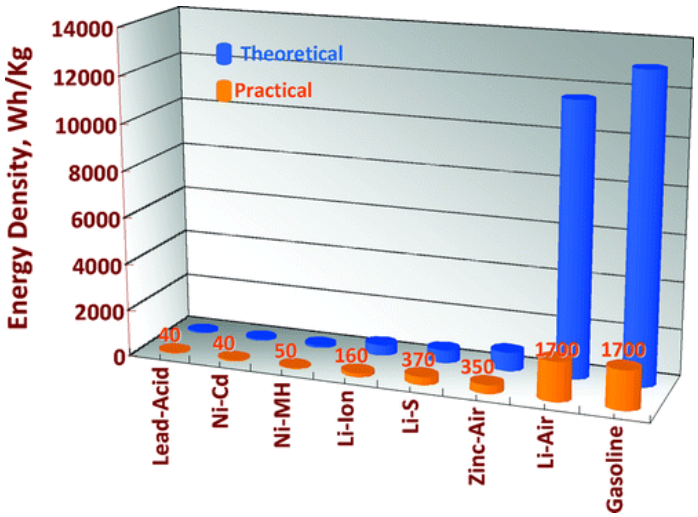

Figure 1.3: Calculated theoretical and practical specific energy of current and future battery technologies. Reprinted from [18].

1.4. A brief history of the Li-air battery

The non-aqueous Li-air battery has a theoretical energy density which is comparable to that of gasoline, as seen in Figure 1.3. In the Li-air battery a Li-anode, under discharge, releases Li^+ to a porous cathode with a gas inlet. At the cathode Li^+ reacts with oxygen to precipitate Li_2O_2. The battery can draw the oxygen from the air, an ability which is needed to reach the promised high capacity and it is then termed a Li-air battery, however many of the batteries found in the scientific literature are tested in pure oxygen and is then named a Li-O_2 battery. Both terms are used in the literature interchangeable. In this thesis "Li-air" is used to term the general concept of the batteries and "Li-O_2" is used more specifically when oxygen alone is involved or considered in a reference or study.

The Li-air battery was first demonstrated by Jiang and Abraham in 1996 [20], and the research in the field was accelerated in 2007 by the demonstration of a Li-O_2 battery with 50 cycles and the measured and confirmed oxygen gas release from the Li-O_2 battery under charge, which demonstrated the possibility of a secondary Li-O_2 battery [21].

The Li-air battery field is challenging and an active research field with many unknown parameters. For the first couple of years the most common solvents of the electrolyte were based on carbonates known from the Li-ion batteries. However, in 2010 it was demonstrated by Mizuno *et al* .[22] that carbonate based electrolyte, 1 M LiTFSI in propylene carbonate, decomposed in the battery and that the final discharge product became the insoluble Li_2CO_3. In 2011 McCloskey e*t al.* [23] found that carbonate based solvents irreversibly decomposed in the cell to form Li_2CO_3, which led

to CO_2 evolution upon charge. This discovery increased the awareness of the need for careful characterization of the researched batteries as impurities can be formed from unwanted reactions with the electrolyte and/or cathode components [24]. Publications are now often supported by *ex situ* and/or *in situ* analyses of cathode materials, discharge product, exhaust gas and electrochemical data. As the Li-air field is under development many subjects are still up for discussion, to mention a few: The importance of catalysts, the composition of both electrolyte and electrodes, and a possible future commercialization of the battery.

1.5. Thesis scope and overview

The thesis is based on three years of work in the period from August, 2012 to June, 2016. The subject is the Li-O_2 battery cathodes. The aim of the project has been to synthesize and investigate different materials as cathode material and to evaluate the capacity and cyclability of the Li-O_2 battery. (This thesis focuses exclusively on Li-O_2 batteries with a non-aqueous electrolyte). At the beginning of the project a graphene cathode held the record of the highest measured capacity [25] in the Li-O_2 battery field, and it was therefore chosen to focus on graphene and graphene based cathodes. Another scope of this project was to investigate reactions at the cathode to gain an understanding of the precipitation of Li_2O_2 on the cathode and battery designs were developed for *in situ* X-ray diffraction (XRD). Many investigated materials showed little promise as future cathode materials compared to a standard carbon black cathode, based on Super C65, and the results of these materials are not reported in the thesis, *e.g.* urea-based and alkali-based synthesized reduced graphene oxide (rGO), MnO_2-covered rGO, and X20 (a porous carbon powder).

The thesis is divided into 8 chapters. Chapter 5-7 describes the individual work of this project. The project has resulted in three papers already published and one recently submitted paper.

Chapter 2 contains a description of the Li-air battery: The battery chemistry, the battery components, test consideration, and some of the challenges regarding those, with an emphasis on the cathode material.

Chapter 3 contains background informations for some of the primary experimental techniques used during the project. Swagelok cell batteries and *in situ* capillary batteries, as well as cathode preparation for these batteries are also described in this chapter.

Chapter 4 describes the synthesis of graphene oxide (GO) through the modified Hummers method and the syntheses for chemical reduction of GO to form hydrazine reduced GO (HyrGO) and thermally reduction of GO to the formation of thermally reduced GO (TrGO).

Chapter 5 describes the results for the synchrotron XRD on the *in situ* study of the modified Hummers method for GO synthesis and the thermal reduction of GO. The chapter is a summary of paper I

Chapter 6 shows the results obtained for an investigation on the effect of changing the oxidation time during the modified Hummers method. The effect is investigated for graphene oxide as well as thermally and chemically reduced graphene oxide (rGO), through characterization with *e.g.* XRD, Raman spectroscopy, X-ray photoelectron spectroscopy (XPS), and solid state nuclear magnetic resonance (SS-NMR). Selected rGO powders were tested and evaluated as cathode materials for Li-O_2 batteries. The chapter is a summary of paper II

Chapter 7 illuminates the Li_2O_2 precipitation and decomposition investigated with *in situ* XRD. Two different *in situ* battery designs are described along with the results for a carbon black cathode and a TrGO cathode. Differential electrochemical mass spectroscopy (DEMS) data for a TrGO cathode with and without 1000 ppm H_2O in the electrolyte are described as well. The chapter is a summary of paper III and IV.

Chapter 8: Conclusion and outlook

1.6. Articles

Paper I

In situ X-ray powder diffraction studies of the synthesis of graphene oxide and formation of reduced graphene oxide

Mie Møller Storm, Rune E. Johnsen, and Poul Norby

Journal of Solid State Chemistry, 240, 49-54 (2016)

Contribution: Data collection was performed by the entire author team at the SNBL. I performed the data analysis and is main author on the paper.

Paper II

Reduced graphene oxide for Li–air batteries: The effect of oxidation time and reduction conditions for graphene oxide

Mie Møller Storm, Marc Overgaard, Reza Younesi, Nini Elisabeth Abildgaard Reeler, Tom Vosch, Ulla Gro Nielsen, Kristina Edström and Poul Norby

Carbon, 85, 233-244 (2015)

Contribution: The oxidation time project was made in close collaboration with master student Marc Overgaard who is co-author on the paper. Mark synthesized the GO and the TrGO, and along with the other authors performed the Raman spectroscopy, XRD and solid state NMR measurements. Mark also collected the SEM pictures of the powders. The XPS was measured together at Uppsala University and the data presented in the thesis were decomposed by me. I synthesized the HyrGO samples, performed the electrochemical testing and compared the solid state NMR results. I wrote the article.

Paper III

Capillary based Li-air batteries for *in situ* synchrotron X-ray powder diffraction studies

Mie Møller Storm, Rune E. Johnsen, Reza Younesi and Poul Norby

Journal of Materials Chemistry A, 3, 3113-3119 (2015)

Contribution: I performed the XRD related experimental work including: cell design and measurements, analysis, and is main author on the paper. The XPS was measured at Uppsala University by Reza Younesi.

Paper IV

In situ analysis of the Li-O_2 battery with thermally reduced graphene oxide cathode: influence of water addition

Mie Møller Storm, Mathias Kjærgård Christensen, Reza Younesi and Poul Norby

Submitted to Journal of Physical Chemistry C

Contribution: I performed the *in situ* XRD, including cell design and data analysis, as well as the TrGO synthesis, the main part of the battery assembling, the DEMS data analysis, SEM measurements, and is main author. The XPS was measured at Uppsala University by Reza Younesi.

Chapter 2

2. Theory

2.1. The Li-air battery

Figure 2.1 gives a schematic overview of a Li-air battery. The Li-air battery consists of a Li anode, an electrolyte, and a cathode. The cathode and anode are in this thesis defined from the discharge reaction of the Li-air battery. Electrochemically the Li-metal is the negative electrode and the oxygen electrode is the positive electrode. Upon discharge electrons are transported through an external circuit from the anode to the cathode and may be used to power for example a car. Under an ideal discharge the Li-ions migrate through the electrolyte (and separator) to the cathode. At the cathode oxygen and the applied current together with Li-ions enable formation of solid Li_2O_2 which precipitate at the cathode, as illustrated by Figure 2.1. Upon charge the reaction is reversed; Li-ions migrates through the electrolyte to the anode and molecular oxygen is released to the atmosphere. Since oxygen is bound in the battery as Li_2O_2 during discharge the battery gains weight when discharging. The Li-air battery in its charged state has a calculated specific energy of 11400 Wh/kg (6080 Wh/l) [26], as the Li-air battery is discharged it also contains the additional Li_2O_2 and the specific energy is changed to 3458 Wh/kg (3445 Wh/l) [26].

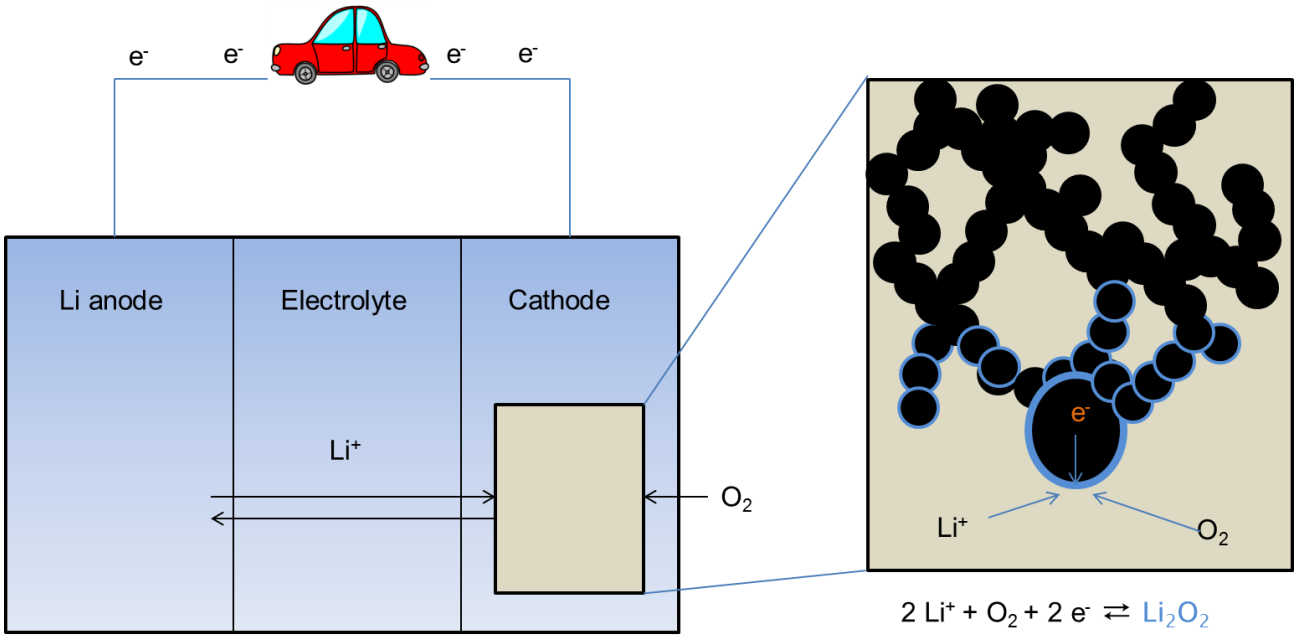

Figure 2.1: A sketch of the Li-air battery. Window: A magnification of the process occurring at the cathode, with the blue cover illustrating the formation of Li_2O_2.

2.1.1. Reaction mechanism

The reaction mechanism for the Li-air battery was proposed by Hummelshøj *et al.* [27] and Laoire *et al.* [28], see step 2.1-2.4. First step is dissolution of Li, followed by the reaction of Li^+ with superoxide at the cathode, and further formation of Li_2O_2 either through an electrochemical reaction (step 2.3) or a chemical reaction (step 2.4).

(2.1)	Step 1	$2Li \rightarrow 2Li^+ + 2e^-$	(anode)
(2.2)	Step 2	$Li^+ + e^- + O_2^* \rightarrow LiO_2^*$	(cathode)
(2.3)	Step 3	$Li^+ + e^- + LiO_2^* \rightarrow Li_2O_2^*$	
(2.4)	Step 4	$LiO_2^* + LiO_2^* \rightarrow O_2 + Li_2O_2^*$	

The * indicates a surface activated species. Although the formation of the LiO_2***** intermediate is not expected to be stable and will transform via either step 2.3 or 2.4, it has however been observed shortly several times. Peng *et al.* [29] observed signals of LiO_2 before Li_2O_2 formation using a combination of CV and surface enhanced Raman spectroscopy, Johnson *et al.* [30] also observed the LiO_2 intermediate in different solvents leading to different types of Li_2O_2 precipitation, and Yang *et al.* [31] observed superoxide like properties on the surface of the bulk Li_2O_2 which disappear at voltages

above 3.7 V. However these observations were later questioned by McCloskey *et al.* [32] as signals assigned to the LiO_2 may origin from decomposition products of the used PVDF binder and the intermediate species are still discussed [33,34]. This discussion is still very active as Bruce *et al.* [30] has observed the LiO_2 signal on a gold surface during CV analysis and Lu *et al.* [35] has observed LiO_2 on an rGO surface along with formation of Li_2O_2.

For many years there was an active discussion in the Li-air field as some research groups observed toroidal shaped Li_2O_2 crystals as discharge products and some observed surfaces covered with Li_2O_2 films, both observed when batteries were operated at low current densities. High current densities resulted in film formation on the cathode. The surface electrochemical mechanism explains the formation of insulating Li_2O_2 film (described by step 2.1-2.4), however the observation of Li_2O_2 toroid shaped particles, which size depended on solvents, additives, and discharge rate was explained by formulation of the concomitant solvation based mechanism, see step 2.5-2.6 [34,36–38].

(2.5) step 5 $LiO_2^* \rightarrow Li^+_{(sol)} + O_2^-{}_{(sol)}$

(2.6) step 6 $O_2^-{}_{(sol)} + Li^+_{(sol)} \rightarrow LiO_2^*$

As LiO_2* is formed on the surface of the cathode during step 2.2 it may either be directly changed through step 2.3 or 2.4 but it may also be solvated if either the electrolyte or additives in the electrolyte can stabilize the $Li^+_{(sol)}$ or/and the $O_2^-{}_{(sol)}$ ions. The solvated ion may then be reassembled as LiO_2* on another surface, such as a toroid. Step 2.3 and 2.4 can then cause the formation of Li_2O_2 as described in the surface electrochemical mechanism. Step 2.4 can even cause the formation of Li_2O_2 on a site inaccessible by electrons. The formation of Li_2O_2 toroids can increase the capacity of the battery as these do not prevent the flow of electrons through the cathode as insulating Li_2O_2 film does. However the charge of the toroids may be a challenge and redox mediators may be employed to reach the Li_2O_2 formed at insulating places by the solution based mechanism.

The reaction upon charge is assumed to be a one-step reaction, reaction 2.7 [39,40].

(2.7) $Li_2O_2 \rightarrow 2\ Li^+ + 2\ e^- + O_2$

As briefly mentioned in chapter 1 challenges in regards to electrolyte decomposition and impurities has been a recurring problem for the Li-O_2 batteries and a completely reversible Li-O_2 battery has to meet several criteria dictated by the electrochemistry and chemistry in order to prove reversible formation of Li_2O_2 [26]: The uptake and

outlet of oxygen should result in an expected ratio of 2 e^-/O_2 both on discharge and charge. Only a stoichiometric equivalent amount of Li_2O_2 should be detected on the cathode after discharge to demonstrate that no other by-products and impurities are formed, as these will decrease the cyclability of the battery. At last only molecular oxygen should be measured from the outlet of a cell upon charge and the amount of oxygen consumed upon discharged should be released upon charge.

2.1.2. Anode

The use of Li-metal as electrode was one of the big challenges for the commercialization of Li-ion batteries. Li-metal is plated and stripped during the cycling of a Li-metal based battery which changes the morphology of the Li-metal. Dendrites are created upon Li-based battery cycling which lead to short-circuiting of the battery and cause a serious safety concerns. Another challenge for the Li-metal electrode is the protection of the very reactive Li-metal by the formation of a flexible and passivating film on the Li-surface, a stable electrolyte interface (SEI) [41,42]. In Li-ion batteries the challenges with Li-metal was solved by using a carbon based electrode with intercalation of Li^+, however the use of pure Li-metal increases the capacity of the entire battery as a carbon based intercalation electrode increases the weight of the battery. It would therefore be ideal to use a pure Li-metal anode in the Li-air battery and any other Li-based batteries. However Li-metal reacts with oxygen, water and nitrogen from the air. Pure Li-metal anodes are often used in the literature, as the problems with the anode are small in comparison to the other challenges of the Li-air battery (see the electrolyte, cathode, and battery test sections). It is therefore also the anode of choice for this project.

2.1.3. Electrolyte

The electrolyte used in this project is non-aqueous which yields a higher theoretical energy density compared to combined electrolyte Li-air batteries or Li-air batteries with aqueous based electrolyte; these are not discussed further in this thesis. The ideal electrolyte has high oxygen solubility and it should furthermore be non-flammable with a low volatility as well as having a high stability towards Li_2O_2 and intermediate products like the superoxide [23,43,44]. As mentioned in chapter 1, the choice of electrolyte has been a challenging field in Li-air. After it was found that carbonate electrolytes decompose to form the insoluble Li_2CO_3 many other electrolyte systems has been tested for decomposition and formation of impurities. McCloskey *et al.* [23] was the first to employ DEMS on a Li-O_2 battery, which measures the exhaust

gasses of the battery and relate the data to the electrochemical information of the battery test. DEMS experiments on a number of non-aqueous solvents [45] and ionic liquids [43], reveals that no electrolyte yet satisfy all the demands of the reversible Li-O_2 battery as described in section 2.1. Even though high cyclability has been reached with Li-O_2 batteries with DMSO [46] and TEGDME [47] based electrolyte, it was chosen to use a 1 M LiTFSI in DME electrolyte in this project as this is currently believed by many to be the lesser evil.

2.1.4. Cathode

Oxygen in the cathode may either be procured from an oxygen tank in a closed system or through an open gas system where the battery is opened to the atmosphere. The use of oxygen from the air gives a range of new challenges in regards to H_2O, as seen from the solution based mechanism [34,36–38] and CO_2, which was found to cause formation of Li_2CO_3 [48–50]**.** Even though N_2 reacts with Li no studies has shown indication of it being a problem for the Li-air battery, neither is Ar [26]**.** The separation of impurities from the air is not further discussed in this thesis.

Many materials have been tested as cathode support materials, but the ideal cathode is made from a cheap, light, stable, and porous material giving the cathode a large surface area. The large surface area of the cathode is important as the solid Li_2O_2 precipitate on the cathode, covering the surface. Li_2O_2 is an insulator which means that electron transport through the cathode will cease when the entire cathode is covered by a sufficient amount of Li_2O_2.

The cathode is often made by casting and drying a mixture of the active material, possible a catalyst and a binder, such as PVDF/kynar, PTFE, or Lithiated nafion. Several of these binders have been found to decompose when combined with Li_2O_2 [51] and their use should be considered, unless a binder free cathode is employed. The use of catalyst to lower the overpotential of the oxygen evolution reaction (OER) is another discussed topic in the Li-air community when exploring the cathode. A small introduction is given in section 2.3.3 however no metal based catalyst has been employed in this thesis.

2.2. Battery test

The overall Li-O_2 battery reaction is given in reaction 2.8.

(2.8) $2\,Li + O_2 \rightleftarrows Li_2O_2$ (ΔG = -570.954 kj/mol [52])

The open circuit voltage (OCV) is the potential difference between the electrodes without circuit. OCV for the Li_2O_2 formation is calculated to 2.96 V from reaction 2.8 from OCV= -ΔG /zF from a 2 electron reaction process (z), faradays constant (F) and the Gibbs free energy (ΔG). However, the measured OCV often starts by being a bit higher at 3.1 V, and then the potential drops below to 2.6-2.7 V upon discharge. A significant overpotential is associated with charging often leading to potentials above 4 V. Figure 2.2 shows a common discharge-charge cycle of a Li-O_2 battery. The large overpotential compared to the standard potential upon charge is believed to be caused by multiple reactions from decomposition of electrolyte and impurities. CO_2 and H_2 gasses are often detected upon charge along with O_2 gas [53]. Figure 2.2 illustrates the overcharging as the charge is longer than the discharge which indicates electrolyte decomposition. The lowering of the overpotential is one of the great challenges in working with Li-air batteries as this would increase the round-trip efficiency of the battery. Figure 2.2 also show how the discharge of the Li-air battery is terminated by a drop in voltage. This is caused by the passivation of the cathode by the insolating Li_2O_2 film preventing charge-transport of the current and is called "the sudden death" [54].

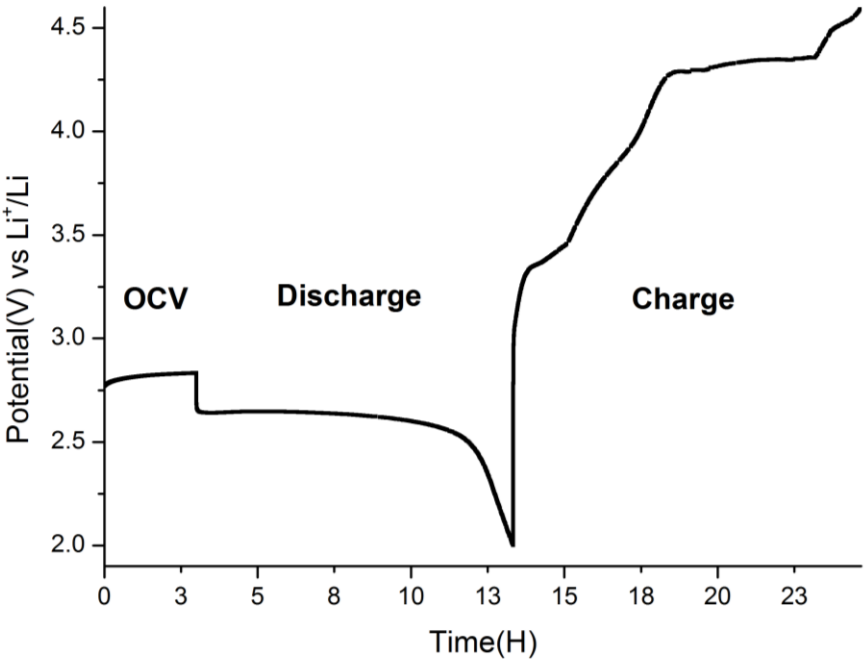

Figure 2.2: A discharge-charge cycle of a Li-O_2 battery

2.2.1. Normalization of current and capacity

Li-air batteries suffer from a poor rate capability, which in ether based solvent has been shoved to origin from the electron transportation through the deposited Li_2O_2 layer at the cathode surface [55].

The measured capacity of the battery is in general normalized to the amount of active material in the cathode. This often results in very high capacities if small amount of active material is used. In order to compare different results it is important to state information of the weight, composition, square footage and if known the height of the cathode. The capacity may also be normalized to the square footage of the cathode area [54].

In this project the current of the graphene cathodes investigated for oxidation times effect was normalization to the area of cathode (paper II), as similar tendencies were observed in other Li-O_2 graphene papers. The current of the DEMS and related measurements was chosen as fast as possible, to allow for the maximum of experiments being performed. In DEMS articles the current is often normalized to the weight of the cathode. The current of the DEMS measurements is high as the fast tests increased measuring frequencies, even though this decreases the capacity.

2.3. Cathode material

2.3.1. Carbon black

Super P, Vulcan XC-72, active carbon, ketjen black, BP2000, calgon, Denka black and JMC are just some of the carbon black tested as cathode materials in Li-O_2 batteries along with several other carbon related cathodes such as carbon nanotubes (CNT), carbon nanofiber, and mesocellular carbon foam [25,56–61]. Carbon black is light, electron conducting and comes with a range of different pore volumes and surface areas available, all features which makes carbon black a good material for cathodes. Carbon black is furthermore cheap and abundant which enhances the advantages of a carbon based cathode. However, Ottakam *et al.* [24] have found by the use of isotope labelled carbon, that the carbon cathode is relative stable below 3.5 V, especially if it has a hydrophobic surface. However, as soon as the battery is cycled to 4 V increased formation of $Li_2{}^{13}CO_3$ from reactions with the cathode was observed and the amounts surpassed the reactions from electrolyte decomposition. They also propose that the carbon cathode enhanced the decomposition of electrolyte, all of which leads to the suggestion of using non-carbon cathodes such as TiC [46] or porous gold cathodes [62]. The decomposition of carbon was supported by McCloskey *et al.* [63] who found that the decomposition upon discharge was due to the electrolyte and salt and their possible chemical reaction with Li_2O_2, and that both the cathode and electrolyte contributed to instabilities upon charge at high potentials. They also found that different carbon cathodes results in slightly different Li_2O_2 yields as different morphologies resulted in different Li_2O_2 surface interfaces and thus different side reactions. The

importance of the carbon surface was also confirmed by Itkis *et al.* [64], who found that the superoxide radicals attack aromatic and defect activated double bonds, so that carbon with a low amount of functional groups and defects demonstrated better stability. Aurbach [65] has suggested to solve the stability challenge between cathode and electrolyte by getting an increased understanding of the Li_2O_2 precipitation, as solid Li_2O_2 forms a barrier that makes a blockage between the cathode and the electrolyte thus protecting both. It is only upon removal of that physical barrier that the problems arise. This suggestion assumes an ideal electrolyte that does not react with strong nucleophiles. He suggested that a fast precipitation, which could be promoted by cathode surface modifications, would make everything less active.

2.3.2. Graphene and other advanced carbon based structures

Graphene consists of single layer 2-dimensional sheet of sp^2 bonded carbon atoms arranged in a honeycomb structure. Graphene has a low density, a high electric conductivity, and a large surface area. For large scale applications the graphene derivative rGO is often used. rGO consist of single or few layers of disordered graphene sheets with scarcely and scattered oxygen functionalities attached. rGO, like graphene, has a large surface area, it has a low density, and electrical conductivity. Graphene based cathodes for Li-O_2 batteries has been investigated both with and without metal catalyst or/and functionalization [66–68]. In general graphene has proven to give very high capacities exceeding those of the carbon black cathodes. In 2011 the highest measured capacity for a Li-O_2 battery of 15,000 mAh/g_{carbon} was reached by a graphene cathode in triglyme electrolyte by Xiao *et al.* [25], this cell was however not charged. The large capacity of graphene is attributed to its morphology. A dual porous structure was proposed by Williford and Zhang [69]. They assumed that a dual porous system would be most efficient for the Li-air battery, where the mesoporous pores can be used for the storage of the decomposition products and the macropores are ideal for transportation of oxygen, thus ensuring oxygen in the entire cathode. Liu *et al.* [70] has recently observed LiOH and Li_2O_2 formation upon discharge on a binderfree graphene based cathode on Al-support with a discharge capacity of 90,000 $mAh/g_{graphene}$, where they ascribe the formation on LiOH as a result of the DMSO based electrolyte. Batteries with thermally annealed graphene foam cathodes and TEGDME based electrolytes has proven to be charged below 3.8 V at cycles of 1000 mAh/g_{carbon} with more defects in the graphene foam cathode observed after 20 cycles [71]. Low charging potentials compared with a possible high surface area and large battery capacity makes graphene and graphene derivative an interesting material for the Li-air battery.

Pristine graphene is often synthesized by chemical vapour deposition or e.g. the scotch tape method [72]. In contrast rGO can be produced at larger scale by several methods in the laboratory. Graphene at different kind of purity levels or with difference in the amount of graphene layers is also commercially available. The functionalities and properties of rGO can be altered by changes in synthesis or by doping.

Several other advanced carbon based designed structures has also been tested as cathode material in Li-O_2 batteries, such as carbon nanotubes [60,61] and mesocellular carbon foam [59]. Some of these structures are binder free as demonstrated for the vertically aligned nitrogen-doped coral-like carbon nanofiber (VA-NCCF) in an array supported by stainless steel [47]. Xu *et al.* [73] developed a free standing honeycomb palladium-modified hollow spherical deposit which were positioned on carbon paper, in order to tailor the initial growth point of LiO_2* growth to control the surface coverage of Li_2O_2. The point of controlling the Li_2O_2 via a tailored cathode was also made by Shu *et al.* [74] who find that their special composition of nitrogen doped graphene and CNT has a specific low barrier for nucleation of Li_2O_2 on the tailored surface. Many different studies with advanced structures are published. These types of structures usually yield good cyclability with high capacity. However, the loading of the active material is often very low resulting in a large specific energy, and a large scale production is rarely considered in the publications.

2.3.3. Additives: Catalyst and redox mediator

The high charge potential of the Li-air battery for the oxygen evolution reaction (OER) has to be lowered to increase the round trip efficiency of the Li-air battery. One of the possibilities investigated by many scientific Li-air battery groups is the use of catalysts. The term "catalyst" is used widely in the Li-air literature, however the mechanism behind the reaction is often unknown and it is not guaranteed that the tested compound is a classic catalyst. MnO_2, Pt, Au, well known from the splitting of the O_2 bond in fuel cells, were all tested in the initial Li-O_2 batteries with the carbonate based electrolytes. However, the discussion of whether they aid to the Li_2O_2 decomposition or aid other reactions was initiated by McCloskey *et al.* [75], who found the general used catalysts to have no positive effects in the battery when tested with a DME based electrolyte. Several catalyst has been tested in many different cathodes and electrolytes with reduction of the overpotential, such as RuO_2 on CNTs [76], $NiCo_2O_4$ nanoflakes with Super C65 [77], TiN nanoparticles supported on Vulcan XC-72 [78], and $LaFeO_3$ on ketjen black carbon [79], however the importance of catalyst is an on-going discussion [26]. One of the challenges in regards to catalysts is its common position on the cathode surface as the surface is covered by the insulating Li_2O_2 and probably

several other by-products during battery cycling. This would make the catalyst inaccessible and render it passivated. Shao-horn *et al.* [80] proposed the presence of soluble metals in the electrolyte to explain the effect of catalysts. These soluble metals were proposed to increase the activation of Li_2O_2 during oxidation by promoting transformation to a lithium metal oxide. Siegel *et al.* [81] used DFT to show how doping of Li_2O_2 with Co-ions may lower the overpotential by enhancing conductivity of Li_2O_2. It was furthermore suggested that the use of catalyst in the cathode causes the presence of metal ions in the electrolyte which dopes the Li_2O_2 as it is formed.

Another interesting study revealing the many possibilities for rGO based cathodes and catalysis was published by Lu *et al.* [35], who showed formation of LiO_2 on a graphene surface with iridium nanoparticles when discharged to 1000 mAh/g without formation of Li_2O_2. Deep discharged cathodes showed formation of both LiO_2 and Li_2O_2 as did the catalyst free 1000 mAh/g discharged rGO cathode. It is assumed that the Ir-rGO cathode favour nucleation and growth of LiO_2 at least during the initial discharge. The allure of LiO_2 is a low overpotential upon charge which could be achieved from better electron conducting abilities of LiO_2. This study show how important the use of catalyst may be for the Li-air battery and how a tailored cathode may affect even the chemistry of the battery.

Another way to possibly lower the overpotential of the cathode is by making the difficult accessible Li_2O_2 available by redox mediators. Gray *et al.* [82] tested an rGO cathode with an LiI redox mediator in 0.25M LiTFSI in DME electrolyte. They found that the use of the redox mediator lowered the over potential to 0.2 V, increased the battery cycle ability to 100 cycles at 1 A/g_{carbon} with a capacity of 8000 $mAh/g_{carbon,}$ but it also changed the decomposition product to LiOH. The mechanism of this redox mediator is unknown but they speculated that the LiI aids in the reaction between LiO_2 and water found in the cell. During the charge a reaction shuttle between electrochemically formed I_3^- and chemically created I^- supposedly aid as the redox mediator. A classic redox mediator was described by Bruce *et al.* [83] who used tetrathiafulvalene (TTF) to carry charge to the solid Li_2O_2 on a nanoporous gold cathode. Upon charge the TTF was oxidized to TTF^+ at the cathode surface which then was reduced at the solid Li_2O_2 and TTF was regenerated. This redox mediator enabled charge at higher rates than for the batteries without redox mediators and it did not change the chemistry of the Li-O_2 battery.

Chapter 3

3. Experimental Techniques

Chapter 3 introduces some of the primary experimental techniques used during the project and presents a summary of the experimental details for the results from paper I-IV. It further more describes the preparation and assemble of the Swagelok cell batteries and *in situ* capillary batteries as well as cathode preparation.

3.1. X-ray diffraction

X-ray diffraction (XRD) can be used for identification of samples and determination of crystal structures. X-rays have a wavelength of ~10^{-10} m which is the approximate range of the distance between atoms in a solid crystal, which means that X-ray may interact with an array of atoms.

A crystal structure is a large atomic structure built up by several similar, periodic and repeated smaller structural units. A crystal consists of unit cells, which are the smallest repeated structure in the crystal. The unit cells are classified into seven different forms termed the lattice system, which can be recognized by the relation of the length of the axes (*a*,*b*,*c*) and difference of the angles (α,β,γ). The crystals contain ordered and "unmoving" atoms and due to the construction of the crystals from smaller cells, the atoms are arranged in a 3D setup causing several different planes of atoms in all directions in the crystals, these planes are termed lattice planes. A lattice plane may be defined by the Miller index describing the plane by three coordinates: *hkl*.

When an X-ray hits an atom it is scattered by the electrons of the given atoms. A similar atom in a parallel miller plane will reflect the X-ray in a similar direction, this may led to constructive interference if Bragg's law is fulfilled [84], Equation 3.1. The diffraction patters reflect the electron distribution of the material.

Equation 3.1 $n\lambda = 2d\sin\theta$ Bragg's law

Where λ is the wavelength of the radiation in Å, n is a whole number, *d* is the planer lattice spacing in Å and θ is the angle of the incoming and reflected radiation in degrees, as illustrated in Figure 3.1. When Bragg's law is fulfilled the scattered X-ray from the second layer of atoms is in phase with the scattered light from the first layer of atoms. This leads to constructive interference enhancing the scattered light, which can be detected in a detector. The intensity of the scattered X-ray is collected in a range of angles, termed 2θ. A powder sample forms a Debye-Scherrer cone signal in XRD. The cone can either be detected using a 2D detector or by measuring the intensity of the light in a range of angles and from this, a 2D diffractogram of intensity vs 2θ is obtained. Each crystal structure has a unique set of diffractions based on the ordering of the atoms in the crystal structure. Miller planes causes the diffraction peaks in a powder diffractogram, and any broadening or other change in a diffraction peak is due to a change in the related direction. X-ray *in situ* studies allow tracking of changes in the crystal structure over time with only the X-ray interfering with the sample.

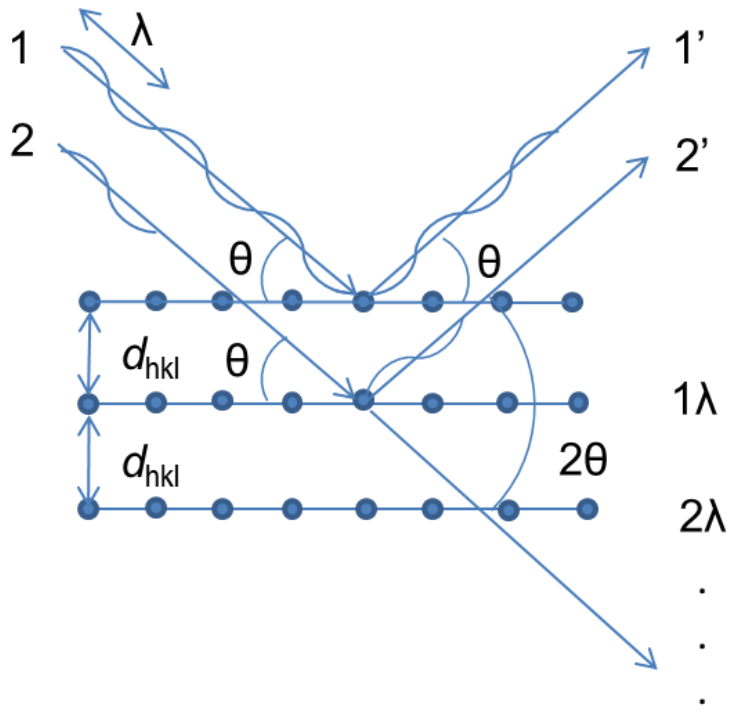

Figure 3.1: An illustration of how atoms diffract X-ray light in accordance to Braggs law, with d_{hkl} being the distance between the crystal plane, 1 and 2 describing incoming X-ray and 1' and 2' the diffracted X-ray, causing whole number in Braggs equation *e.g.* 1λ and 2λ.

Experimental details
In-house XRD of GO and rGO powders for the oxidation time experiments were measured on a BrukerD8 diffractometer with CuKα radiation. XRD investigations of cathodes were measured after disassembly of the battery and cleaning of the cathode with DME to rinse of residual salt of the surface. The cathodes were handled inside a glovebox with oxygen and water levels below 5 ppm. The XRD measurements were carried out with an almost air tight dome containing Ar atmosphere or in a sealed capillary. XRD measurements of the modified Hummers synthesis sample and TrGO capillary battery were performed on a Rigaku smartlab X-ray diffractometer with CuKα radiation.

3.1.1. Synchrotron XRD

Synchrotron X-rays are created by the bending of highly accelerated electrons with a magnetic field leading to emission of electromagnetic radiation. Electrons are accelerated close to the speed of light and are then injected to the storage ring (synchrotron ring) of the synchrotron facility. The electrons travel in the storage ring through different kinds of magnets, such as bending magnets, undulators and wigglers, which bend the electron path thus generating multiple radiation. Synchrotron X-ray radiation has higher intensity, higher brightness, better angular resolution, and tuneable wavelength compared to common in-house X-ray source. This means that short-time exposure experiment with good intensity and a localized beam is possible, which is ideal for *in situ* studies of batteries. Further information on XRD and synchrotron X-ray can be found in refs. [85,86].

Experimental details
The measurements were performed at the European Synchrotron Radiation Facility (ESRF) Swish-Norwegian beamline (SNBL) and at the I711 Maxlab beamline. Capillary batteries were measured at Beamline I711 at MAX-lab. Between the XRD measurements the shutter was primarily closed for 10 minutes in order to minimize any radiation-induced degradation of the sample. A single battery was measured at the ESRF at the SNBL. The investigation of the modified Hummers method and thermal reduction of GO in capillaries were performed at the SNBL at ESRF. Fit2D[87], Topaz[88], EVA[89], PDXL[90] and Powder3D[91] were used for the XRD data analysis.

3.2. X-ray photoelectron spectroscopy

X-ray photoelectron spectroscopy (XPS) is a surface sensitive analysis technique, which reveals the chemical constituent of atoms at the surface of a material. In XPS, a

sample in vacuum is exposed to monochromatic X-ray light of such energy that an electron from the inner core of the atom is ejected. The XPS detect the amount of electrons removed from the 1-10 nm depth of the sample surface by the X-ray radiation and the kinetic energy, as shown in Figure 3.2A. The atomic origin of the expelled electron can be determined by its known binding energy, using equation 3.2.

Equation 3.2 $$E_{binding} = E_{photon} + (E_{kinetic} + \varphi)$$

$E_{binding}$ is the binding energy of the detected atom, E_{photon} is the energy of the used X-ray, $E_{kinetic}$ is the detected kinetic energy, and φ is a work function, which depends on the instrument.

Different atoms have different binding energies and may also result in multiple signals depending on which orbitals are affected by the X-ray. XPS does not only identify the atoms of the surface, it is further more possible to reveal small difference in the binding energy of the atoms, which is caused by the local environment, such as neighbouring atoms, oxidation state, and coordination.

A XPS diagram consists of a plot of binding energy vs count of electrons, Figure 3.2B. The XPS signal of a specific atom can be deconvoluted into different minor peaks based on the environment of the atom. The binding energy may be affected by electron withdrawing or electron donating neighbouring atoms, as well as oxidation state and hybridization. The size of the signal is directly related to the amounts of atoms in the surface of the sample, it is therefore possible to directly compare the ratio of different atoms and their surroundings, meaning that it is both possible to calculate a C/O ratio as well as a C-O/C=O ratio. However the deconvolution may be difficult when comparing specific atomic environments to one another. The deconvolution can be subjective and dependent on the operator, it is therefore easier to make conclusions about changes in signals from two slightly different samples than it is to compare actual numbers. More information on XPS can be found in Heide 2012 [92] and in Pleul and Simon, 2008 [93].

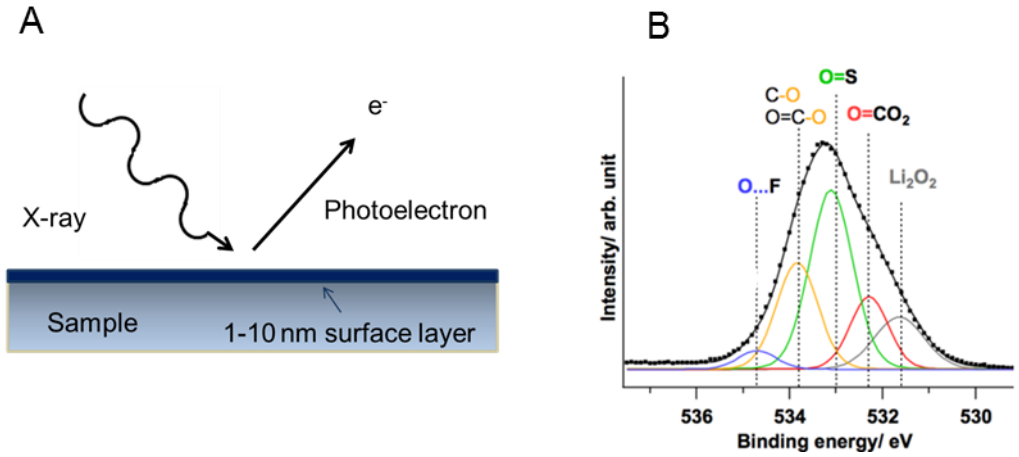

Figure 3.2: A: A sketch of the XPS technique. B: An O1s XPS diagram deconvoluted into peaks corresponding to the local environment of the different oxygen atoms in the sample.

Experimental details

XPS was conducted at University of Uppsala, Department of Chemistry - Ångström Laboratory, Structural Chemistry. Cleaned samples were inserted directly into the XPS after being placed on the sample holder with Cu-tape. Tested cathodes were removed from the battery in a glovebox and cleaned with DME before drying. The samples were prepared in glovebox on Cu-tape and transported to the XPS machine inside an airtight transfer chamber. XPS measurements were performed on a commercial in-house PHI 5500 spectrometer with monochromatic Al Kα radiation. Igor Pro[94] was used for spectra analysis. Associate Prof. Reza Younesi either assisted or performed the XPS measurements as well as XPS spectra deconvolution.

3.3. Solid state nuclear magnetic resonance

Nuclear magnetic resonance (NMR) is used to identify the local environment of certain elements in a molecule. A nucleus with a spin $\neq 0$ in a magnetic field will absorb and reemit electromagnetic radiation as the magnetic field makes the spin states non-degenerate, see Figure 3.3A. The strength of the radiation will depend on the magnetic field as well as the nuclei. A particular nucleus absorbs in a certain radiofrequency area with variations induced by the nearest neighbours. This is used in NMR where radiation of a certain frequency will give information in regards to for example either ^{1}H or ^{13}C atoms.

NMR is usually measured in liquid where the molecule in question has free movement around its axes. In solid state NMR, the solid locked samples often makes

the NMR more complicated, as seen in Figure 3.3B. The energy of the divided spin of a single atom is affected by the environment, the directly connected neighbours but also other atoms, which may be locked in close proximity in a crystal structure. This means that the signals of solid state NMR usually are broad. In order to reduce the amounts of interactions spinning a solid sample at the "magic angle" of 54.57° in relation to the magnetic field suppress the dipolar anisotropic interactions. This is called the Magic-angle-spinning (MAS). Other enhancement techniques are also available, such as cross-polarization which enhances the signal to noise level by transfer of polarization from abundant isotopes to more scarce NMR active nuclei. A small introduction to solid state NMR (SSNMR) is given in [95].

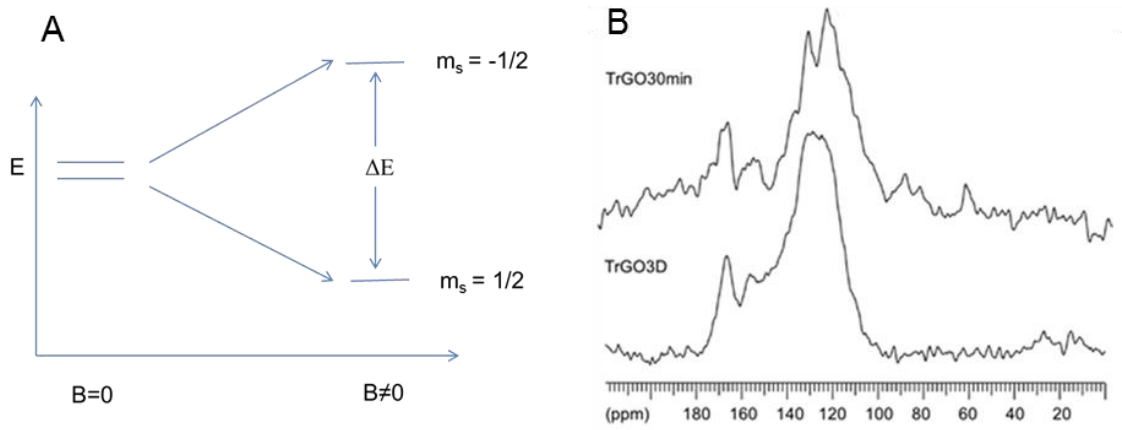

Figure 3.3: A: When a magnetic field is present the former degenerate spin states of nuclei ($S \neq 0$) shifts in energy. B: The broad solid state NMR spectra of two TrGO samples.

Experimental details

The ^{13}C MAS NMR was performed at Department of Physics, Chemistry and Pharmacy, University of Southern Denmark, at 11.7 T (125.6 MHz) using a 3.2 mm MAS NMR probe by associate Prof. Ulla Gro Nielsen, who also assigned ^{13}C resonances. Single pulse ^{13}C MAS NMR spectra of chosen GO and rGO samples were recorded using 15 kHz spinning speed and the spectra were analysed by MestraNova software[96].

3.4. Scanning electron microscopy

A scanning electron microscope (SEM) utilizes a focused electron beam to create an image of a sample surface. The electron beam interacts with the surface of the sample and may explore the various elemental compositions and the topography. As a

sample placed in vacuum is hit with the focused electron beam, it interacts in a specific teardrop shaped sample-volume, where the teardrop is starting at the top surface and is formed down in the sample. The size of the teardrop and thus the investigated area of the sample depends of the strength of the electron beam. The focused electron beam causes several situations, all resulting in signals which may be detected in the SEM. Secondary electrons are often ejected from the k-shell of the atom by inelastic scattering. They are caused by the interaction of the electron beam in the sample with an atom where the affected electron then have to "escape" the solid to be detected. Secondary electrons are usually of low energy and only the electrons from the top layer can be detected. Backscattered electrons are caused by the electrons of the beam being reflected or back-scattered out of the sample by elastic scattering interactions, these electrons are used for exploring chemical composition as the scattering angles depends on the atomic number. Furthermore, if an electron is excited by the electron beam and then emits light as it returns to the ground stage, this is called cathodeluminesence. X-ray may also be formed as a result of an electron dropping to the empty k-shell, formed from the secondary electrons, while emitting X-ray light.

In order to create an image, the focused electron beam scan the sample in a raster pattern of the surface, and the emitted electrons are collected for each position in the scanned area by an electron detector. The electrons escape the top layer of the surface and are used to form the 2D-image of the surface topography. The SEM samples have to be electrical conductive to avoid accumulation of charge which causes artefacts on the image, otherwise a conducting coating may be used. More information on SEM measurements may be found in Egerton, 2005 [97] and in Brandon and Kaplan 2008 [98].

Experimental details:
SEM images were obtained on a TM3000 table top SEM (Hitachi High technologies America Inc.) with an acceleration voltage of 15 keV or on a Carl Zeiss Supra-35 instrument, with 2 keV or 15 keV acceleration voltage. Some of the data was collected by Marc Overgaard.

3.5. Raman spectroscopy

A Raman spectrum can be used to identify a certain compound or to find Raman active vibrations and thus identify specific atoms in a sample.

Raman spectroscopy is an experimental technique that give information in regards to rotational and vibrational modes in a molecule. Raman spectroscopy is the detection of inelastic scattered radiation after illumination of a sample. When a sample is

illuminated with a Raman laser the light may cause a change in vibrational modes of the molecule. Some of the laser light will be scattered at the same frequency (elastic scattering) as it was initially. This light is termed Rayleigh scattering, and is not detected in Raman spectroscopy. However, some of the light will, due to interactions with vibrational modes in the sample, either be scattered with slightly more or slightly less energy than the initial laser light (termed anti-Stokes and Stokes Raman scattering), and this is detected in Raman spectroscopy. Further information in regards to Raman spectroscopy and Raman active vibrations can be found in Atkins and Paula, 2006 [85].

Experimental details:
Raman spectroscopy on GO and rGO from the oxidation time project in paper II was measured by Marc Overgaard and Nini Elisabeth Abildgaard Reeler on an in-house micro-Raman spectrometer with a 514 nm CW Argon Ion laser, at the University of Copenhagen, Department of Chemistry.

3.6. Galvanostatic discharge and charge

The Li-O_2 batteries in this project were evaluated by galvanostatic discharge-charge cycles. During the discharge-charge the current rate was fixed, with a negative current causing discharge and a positive current causing charge. The Li-O_2 batteries were discharge to a minimum of 2 V and charged to a maximum of 4.6 V. At the high voltage regimes the electrolyte started decomposing and the low voltage of 2 V ensured complete sudden death and maximal covering of the cathode with Li_2O_2 and other side products. The data was measured using BioLogic VMP-3 or MPG-2 potentiostats or a Gamry REF600 potentiostat.

3.7. Differential electrochemical mass spectrometry

In the DEMS, a mass spectrometer is attached to a special gas tight battery, along with pressure controllers and a potentiostat. The setup at Risø DTU uses a Swagelok cell that was optimized for the Li-O_2 battery. The cell is either closed or open to the DEMS setup due to a 2-position 6-way valve, as illustrated in Figure 3.4. An open cell records the pressure change during the battery test. A closed cell collects the gasses evolved during the battery test. The DEMS tracks some of the changes in a Li-O_2 battery during discharge and charge. The pressure of the gas may be measured during discharge and charge and the electron count can be related to the amount of oxygen consumed or released (assuming that only oxygen is released). The mass of evolved

gasses during charge may be analysed by a highly sensitive mass spectrometer. The DEMS at DTU was calibrated to the measurements of O_2 and CO_2, and quantitative information can be obtained for these two gasses. In order to investigate the gasses the battery cell is flushed several times upon charge with an inert carrier gas, argon, at certain points and the mass spectrometer collect the data for the amount and weight (m/z) of the gasses. After a flush the battery is closed to the DEMS and continues its simultaneous charge, and can thus be flushed again later. In a Li-O_2 battery the important gasses to investigate upon charge are: oxygen, from the decomposition of Li_2O_2 upon charge, and CO_2 and H_2 from the many possible side reactions in the battery.

3.7.1. Calculation of e^-/O_2

The electron to oxygen ratio may be calculated from the measurements of the pressure and the current in the battery both on discharge and charge as seen in Equation 3.3 [99]. Upon charge this calculation assumes that the pressure is caused by oxygen alone. 2 e^-/O_2 is expected for the perfect formation and decomposition of Li_2O_2, any deviation from 2 is expected to be caused by formation of other discharge product on discharge, the consumption of oxygen and/or decomposition of by-products besides Li_2O_2 upon charge.

Equation 3.3:

$$\Delta ne^- = \frac{R\ T\ \Delta Q}{\Delta P\ F\ V_{cell}}$$

P is the pressure, F is Faradays constant, V_{cell} is the volume of the cell, Q is the capacity calculated from the current and time, R is the ideal gas law constant and T is the temperature.

Another way to investigate the DEMS data is by fitting the measured pressure to the calculated pressure by fitting the variable $n_{electrons}$, as seen in Equation 3.4 and 3.5. where t is time and I is current.

Equation 3.4 $$\Delta P = \frac{n_{O2\ consumed} R\ T}{V}$$

Equation 3.5 $$n_{O2\ consumed} = \frac{I * t}{n_{electron} * F}$$

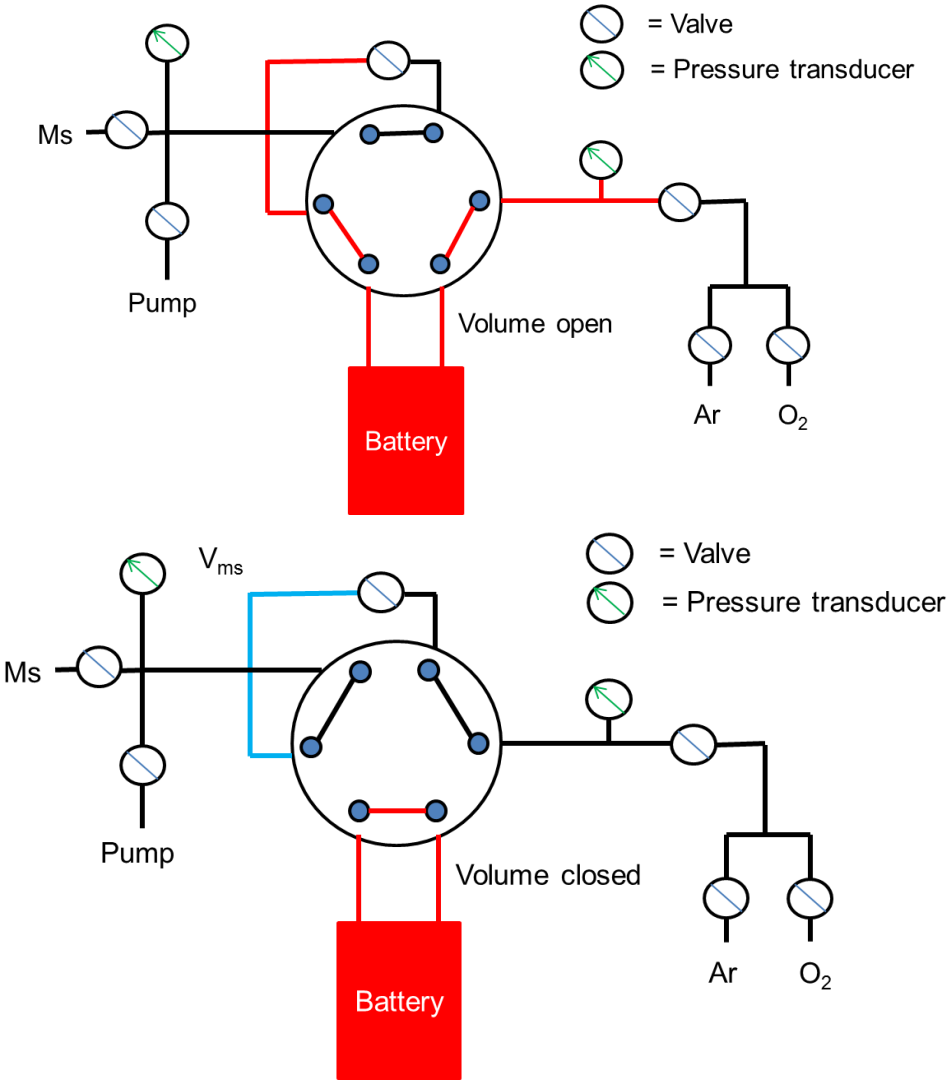

Figure 3.4: Top: A sketch of the open DEMS setup, with the pressure changes of the cell being recorded for the open volume (marked in red). Bottom: A sketch of the closed DEMS setup, with gasses collected for the battery (marked in red) and flushed to the mass spectrum volume (marked in blue) before measurement. Figure inspired from ref [100].

Experimental details:

The DEMS at Risø, DTU was developed by Jonathan Højberg, Andreas Hansen Poulsen and Mathias Kjærgård Christensen for the Reliable project, and more information in regards to the physical setup may be found in [100]. The DEMS setup was inspired by the one developed by McCloskey *et al.* [23].

A DEMS Swagelok cell was assembled with a Li anode (diameter of 10 mm), 2 cleaned and dried Whatmann separators (cleaned in isopropanol and acetones, dried in vacuum furnace 200 °C for 12 hrs), 80 µl of 1M LiTFSI in DME electrolyte, a spray

coated cathode (diameter of 10 mm), and a stainless steel (SS) current collector. The battery was assembled in the glovebox with oxygen and water levels below 5 ppm. Two different measurements were performed on the DEMS: One were the pressure of the battery was monitored upon discharge and charge and a second were the pressure was measured upon discharge and the m/z of the exhaust gas was collected upon charge. The battery was investigated at cycling at 120 μA (0.15 mA/cm^2) between 2 - 4.6 V and between 2.7 - 4.6 V.

3.8. Battery designs

3.8.1. Swagelok batteries

The Swagelok cell was used both for testing of batteries in the DEMS but also as two-electrode batteries for discharge/charge measurements, which were performed on a BioLogic VMP-3 or MPG-2 potentiostats. Figure 3.5 shows a picture of a collected Swagelok cell used as two-electrode batteries and its components.

The battery is assempled between two SS current collectors with a glass tube between them; the glass tube is sealed with two O-rings. It is important to ensure a dry and contaminant-free environment of the battery, thus the separator, current collectors and O-rings all has to be cleaned and dried before battery assembly. The battery parts are cleaned extensively in soap water, demineralized water, ethanol and acetone before drying at 120 °C overnight. The top current collector in the Swagelok cells, the one closest to the cathode, has a 10 ml gas volume with an attachable gas inlet and outlet system. The two current collectors and the glass tube are held together by a Swagelok cell with a PTFE ferrule in each end. The DEMS cells have the additional feature that a screw in the top and bottom of the current collectors makes it possible to tighten the O-ring inside the glass tube. This makes the DEMS design even more air tight. The DEMS cell has a gas inlet without the 10 ml volume, as it is connected to the DEMS while running.

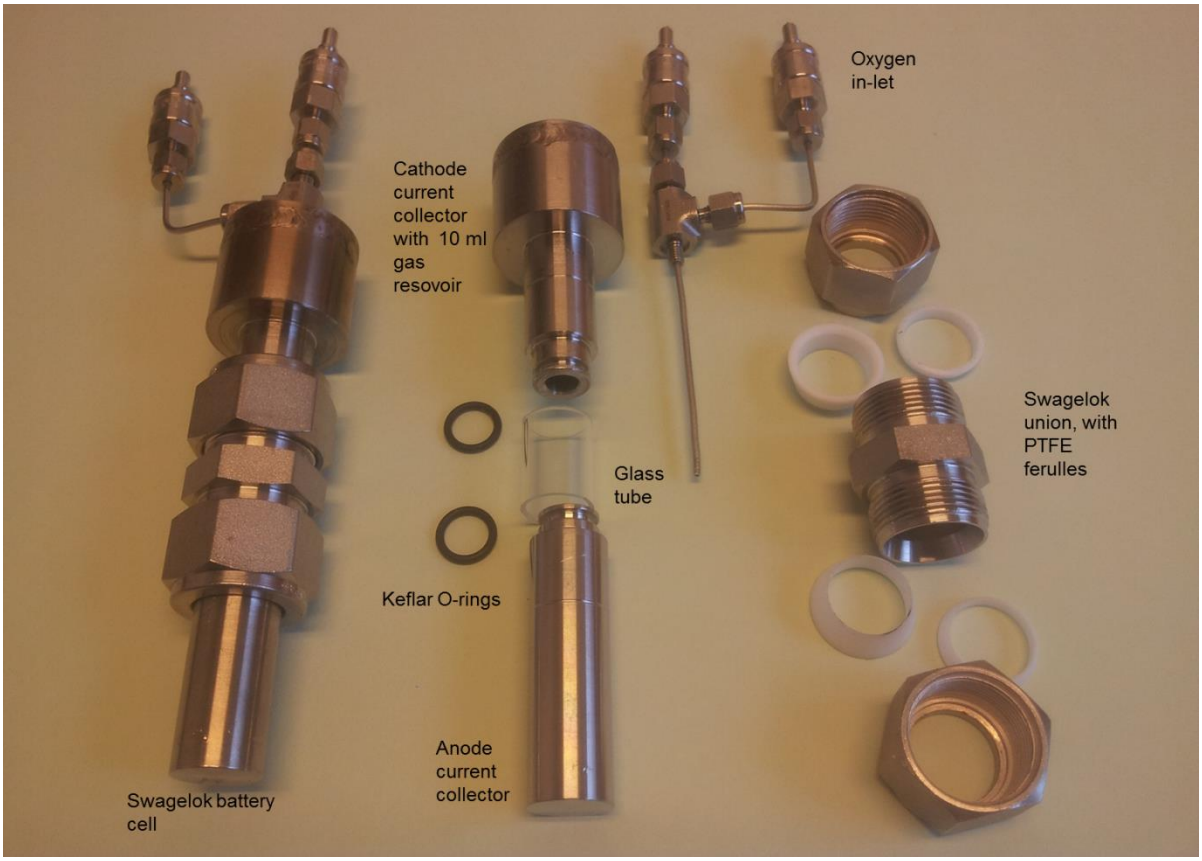

Figure 3.5: An assembled and unassembled Swagelok cell and its components.

Experimental details:

The batteries were assembled with a circular 10 mm Li disk (99,9 % purity), 1 M LiTFSI in DME electrolyte, separators (either 2 celgard disks or 2 Whatman glassfiber disks (GE healthcare, GF/A)) and a cathode. The electrolyte was made by drying the DME (BASF) and LiTFSI (Sigma Aldrich) separately before mixing the electrolyte. The drying procedure changed during the project and the individual drying process for each project is described in the corresponding paper. The battery was assembled in a glovebox and flushed with oxygen for activation and left with an overpressure of approx. 1 bar. The battery was then left at OCV for 3 hrs before discharge to ensure sufficient level of oxygen near the cathode.

The choice of cathode type depended on the amount of available cathode material and the purpose of the cathode. For drop-casted cathode, a slurry of 10% PVDF and 90 w/w % material was prepared by mixing with NMP (50 % PVDF for TrGO cathodes). The slurry was dropped onto a circular cut SS mesh which had been sonicated for 1 hr in 2 M H_2SO_4 and washed with water and acetone, see Figure 3.6A. The cathodes were heated in a vacuum oven inside the glovebox for 12 hrs at 80 °C. The average weight of the cathode depended on the material: TrGO 0.9 mg, HyrGO 1.4 mg and 0.9 mg for

Super C65 (Timcal). The cathode had an average size of 4*4 mm. A minimum of three drop-casted cathodes of each material were tested at a rate of 0.1 mA/cm^2. The syntheses method of TrGO and HyrGO are described in Chapter 4.

Cathodes for the DEMS were prepared by air spraying a slurry on a 316SS 100 mesh, that had been cleaned and dried with ethanol and acetone before use [101]. Slurries were prepared mixing doubled sieved TrGO (sieved through the SS-mesh before mixing) with PTFE (60 wt% dispersion in water, Sigma Aldrich) in a 3:1 wt/wt ratio in a 4:1 water/isopropanol mixture. The slurries were sonicated and sprayed onto the SS mesh with a Badger model 350 air sprayer. The coated mesh was air-dried before being punched into 10 mm disks, see Figure 3.6B. The cathodes were dried in a glovebox at 180 °C for 12 hrs before use. TrGO cathodes had a weight of between 0.3 – 0.5 mg. The cathodes were tested at 120 μA (0.15 mA/cm^2).

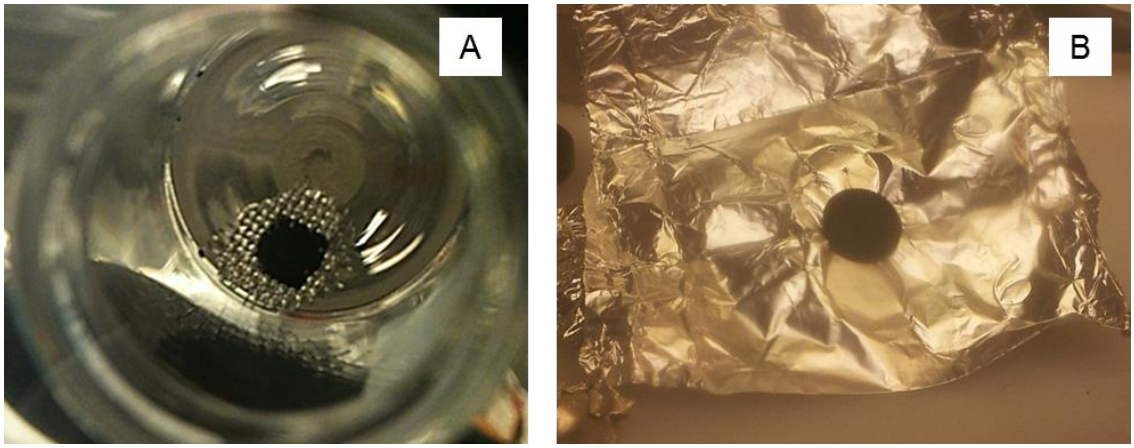

Figure 3.6 A: Drop-casted Super C65 cathode, B: Spray casted TrGO cathode.

3.8.2. Capillary batteries

The capillary batteries were designed for *in situ* XRD. The aim of the designs was to have a small cathode suspended inside a capillary above a Li-anode. Capillary batteries for *in situ* XRD were designed by Norby and Johnsen [102], and it was these type of batteries that formed the initial inspiration for the capillary batteries with a gas inlet. Two designs were developed, see Figure 3.7. In design 1 the cathode is suspended on a stainless steel wire into a round capillary, with an oxygen gas inlet attached to the top of the capillary. In this design boron silicate glass was used for in-house experiments and quartz glass was used at the synchrotron. In design 2 the cathode was suspended into a square capillary on a hollow SS wire with an outer diameter of 0.7 mm. The oxygen inlet was attached to the hollow wire and oxygen accessed the battery via the cathode. The outer diameter of the SS wire needed for a working battery was tested by assemble of a battery and measuring of the OCV after addition of oxygen. After two weeks the battery with a hollow SS wire of 0.3 mm had yet to reach an OCV

of 2.9 V, the 0.5 mm hollow wire took 5 hrs (which was deemed too long for synchrotron wait time) which is why the 0.7 hollow SS wire was chosen.

The cathode was made with PVDF, despite the fact that it has been found to decompose [103]. The decision of working with PVDF came from the fact that we had a working cathode, and that several other possible decompositions probably were taking place in the battery anyway. As the PVDF did not decompose to crystalline material on the first cycle it was concluded that the use of binder was not disturbing the *in situ* investigation. Cable connection problems were observed when the batteries were tested at the synchrotron facilities, leading to noisy discharge-charge curves, however as the capillary batteries resulted in normal discharge-charges on the BioLogic VMP-3 or MPG-2 potentiostat it was deemed safe to smooth the curves mathematically, instead of dismissing the data.

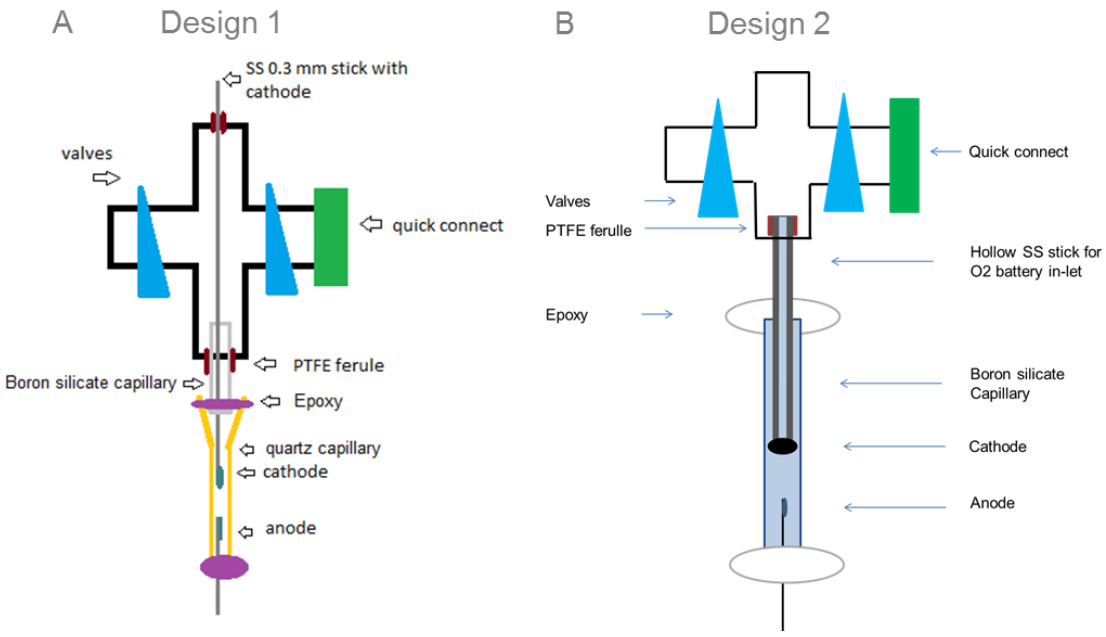

Figure 3.7: A: *In situ* XRD capillary battery with oxygen inlet through the capillary. B: *In situ* XRD capillary battery with oxygen inlet through the cathode.

Experimental details:

Capillary cathodes were prepared by dip coating a cleaned and honed SS wire in slurry several times and dry between the dipping with a heating gun at 100-130 °C until the wanted cathode size was reached, ~ 0.1-0.2 mg. The SS wire either had a thickness of 0.3 mm or was hollow with an outer diameter of 0.7 mm. The slurry for the 0.3 mm wire (design 1) was made from a mixture of Super C65 and 15-20% wt PVDF in NMP and the mixture for the hollow SS wire (design 2) was made by a 50 w/w % mixture of TrGO and PVDF or SuperC65 and PVDF in NMP. The cathodes were dried in vacuum

owen in the glovebox (0.3 mm: 80° for 12 hrs, 0.7 mm: 180° for 12 hrs). Li-metal was smeared on a 0.4 mm SS wire and glued to either a square or round capillary. The capillary was filled with electrolyte and the 0.3 mm wire batteries were assembled by attaching the cathode wire and the capillary to the oxygen inlet unit. For the 0.7 mm batteries the cathode was glued onto the capillary and the oxygen inlet was later attached to the hollow SS wire. The batteries were flushed with approximately 1 bar overpressure of O_2 and after a waiting time of 3 hrs the battery tests could be initiated. The batteries were tested at currents of 3-6μA.

Chapter 4

4. GO and rGO syntheses

Chapter 4 introduces the syntheses for formation of GO, HyrGO and TrGO, as well as the experimental details of the procedures. Some of the syntheses described are investigated in paper I and used in paper II and IV.

4.1. Graphene oxide

GO may be used as a precursor for synthesis of large scale production of rGO [104,105], however it may also be used for sensors, for its luminescence abilities and it can be functionalized. Several review articles have been published concerning GO, rGO and graphene, and can be recommended for further information on the many applications, procedures, and characteristics of the compounds [106–109].

The structure of GO is unknown and several different structures have been proposed, the current popular model is the Lerf-Klinowski model as seen in Figure 4.1. In this model GO consist of a graphene like sheet backbone, with sp_2 hybridized hexagonal carbons, which is functionalized with several different oxygen groups both on the centre of the sheet and at the edges [106]. The functional groups disturb the perfect graphene structure which explains why GO is less conducting than graphene.

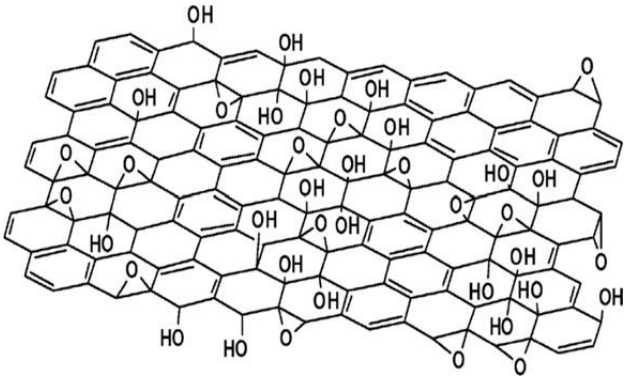

Figure 4.1: The Lerf-Klinowski model for the structure of GO with carboxyl, epoxides, carbonyl and hydroxygroups functionalizing the graphene sheet and edges. Reprinted from [106].

Graphene oxide was prepared in 1859 by Brodie [110], however his method was highly chemically unstable and toxic gasses developed from the synthesis. Staudenmaier [111] in 1898 and Hummer and Offeman [112] in 1958 proposed their own synthesis routes to GO. The Hummers method is based on forming a highly oxidizing environment with concentrated sulfuric acid, permanganate and nitrate, which oxidize graphite into GO. Several modifications have been made to the Hummers methods [113–115] which now is known as the modified Hummers method.

The modified Hummers method is based on oxidation of graphite. Graphite is built from stacked ordered carbon layers with the carbon placed in a hexagonal structure. This structure could be important for the synthesis as it was not possible to perform the synthesis on amorphous isotope labelled ^{13}C. The importance of the layered and ordered carbon could be explained with the first step in the synthesis being intercalation, as discussed in chapter 5.

The mechanism of the modified Hummers method is unknown but Dreyer *et al.* [116] suggested that the active oxidizing species comes from the reaction of permanganate and sulfuric acid, which forms the diamanganese heptoxide, see reaction 4.1 and 4.2. Their consideration is based on Mn_2O_7 ability to selectively oxidize unsaturated aliphatic double bonds over aromatic bonds. The presence of this specie has yet to be confirmed.

Reaction 4.1: $KMn^{VII}O_4 + 3\ H_2SO_4 \rightarrow K^+ + Mn^{VII}O_3^+ + H_3O^+ + 3\ HSO_4^-$
Reaction 4.2: $MnO_3^+ + MnO_4^- \rightarrow Mn_2O_7$

Dimiev and Tour [117] investigated physical changes to the graphite layer during the oxidation using SEM and Raman spectroscopy and observed three stages: Graphite intercalation, graphite oxidation, and formation of GO.

The modified Hummers method was used in this project for preparation of GO for paper I, II and IV.

Experimental details for the modified Hummers method synthesis:
3.00 g of natural flake graphite, 325 mesh, with 99.8 % metals basis (Alfa Aesar) and 1.50 g $NaNO_3$ was placed in an Erlenmeyer flask on ice bath. 100 ml concentrated H_2SO_4 was added under stirring resulting in a thick black dispersion. After cooling for 10 minutes 12.00 g of $KMnO_4$ was added slowly over 40 minutes, and a colour change from dark purple to green was observed indicating a clear change of the permanganate ion. The solution was kept on ice during this step. Upon completed addition of $KMnO_4$ the solution was kept on an ice bath for 2 hrs in order to ensure proper cooling of the highly exothermic mixture. After the cooling of the reaction mixture, the mixture was

heated to 35 °C with a water bath and then stirred at 35 °C for selected oxidation time that varied between 30 min to 3 days (3 hrs is standard time and used if no other information is given). A thick dark/red paste formed during the heating. Oxidation was terminated by placing the solution on ice and diluting with 100 ml ice cooled water following by slow addition of 25 ml H_2O_2 (30% w/w in H2O). Addition of the first 5 ml of H_2O_2 resulted in a heavy exothermic O_2 gas evolution**.** When gas evolution ceased the solution was centrifuged at 4500 rpm (3260 g) for 10 minutes and the supernatant was removed. The precipitate was washed with 0.1 M H_2SO_4 and dried in vacuum oven at 25 °C overnight. The GO was purified further by an acid-acetone purification [118], where the GO powder was washed 4 times with 0.1 M HCl, dried in vacuum oven at 25 °C followed by washing four times with acetone and vacuum oven drying at 25 °C.
The isolated GO powders were brown/greyish in appearance and yielded a brown/yellowish dispersion in water. After reduction the rGO powder could not be dispersed in water due to lack of the polarizing oxygen groups.

Experimental details for in situ XRD:
A simplified Hummers synthesis was performed in a quartz glass capillary reaction chamber (outer diameter 0.7 mm) where a graphite/sulfuric acid suspension was pushed by N_2 gas into $KMnO_4$ powder during synchrotron X-ray measurements. The capillary was closed with fiber plugs which dried the sample during the synthesis, however the colours of the laboratory synthesis, purple, green, and black was still observed in the capillary. A comparison of the terminal X-ray diffraction image of the capillary synthesis was similar to a sample from the laboratory scaled synthesis taken before H_2O_2 additions. These are all indicators to that the mechanism of the laboratory based synthesis may be discussed from the capillary gained data.

4.2. Reduced graphene oxide

rGO may be synthesized from several different routes, all leading to slight differences in the product. The most common routes are chemical reduction and thermal reduction of GO. Chemical reduction may among other be performed with hydrazine hydrate [119], urea [120] and by alkaline reduction [121]. Thermal reduction is performed by heating GO in an inert atmosphere either by controlled ramp heating or shock heating. These two methods, based on the reduction of GO, often yield large amount of defect rich and functionalized rGO. The two methods were chosen for the project based on their popularity but also for the formation of defect rich oxygen filled surfaces, as DFT calculations show a stronger binding between Li_2O_2 and defect filled

graphene surfaces, compared to defect free graphene. A strength which was enhanced by the presence of COOH groups [25]. This enhanced binding strength indicates that Li_2O_2 is more likely to bind near defect filled sites and oxygen functionalities, a conclusion that also supports that tailored structured material might result in better nucleation of Li_2O_2.

Other methods, which results in bulk amount of more pristine graphene, such as electrochemical exfoliation [122] and shear mixing of graphite [123], has not been explored in this project.

4.2.1. Chemical reduction of GO

The basis of the chemical reduction with hydrazine hydrate is exfoliation of the GO sheets in water followed by reduction of target oxygen groups [119]. The hydrazine reduction mechanism is proposed to go through a ring opening of epoxides followed by removal of water and formation of hydrazino alcohol. Hydrazine may then be removed followed by reformation of the double bond. The hydrazine reduction introduces traces of nitrogen into the final rGO product which is explained by reaction of hydrazine with lactones, anhydrides and quinones as reactions with these forms hydrazides and hydrazones. Other mechanism has been suggested as well.

Chemical reduction of GO with hydrazine hydrate was used in paper II.

Experimental details:

The synthesis was initiated by delamination of 0.2 g GO in 200 ml water by sonication for at least 1 hr followed by filtration on a Büchner funnel with filter paper, which removed unwanted insoluble impurities. To a round bottom flask containing the delaminated GO 2.0 ml of hydrazinium hydroxide was added for the reduction. The solution was then heated under reflux at 100 °C for 24 hrs, causing precipitation of solid black rGO. The solution was filtered and the rGO was washed with 5x500 ml milliQ water and 5x100 ml methanol. The rGO was dried in air overnight and afterwards dried in an oven at 90 °C for 12 hrs.

4.2.2. Thermal reduction of GO

GO contains water and oxygen functionalities that enable the thermal reduction of GO. Upon heating CO_2, CO and water expand and the gas pressure rips apart the layers of GO, while some oxygen functionalities are being removed and defects are created [124]. It has been observed that a slow heating ramp causes a rGO with a higher order observed by XRD compared to rGO created by shock heating. Upon slow heating a defined 002 rGO diffraction peak is observed whereas shock heating results in rGO

where only a small and broad 002 diffraction peak may be observed. This was explained by McAllister *et al.* [125], by assuming that the slowly heated sample resulted in a smaller pressure between the graphite layers causing lesser disorder.

Experimental details:
Thermal reduction was performed in a tube furnace (Carbolite) preheated to 1100 °C. 0.2-0.3 g GO was placed in an alumina boat in a quartz tube, which was flushed with Ar. The quartz tube was inserted in the furnace for 2 min of shock heating, the glass was extracted, cooled and the rGO powder was collected and washed with acetone.

Experimental details for in situ XRD:
For *in situ* synchrotron XRD analysis of the thermal reduction of GO, a 0.5 mm capillary was filled with approx. 1.5 cm of synthesized GO and both ends were closed with quartz glass fiber or quartz wool plugs. The beam was optimized on the GO sample, which was heated using a hot-air blower with heating ramps of 1, 5, 10, 20, and 50 °C/min. The temperature was increased from 25 to 690 °C and data were also collected during cooling. The temperature of the hot-air blower was calibrated with a powdered silver sample using the thermal expansion (unit cell volume as a function of temperature). The hot-air blower had a non-linear increase in temperature. A flow of N_2 was used on all samples except one. Samples of differently synthesized GO was tested *in situ* as was the addition of trace amounts of diamond powder to the sample.
Thermal reduction of GO was used in paper II and IV, and *in situ* XRD was described in paper I.

Chapter 5

5. *In situ* XRD of GO and rGO syntheses

5.1. *In situ* XRD of the modified Hummers synthesis

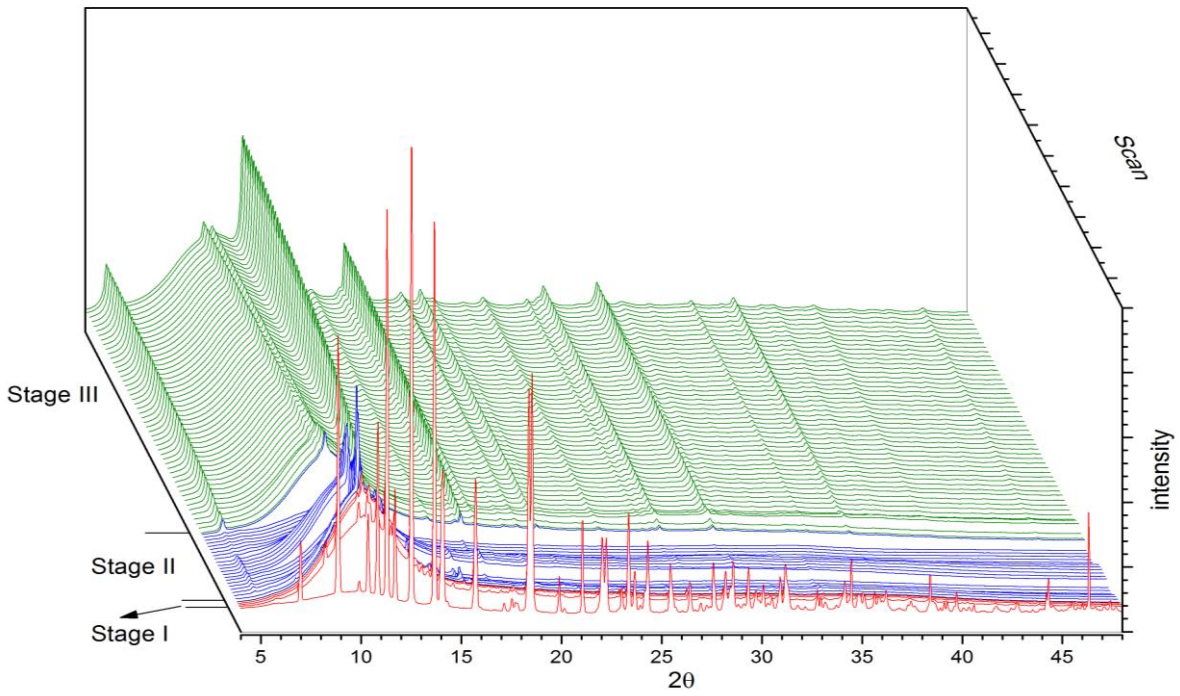

Figure 5.1: The *in situ* XRD patterns of the modified Hummers synthesis in a capillary. Stage I displays every scan, stage II every 2nd and stage III every 3rd, one scan is 30 s long.

The X-ray diffraction of the modified Hummers methods is shown in Figure 5.1. The data was separated into three different stages based on the change around 10° in 2θ. As the graphite/sulfuric acid dispersion was pushed into permanganate, the permanganate diffractions quickly diminished and stage II was initiated. Stage II displays few diffraction peaks with its main feature being the single peak 10.18° in 2θ. The single peak of stage II was split into two smaller peaks at 9.89 and 10.31° in 2θ which was determined to be stage III. As early as stage II the 001 diffraction of GO was observed at 5.05° in 2θ, showing how the GO evolves early during the synthesis along with the other changes observed in stage II and III.

The diffractions and their assignment of stage II is displayed in Figure 5.2 and Table 5.1. As mentioned above the GO diffraction peak is observed already as early as stage II showing how some of the graphite is oxidized very fast. During stage II the diffraction peaks match the diffraction peaks of graphite-hydrogensulfate, which indicate intercalation of the sulfuric acid and/or hydrogensulfate ions into the graphitic layer. Water may also be intercalated during this step. Whether this intercalation is an oxidative intercalation cannot be determined by XRD, but as the synthesis mixture is highly oxidizing and since GO forms very fast during the synthesis, it is plausible. A small diffraction peak at 11.8° in 2θ may be the 002 graphite diffraction. From the observed diffractions of graphite-hydrogensulfate the XRD results indicate intercalation as first part of the synthesis. The intercalation was also observed by Dimiev and Tour [117], however they observed the formation of GO last, in contrast to these observations.

Angle / ° 2θ	*d*-value/ Å	Integrated Intensity/Count	Assignment
5.048	7.970	409	GO (001)
10.186	3.954	2434	Graphite-hydrogensulfate
10.490	3.840	1420	Shoulder, possibly GO
11.797	3.415	977	Graphite (002)
15.333	2.631	556	Graphite-hydrogensulfate
16.878	2.392	429	
19.073	2.119	394	

Table 5.1: The diffraction peaks of stage II and their assignment.

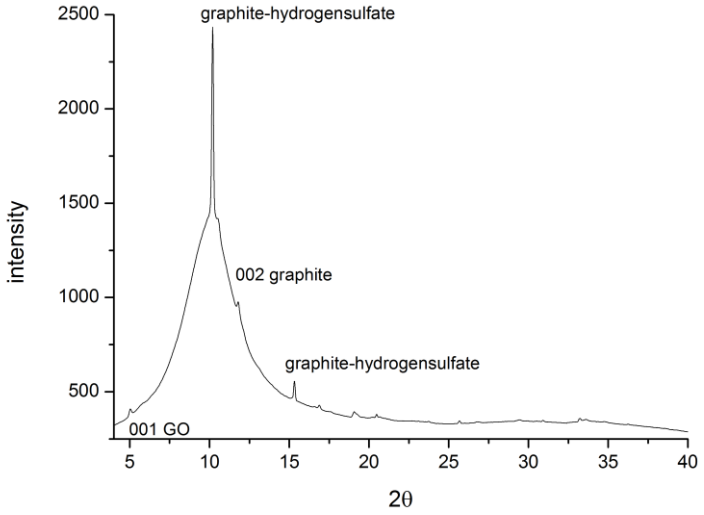

Figure 5.2: The XRD of stage II of the modified Hummers synthesis.

Angle/ ° 2θ	*d*-value/ Å	Intensity/ Count	Assignment
5.050	7.967	958	GO (001)
9.893	4.071	1545	GO' (002)
10.312	3.906	1483	GO* (002)
11.840	3.403	2741	Graphite (002)
15.255	2.644	599	GO (003)
16.645	2.425	631	
16.927	2.385	1251	Cubic (110)
17.671	2.285	610	
18.952	2.132	469	GO (100)
19.737	2.048	561	GO' (004) and graphite (101)
20.708	1.953	603	GO* (004)
21.305	1.899	482	
23.831	1.700	490	Graphite (004)
26.026	1.559	466	Graphite (103)
26.855	1.512	652	Cubic (210)
29.507	1.378	704	Cubic (211)
29.943	1.359	450	
30.755	1.324	433	GO (006)
34.209	1.193	448	Cubic (220)
36.333	1.126	488	Cubic (300)
45.785	0.902	343	Cubic (321)

Table 5.2: The diffraction peaks of stage III in the modified Hummers synthesis and their assignment

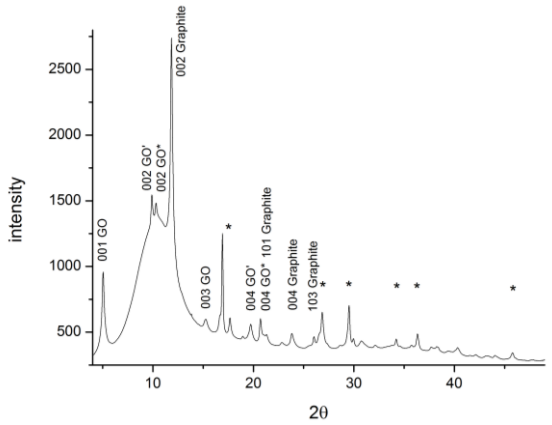

Figure 5.3: The XRD spectra of stage III, * marks the cubic diffraction peaks.

The assignment and diffraction peaks of stage III can be seen in Figure 5.3 and Table 5.2. The diffraction peaks observed *in situ* during stage III were similar to a sample taken from a laboratory scale Hummers synthesis before the addition of ice cooled water and H_2O_2. This indicates that stage III is formed without the influence of nitrate, as no nitrate is added in the capillary synthesis. The laboratory sample changed in air, this was not observed for the capillary synthesis probably due the confined space. As sulfuric acid does not evaporate and plenty of oxygen is present in the synthesis mixture the reaction with air could be caused by adsorption of water. As the air sensitive reaction took place the colour of the sample changed from dark to light brown/purple. A difference between the two samples was the seemingly drying of the capillary sample. With the drying of the capillary sample it would be expected that graphite diffraction peaks as assigned in stage III, Table 5.2, could be present in the capillary XRD. However as similar XRD data was observed *ex situ* it is probably either graphite in both the *in situ* synthesis and the normal *ex situ* modified Hummers synthesis or the explanation of these graphitic like diffraction peaks are even more elaborate, as no graphitic impurities were observed in the final laboratory synthesized GO.

What complicated the deconvolution of stage III even more was that a triclinic unit cell with the parameters of a=4.763 Å, b=8.268 Å, c=4.711 Å, α=105.5°, β=119.4°, γ=74.6°, and V=154.65 $Å^3$ was found by indexing and parameterizing the *ex situ* XRD. Care should always be employed when fitting any diffraction spectra to a triclinic unit cell, however this unit cell is close to a hexagonal unit cell, which is the normal cell for GO, and only few diffractions were calculated which were not accounted for in the measured spectra giving credibility to the triclinic fit. This triclinic structure was interpreted to mean that even though we have separate diffracting phases in stage III they are linked together.

In stage III the 001 GO diffraction peak was observed, furthermore were several peaks which may be linked to GO, such as the 003 diffraction peak. The even numbered diffraction peaks of GO the 002 and 004 was not observed, however double peaks were observed surrounding the expected 002/004 position and it seemed that the peaks were split. The split peaks are marked as the *GO and the ‘GO peaks in Figure 5.3. The split peaks could be caused by intercalation into the GO sheets. The reduced number of diffraction peaks observed in the solid GO could be explained from elimination of solvent interaction by washing. After the tentative identification of the graphite and GO diffraction peaks in stage IIII many diffraction peaks are still unidentified. Several of these peaks could be grouped together by a cubic unit cell structure, as marked in Figure 5.3.

From the *in situ* XRD on the modified Hummers mechanism it was found that the oxidation of graphite is initiated after the dissolution of potassium permanganate, by the intercalation of sulfuric acid and/or hydrogensulfate into the graphite and then formation of crystalline material. The 001 GO diffraction peak was observed early in the synthesis during stage II, and continued growing during stage III.

5.2. *In situ* XRD on thermal reduction of GO

TrGO heated at 1, 5, 10, and 20 °C/min resulted in similar shaped XRD, as shown in Figure 5.4.

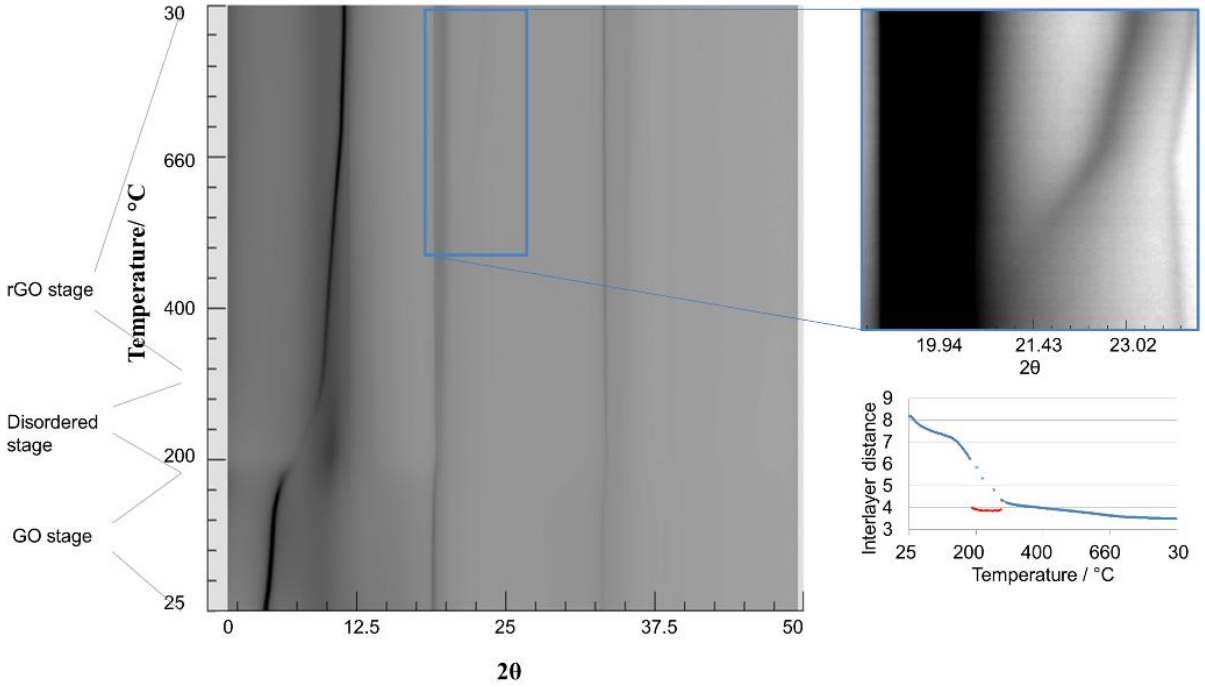

Figure 5.4: A 2D plot of diffraction patterns during transformation of GO to rGO measured from 10-50° in 2θ, for a heating rate of 5° C/min. The 2D plots for 1, 10 and 20 °C/min were of similar shape. The temperature was calibrated to an Ag sample. Inset: The appearance of a small peak at 22.5° in 2θ. Right, below: Plot of the interlayer distance of the 00*l* diffraction peak vs. temperature.

Before heating the GO was identified by the 001 diffraction peak at 4.9° in 2θ (*d*=8.20 Å), the 100 diffraction peak at 18.94° in 2θ (*d*=2.13 Å) and the 110 diffraction peak at 33.10° in 2θ (*d*=1.23 Å). A small graphitic impurity from the synthesis was indicated by the graphite 002 diffraction peak at 12° in 2θ (*d*=3.37 Å), see Figure 5.5A.

Upon heating three stages were observed from the development of the 001 GO diffraction peak. The GO diffraction peak decreased in *d*-value until the temperatures of 210 °C for the 5, 10 and 20 °C/min ramps and 190 °C for the 1°C/min ramp. As the GO diffraction disappeared a small broad diffraction peak was observed along with a small moving diffraction peak; this stage was named the disordered stage. The disordered stage has a resemblance to rGO formed by shock heating. The small moving diffraction peak moved through the disordered stage from the position of the 001 GO diffraction peak, it started to sharpen and grow as the 002 rGO diffraction peak, thus initiating the ordered rGO stage at 285 °C for the 5, 10 and 20 °C/min ramps and 230 °C for the 1 °C/min ramp. The stages can be seen by the development in the interlayer distance of the primary diffraction peak as seen in the plot in Figure 5.4. The interlayer distance changed from 8 to 6 Å in the GO stage, to 4 Å in the disordered stage and from 4.2 to 3.5 Å of the rGO stage. During the change from GO to rGO the 100

diffraction peak at 18.94° in 2θ (*d*=2.13 Å) broadens and splits and the 110 diffraction peak at 33.10° in 2θ (*d*=1.23 Å) sharpens. The diffraction of the rGO stage are seen from Figure 5.5B.

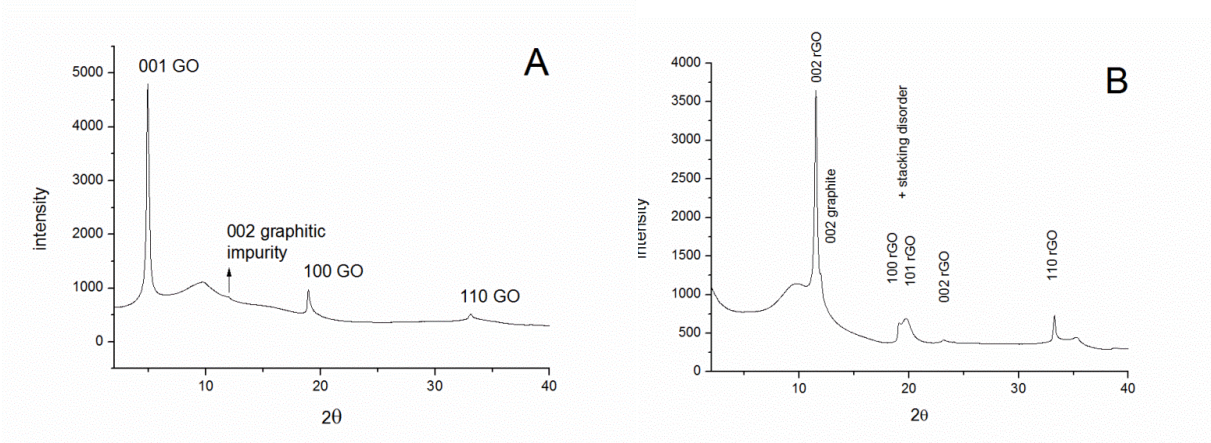

Figure 5.5: (A) The GO stage of the GO reduction, (B) The rGO stage of the GO reduction

The graphitic impurity from the synthesized GO resulted in a shoulder on the 002 rGO diffraction peak in the rGO stage. Neither of the rGO 002 diffraction peaks reached *d*-value similar to the 002 graphitic diffraction peak indicating that the heating did not resolve in a complete reformation of the initial graphitic order.

When heating a sample at 20 °C/min without N_2 flow an additional peak was observed. Formation of an additional compound in the air sample would usually result in formation of more diffraction peaks than only one. This could indicate that only small changes were caused by the presence of air. However, as we see a small change it is concluded that the use of inert atmosphere is important even in a small confined synthesis container.

In situ thermal reduction of a GO sample, which had been heated for 3 days at 35 °C during the modified Hummers synthesis in comparison to a GO sample heated for 3 hrs, resulted in similar spectra. However a single additional peak at 24.1° in 2θ was observed in the 3 hrs sample. The additional peak was probably due to the graphite impurity, which was not observed in the 3 days sample.

The fast heating ramp of 50 °C/min resulted in formation of a rGO with lesser order compared to the other heating ramp rates as illustrated by the smaller and broad 002 rGO diffraction peak (11.5° in 2θ), as seen in Figure 5.6. The graphitic diffraction peak remained the same, which indicate that eventhough the fast heating ramp caused visible moving of the material most of the material were still in the XRD beam. The synthesis moved through all the three stages of the slower heated GO reductions: The

GO stage, the disordered stage and the ordered rGO stage were all observed. Addition of trace amount of diamond powder to the GO before heating resulted in formation of a more ordered rGO which may be caused by changes in the thermal properties from the diamond powder.

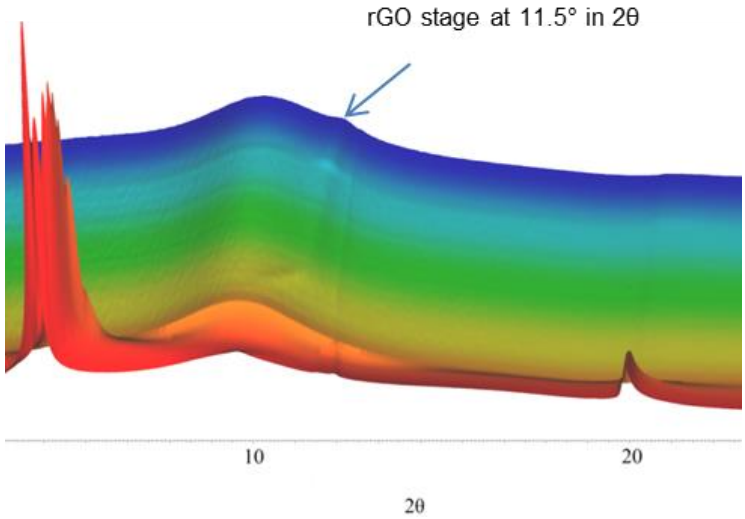

Figure 5.6: XRD 3D surface plot of the thermal reduction of GO at 50 °C/min.

The observation of the disordered stage during all the temperature ramp rates means that the graphene oxide planes are ripped apart from one another for all the different temperature ramp rates, and not only the faster heated ones. This could suggest that the smaller pressure built-up in slowly heated rGO is not the full explanation for the formation of the ordered rGO, as suggested in [125]. The lower pressure may enable rGO to form a relative ordered layered structure, revealed by the observed sharp 002 rGO diffraction peak, but some order is also reformed for the fast heated samples. These results were obtained in a space limiting capillary which could have an influence and to obtain a full understanding of the thermal reduction mechanism this aspect should be further investigated.

5.2.1. In situ Raman spectroscopy on the thermal reduction of GO

In situ Raman spectroscopy was initiated along with the *in situ* XRD on the thermal reduction of GO. The Raman beam was optimized on the GO sample in the capillary and Raman measurements were initiated simultaneously with the XRD. However, it was only possible to observe the D peak (~1400 cm^{-1}) and G peak (~1600 cm^{-1}) of GO below 200 °C as the increase in temperature elevated the scattering background, as seen in Figure 5.7. It was therefore not possible to see the changes of states for the *in situ* Raman results.

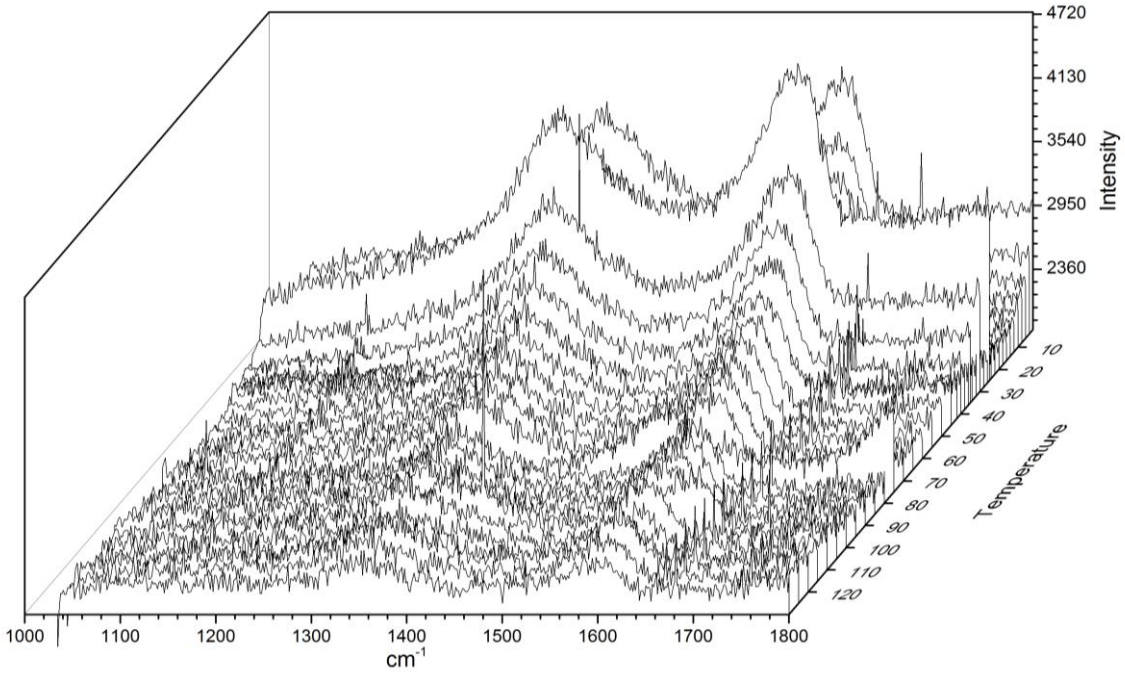

Figure 5.7: *In situ* Raman spectroscopy on the initial GO stage during the thermal reduction of GO.

5.3. Sub-conclusion

The modified Hummers method synthesized GO through intercalation and then formation of additional crystalline material. The GO formation was observed early on, as soon as the permanganate was dissolved, and the formation was continued through the third stage of the synthesis. The GO in solution revealed additional peaks, which was not observed in cleaned GO samples and which could be caused by intercalation of the solvent. Finally, all the diffraction peaks of the final GO stage may be indexed to a triclinic unit cell and an unidentified cubic phase was also observed.

The thermal reduction of GO to rGO goes through three stages: The GO stage, the disordered stage and the ordered rGO stage. The reduction may be affected by atmosphere, additives and the heating ramp. All three stages have been observed for all performed experiments. A fast heating ramp resulted in a more disordered rGO but the XRD still showed the disordered stage between the GO and rGO stage, indicating that some reordering could take place even with the fast heating of the GO sample.

Chapter 6

6. Oxidation time effects on GO and rGO

6.1. GO oxidation time effect

The effect of oxidation time for the modified Hummers synthesis was tested on five different oxidized samples of GO and the following chemically and thermally reduced GO. The modified Hummers method was performed five times as described in section 4.1.1, with oxidation time (heating at 35 °C) of 30 min, 1 hr, 3 hrs, 1 day and 3 days (termed GO30min, GO1H, GO3H, GO1D, and GO3D). The standard heating time usually reported for the modified Hummers method is 3 hrs, and it was expected that the lesser oxidized samples would have less defects and a smaller amount of edge bonded oxygen functionalities. The opposite was expected for the longer oxidized samples. The investigation was also aimed at the final products of HyrGO and TrGO in order to investigate if the possible oxidation time effects transcended the syntheses as this would open up for more precise considerations for the performance of the modified Hummers method. Furthermore, the possible oxidation time effect in the Li-O_2 battery was also investigated. The TrGO and HyrGO samples were termed HyrGO30min, HyrGO1H, HyrGO3H, HyrGO1D, HyrGO3D, TrGO30min, TrGO1H, TrGO3H, TrGO1D and TrGO3D. 15 different powders were prepared and analysed for the oxidation time project, and the study was published in paper II.

6.2. TGA-MS, SEM and BET

Thermogravimetric analysis coupled to a mass spectrometer (TGA-MS) was measured from 25-1050 °C for the GO samples, showing an increasing trend where prolonged oxidation time caused a larger loss of mass, ranging from a total remaining

mass of 34% for the GO30min sample down to 22 % remaining mass for GO3D. All the samples had a substantial mass loss both from intercalated water and CO_2 from thermal reduction of GO. The larger mass loss for the more oxidized sample indicated increased water intercalation and possibly increased oxidation to the graphite sheet.

SEM was performed on all samples, however it was only possible to distinguish GO and rGO from one another, as seen in Figure 6.1.

The GO had a flat crumpled structure, whereas the rGO materials showed a 3D structure. The rGO structure resembled small aggregates with cavities and a number of crumpled layers.

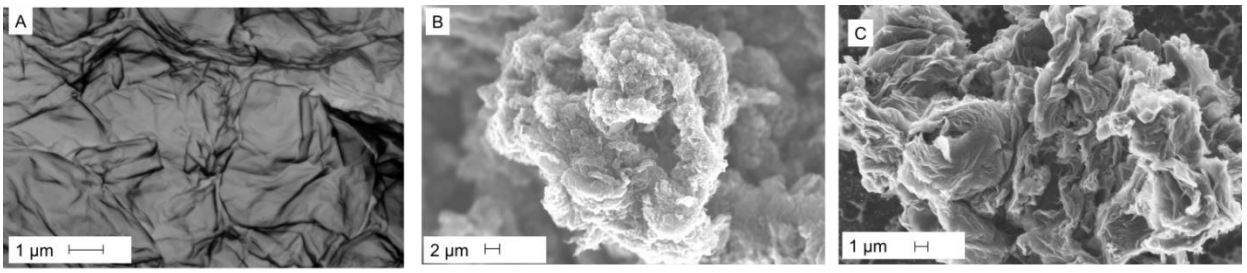

Figure 6.1: SEM micrographs of (A) GO30min, (B) HyrGO3D, and (C) TrGO3D.

The BET surface areas of HyrGO ranged from 353 m^2/g to 497 m^2/g and for the TrGO samples the surface areas ranged from 343 m^2/g to 484 m^2/g. No trend was observed for the HyrGO samples but the BET values of the TrGO samples indicated that increase in oxidation time led to an increased surface area, which could be caused by increased edge and defect formation during the prolonged oxidation time. That this was not observed for the HyrGO samples could be explained by the aggregation of HyrGO during the synthesis, which may affect the surface area in a higher degree than oxidation time.

6.3. XRD

GO was identified by XRD by its 001 diffraction peak around 10 ° in 2θ, *d*-value around 8 Å, as shown in Figure 6.2. The GO30min sample had a small *d*-value (*d* = 7.78 Å), increased oxidation time for the GO1H, GO3H, and GO1D caused *d*-values around 7.9 Å and the prolonged oxidation of GO3D resulted in a *d*-value of 8.44 Å. The increase in *d*-value upon prolonged oxidation time could be explained by an increase in water intercalation, which is supported by the TGA-MS measurement.

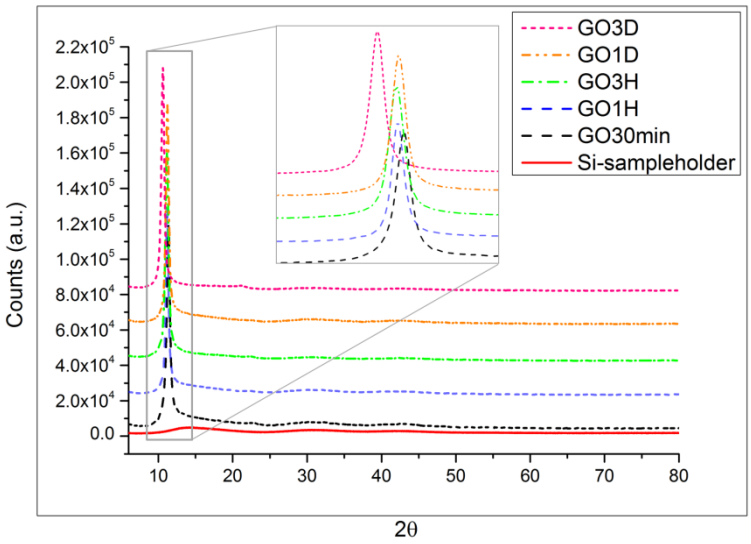

Figure 6.2: X-ray diffractograms of GO30min-GO3D showing an increasing *d*-spacing (decreasing 2θ value) of the graphene layers as a function of oxidation time. The inset shows an expansion for the region of the 001 diffraction peak.

It was not possible to find a clear trend distinguishing the different oxidized samples of HyrGO and TrGO, however this was not expected as XRD displays difference in crystal lattice and atomic compositions. The XRD revealed how the two different synthesis routes to rGO led to formation of two different types of materials. Both types of rGO displayed a diffractogram of a material with a lesser order compared to GO, however the HyrGO sample had a more defined 002 diffraction peak compared to the TrGO samples. The HyrGO samples showed a broad 002 diffraction peak at $d \cong 3.7$ Å as well as the 100 diffraction peak. The 002 diffraction peak of the TrGO samples were weaker with $d = 3.7$ Å for TrGO30min and $d \cong 3.4$ Å for TrGOX (X = 1H, 3H, 1D, and 3D), as was the 100 diffraction peak. The lesser order for the TrGO samples is probably caused by the pressure of CO_2, CO and water ripping the oxidized layers apart during heating compared to delamination of the layers in water during the HyrGO reduction.

6.4. Raman spectroscopy

Raman spectra of GO, TrGO, HyrGO, (all based on 3 hrs oxidation time) and graphite is displayed in Figure 6.3. The Raman spectra of carbon materials may be described by D and G peaks. The G peak is often interpreted as the order in the 2D graphitic plane and the D peak is assigned as the disorder caused in GO and rGO by oxygen functionalities and defects in the carbon network. This is illustrated by the spectra of the ordered graphite which have a high G peak and only a small D peak.

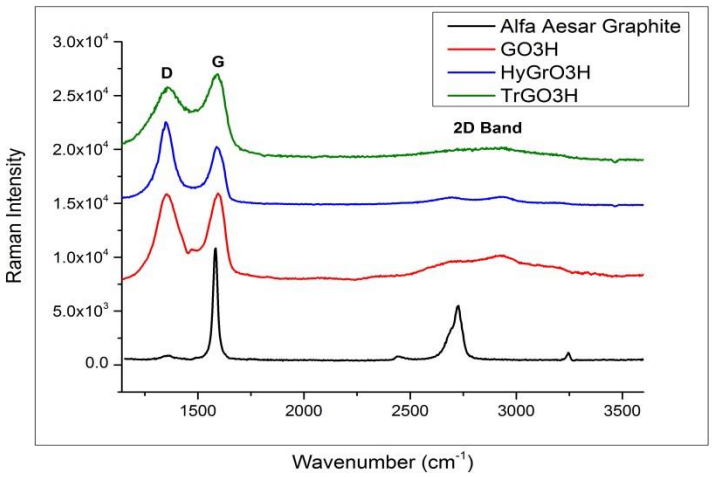

Figure 6.3: Raman spectra of graphite, GO3H, HyrGO3H, and TrGO3H

The GO samples had I(D)/I(G) ratios ranging from 1.4-1.8, whereas HyrGO had I(D)/I(G) ratios of 1.9-2.6, and TrGO had even higher ratios of 3.2-3.9. The ratio of I(D)/I(G) is often reported as a measure of the disorder in the carbon material [126]. Therefore, a decrease in the I(D)/I(G) ratio is expected upon reduction if the graphene sheet is restored, however this is not observed. Similar results have been reported earlier [127] and this was explained by the creation of graphitic domains in rGO, which are more abundant but which are smaller in size than in GO.

The peaks around 2500-3000 cm^{-1} are caused by the 2D band, which was not further investigated in this project. The Raman spectrum of TrGO has some resemblance to carbon black with the low gap between the D and G peak, this is not observed for the HyrGO sample. Hiramitsu *et al.*[128] observed a peak around 1750 to 1850 cm^{-1} related to C=O vibrations. The Raman spectra of the GO samples display a tendency to a very small shoulder in the area of 1840 cm^{-1}, although the signal is too weak to make any definitive conclusion.

The Raman spectra of the GO, HyrGO and TrGO samples showed similar spectra not varying with changes in oxidation time and no trends were observed.

6.5. XPS

XPS provides very precise information describing the energy of the surface of a sample. In order to provide information of the different chemical bonds of the surface the spectra have to be deconvoluted. The fitting of the tail of the rGO is difficult as a large π-π^* transition is observed and the GO spectra showed a large charging effect..

Figure 5.4 shows how the XPS spectra were deconvoluted for the GO and rGO samples. The HyrGO sample contained the additional C-N bond as a result of the hydrazine reduction. In order to ensure a high chemical accuracy of the HyrGO fitting chemical guideline inspired from ref. [106] was used.

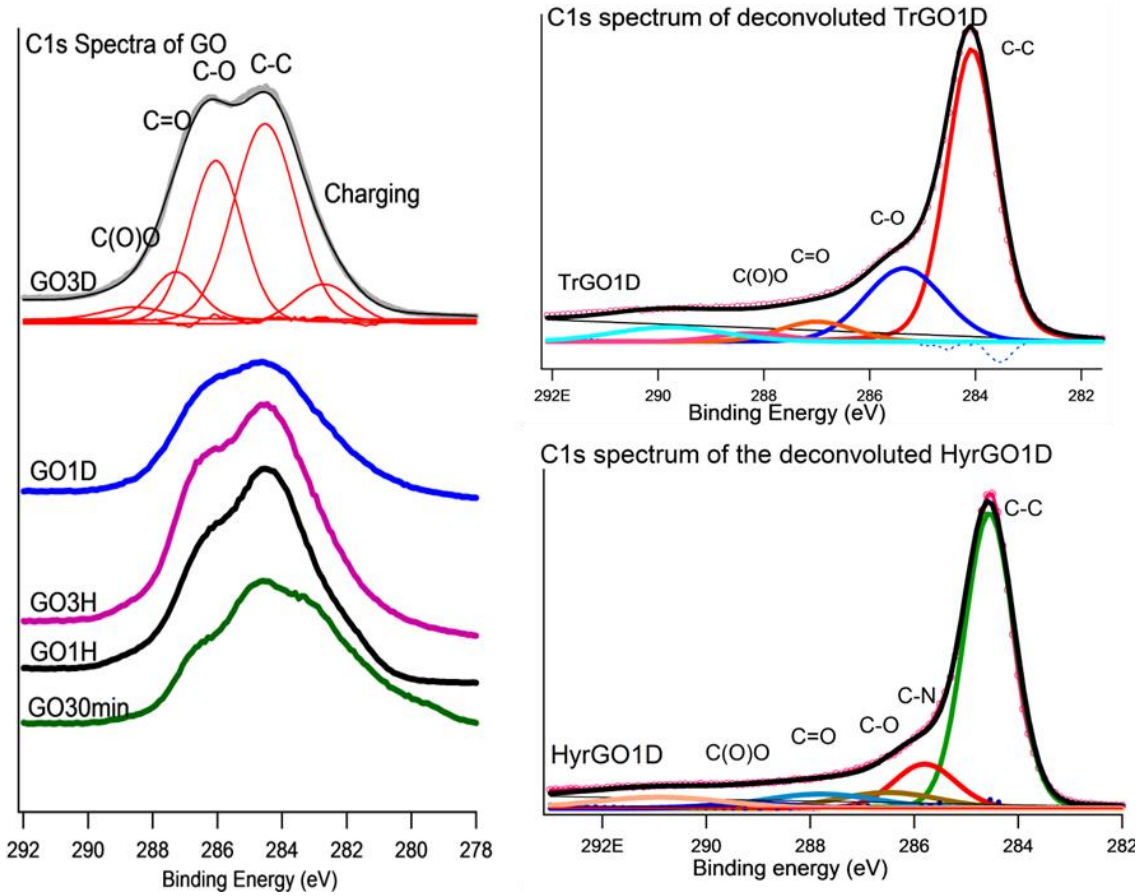

Figure 6.4: C1s spectra of GO (left), TrGO1D (rigth, top), and HyrGO1D (rigth, bottom).

The relative contribution of each bond was determined based on the deconvoluted C1s spectra. The XPS on GO showed how increase in oxidation time during the modified Hummers synthesis affected the GO material. Increase in oxidation time led to a decrease in the ratio of the C-C bonds compared to an increase in the ratio of the C-O, C=O, and COO groups. The increase of C=O and C(O)O could indicate a degeneration and destruction of the carbon backbone as these functional groups are expected to be situated at the edges of the graphene sheet.

The HyrGO samples had a decrease of C-C bond ratio, and an increase of C=O and COO groups with increased oxidation time (the edge groups are in line with the guideline used for fitting of the peaks, see paper II). The ratio of the C-N bonds grew with prolonged oxidation time, a trend which was also observed by comparison of the

elemental quantities. The increase in C-N bond can be explained by an increase in epoxy groups (C-O-C) of the GO as the oxidation time is increased [119,129]. This demonstrates that the increasing amounts of C-O groups in GO is carried through to HyrGO. The trends seen for the C-C and C-O bonds in GO seems to be transferred to the HyrGO samples.

The TrGO samples showed an increase in the C-C bond with increased oxidation time however the ratio of the C-O did not depend on the GO oxidation time. The ratios of C=O were increased up to TrGO3H and the C(O)O functional groups were similar to the GO values thus the trends observed in GO for C-C, C=O, and C(O)O seems to be extended to the TrGO samples.

The ratio of C-C both for the HyrGO and TrGO samples are higher than the one in GO, which is expected as the reduction removes functional groups.

6.6. Solid state ^{13}C-MAS NMR

Four samples were investigated with Solid State ^{13}C MAS NMR: GOX and TrGOX at X=30min and 3 days respectively. As this analysis method is very slow for rGO only few samples were investigated.

SS ^{13}C-NMR showed the composition of the bulk material in comparison to the surface data acquired by the XPS analysis. The ^{13}C -NMR on GO revealed the presence of C(O)O, C-C, C-OH, C-O-C, and CH_3 groups, where the methyl group was assigned as washing impurities from acetone. The GO samples were rather similar with the major resonances (90%) arising from the aromatic C backbone of the graphene sheet as well as C-OH and C-O-C groups. The concentrations of the different functional groups calculated from XPS and ^{13}C-NMR were not similar, but as both measurements resulted in broad spectra this is not unexpected. However, both XPS and ^{13}C-NMR of the GO samples showed a decrease in the amount of C-C bond upon oxidation and an increasing amount of C-OH. ^{13}C-NMR found the opposite trend than XPS for the C-O-C groups; which decreased in ratio with increasing oxidation time.

The TrGO samples consisted mainly of C=C, aromatic C, and carbonyls where the amount of C(O)O greatly exceeded that observed by XPS. No C-O groups were observed in ^{13}C-NMR as in the XPS data. However, the ^{13}C-NMR spectra of rGO showed the formation of two new functionalities compared to the GO: A Sp_2 carbon single-bonded to an oxygen atom, C_{sp2}-O, and a lactol group, as seen in Figure 6.5. If these types of structures are formed during the heating, they explain the presence of C-O groups in both XPS and the formation of the new groups in ^{13}C-NMR.

The trend observed for the TrGO in XPS was not entirely similar to the data observed with NMR. However, the relative amounts of C(O)O and lactol groups increased with increased oxidation time, which correlates to the XPS data. It is difficult to make a definitive conclusion in regards to the conservation of trends in GO from NMR. A clear difference is observed for the GO samples as well as the TrGO samples depending on the oxidation time during the modified Hummers method.

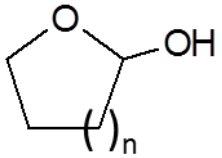

Figure 6.5: Lactol group, which was identified in TrGO by SS ^{13}C-NMR

6.7. Electrochemical evaluation

The HyrGOX and TrGOX (X=30 and 3days) samples were tested as drop-casted cathodes for Li-O_2 batteries with 10 wt% PVDF for the HyrGO and 50% PVDF binder for the TrGO cathodes at 0.1 mA/cm^2. A minimum of three batteries were tested for each cathode. Super C65 was chosen for comparison of the rGO samples to a standard carbon black material, cathodes were made with 10 % PVDF binder. As the rGO materials were rather different to work with the cathodes were similar looking but with different weight of the cathode. The collected cathodes had an average weight of 1.4 mg for HyrGO, 0.9 mg for TrGO cathodes and 0.9 mg for the Super C65 carbon cathodes. The electrochemical tests were some of the early one measured during the project and later it was found that the procedures used for the drying of the electrolyte and cathodes were insufficient. This means that small amount of water could be present in the batteries which may lead to an increased capacity, as described from the solution based mechanism in section 2.1.1.

The battery tests were initiated with 3 hrs at OCV followed by three cycles of discharge-charge with duration of 10 hrs, and lastly the battery was deep discharged to 2 V. A single battery was measured with a TrGO cathode of 0.37 mg, which gave a specific discharge capacity of approx. 60,000 mAh/g_{carbon}, which was the current record for Li-O_2 batteries (most likely reached with the presents of water impurities). No other of the tested batteries resulted in discharge capacities of this size. The cathode was analysed by XRD and XPS, which confirmed the presence of Li_2O_2 as the only discharge product. The charge of the battery was poor with capacity retention of 25%.

6.7.1. Specific discharge capacity

The averaged specific discharge capacities of the five different tested cathodes are presented in Table 6.1.

Cathode	Binder content/ %	Average specific capacity/ mAh/g_{carbon}
Super C65	10	2922
HyrGO30min	10	4063
HyrGO3D	10	1457
TrGO30min	50	6947
TrGO3D	50	11038

Table 6.1: The average specific capacity obtained in the Li-O_2 battery test for Super C65, HyrGO and TrGO cathodes.

It is clear that the TrGO samples resulted in a higher specific capacity than the HyrGO samples. The HyrGO3D sample is of even lower capacity than the Super C65 sample. This, together with the fact that the HyrGO30min has a three times higher capacity than the HyrGO3D sample, may indicate that increasing C-N groups are decreasing the capacity below that of carbon black. However other studies on rGO have found that nitrogen bound to the surface increases the capacity [130].

The large difference between TrGO30min and TrGO3D could be explained with the formation of edge groups such as C=O and C(O)O affecting the capacity. TrGO3D (484 m^2/g) has a larger surface area than to TrGO30min (342 m^2/g) and this might be the simpler explanation for the difference in capacity. However, BET results for the HyrGO samples are rather similar: HyrGO30min 383 m^2/g and HyrGO3D of 399 m^2/g. If surface area was the defining capacity factor we would expect similar capacities for samples with similar surface area. In general also the morphology of the cathodes could affect the discharge capacities. It is not possible to make any definitive conclusion based on these data, however, it is clear that difference in oxidation time may affect the specific discharge capacity. Nevertheless, it is important to remember that the specific capacity is calculated based on the amount of carbon in the material, and if it was calculated based on the entire cathode the TrGO samples would be in the range of the HyrGO samples.

Paint casted cathodes of the TrGO cathodes tested at lower rate pr m^2 resulted in a similar trend for the TrGO samples. The capacity of the paint casted cathodes was larger for the TrGO3D sample, but smaller for the TrGO30min sample, which signifies

that the testing conditions and preparation methods of cathodes as well as the material have to be considered in order to optimize the battery.

6.7.2.Cycling

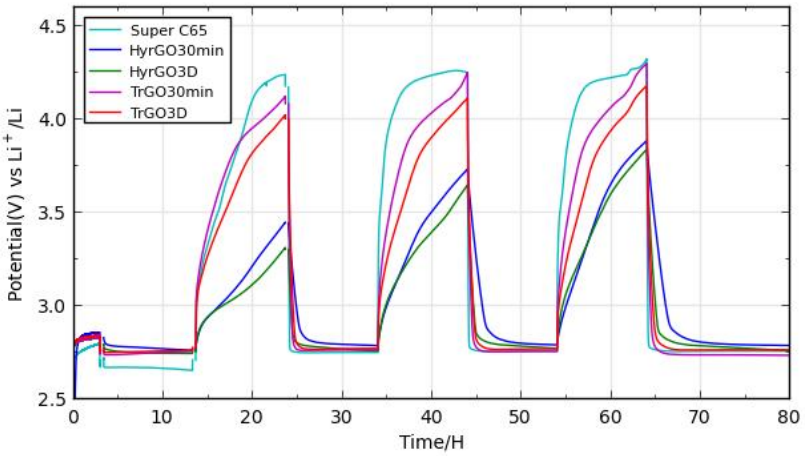

Figure 6.6: Cycling curves for the time limited battery discharge-charge of the five different cathodes.

Figure 6.6 shows the time limiting cycles for the five different cathodes and it is clear that the different types of material result in different charge curves. The Super C65 cathodes and the TrGO cathodes have a steeper climb to higher voltages than HyrGO, which is more linear. As cycling with a low overpotential is very important for Li-air batteries, this shows how a tailored material may be the solution to lowering the overpotential. However, as the cycle number increases, the HyrGO samples become more similar to the TrGO samples and the effect could be waring of. As the HyrGO samples are the only sample type with C-N bonds, the C-N bonds may affect the overpotential. However, other surface effects and morphology could also explain this difference in cycling. The TrGO cathodes result in a battery cycling which is more similar to Super C65. However, the TrGO cathodes demonstrate a lower end-potential and a 2^{nd} and 3^{rd} cycle which are not increasing in potential as steeply as the Super C65 cathodes, this could be an indication of the assumed superior morphology of rGO.

6.8. Sub-conclusion

Change in oxidation time during the modified Hummers method for the synthesis of GO affects the produced material. Prolonged oxidation time results in a GO with a

higher amount of intercalated water observed from XRD and TGA-MS. XPS results of the GO show how longer oxidation time decreases the amount of C-C backbone and increases the amount of oxygen groups, both the sheet bonded oxygen groups as well as the edge bonded oxygen functionalities, indicating a higher defect formation in the graphene backbone. XPS also revealed how some of the oxidation time effects are transported to both chemically and thermally reduced GO. The TrGO samples have similar trends in regards to C-C, C=O, and C(O)O development. The HyrGO have the same trend for the C-C bonds as well as an increasing trend for C-N formation with increasing oxidation time, which follows the C-O trend of GO. SS-NMR showed discrepancies with the XPS result, but revealed different composition for the differently oxidized samples, showing how change in oxidation time affects both GO and TrGO. The use of TrGOX and HyrGOx (X=30min and 3days) as cathode materials showed how the change in oxidation time seemed to affect the specific discharge capacity and how the choice in material affected the overpotential during time limited charging.

Chapter 7

7. *In situ* analysis of Li-O_2 cathodes

7.1. Battery designs

The two different battery designs for *in situ* XRD are seen in Figure 7.1 and the construction of the batteries are described in section 3.8.2. The battery design with the oxygen inlet through the capillary is named design 1 and the battery design with the oxygen inlet through the cathode is named design 2. Capillary design 1 is described in paper III and capillary battery design 2 is described in paper IV. Even though battery design 1 and 2 are very similar there are different advantages and disadvantages to each.

In design 1 the cathode is larger which makes *ex situ* analysis such as XPS easier. All the components are prepared in advance and the battery is assembled directly before use. The quartz glass for the *in situ* XRD is very sensitive and breaks easily, the electrolyte evaporates, and bobble formation between the cathode and the anode may disconnect the battery.

Battery design 2 uses a square glass which ensures that small bobbles formed during the testing of the battery will not disconnect the battery. However, the boron silicate glass may lead to a larger background in the XRD. There is less electrolyte evaporation from battery design 2 as the only outlet is through the SS-wire. However, the filling of oxygen is more difficult as a small blockage in the tube can ruin the battery and electrolyte may be removed. The square capillary battery may be prepared in advance and connected to the oxygen container days later. As the oxygen inlet point is known for design 2 it should be possible to explore different sites on the cathode. However, the oxygen inlet end may be a bit crumpled or have rough edges making the positioning of the beam a challenge and no large difference in the XRD diffractograms were observed

when this possibility was explored. Battery design 2 is more difficult to assemble, as the closing epoxy glue easily slides through the large square opening in the top of the glass if the use of sealing vacuum grease has not been efficient. Epoxy glue hardens in the electrolyte and destroys the battery. Also the dip-coating of the cathode is more challenging as it is more difficult to get an even coating all around the oxygen inlet hole on the SS-wire.

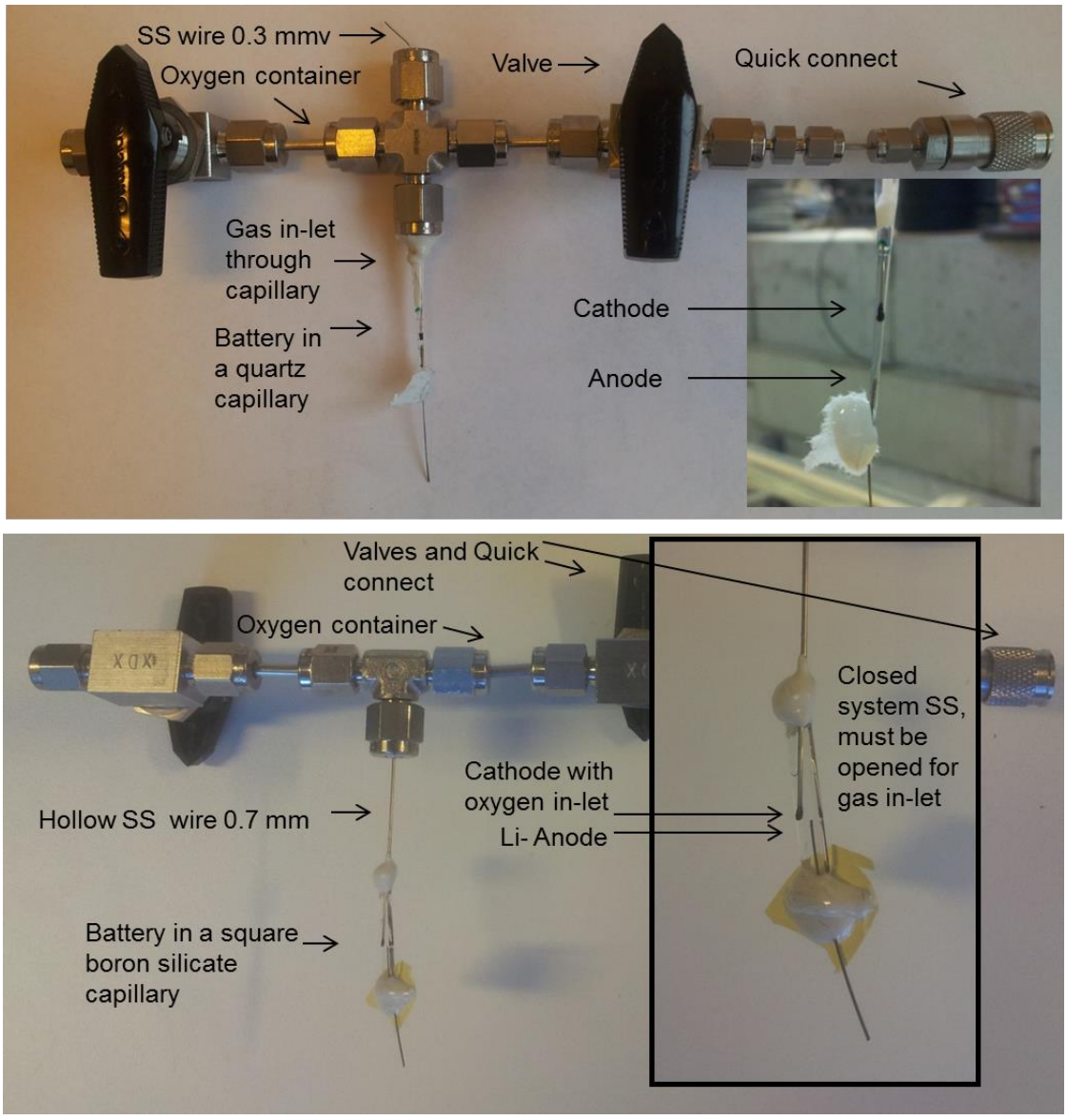

Figure 7.1: Top: *In situ* XRD battery cell design 1 with oxygen inlet through the capillary. Bottom: Design 2: *In situ* XRD battery cell design 2 with oxygen inlet through the cathode.

Design 1 was used for the *in situ* XRD on a Super C65 cathode and design 2 for the *in situ* XRD investigation of a TrGO cathode. Both cathodes were analysed *ex situ*

with XRD and the TrGO material was investigated further as spray casted cathodes by DEMS analysis.

7.2. Li_2O_2 on a Super C65 cathode

The capillary battery design 1 could be discharged and charge up to 5 times with decent capacity with a Super C65 cathode, as seen in Figure 7.2A. The discharge had the expected voltage plateau around 2.6-2.8 V upon discharge and a charge in the high voltage area with a plateau above 4 V.

Li_2O_2 was observed for a battery discharged at three different rates as seen in Figure 7.2C. Four diffraction peaks of Li_2O_2 grew upon discharge; 100, 101, 102 and 110, the additional diffraction peaks in the diffractogram are caused by the steel wire. The battery was discharge to a total of 72 μAh.

The battery was discharged at three different rates showing a linear precipitation of Li_2O_2, when comparing capacity to the area of the diffraction peaks (see Figure 7.2B). Even though the discharge was linear the fitting of the slope revealed that the fit did not start in origin, indicating that some electrons in the battery participated in other reactions than precipitation of Li_2O_2. However, as side reactions in Li-O_2 batteries are very common this was not unexpected. XRD gave no indication of by-products.

The battery was charged to approx. 32 μAh before gas formation disconnected the battery. Decomposition of Li_2O_2 was observed upon charge, but it was slow compared to the discharge. At approximately 33 % charge retention a reduction of only 10-20% was observed for the intensity of the Li_2O_2 diffraction peaks. This may be explained by side reactions such as electrolyte decomposition, especially at high voltage.

The full width at half maximum (FWHM) of the 100 and 101 diffraction peaks decreased upon discharge, whereas the FWHM of the 102 and 110 diffraction peaks seemed to be constant. However, the uncertainty of the parameters was higher for the 102 and 110 diffraction peaks as the intensity of these peaks were lower and the FWHM could only be determined in the last part of the discharge. Upon charge the FWHM of the 100 diffraction peak increased as did the FWHM of the 101 diffraction peak. The FWHM development of the 100 and 101 diffraction peaks indicate crystallite growth in these directions upon discharge. The FWHM values of the 101 and 102 diffraction peaks were higher than those of the 100 and 110 diffraction peaks. This could indicate anisotropic morphology of the Li_2O_2 crystallites or defect formation along the *c*-axis.

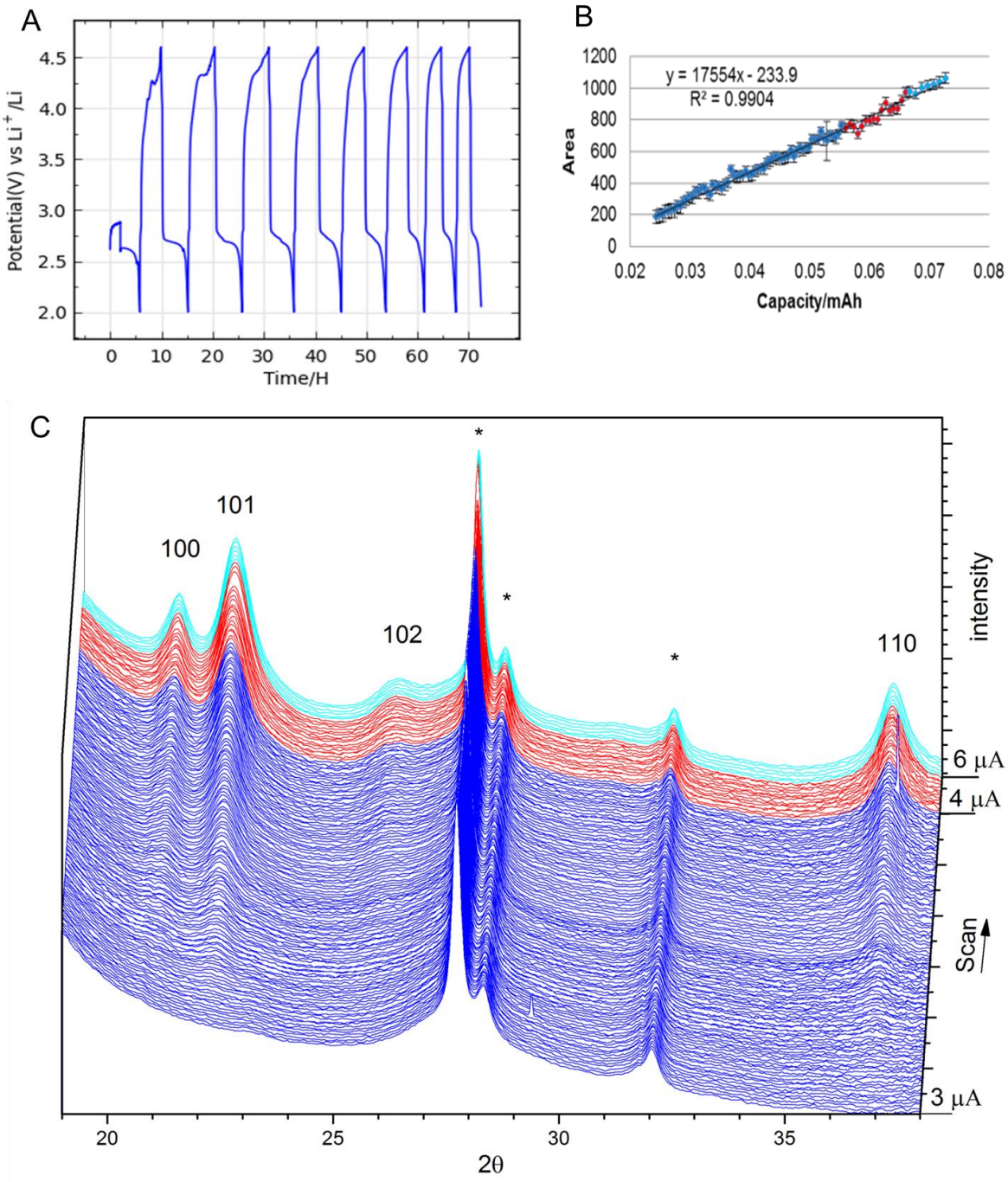

Figure 7.2: A: Discharge-charge curve of a capillary Li-O_2 battery design 1 with a Super C65 cathode. B: Area of the 100 diffraction peak vs capacity showing a linear increase in Li_2O_2 formation with increased capacity. C: *In situ* diffraction patterns for the discharge of battery 1 showing the appearance of four diffraction peaks of Li_2O_2 and the ones of the SS wire (*). Blue represent a discharge current of -3 µA, red=-4 µA and light blue= -6 µA.

A second battery was discharged *ex situ*, and then charged *in situ*. First it was charged with an X-ray exposure time of 30 sec followed by a 10 min wait at a rate of 4 and 5 μA. Later it was charged at a rate of 5 μA with a constant exposure to X-ray. The second battery showed the 100, 101 and 110 Li_2O_2 diffraction peaks in the XRD. Initially upon charge the Li_2O_2 decomposed linearly for all three diffraction peak. When the constant X-ray was applied the rate of the Li_2O_2 decomposition for the 100 and 101 diffraction peaks changed dramatically as the decomposition rate increased. The 110 diffraction peak also had a change in decomposition rate, this was however smaller. The FWHM of 100 and 101 grew upon charge, thus matching the result of the first battery. However, when constant X-ray was applied this trend was dramatically more pronounced. The 110 diffraction peak also showed a dramatic reaction to X-ray with a FWHM decreasing upon charge. The combined observation of constant X-rays effect on intensity and FWHM of the Li_2O_2 diffraction peaks indicates that X-rays affects the decomposition of Li_2O_2. An accelerated electrochemical decomposition of Li_2O_2 by X-rays during charging was observed by Liu *et al.*[131]. They detected decomposition of Li_2O_2 in a Li-O_2 battery fabricated with a porous Li_2O_2 electrode with a propylene carbonate electrolyte. The capillary battery results support the observation of increased Li_2O_2 decomposition by X-rays for reactions in DME. The results demonstrate that the enhanced decomposition also is observed for Li_2O_2 which has been precipitated electrochemically during "normal" Li-O_2 battery discharge. Furthermore these results open up for a discussion of how "non-invasive" *in situ* methods in general are.

The second discharge of a third battery was investigated *in situ* which showed very small diffraction peaks of Li_2O_2. Together with XPS analysis of cathodes discharged one and two times, this demonstrated how less Li_2O_2 was precipitated upon increased cycling. The enhanced formation of by-products were observed on the two times discharged cathode.

7.3. Li_2O_2 and LiOH on a TrGO cathode

Figure 7.3 display the X-ray diffractogram for a discharge of a TrGO cathode in a capillary battery design 2, which was described in paper IV. The battery cathode was measured at two positions, however very little variation was observed between position 1 and 2. Upon discharge the TrGO cathode showed diffraction peaks assigned to Li_2O_2 and LiOH, as well as a single unassigned diffraction peak at d=2.964.

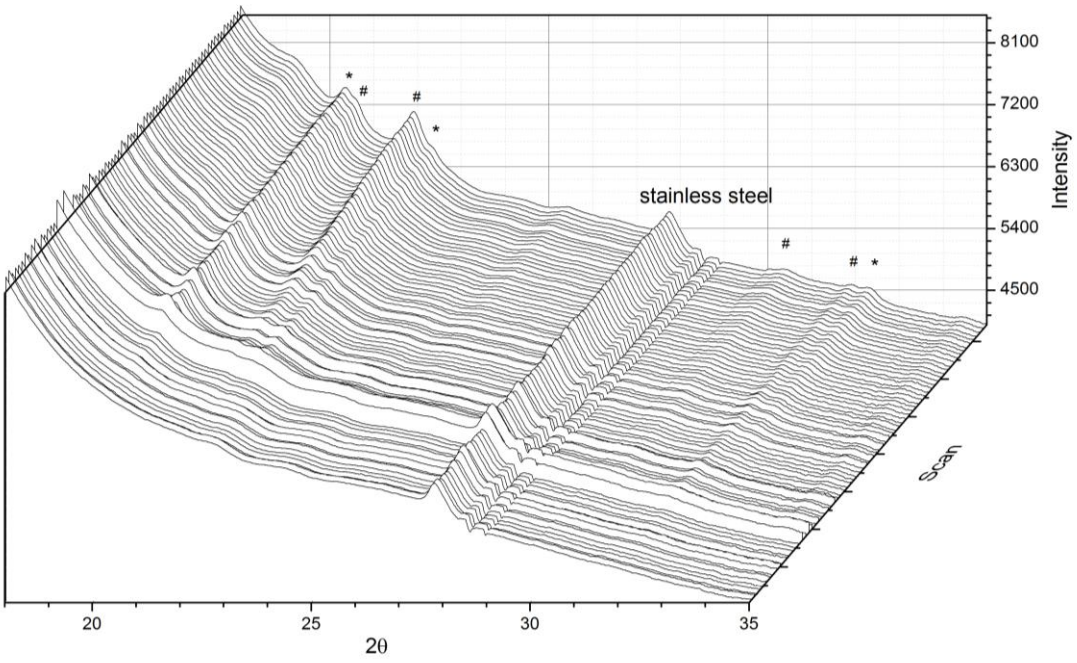

Figure 7.3: XRD of a TrGO cathode during discharge in a capillary battery design 2, showing formation of LiOH (*) and Li_2O_2 (#).

The initial five diffraction peaks were investigated and the height of the diffraction peaks increased with discharge. The FWHM of all the diffraction peaks decreased, which can be interpreted to indicate crystal growth upon discharge. The decrease of the FWHM for the Li_2O_2 diffraction peaks were similar to the observations for the Super C65 cathode in paper III, and can be interpreted to indicate similar formation of Li_2O_2 for the two different cathodes. Charging of the battery was poor with a decrease of the Li_2O_2 intensity with 19 % in measuring position 1 and 6 % in position 2.

The formation of LiOH observed for the capillary battery with a TrGO cathode could be explained by the presence of water and the surface of graphene. Therefore, TrGO cathodes with electrolyte with and without 1000 ppm added water were investigated. It was not possible to observe LiOH formation of cathodes discharged to 2 V in either wet (1000 ppm H_2O) or dry electrolyte with *ex situ* XRD. However, XPS analysis of both wet and dry discharged cathodes revealed formation of both LiOH and Li_2O_2. That only crystalized LiOH was formed in the capillary batteries can have several explanations such as the difference in the battery types, difference in binder, or the use of X-rays for the *in situ* batteries all which may affect the discharge product. The formation of LiOH might be caused by reactions with the electrolyte and/or the graphene surface.

To further analyse the effect of water DEMS measurements were performed on cells with and without 1000 ppm H_2O in the electrolyte, as presented in paper IV.

7.3.1. DEMS on a TrGO cathode

The discharge of both the dry and the wet cells were similar with a flat plateau forming at 2.7 V followed by sudden death. The discharge capacity of the wet cells were not remarkable enhanced as would be expected from the solution based mechanism, as observed for carbon black based cathodes. This indicates that the type of cathode affects the formation of Li_2O_2 just like additives in the electrolyte does. The pressure analysis on discharge revealed an electron count close to 2 e^-/O_2 for the dry cells (2.01 ± 0.06) indicating formation of Li_2O_2 and a lower electron count of 1.83 ± 0.10 e^-/O_2 for the wet cells. The lower electron count indicates that additional reactions takes place in the wet batteries such as electrochemical reactions with a lower electron count or chemical reactions consuming oxygen. The electron count of 2 e^-/O_2 for the dry cells indicates that LiOH is formed by a chemical reaction.

The charging of the dry and the wet cells were rather similar with a plateau forming above 4 V as seen in Figure 7.4, which also presents the DEMS data upon charge.

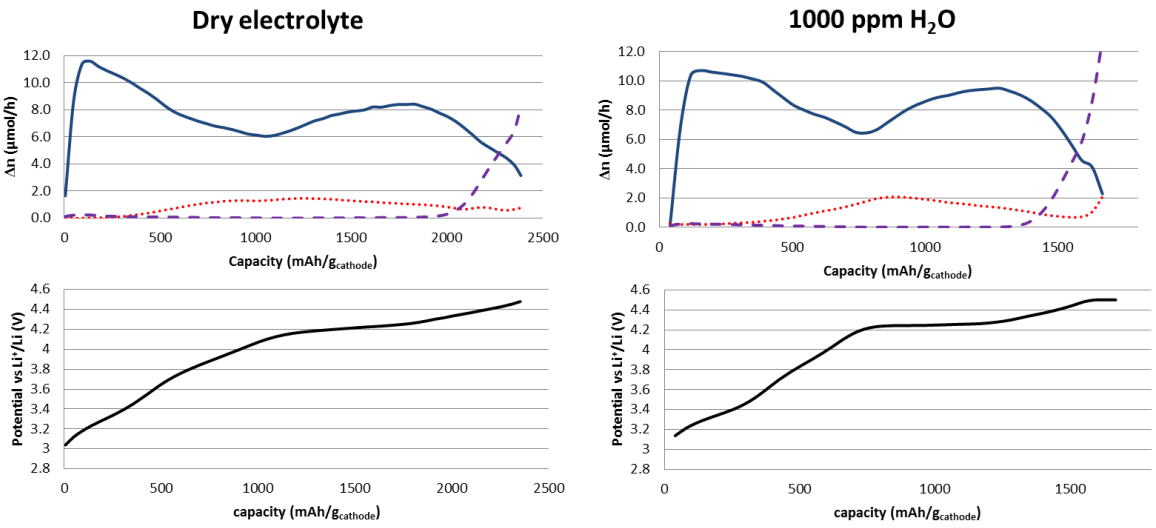

Figure 7.4: Top: DEMS analysis showing the O_2, H_2 and CO_2 gas evolution during charging of a TrGO cathode in dry and wet electrolyte. Bottom: Charge curve for a TrGO cathode in dry and wet electrolyte. DEMS analysis: Blue (full line) = Oxygen, red (….) = Hydrogen and purple (---) = CO_2

Both the dry and the wet battery cells showed oxygen evolution during the entire charge, and an increase in CO_2 formation during the last part of the charge. The CO_2 is expected to origin from decomposition of electrolyte [23] and possible decomposition of the cathode, as the stability of a TrGO cathode has yet to be investigated. Hydrogen evolution was observed for both types of batteries, possibly coming from decomposition of electrolyte for the dry battery. The hydrogen evolution of the wet

batteries seamed slightly increased during the charge compared to the dry batteries and showed an increasing hydrogen formation during the high voltage at the end of charge, possibly arising from the additional water. However it is worth to notice that the DEMS was not calibrated to hydrogen gas, which means that the data are not quantitative. The DEMS data clearly showed how the decomposition is a challenge for both the wet and the dry batteries.

7.4. Sub-Conclusion

In situ X-ray diffraction studies of both a Super C65 cathode and a TrGO cathode revealed the formation of crystalline Li_2O_2 during discharge of the Li-O_2 battery, with the FWHM of the Li_2O_2 having similar trends indicating similar formation of Li_2O_2. Charge was a challenge to both cathode types with a lesser decomposition of Li_2O_2, and the Super C65 cathodes showed lesser formation of Li_2O_2 on second discharge. The TrGO cathodes showed additional formation of LiOH, both in cells with and without water added to the electrolyte. The addition of water to the electrolyte for the TrGO cathode did not increase the capacity as initially expected, indicating that the mechanism behind Li_2O_2 formation also depends on cathode material. DEMS analysis upon charge of the TrGO cathode showed formation of oxygen, hydrogen and CO_2 gas, with a seemingly slight increase in hydrogen levels for batteries with added water. It was furthermore proven that X-ray affects the decomposition of Li_2O_2 giving the indication that care should be taken to avoid *in situ* XRD to become invasive.

Chapter 8

8. Conclusion and Outlook

8.1. Conclusion

The *in situ* study of the modified Hummers method revealed an early appearance of the GO diffraction peak. The Hummers method was initiated by the dissolution of permanganate followed by intercalation of graphite and then formation of ordered material. The third stage could also be indexed based on a triclinic structure, with some resemblance to a hexagonal unit cell. Furthermore new diffraction peaks for GO were observed in the synthesis mixture, which have not been observed for the cleaned solid product.

The *in situ* XRD on the thermal reduction revealed three stages which appeared for all tested temperature ramp rates: The GO stage, a disordered stage, and a rGO stage. The appearance of the disordered stage indicated that some reordering of the sample may take place before the formation of rGO. An rGO sample reduced at higher temperature ramps had a less order than the slower heated samples, but still showed the appearance of the disordered stage, indicating reformation of order during heating even for fast heated samples.

The *in situ* study of the modified Hummers method revealed that GO is produced early on during the synthesis, however the oxidation time study showed how the oxidation time alone is an important factor in regards to the crystal structure and chemical composition of GO. The oxidation time does not only affect GO, it also influences the product of rGO when GO is used as a precursor for rGO production, both for chemical and thermal reduction of GO. This oxidation time effect can be observed both by XPS and SS-NMR in GO and rGO, but furthermore the difference induced by the oxidation time may also have an effect when the materials are used as cathodes in the Li-air battery. The oxidation time affects the discharge capacity and the type of reduction seems to influence the overpotential upon charge in the Li-O_2 battery.

In the Li-O_2 battery the only wanted precipitation is Li_2O_2, which was studied by *in situ* XRD with two different *in situ* XRD battery cell designs. The Super C65 carbon black cathode showed only diffraction peaks related to Li_2O_2, however small indicators in XRD and XPS on discharged cathodes showed precipitation of addition material. For the TrGO cathodes the *in situ* XRD showed both Li_2O_2 and LiOH, which was confirmed by XPS measurements of a cathode discharged to 2 V in both a normal electrolyte and in an electrolyte with 1000 ppm added water. Furthermore, Li-O_2 batteries with TrGO cathodes with and without addition of water to the electrolyte showed rather similar charge and gas exhaustion on charge. However, water did not increase the capacity as expected. The electrolyte containing water had indications of additional chemistry taking place during discharge. The study of the two different cathodes show the importance of cathode material, and also indicate that the cathode influence the battery chemistry and electrochemistry.

8.2. Outlook

As Li-air still is a field with many unknown questions and answers there are plenty of opportunities to improve our understanding, even within the small areas covered in this project:

The isolation of the unknown Hummers synthesis product along with further confirmation of the possible GO diffraction peaks will possibly lead to the discovery of a new crystal compound and increase our understanding of GO. It would also be interesting to isolate the disordered stage of the thermal reduction of GO, for further investigation.

Further investigation of the oxidation time effect on rGO could focus on further understanding of the defects, doping, and oxygen functionalities effect in Li-O_2 batteries. As tailored cathode material has seemed to improve the capacity and overpotential of the Li-O_2 battery we need to understand if this enhancement is a morphology effect, is it caused by nucleation sites close to defects or oxygen functionalities and/or what is the effect of doping.

The *in situ* investigations of batteries with graphene-like materials have many possibilities to explore: Will other rGO's result in both type of decomposition product? What is the effect of catalyst? And what actually happens in the battery when additives are used? What is the cause of LiOH formation? It is also possible to continue the development of the capillary battery design, possibly to include further analysis methods such as Raman spectroscopy or to try and investigate different metal-air chemistries such as Na-air and Zn-air.

Bibliography

[1] World Development Indicators 2014, (2014) Structural Adjustment Participatory Review Interna.

[2] World Population Prospects The 2015 Revision, (2015) UN Department of Economic and Social Affairs.

[3] IPCC, Climate Change 2014 Synthesis Report Summary Chapter for Policymakers, (2014).

[4] M.J. Molina, L.T. Molina, Megacities and Atmospheric Pollution., J. Air Waste Manag. Assoc. 54 (2004) 644–680.

[5] International Energy Agency, Key World Energy Statistics 2015, (2015) 81.

[6] International Energy Agency, Key World Energy Statistic, (2014).

[7] I. Hadjipaschalis, A. Poullikkas, V. Efthimiou, Overview of Current and Future Energy Storage Technologies for Electric Power Applications, Renew. Sustain. Energy Rev. 13 (2009) 1513–1522.

[8] L. Situ, Electric Vehicle Development: The Past, Present & Future, Power Electron. Syst. Appl. (2009) 1–3.

[9] U.S. department of Energy, https://www.fueleconomy.gov/feg/evtech.shtml, (2016) May.

[10] Deloitte, Unplugged: Electric vehicle realities versus consumer expectations, (2011) 32.

[11] http://www.nissan.dk/DK/da/vehicle/electric-vehicles/leaf/charging-and-battery/range.html, (2016) February.

[12] https://www.teslamotors.com/da_DK/models/preowned?, (2016) May.

[13] L.A. Viterna, Ultra-Capacitor Large Energy Electric Storage Bus in a Hybrid, NASA. (1997).

[14] Tyler Hamilton, Next Stop: Ultracapacitor Buses, MIT Technol. Rev. (2009) https://www.technologyreview.com/s/415773/next–sto.

[15] D. Linden, T.B. Reddy, HANDBOOK OF BATTERIES, third edit, McGraw-Hill, 2001.

[16] International Energy Agency, (IEA), Technology Roadmap - Electric and plug-in hybrid electric vehicles, 2011.

[17] B. Dunn, H. Kamath, J.-M. Tarascon, Electrical Energy Storage for the Grid: A Battery of Choices, Science. 334 (2011) 928–935.

[18] G. Girishkumar, B.D. McCloskey, A.C. Luntz, S. Swanson, W. Wilcke, Lithium-Air

Battery: Promise and Challenges, J. Phys. Chem. Lett. 1 (2010) 2193–2203.

[19] M. Park, X. Zhang, M. Chung, G.B. Less, A.M. Sastry, A Review of Conduction Phenomena in Li-Ion Batteries, J. Power Sources. 195 (2010) 7904–7929.

[20] K.M. Abraham, Z. Jiang, A Polymer Electrolyte-Based Rechargeable Lithium/Oxygen Battery, J. Electrochem. Soc. 143 (1996) 1–5.

[21] T. Ogasawara, A. Débart, M. Holzapfel, P. Novák, P.G. Bruce, Rechargeable Li2O2 Electrode for Lithium Batteries, J. Am. Chem. Soc. 128 (2006) 1390–1393.

[22] F. MIZUNO, S. Nakanishi, Y. Kotani, S. YOKOISHI, H. Iba, Rechargeable Li-Air Batteries With Carbonate-Based Liquid Electrolytes, Electrochemistry. 5 (2010) 403–405.

[23] B.D. McCloskey, D.S. Bethune, R.M. Shelby, G. Girishkumar, A.C. Luntz, Solvents ' Critical Role in Nonaqueous Lithium-Oxygen Battery, J. Phys. Chem. Lett. 2 (2011) 1161–1166.

[24] M.M. Ottakam Thotiyl, S.A. Freunberger, Z. Peng, P.G. Bruce, The Carbon Electrode in Nonaqueous Li-O2 cells, J. Am. Chem. Soc. 135 (2013) 494–500.

[25] J. Xiao, D. Mei, X. Li, W. Xu, D. Wang, G.L. Graff, W.D. Bennett, Z. Nie, L. V. Saraf, I.A. Aksay, J. Liu, J.G. Zhang, Hierarchically Porous Graphene as a Lithium-Air Battery Electrode, Nano Lett. 11 (2011) 5071–5078.

[26] A.C. Luntz, B.D. Mccloskey, Nonaqueous Li-Air Batteries: A Status Report., Chem. Rev. 114 (2014) 11721–11750.

[27] J.S. Hummelshøj, J. Blomqvist, S. Datta, T. Vegge, J. Rossmeisl, K.S. Thygesen, A.C. Luntz, K.W. Jacobsen, J.K. Nørskov, Communications: Elementary Oxygen Electrode Reactions in the Aprotic Li-Air Battery, J. Chem. Phys. 132 (2010) 71101.

[28] C.O. Laoire, S. Mukerjee, K.M. Abraham, E.J. Plichta, M.A. Hendrickson, Elucidating the Mechanism of Oxygen Reduction for Lithium-Air Battery Applications, J. Phys. Chem. C. 113 (2009) 20127–20134.

[29] Z. Peng, S.A. Freunberger, L.J. Hardwick, Y. Chen, V. Giordani, F. Bardé, P. Novák, D. Graham, J.-M. Tarascon, P.G. Bruce, Oxygen Reactions in a Non-Aqueous Li+ Electrolyte, Angew. Chemie Int. Ed. 50 (2011) 6351–6355.

[30] L. Johnson, C. Li, Z. Liu, Y. Chen, S. a. Freunberger, P.C. Ashok, B.B. Praveen, K. Dholakia, J.-M. Tarascon, P.G. Bruce, The Role of LiO2 Solubility in O2 Reduction in Aprotic Solvents and its Consequences for Li–O2 Batteries, Nat. Chem. 6 (2014) 1091–1099.

[31] J. Yang, D. Zhai, H.-H. Wang, K.C. Lau, J. a Schlueter, P. Du, D.J. Myers, Y.-K. Sun, L. a Curtiss, K. Amine, Evidence for Lithium Superoxide-Like Species in the Discharge Product of a Li-O2 Battery., Phys. Chem. Chem. Phys. 15 (2013) 3764–71.

[32] B.D. McCloskey, C.M. Burke, J.E. Nichols, S.E. Renfrew, Mechanistic Insights for the Development of Li–O2 Battery Materials: Addressing Li2O2 Conductivity Limitations and Electrolyte and Cathode Instabilities, Chem. Commun. 51 (2015) 12701–12715.

[33] F. Gittleson, K.P.C. Yao, D.G. Kwabi, S.Y. Sayed, W.-H. Ryu, Y. Shao-Horn, A. Taylor,

Raman Spectroscopy in Lithium-Oxygen Battery Systems, ChemElectroChem. 12613 (2015) 1446–1457.

[34] K.M. Abraham, Electrolyte-Directed Reactions of the Oxygen Electrode in Lithium-Air Batteries, J. Electrochem. Soc. 162 (2015).

[35] J. Lu, Y. Jung Lee, X. Luo, K. Chun Lau, M. Asadi, H.-H. Wang, S. Brombosz, J. Wen, D. Zhai, Z. Chen, D.J. Miller, Y. Sub Jeong, J.-B. Park, Z. Zak Fang, B. Kumar, A. Salehi-Khojin, Y.-K. Sun, L.A. Curtiss, K. Amine, A Lithium–Oxygen Battery Based on Lithium Superoxide, Nature. (2016) 1–7.

[36] N.B. Aetukuri, B.D. McCloskey, J.M. García, L.E. Krupp, V. Viswanathan, A.C. Luntz, Solvating Additives Drive Solution-Mediated Electrochemistry and Enhance Toroid Growth in Non-Aqueous Li–O2 Batteries, Nat. Chem. 7 (2014) 50–56.

[37] C.M. Burke, V. Pande, A. Khetan, V. Viswanathan, B.D. McCloskey, Enhancing Electrochemical Intermediate Solvation Through Electrolyte Anion Selection to Increase Nonaqueous Li–O2 Battery Capacity, PNAS. 112 (2015) 9293–9298.

[38] S. Meini, S. Solchenbach, M. Piana, H. a Gasteiger, The Role of Electrolyte Solvent Stability and Electrolyte Impurities in the Electrooxidation of Li2O2 in Li-O2 Batteries, J. Electrochem. Soc. 161 (2014) A1306–A1314.

[39] C.O. Laoire, S. Mukerjee, K.M. Abraham, E.J. Plichta, M.A. Hendrickson, Elucidating the Mechanism of Oxygen Reduction for Lithium-Air Battery Applications, J. Phys. Chem. C. 113 (2009) 20127–20134.

[40] Z. Peng, S. a. Freunberger, L.J. Hardwick, Y. Chen, V. Giordani, F. Bardé, P. Novák, D. Graham, J.M. Tarascon, P.G. Bruce, Oxygen Reactions In a Non-Aqueous Li+ Electrolyte, Angew. Chemie - Int. Ed. 50 (2011) 6351–6355.

[41] Y.S. Cohen, Y. Cohen, D. Aurbach, Micromorphological Studies of Lithium Electrodes in Alkyl Carbonate Solutions Using in Situ Atomic Force Microscopy, J. Phys. Chem. B. 104 (2000) 12282–12291.

[42] J. Christensen, P. Albertus, R.S. Sanchez-Carrera, T. Lohmann, B. Kozinsky, R. Liedtke, J. Ahmed, A. Kojic, A Critical Review of Li/Air Batteries, J. Electrochem. Soc. 159 (2012) R1.

[43] S. Das, J. Højberg, K.B. Knudsen, R. Younesi, P. Johansson, P. Norby, T. Vegge, Instability of Ionic Liquid-Based Electrolytes in Li–O $_2$ Batteries, J. Phys. Chem. C. 119 (2015) 18084–18090.

[44] R. Younesi, P. Norby, T. Vegge, A New Look at the Stability of Dimethyl Sulfoxide and Acetonitrile in Li-O2 Batteries, ECS Electrochem. Lett. 3 (2014) A15–A18.

[45] B. McCloskey, D.S. Bethune, R.M. Shelby, T. Mori, R. Scheffler, A. Speidel, M. Sherwood, A.C. Luntz, Limitations in Rechargeability of Li-O2 Batteries and Possible Origins, J. Phys. Chem. Lett. 3 (2012) 3043–4047.

[46] M.M. Ottakam Thotiyl, S.A. Freunberger, Z. Peng, Y. Chen, Z. Liu, P.G. Bruce, A Stable Cathode for the Aprotic Li-O2 Battery., Nat. Mater. 12 (2013) 1050–6.

[47] J. Shui, F. Du, C. Xue, Q. Li, L. Dai, Vertically Aligned N Doped Coral-like Carbon Fiber Arrays as Efficient Air Electrodes for High-Performance Nonaqueous Li-O2 batteries, ACS Nano. (2014) 3015–3022.

[48] Y.S. Mekonnen, K.B. Knudsen, J.S.G. Myrdal, R. Younesi, J. Højberg, J. Hjelm, P. Norby, T. Vegge, Communication: The Influence of CO2 Poisoning on Overvoltages and Discharge Capacity in Non-Aqueous Li-Air Batteries, J. Chem. Phys. 140 (2014) 2012–2017.

[49] S.R. Gowda, A. Brunet, G.M. Wallraff, B.D. McCloskey, Implications of CO2 Contamination in Rechargeable Nonaqueous Li-O2 Batteries, J. Phys. Chem. Lett. 4 (2013) 276–279.

[50] H. Lim, H. Lim, K. Park, D. Seo, H. Gwon, J. Hong, W. a Goddard, H. Kim, K. Kang, Toward a Lithium – "Air" Battery: The ffect of CO2 on the Chemistry of a Lithium–Oxygen Cell, J. Am. Chem. Soc. 742 (2013) 9733–9742.

[51] C. V. Amanchukwu, J.R. Harding, Y. Shao-Horn, P.T. Hammond, Understanding the Chemical Stability of Polymers for Lithium–Air Batteries, Chem. Mater. 27 (2015) 550–561.

[52] M.W. Chase Jr., J. Phys. Chem. Ref. Data, Monograph 9, 1998.

[53] J. Hojberg, K.B. Knudsen, J. Hjelm, T. Vegge, Reactions and SEI Formation during Charging of Li-O2 Cells, ECS Electrochem. Lett. 4 (2015) A63–A66.

[54] K.B. Knudsen, A.C. Luntz, S.H. Jensen, T. Vegge, J. Hjelm, Redox Probing Study of the Potential Dependence of Charge Transport Through Li2O2, J. Phys. Chem. C. 119 (2015) 28292–28299.

[55] Y.-C. Lu, D.G. Kwabi, K.P.C. Yao, J.R. Harding, J. Zhou, L. Zuin, Y. Shao-Horn, The Discharge Rate Capability of Rechargeable Li–O2 Batteries, Energy Environ. Sci. 4 (2011) 2999.

[56] J. Xiao, D. Wang, W. Xu, D. Wang, R.E. Williford, J. Liu, J.-G. Zhang, Optimization of Air Electrode for Li/Air Batteries, J. Electrochem. Soc. 157 (2010) A487.

[57] Y. Gao, C. Wang, W. Pu, Z. Liu, C. Deng, P. Zhang, Z. Mao, Preparation of High-Capacity Air Electrode for Lithium-Air Batteries, Int. J. Hydrogen Energy. 37 (2012) 12725–12730.

[58] Y. Li, J. Wang, X. Li, D. Geng, R. Li, X. Sun, Superior Energy Capacity of Graphene Nanosheets for a Nonaqueous Lithium Oxygen Battery., Chem. Commun. 47 (2011) 9438–9440.

[59] X. Yang, P. He, Y. Xia, Preparation of Mesocellular Carbon Foam and Its Application for Lithium/Oxygen Battery, Electrochem. Commun. 11 (2009) 1127 – 1130.

[60] B.M. Gallant, R.R. Mitchell, D.G. Kwabi, J. Zhou, L. Zuin, C. V Thompson, Y. Shao-Horn, Chemical and Morphological Changes of Li-O2 Battery Electrodes upon Cycling, J. Phys. Chem. C. 116 (2012) 20800–20805.

[61] G.Q. Zhang, J.P. Zheng, R. Liang, C. Zhang, B. Wang, M. Hendrickson, E.J. Plichta, Lithium–Air Batteries Using SWNT/CNF Buckypapers as Air Electrodes, J. Electrochem. Soc. 157 (2010) A953.

[62] Z. Peng, S. a. Freunberger, Y. Chen, P.G. Bruce, A Reversible and Higher-Rate Li-O2 Battery, Science. 337 (2012) 563–566.

[63] B.D. McCloskey, A. Valery, A.C. Luntz, S.R. Gowda, G.M. Wallraff, J.M. Garcia, T. Mori,

L.E. Krupp, Combining Accurate O2 and Li2O2 Assays to Separate Discharge and Charge Stability Limitations in Nonaqueous Li-O 2 Batteries, J. Phys. Chem. Lett. 4 (2013) 2989–2993.

[64] D.M. Itkis, D.A. Semenenko, E.Y. Kataev, A.I. Belova, V.S. Neudachina, A.P. Sirotina, M. Hävecker, D. Teschner, A. Knop-Gericke, P. Dudin, A. Barinov, E.A. Goodilin, Y. Shao-Horn, L. V. Yashina, Reactivity of Carbon in Lithium-Oxygen Battery Positive Electrodes, Nano Lett. 13 (2013) 4697–4701.

[65] Doron Aurbach, IMLB, invited pressentation: On the Frontier of Li Ion Batteries and the Horizon Beyond Them, (2014).

[66] Y. Yang, M. Shi, Y.-S. Li, Z.-W. Fu, MnO2-Graphene Composite Air Electrode for Rechargeable Li-Air Batteries, J. Electrochem. Soc. 159 (2012) A1917–A1921.

[67] S. Dong, X. Chen, K. Zhang, L. Gu, L. Zhang, X. Zhou, L. Li, Z. Liu, P. Han, H. Xu, J. Yao, C. Zhang, X. Zhang, C. Shang, G. Cui, L. Chen, Molybdenum Nitride Based Hybrid Cathode for Rechargeable Lithium–O2 Batteries, Chem. Commun. 47 (2011) 11291.

[68] Y. Yang, M. Shi, Q.F. Zhou, Y.S. Li, Z.W. Fu, Platinum Nanoparticle-Graphene Hybrids Synthesized by Liquid Phase Pulsed Laser Ablation as Cathode Catalysts for Li-Air Batteries, Electrochem. Commun. 20 (2012) 11–14.

[69] R.E. Williford, J.-G. Zhang, Air Electrode Design for Sustained High Power Operation of Li/Air Batteries, J. Power Sources. 194 (2009) 1164 – 1170.

[70] C. Liu, R. Younesi, C.-W. Tai, M. Valvo, K. Edström, T. Gustafsson, J. Zhu, 3-D Binder-Free Graphene Foam as Cathode for High Capacity Li-O2 Batteries, J. Mater. Chem. A. (2016).

[71] W. Zhang, J. Zhu, H. Ang, Y. Zeng, N. Xiao, Y. Gao, W. Liu, H.H. Hng, Q. Yan, Binder-Free Graphene Foams for O2 Electrodes of Li-O2 Batteries., Nanoscale. 5 (2013) 9651–8.

[72] K.S. Novoselov;, A.K. Geim;, S. V. Morozov;, D. Jiang;, Y. Zhang;, S. V. Dubonos;, I. V. Grigorieva;, A.A. Firsov;, Electric Field Effect in Atomically Thin Carbon Films, Science. 306 (2004) 666–669.

[73] J.-J. Xu, Z.-L. Wang, D. Xu, L.-L. Zhang, X.-B. Zhang, Tailoring Deposition and Morphology of Discharge Products Towards High-Rate and Long-Life Lithium-Oxygen Batteries., Nat. Commun. 4 (2013) 2438.

[74] C. Shu, B. Li, B. Zhang, D. Su, Hierarchical Nitrogen-Doped Graphene/Carbon Nanotube Composite Cathode for Lithium-Oxygen Batteries, ChemSusChem. 8 (2015) 3973–3976.

[75] B.D. McCloskey, R. Scheffler, A. Speidel, D.S. Bethune, R.M. Shelby, A.C. Luntz, On the Efficacy of Electrocatalysis in Nonaqueous Li-O2 Batteries, J. Am. Chem. Soc. 133 (2011) 18038–18041.

[76] E. Yilmaz, C. Yogi, K. Yamanaka, T. Ohta, H.R. Byon, Promoting Formation of Noncrystalline Li2O2 in the Li–O2 Battery with RuO2 Nanoparticles, Nano Lett. 13 (2013) 4679–4684.

[77] L. Zhang, S. Zhang, K. Zhang, G. Xu, X. He, S. Dong, Z. Liu, C. Huang, L. Gu, G. Cui, Mesoporous NiCo2O4 Nanoflakes as Electrocatalysts for Rechargeable Li–O2

Batteries, Chem. Commun. 49 (2013) 3540.

[78] F. Li, R. Ohnishi, Y. Yamada, J. Kubota, K. Domen, A. Yamada, H. Zhou, Carbon Supported TiN Nanoparticles: An Efficient Bifunctional Catalyst for Non-Aqueous Li-O2 Batteries., Chem. Commun. 49 (2013) 1175–7.

[79] J.-J. Xu, Z.-L. Wang, D. Xu, F.-Z. Meng, X.-B. Zhang, 3D Ordered Macroporous LaFeO3 as Efficient Electrocatalyst for Li–O2 Batteries with Enhanced Rate Capability and Cyclic Performance, Energy Environ. Sci. 7 (2014) 2213.

[80] K.P.C. Yao, M. Risch, S.Y. Sayed, Y.-L. Lee, J.R. Harding, A.J.L. Grimaud, N. Pour, Z.J. Xu, J. Zhou, A.N. Mansour, F. Bardé, Y. Shao-Horn, Solid-State Activation of Li2O2 Oxidation Kinetics and Implications for Li-O2 Batteries, Energy Environ. Sci. (2015) 2417–2426.

[81] M.D. Radin, C.W. Monroe, D.J. Siegel, How Dopants can Enhance Charge Transport in Li2O2, Chem. Mater. 27 (2015) 839–847.

[82] T. Liu, M. Leskes, W. Yu, A.J. Moore, L. Zhou, P.M. Bayley, G. Kim, C.P. Gray, Cycling Li-O2 Batteries via LiOH Formation and Decomposition, Science. (2015) 530–533.

[83] Y. Chen, S. a Freunberger, Z. Peng, O. Fontaine, P.G. Bruce, Charging a Li-O2 Battery Using a Redox Mediator, Nat. Chem. 5 (2013) 489–94.

[84] W.H. Bragg, W.L. Bragg, The Reflection of X-rays by Crystals, Proc. R. Soc. London A Math. Phys. Eng. Sci. 88 (1913) 428–438.

[85] P. Atkins, J. De Paula, Atkins Physical Chemistry, 8th edition, Oxford, 2006.

[86] S. Mobilio, F. Boscherini, C. Meneghini, Synchrotron Radiation -Basics, Methods and Applications, Springer Berlin Heidelberg, 2015.

[87] A P Hammersley, FIT2D: An Introduction and Overview, ESRF Intern. Rep. ESRF97HA02 (1997).

[88] Bruker, Topas3, (2000).

[89] Bruker, DIFFRAC.EVA, DIFFRAC.EVA – next Era Phase Anal.

[90] Rigaku, Integrated X-ray powder diffraction software, Rigaku J. 26 (2010) 23–27.

[91] B. Hinrichsen, R.E. Dinnebier, M. Jansen, Powder3D 1.2, (2004) Max Planck Institute for Solid State Research.

[92] Paul van der Heide, X-Ray Photoelectron Spectroscopy: An Introduction to Principles and Practices, 2012.

[93] D. Pleul, F. Simon, X-Ray photoelectron spectroscopy, in: Polym. Surfaces Interfaces Charact. Modif. Appl., Springer Berlin Heidelberg, 2008: pp. 71–89.

[94] IGORPro, WaveMetric. (1989) Version 4.0.

[95] D.L. Bryce, G.M. Bernard, M. Gee, M.D. Lumsden, K. Eichele, R.E. Wasylishen, Practical Aspects of Modern Routine Solid-State Multinuclear Magnetic Resonance Spectroscopy : One-Dimensional Experiments, Can. J. Anal. Sci. Spectrosc. 46 (2001) 46–82.

[96] Mestranova, Mestralab Res. Chem. Softw. Solut.

[97] R.F. Egerton, Physical Principles of Electron Microscopy, Mater. Today. 8 (2005) 60–60.

[98] D. Brandon, W.D. Kaplan, Scanning Electron Microscopy, in: Microstruct. Charact. Mater., John Wiley & Sons, Ltd, 2008: pp. 261–331.

[99] K.B. Knudsen, Alkali Metal-O2 Batteries Performance and Lifetime Limiting Effects, Technical University of Denmark, 2015.

[100] J. Højberg, Fundamental Mechanisms in Li-Air Battery Electrochemistry, Technical University of Denmark, 2015.

[101] J. Højberg, B.D. McCloskey, J. Hjelm, T. Vegge, K. Johansen, P. Norby, A.C. Luntz, An Electrochemical Impedance Spectroscopy Investigation of the Overpotentials in Li-O2 Batteries, ACS Appl. Mater. Interfaces. 7 (2015) 4039–4047.

[102] R.E. Johnsen, P. Norby, Capillary-Based Micro-Battery Cell for in situ X-ray Powder Diffraction Studies of Working Batteries: A Study of the Initial Intercalation and Deintercalation of Lithium into Graphite, J. Appl. Crystallogr. 46 (2013) 1537–1543.

[103] S.R. Younesi, M. Hahlin, F. Bjorefors, P. Johansson, K. Edstrom, Li-O2 Battery Degradation by Lithium Peroxide: A Model Study, Chem. Mater. 25 (2013) 77–84.

[104] M. Segal, Selling Graphene by the Ton., Nat. Nanotechnol. 4 (2009) 612–614.

[105] Q. Zhuo, J. Gao, M. Peng, L. Bai, J. Deng, Y. Xia, Y. Ma, J. Zhong, X. Sun, Large-Scale Synthesis of Graphene by the Reduction of Graphene Oxide at Room Temperature Using Metal Nanoparticles as Catalyst, Carbon. 52 (2013) 559–564.

[106] S. Pei, H.M. Cheng, The Reduction of Graphene Oxide, Carbon. 50 (2012) 3210–3228.

[107] K.P. Loh, Q. Bao, G. Eda, M. Chhowalla, Graphene Oxide as a Chemically Tunable Platform for Optical Applications., Nat. Chem. 2 (2010) 1015–1024.

[108] Y. Zhu, S. Murali, W. Cai, X. Li, J.W. Suk, J.R. Potts, R.S. Ruoff, Graphene and Graphene Oxide: Synthesis, Properties, and Applications, Adv. Mater. 22 (2010) 3906–3924.

[109] O.C. Compton, S.T. Nguyen, Graphene oxide, Highly Reduced Graphene Oxide, and Graphene: Versatile Building Blocks for Carbon-Based Materials, Small. 6 (2010) 711–723.

[110] B.C. Brodie, On the Atomic Weight of Graphite, Philos. Trans. R. Soc. London. 149 (1859) 249–259.

[111] L. Staudenmaier, Verfahren zur Darstellung der Graphitsäure, Berichte Der Dtsch. Chem. Gesellschaft. 31 (1898) 1481–1487.

[112] J. William S. Hummers, R.E. Offeman, Preparation of Graphitic Oxide, J. Am. Chem. Soc. 80 (1958) 1339.

[113] D.C. Marcano, D. V Kosynkin, J.M. Berlin, a Sinitskii, Z.Z. Sun, a Slesarev, L.B. Alemany, W. Lu, J.M. Tour, Improved Synthesis of Graphene Oxide, ACS Nano. 4 (2010) 4806–4814.

[114] N.I. Kovtyukhova, P.J. Ollivier, B.R. Martin, T.E. Mallouk, S.A. Chizhik, E. V. Buzaneva, A.D. Gorchinskiy, Layer-by-Layer Assembly of Ultrathin Composite Films from Micron-Sized Graphite Oxide Sheets and Polycations, Chem. Mater. 11 (1999) 771–778.

[115] M. Hirata, T. Gotou, S. Horiuchi, M. Fujiwara, M. Ohba, Thin-film Particles of Graphite Oxide 1: High-Yield Synthesis and Flexibility of the Particles, Carbon. 42 (2004) 2929–2937.

[116] B.C. Brodie, Graphite Oxide, Chem. Soc. Rev. 39 (2010) 1–4.

[117] A.M. Dimiev, J.M. Tour, Mechanism of Graphene Oxide Formation, ACS Nano. (2014) 3060–3068.

[118] D. Krishnan, F. Kim, J. Luo, R. Cruz-Silva, L.J. Cote, H.D. Jang, J. Huang, Energetic Graphene Oxide: Challenges and Opportunities, Nano Today. 7 (2012) 137–152.

[119] S. Stankovich, D. a. Dikin, R.D. Piner, K. a. Kohlhaas, A. Kleinhammes, Y. Jia, Y. Wu, S.T. Nguyen, R.S. Ruoff, Synthesis of Graphene-Based Nanosheets via Chemical Reduction of Exfoliated Graphite Oxide, Carbon. 45 (2007) 1558–1565.

[120] J.H. Lee, W.H. Shin, M.-H. Ryou, J.K. Jin, J. Kim, J.W. Choi, Functionalized Graphene for High Performance Lithium Ion Capacitors., ChemSusChem. 5 (2012) 2328–33.

[121] X. Fan, W. Peng, Y. Li, X. Li, S. Wang, G. Zhang, F. Zhang, Deoxygenation of Exfoliated Graphite Oxide Under Alkaline Conditions: A Green Route to Graphene Preparation, Adv. Mater. 20 (2008) 4490–4493.

[122] K. Parvez, R. Li, S.R. Puniredd, Y. Hernandez, F. Hinkel, S. Wang, X. Feng, K. Müllen, Electrochemically Exfoliated Graphene as Solution-Processable, Highly Conductive Electrodes for Organic Electronics, ACS Nano. 7 (2013) 3598–3606.

[123] K.R. Paton, E. Varrla, C. Backes, R.J. Smith, U. Khan, A. O'Neill, C. Boland, M. Lotya, O.M. Istrate, P. King, T. Higgins, S. Barwich, P. May, P. Puczkarski, I. Ahmed, M. Moebius, H. Pettersson, E. Long, J. Coelho, S.E. O'Brien, E.K. McGuire, B.M. Sanchez, G.S. Duesberg, N. McEvoy, T.J. Pennycook, C. Downing, A. Crossley, V. Nicolosi, J.N. Coleman, Scalable Production of Large Quantities of Defect-Free Few-Layer Graphene by Shear Exfoliation in Liquids, Nat. Mater. 13 (2014) 624–630.

[124] H.C. Schniepp, J.L. Li, M.J. McAllister, H. Sai, M. Herrera-Alonson, D.H. Adamson, R.K. Prud'homme, R. Car, D.A. Seville, I.A. Aksay, Functionalized Single Graphene Sheets Derived from Splitting Graphite Oxide, J. Phys. Chem. B. 110 (2006) 8535–8539.

[125] M.J. Mcallister, J. Li, D.H. Adamson, H.C. Schniepp, A.A. Abdala, J. Liu, O.M. Herrera-alonso, D.L. Milius, R. Car, R.K. Prud, I.A. Aksay, Single Sheet Functionalized Graphene by Oxidation and Thermal Expansion of Graphite, Chem. Mater. 19 (2007) 4396–4404.

[126] F. Tuinstra, L. Koenig, Raman Spectrum of Graphite, J. Chem. Phys. 53 (1970) 1126–1130.

[127] P.-G. Ren, D.-X. Yan, X. Ji, T. Chen, Z.-M. Li, Temperature Dependence of Graphene Oxide Reduced by Hydrazine Hydrate., Nanotechnology. 22 (2011) 055705.

[128] Y. Hiramitsu, H. Sato, H. Hosomi, Y. Aoki, T. Harada, Y. Sakiyama, Y. Nakagawa, K. Kobayashi, M. Hori, Influence of Humidification on Deterioration of Gas Diffusivity

in Catalyst Layer on Polymer Electrolyte Fuel Cell, J. Power Sources. 195 (2010) 435–444.

[129] M.C. Kim, G.S. Hwang, R.S. Ruoff, Epoxide Reduction with Hydrazine on Graphene: A First Principles Study, J. Chem. Phys. 131 (2009) 1–6.

[130] Y. Li, J. Wang, X. Li, D. Geng, M.N. Banis, R. Li, X. Sun, Nitrogen-Doped Graphene Nanosheets as Cathode Materials with Excellent Electrocatalytic Activity for High Capacity Lithium-Oxygen Batteries, Electrochem. Commun. 18 (2012) 12–15.

[131] J. Liu, M. Roberts, R. Younesi, M. Dahbi, J. Zhu, Accelerated Electrochemical Decomposition of Li2O2 under X-ray Illumination, J. Phys. Chem. Lett. (2013) 1–3.

Appendix

Paper I

Journal of Solid State Chemistry 240 (2016) 49–54

Contents lists available at ScienceDirect

Journal of Solid State Chemistry

journal homepage: www.elsevier.com/locate/jssc

In situ X-ray powder diffraction studies of the synthesis of graphene oxide and formation of reduced graphene oxide

Mie Møller Storm*, Rune E. Johnsen, Poul Norby

Department of Energy Conversion and Storage, Technical University of Denmark, Frederiksborgvej 399, 4000 Roskilde, Denmark

ARTICLE INFO

Article history:
Received 10 March 2016
Received in revised form
3 May 2016
Accepted 17 May 2016
Available online 17 May 2016

Keywords:
Hummers method
Thermal reduction
Graphene oxide
Reduced graphene oxide
X-ray diffraction
In situ

ABSTRACT

Graphene oxide (GO) and reduced graphene oxide (rGO) are important materials in a wide range of fields. The modified Hummers methods, for synthesizing GO, and subsequent thermal reduction to rGO, are often employed for production of rGO. However, the mechanism behinds these syntheses methods are still unclear. We present an *in situ* X-ray diffraction study of the synthesis of GO and thermal reduction of GO. The X-ray diffraction revealed that the Hummers method includes an intercalation state and finally formation of additional crystalline material. The formation of GO is observed during both the intercalation and the crystallization stage. During thermal reduction of GO three stages were observed: GO, a disordered stage, and the rGO stage. The appearance of these stages depends on the heating ramp. The aim of this study is to provide deeper insight into the chemical and physical processes during the syntheses.

1. Introduction

Graphene oxide (GO) and reduced graphene oxide (rGO), synthesized from GO, has a future in fields ranging from electronics to energy technologies [1]. Small changes in the GO synthesis affects properties such as water intercalation [2] and surface functionalities [3], whereas changes in the thermal reduction routes causes changes in the deoxygenation process [4]. As small changes in the synthesis affects the product, thorough knowledge of the reactions could influence the choice in synthesis methods depending on the use of the material.

Graphene oxide was prepared as early as 1859 by Brodie [5]. Staudenmaier,1898 [6] and Hummer and Offeman, 1958 [7] proposed their own synthesis routes to GO formation, which improved the chemical safety and reduced the evolution of toxic gasses. Different modifications to the oxidation process have been made on the Hummers method [8–10], and these are now often known as modified Hummers methods. Even though several different variations of this process have been employed, the foundation of the methods remains the same: concentrated sulfuric acid, permanganate and possibly nitrate form a highly oxidizing environment, which partially oxidize graphite into graphene layers with oxygen functionalities and defects [11]. The final step includes termination of the synthesis by H_2O_2 and water addition.

Even though the detailed structure of GO is still unknown, GO may be used in a range of applications [12,13], as well as the more commonly known function as a possible precursor for large scale synthesis of the graphene-like material reduced graphene oxide (rGO) [1,14–16].

Dreyer et al. [16] suggested that the active oxidizing species in the oxidation is dimanganese heptoxide, created by the reaction of permanganate and sulfuric acids.

$$Mn^{VII}O_4^- + 3H_2SO_4 \rightarrow Mn^{VII}O_3^+ + H_3O^+ + 3HSO_4^-$$

$$MnO_3^+ + MnO_4^- \rightarrow Mn_2O_7$$

This suggestion was based on Mn_2O_7 ability to selectively oxidize unsaturated aliphatic double bonds, compared to aromatic bonds. The presence of this species has yet to be confirmed.

Dimiev and Tour [17] investigated samples obtained during the modified Hummers method by optical microscopy and Raman spectroscopy. Centrifuged and separated samples were analyzed by X-ray diffraction (XRD). They observed three stages during the modified Hummers method; graphite intercalation, graphite oxidation and formation of GO. Kang et al. [18] observed that the addition of water during the termination of the synthesis also affect the GO product, showing how small changes in the synthesis affects the results.

Different reduction methods have been used for the transformation of GO to rGO. Chemical or thermal reduction are common synthesis routes towards rGO. Chemical reduction by hydrazine removes many of the oxygen functionalities and introduces

* Corresponding author.
E-mail address: mmst@dtu.dk (M.M. Storm).

http://dx.doi.org/10.1016/j.jssc.2016.05.019
0022-4596/

nitrogen atoms to the rGO [19]. Other variation in the methods and other chemical reduction methods have been successfully employed as well and has been described in various reviews along with the many properties of rGO [11,16,20]. That GO undergoes changes upon heating was observed by Brodie, as a reduction of the oxygen and hydrogen components compared to carbon was observed when GO was heated [5]. Thermal reduction leads to decomposition and expansion of the GO layers by formation of CO_2, CO and H_2O gas [21], which causes pressure between the carbon planes in GO. The change from ordered GO to a more amorphous rGO upon shock heating is clearly observed by XRD studies where GO, with a sharp 001 diffraction peak, is changed to disordered rGO [22]. Thermal reduction of GO causes structural damage and lattice defects to the graphene plane as carbon atoms are removed [11]. Thermal reduction can be performed in various atmospheres and at different heating rates [20]. Few *in situ* studies of the formation of rGO have been made. Osswald et al. [23] studied the reduction expansion synthesis of GO with urea to graphene with *in situ* Raman spectroscopy from 25 to 800 °C. The G band and the corresponding full width at half maximum changed upon reaction indicating clear irreversible changes. The G band was downshifted which can be caused by changes in the oxygen surface groups, healing of structural defects or changes in interlayer spacing. A minimum temperature of 800 °C was needed during the synthesis with urea as expansion agent.

In this paper we present results from *in situ* XRD experiments during GO synthesis by the modified Hummers method and the thermal reduction of GO with both reactions being performed in capillary cells. The modified Hummers methods shows new diffraction peaks for GO and the thermal reduction reveals a new stage in the transition between GO and rGO.

2. Experimental

2.1. Ex situ synthesis of GO

3 g natural flake graphite (325 mesh, 98% metal basis supplied by Alfa Aesar) was mixed with 1.5 g $NaNO_3$ (Alfa Aesar) in an Erlenmeyer flask on ice. 100 ml conc. H_2SO_4 (Sigma Aldrich) was added under stirring, and after 10 min with ice bath cooling 12.0 g $KMnO_4$ (Alfa Aesar) was added over a time period of 40 min The dispersion was cooled on ice for 2 h, before the reaction mixture was heated in a water bath to 35 °C. Samples with reaction times of 3 h and 3 days were prepared. A sample of the mixture was extracted for *ex situ* XRD after heating for 3 h and stored in a small Duran laboratory bottle (named the GO-intermediate). The Erlenmeyer flask and the small extracted sample were placed on ice to terminate the reaction. The reaction mixture was diluted with 100 ml ice cooled water which was followed by slow addition of 25 ml H_2O_2 (30% w/w in water, from Sigma Aldrich). The GO powder was isolated by centrifugation at 4500 rpm for 10 min, and the precipitate was washed with 0.1 M H_2SO_4 and dried in a vacuum oven at 25 °C overnight. The GO was washed four times with 1 M HCl with centrifugation and dried in a vacuum oven overnight at 25 °C. This washing process was repeated with acetone.

2.2. The in situ modified Hummers method

0.15 g Alfa Aesar graphite was mixed with 5 ml conc. H_2SO_4 by magnetic stirring for approx. 1 d, forming a graphite suspension. A quartz glass capillary cell (0.7 mm outer diameter) was prepared having quartz wool in one end, followed by 5 mm of loosely packed carefully grinded $KMnO_4$ powder. Approximately 7 mm graphite suspension was placed with a 5 mm gap to the $KMnO_4$ powder in the capillary (Fig. 1). Fig. S1, in supplementary material, shows a picture of the actual set-up. The capillary was mounted in a Swagelok based gas inlet system with a Vespel/graphite ferrule; a rather similar setup was described in [24]. The capillary was aligned in the X-ray beam on the $KMnO_4$ powder for X-ray measurements with an exposure time of 30 s. The XRD data collection was initiated and the graphite suspension was mixed with the $KMnO_4$ powder by gently adding a pressure of N_2 gas inside the capillary. Similar *in situ* experiments were performed three times at the synchrotron, with similar results.

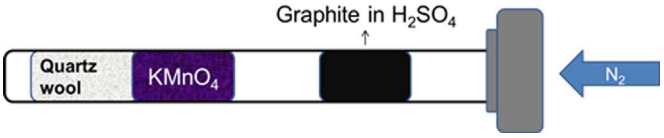

Fig. 1. The capillary set-up for the graphite oxidation.

2.3. In situ GO thermal reduction

A quartz glass capillary (0.7 mm outer diameter) was filled with quartz wool plugs in both ends with GO between the wool plugs. The GO was synthesized by the modified Hummers method with oxidation time of 3 h or 3 days, as described above [3]. Unless otherwise stated the GO powder used during the synthesis was the GO powder with an oxidation time of 3 h. The capillary was open in both ends and mounted in a modified Swagelok cell using a Vespel/graphite ferrule and connected to a gas delivery system. A small constant flow of N_2 gas was applied before the heating was initiated. The samples were measured with an exposure time of 30 s and different temperature ramps of 1, 5, 10, 20 and 50 °C/min. A hot-air blower was used to increase the temperature from 25 to 690 °C, and data were also collected during cooling. The temperature of the hot-air blower was calibrated using the known thermal expansion of metallic silver. A powdered silver sample in a capillary was heated and the unit-cell parameters were determined using Rietveld refinement as a function of the set-temperature. From these data a calibration curve was determined, allowing the actual sample temperature to be estimated. In order to decrease the effect of thermal gradients in the capillary, the X-ray beam is kept much smaller than the width of the hot-air blower. We believe that the calibrated temperatures are correct to within a few degrees. The hot-air blower had a non-linear increase in temperature despite its settings, as seen from the y-axis in Fig. 5.

2.4. X-ray diffraction

2.4.1. Synchrotron XRD

X-ray powder diffraction data were collected at the Swiss Norwegian beamline (SNBL), ESRF, with a wavelength of 0.7020 Å, a beam size of 0.5 × 0.5 mm and a sample-to-detector distance of 199.72 mm. The data were integrated by Fit2D [25] and normalized to a small 2θ range of the background (3.4–3.8° in 2θ for the GO synthesis and 24–27° in 2θ for the thermal reductions) in Powder3D [26]. Peak positions, intensity and *d*-values of *in situ* data was analyzed by Diffract suite EVA (Bruker software).

The graphite diffraction peaks described in the result and discussion section are dominantly from graphite 2 H.

2.4.2. Ex situ XRD

X-ray powder diffraction patterns of the GO-intermediate sample were collected on a Rigaku Smartlab X-ray diffractometer (Cu-Kα radiation) with a step size of 0.02 in 2θ at 1°/min from 5° to 120° in 2θ using Bragg-Brentano geometry and in transmission

geometry (focusing optics) for the capillary data (5–90° in 2θ, step size 0.02° in 2θ). XRD measurements of the GO-intermediate sample were performed after synthesis on an open sample holder. After 10 days confinement of the sample in a Duran laboratory glass bottle, the sample was measured in a capillary. The XRD diffraction patterns were similar.

3. Results and discussion

3.1. The modified Hummers method

Fig. 2 shows the XRD patterns of the modified Hummers method of GO synthesis in the capillary setup, which displayed three different stages. The intensity of the measured diffraction patterns decreased strongly during stage II, as seen in Fig. 2. This might be related to movements of the solvent in the capillary.

The first changed observed in the XRD patterns (termed stage I) consisted of the dissolution of $KMnO_4$. This was succeeded by an intercalation of the synthesis mixture into graphite (stage II) which was followed by formation of additional crystalline material (stage III). The GO was observed early during the synthesis by the 001 diffraction peak[1] at 5.01° in 2θ, d=7.97 Å, which increased in intensity through both stage II and III. This shows how GO is formed from the very beginning of the synthesis and continues to be formed during the synthesis. The last stage III of the modified Hummers methods show GO formation along with new previously unobserved diffraction peaks assigned to GO. The additional diffraction peaks of GO are not observed in the final product and reveals an ordered structure for GO during synthesis. Furthermore an additional unidentified new crystalline compound is observed in stage III as well.

Stage II displayed few diffraction peaks as seen in Fig. 3 (assignment in Table S1). During stage II peaks which may be assigned to graphite-hydrogensulphate appeared [27]. Graphite-hydrogensulphate is further discussed in SI. These diffraction peaks could indicate that the modified Hummers method have an intercalation of sulfuric acid or hydrogensulphate into the graphite layers, followed by further oxidation and water intercalation upon the GO formation. The sharp diffraction peak at 10.19° in 2θ during stage II has a small high-angle shoulder at 10.49° in 2θ which may be indexed as the 002 diffraction peak of GO.

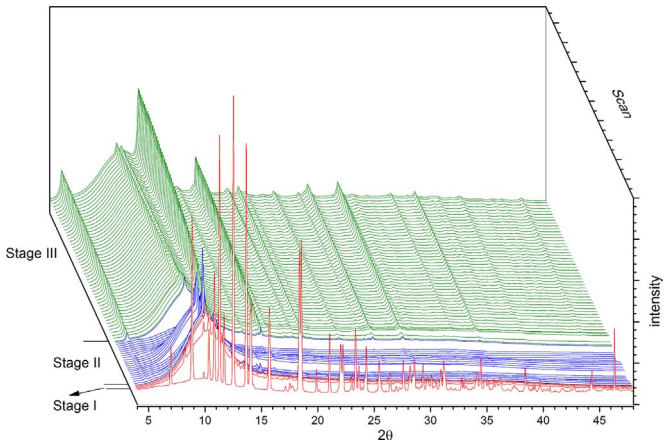

Fig. 2. The *in situ* XRD patterns for the GO capillary synthesis. Stage I displays every scan, stage II every 2nd and stage III every 3rd.

[1] For GO the patterns are indexed based on a hexagonal unit cell, where the length of the *c*-axis is equal to the interlayer distance.

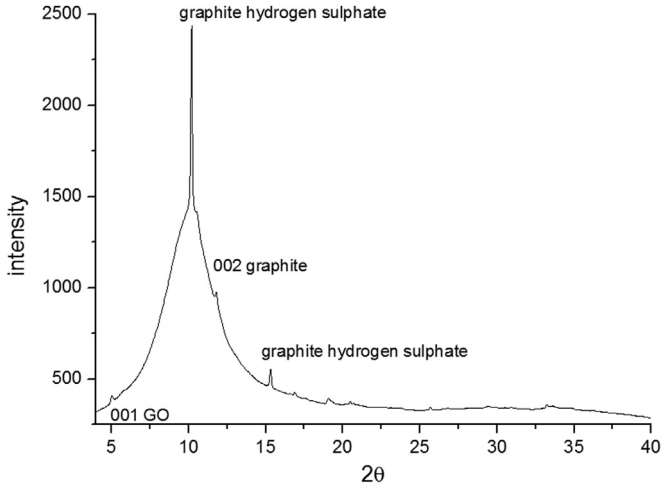

Fig. 3. Stage II of the GO synthesis.

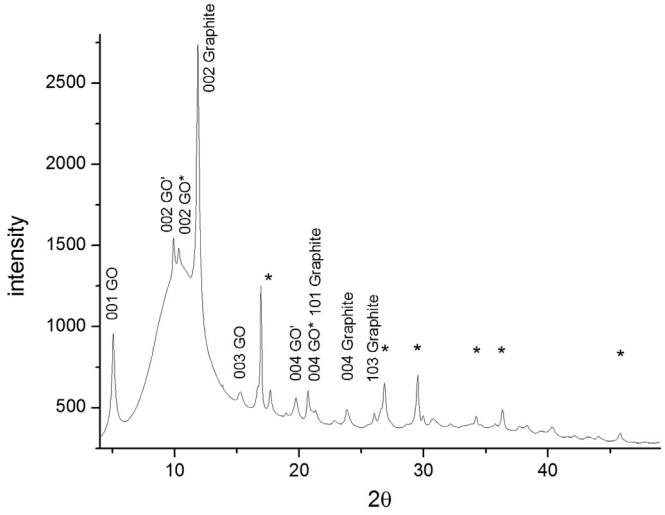

Fig. 4. Stage III of the GO synthesis, showing a split of the GO diffraction peaks, here termed GO* and GO', the calculated GO diffraction peak is placed between the double peaks. *mark the cubic reflections.

The diffraction peaks and the assignment of diffraction peaks of stage III for the *in situ* data can be seen in Fig. 4 and Table S2. Most peaks were identified but a complete assignment of the diffraction peaks for stage III was not possible. The diffraction peaks assigned to graphite in Fig. 4 are discussed in Supplementary material (SI).

For stage III several diffraction peaks were observed which can be ascribed to GO. A splitting of the GO diffraction peak was observed for the *in situ* diffraction patterns (Fig. 4 shows some of the diffraction peaks assigned as GO' or GO*). The split GO diffraction peaks have not been reported for *ex situ* XRD patterns of synthesized and washed GO. The expected and calculated *d*-value of GO (00*l*) lies between the observed GO' and GO**d*-values. The splitting of these diffraction peaks could be caused by different solvent intercalation. The splitting of the GO peaks during synthesis are not observed in the solid samples (see Fig. 6(A) for a GO diffractogram). The reduced number of diffraction peaks observed in the solid GO could be explained from elimination of solvent interaction by washing.

It was not possible to identify any compounds related to the other diffraction peaks at stage III, however a number of diffraction peaks (see Fig. 4) can be indexed based on a cubic unit cell with a=3.37 Å. It has been suggested that Mn_2O_7 plays a major role in the Hummers synthesis [17], but as Mn_2O_7 is liquid at room

temperature it cannot be observed by diffraction. It is worth noting that Mn_2O_7 is often formed as a highly explosive dark-green oil.

The XRD pattern of the laboratory GO-intermediate sample (which was extracted after the oxidation of graphite before termination of the experiment and measured "as is") resembled the XRD pattern obtained *in situ* at stage III in a capillary, with more well defined peaks, indicating that no significant changes were caused by the confined space of the capillary sample or the addition of $NaNO_3$ in the *ex situ* synthesis. The diffraction pattern of stage III, measured *ex situ*, can be indexed based on a triclinic unit cell. The unit cell was found by indexing and profile refinement to have the following parameters: $a=4.763$ Å, $b=8.268$ Å, $c=4.711$ Å, $\alpha=105.5°$, $\beta=119.4°$ and $\gamma=74.6°$, unit cell volume 154.65 Å^3. The profile fit can be seen in supplementary material Fig. S2. Care must be taken to validate the suggested unit cell when a structure is indexed as triclinic, but all peaks were indexed and only some calculated peaks were not observed. The triclinic unit cell has some similarities to the hexagonal unit cell of GO with a β-angle close to 120° and *a* close to *c*. It was not possible to find a known crystal structure with similar triclinic unit cell parameters. Further investigations are needed to elucidate the structure and composition of this phase in the modified Hummers synthesis.

3.2. Thermal reduction of graphene oxide

The GO thermal reduction goes through three stages, clearly observed from the changes in the initial 001 GO diffraction peak (4.9° in 2θ, $d=8.20$ Å). See Fig. 5 where the evolution in the diffraction pattern during heating at 5 °C/min is shown. The trend is similar for the heating ramps of 1, 10 and 20 °C/min. For a 3D plot of the GO reduction at 5 °C/min see Fig. S3. The *in situ* XRD shows three stages: a GO stage, a disordered stage and an ordered rGO stage. The disordered stage is observed for both high and low temperature ramps for heating of GO and has, to our knowledge, not been identified before. The low temperature disordered stage appear for all temperature ramps indicating that even at slow heating a disordered transition stage is involved. Reordering of rGO may take place during the heating depending on the ramp rate. The disordered stage has a resemblance to rGO formed by shock heating, while it has previously been assumed that the graphene layers of GO were ripped apart only upon fast heating.

Fig. 5 shows that the interlayer distances in GO decreased as the temperature increased, probably due to evaporation of intercalated water and partial reduction. Just below 200 °C the intensity of the 001 reflection decreased sharply and a broad peak appeared (at a *d*-value of approx. 4 Å, marked with red in the plot of temperature *vs* interlayer distance in Fig. 5) indicating formation of a disordered phase (here named the disordered stage). However, the 001 reflection did not disappear completely; a low intensity contribution from the 001 reflection continued to move toward lower *d*-values as seen in Fig. 5 and eventually reached the rGO stage. The 100 and 110 reflections of GO were observed during the disordered stage, see Figs. 5 and 6(A). The rGO phase was formed upon further heating, as the broad peak of the disordered stage changed into a more well-defined peak with *d*-values similar to the 002 diffraction peak observed for rGO [28]. The 002 reflection from graphite was present during the entire experiment as an impurity in the GO material. The position of the 002 rGO diffraction peak ($d=3.50$ Å, after cooling) during growth did not reach the *d*-value of the graphite reflection ($d=3.37$ Å) for the 5 and 20 °C/min experiments, indicating an incomplete reduction. For the controlled temperature ramp of 1 and 10 °C/min the interlayer distance of the rGO phase ended up closer to the 002 graphite diffraction peak after cooling ($d=3.43$ Å), indicate more complete conversion to graphite. The stages of the thermal reduction can be separated by grouping of the interlayer distance, as seen in Fig. 5. The GO interlayer distance decreased from 8.2 to 6.4 Å, the disordered stage is below 4 Å and the rGO stage decreased from 4.5 to 3.5 Å.

The three stages, the GO stage, the disordered stage and the rGO stage, were observed during heating of GO with temperature ramps of 1, 5, 10 and 20 °C/min. The diffraction peaks of the GO and the rGO stages were assigned as seen in Fig. 6 (The diffraction peaks of the rGO stage are given in Table S3 and the GO diffraction peaks are described in SI).

The on-set temperature of the disordered stage varied with temperature ramp rate. The disordered stage was observed in the same temperature range for the 5, 10 and 20 °C/min temperature ramps, from approximately 210–285 °C. The 1 °C/min temperature ramp displayed the disordered stage from approximately 190° to 230 °C. Decreasing the temperature ramping rate lowers the

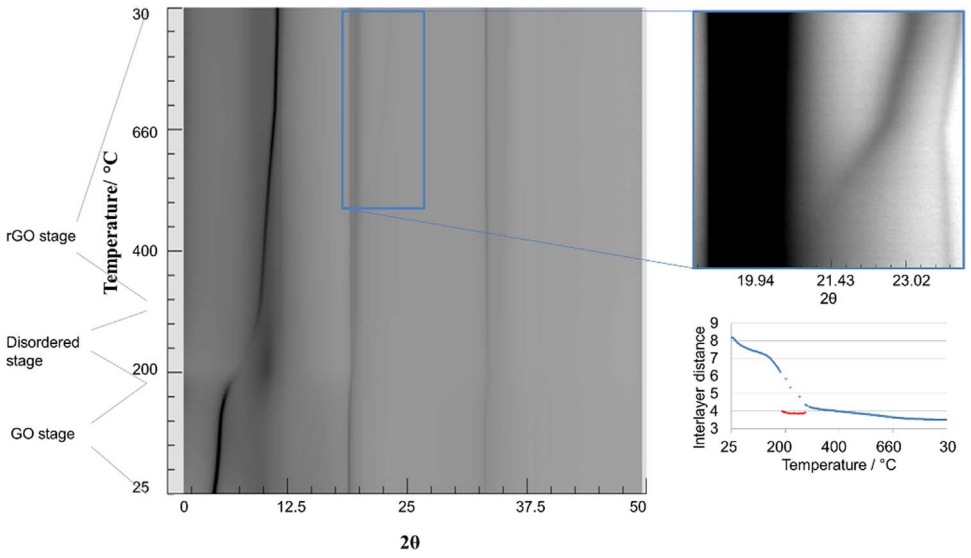

Fig. 5. A 2D plot of diffraction patterns during transformation of GO to rGO measured from 10° to 50° in 2θ, for the 5 °C/min heating rate, the approximate duration of the GO, disordered and rGO stage have been indicated. Inset: the appearance of a small peak at 22.5° in 2θ. Right, below: Plot of the interlayer distance *vs.* temperature, the dots connecting the two solid blue lines indicate the estimated *d*-spacing of the weak diffraction peak connecting the GO and rGO stage. (For interpretation of the references to color in this figure legend, the reader is referred to the web version of this article.)

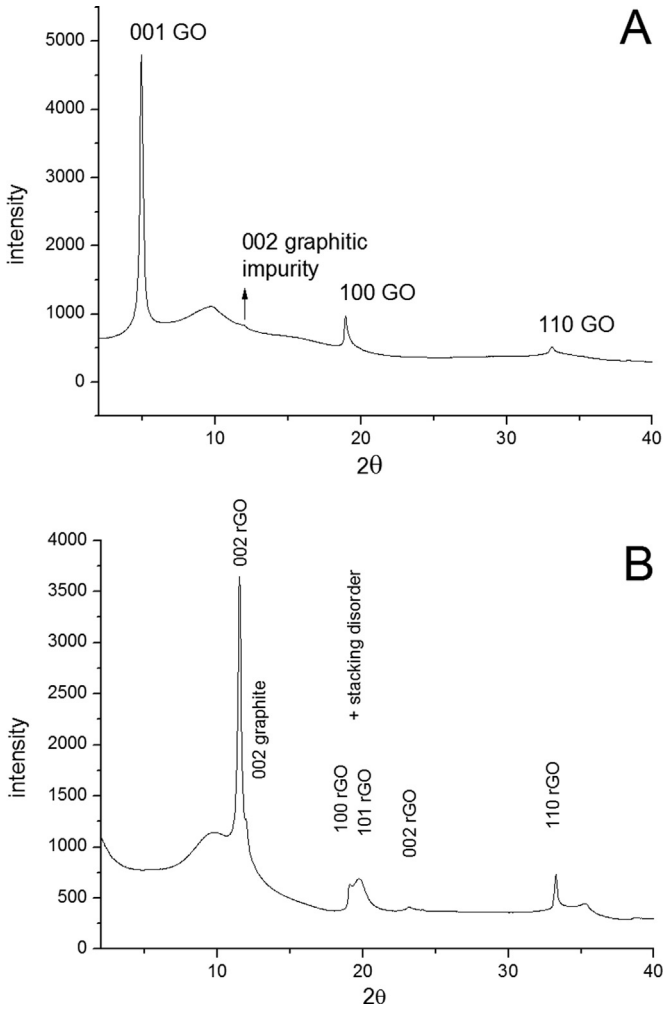

Fig. 6. (A): A diffraction pattern of the initial GO stage of the thermal reduction of GO, (B): A diffraction pattern of the rGO stage of the thermal reduction of GO.

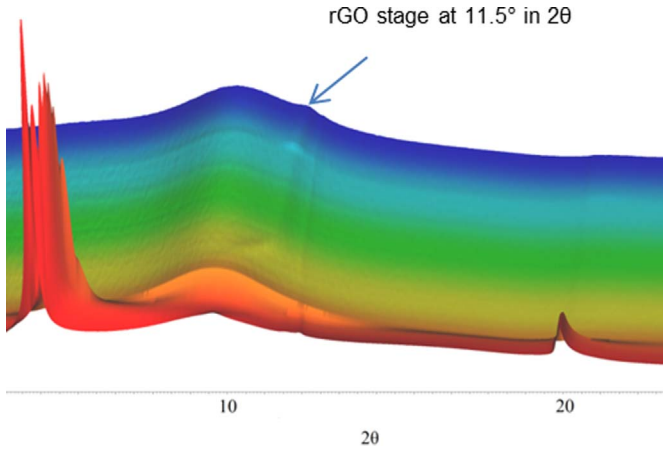

Fig. 7. XRD 3D surface plot of the thermal reduction of GO at 50 °C/min.

transition temperature due to thermally activated processes.

At increased temperature ramping rate of 50 °C/min a decrease of the diffraction intensity of the 002 rGO reflection was observed, see Fig. 7. Visual observation showed that some of the GO material had moved in the capillary, most likely due to the rapid expansion during thermal reduction. However, as the 002 graphite reflection was observed with a rather constant intensity throughout the entire scan series we assume that the movement did not affect the amount of material in the X-ray beam. The low intensity 002 rGO peak (at 11.5° in 2θ, see Fig. 7) indicates that almost all of the synthesized rGO was disordered at this high temperature ramp.

Thermal reduction of GO, with the GO inserted directly into a furnace at around 1000 °C, resulted in a similar very broad or absent 002 rGO peak. It is plausible that a high heating rate and the rapid decomposition inhibit the formation of a more ordered material. The formation of an amorphous product upon shock heating of GO was also observed by McAllister et al. [22], whereas they also observed a sharp diffraction peak and a high order rGO when the GO was heated at 1 °C/min. They suggested that the diffusion of the evolved gases during the synthesis was sufficient slow, for slower heated samples, to avoid exfoliation of the graphene oxide thus forming the ordered rGO.

Our rGO results show similar XRD pattern as those which were made in regular furnace. However as we perform *in situ* XRD we observe the formation of a disordered phase at an earlier stage in the reduction. This could suggest that the smaller pressure in the slowly heated rGO is not the full explanation for the formation of the ordered rGO. The lower pressure may enable rGO to form a relative ordered layered structure, revealing in the observed sharp 002 rGO diffraction peak, but as some order is re-gained also for the fast heated samples, this indicate that even samples which have been ripped apart may re-order to some degree. However, as our results are obtained by reaction in a capillary they could differ from what would be obtained in a furnace.

The three different stages for the thermal reduction of GO was also observed for a more oxidized sample GO sample (3 days oxidation time), details in SI. The observation of the same stages indicates that formation of a disordered stage is a common occurrence for all GO samples.

The disordered stage was observed for all the different reductions of GO which opens up for considerations of possible isolation of the disordered stage as a separate compound from low temperature treatment.

4. Conclusions

In situ XRD diffraction data for the modified Hummers method and thermal reduction of GO performed in a capillary were obtained. The oxidation by the modified Hummers method started with intercalation where sulfuric acid and HSO_4^+ was intercalated into the graphite. Formation of GO was observed concomitant with the intercalation and GO formation was continued into the last stage. In the last stage new diffraction peaks from GO during synthesis appeared, which were not observed in dried and cleaned GO. Stage III furthermore showed the development of a possible GO related crystalline material. Thermal reduction of GO to rGO occurs over three different stages. Small changes in the interlayer distance of GO were observed during the first stage with the *d*-value decreasing upon heating. The second disordered stage was observed at all heating rates. The temperature rate depended on the heating rate. following the disordered stage formation of ordered rGO was observed by XRD. However, at high heating rates the final rGO stage is more disordered than at lower heating rates. The observation of a disordered stage for all the investigated thermal reductions of GO indicate that the final rGO product results from reordering of the graphene layers.

Acknowledgement

The authors acknowledge and thanks for the support given by the staff at the Swiss-Norwegian beam-line, ESRF, the ReLiable

project funded by the Danish Council for Strategic Research-Programme Commission on Sustainable Energy and Environment (project no. 11-116792), and The Danish Research Council for the financial support of synchrotron measurements (DANSCAT).

Appendix A. Supplementary material

Supplementary data associated with this article can be found in the online version at http://dx.doi.org/10.1016/j.jssc.2016.05.019.

References

[1] M. Segal, Selling graphene by the ton, Nat. Nano 4 (2009) 612–614.
[2] T.N. Blanton, D. Majumdar, X-ray diffraction characterization of polymer intercalated graphite oxide, Powder Diff. 27 (2012) 104–107.
[3] M.M. Storm, M. Overgaard, R. Younesi, N.E.A. Reeler, T. Vosch, U.G. Nielsen, K. Edström, P. Norby, Reduced graphene oxide for Li-air batteries: the effect of oxidation time and reduction conditions for graphene oxide, Carbon 85 (2015) 233–244.
[4] A. Ganguly, S. Sharma, P. Papakonstantinou, J. Hamilton, Probing the thermal deoxygenation of graphene oxide using high-resolution in situ X-ray-based spectroscopies, J. Phys. Chem. C 115 (2011) 17009–17019.
[5] B.C. Brodie, On the atomic weight of graphite, Philos. Trans. R. Soc. Lond. 149 (1859) 249–259.
[6] L. Staudenmaier, Verfahren zur Darstellung der Graphitsäure, Ber. Dtsch. Chem. Ges. 31 (1898) 1481–1487.
[7] W.S. Hummers, R.E. Offeman, Preparation of graphitic oxide, J. Am. Chem. Soc. 80 (1958) 1339–1339.
[8] D.C. Marcano, D.V. Kosynkin, J.M. Berlin, A. Sinitskii, Z. Sun, A. Slesarev, L. B. Alemany, W. Lu, J.M. Tour, Improved synthesis of graphene oxide, ACS Nano 4 (2010) 4806–4814.
[9] N.I. Kovtyukhova, P.J. Ollivier, B.R. Martin, T.E. Mallouk, S.A. Chizhik, E. V. Buzaneva, A.D. Gorchinskiy, Layer-by-layer assembly of ultrathin composite films from micron-sized graphite oxide sheets and polycations, Chem. Mater. 11 (1999) 771–778.
[10] M. Hirata, T. Gotou, S. Horiuchi, M. Fujiwara, M. Ohba, Thin-film particles of graphite oxide 1: high-yield synthesis and flexibility of the particles, Carbon 42 (2004) 2929–2937.
[11] S. Pei, H.-M. Cheng, The reduction of graphene oxide, Carbon 50 (2012) 3210–3228.
[12] K.P. Loh, Q. Bao, G. Eda, M. Chhowalla, Graphene oxide as a chemically tunable platform for optical applications, Nat. Chem. 2 (2010) 1015–1024.
[13] D. Chen, H. Feng, J. Li, Graphene oxide: preparation, functionalization, and electrochemical applications, Chem. Rev. 112 (2012) 6027–6053.
[14] L. Zhang, J.J. Liang, Y. Huang, Y.F. Ma, Y. Wang, Y.S. Chen, Size-controlled synthesis of graphene oxide sheets on a large scale using chemical exfoliation, Carbon 47 (2009) 3365–3368.
[15] Q.Q. Zhuo, J. Gao, M.F. Peng, L.L. Bai, J.J. Deng, Y.J. Xia, Y.Y. Ma, J. Zhong, X. H. Sun, Large-Scale synthesis of graphene by the reduction of graphene oxide at room temperature using metal nanoparticles as catalyst, Carbon 52 (2013) 559–564.
[16] D.R. Dreyer, S. Park, C.W. Bielawski, R.S. Ruoff, The chemistry of graphene oxide, Chem. Soc. Rev. 39 (2010) 228–240.
[17] A.M. Dimiev, J.M. Tour, Mechanism of graphene oxide formation, ACS Nano 8 (2014) 3060–3068.
[18] J.H. Kang, T. Kim, J. Choi, J. Park, Y.S. Kim, M.S. Chang, H. Jung, K.T. Park, S. J. Yang, C.R. Park, Hidden second oxidation step of Hummers method, Chem. Mater. 28 (2016) 756–764.
[19] S. Stankovich, D.A. Dikin, R.D. Piner, K.A. Kohlhaas, A. Kleinhammes, Y. Jia, Y. Wu, S.T. Nguyen, R.S. Ruoff, Synthesis of graphene-based nanosheets via chemical reduction of exfoliated graphite oxide, Carbon 45 (2007) 1558–1565.
[20] S. Mao, H. Pu, J. Chen, Graphene oxide and its reduction: modeling and experimental progress, RSC Adv. 2 (2012) 2643–2662.
[21] H.C. Schniepp, J.-L. Li, M.J. McAllister, H. Sai, M. Herrera-Alonso, D.H. Adamson, R.K. Prud'homme, R. Car, D.A. Saville, I.A. Aksay, Functionalized single graphene sheets derived from splitting graphite oxide, J. Phys. Chem. B 110 (2006) 8535–8539.
[22] M.J. McAllister, J.-L. Li, D.H. Adamson, H.C. Schniepp, A.A. Abdala, J. Liu, M. Herrera-Alonso, D.L. Milius, R. Car, R.K. Prud'homme, I.A. Aksay, Single sheet functionalized graphene by oxidation and thermal expansion of graphite, Chem. Mater. 19 (2007) 4396–4404.
[23] M. Mowry, D. Palaniuk, C.C. Luhrs, S. Osswald, In situ Raman spectroscopy and thermal analysis of the formation of nitrogen-doped graphene from urea and graphite oxide, RSC Adv. 3 (2013) 21763–21775.
[24] R.E. Johnsen, F. Krumeich, P. Norby, Structural and microstructural changes during anion exchange of CoAl layered double hydroxides: an in situ X-ray powder diffraction study, J. Appl. Crystallogr. 43 (2010) 434–447.
[25] A.P. Hammersley, 1997, FIT2D: An Introduction and Overview, ESRF Internal Report ESRF97HA02T.
[26] B. Hinrichsen, R.E. Dinnebier, M. Jansen, 2004, Powder3D 1.2, DOI. Max Planck Institute for Solid State Research.
[27] L. Monyakina, V. Avdeev, I. Nikol'skaya, A. Litvinenko, N. Fadeeva, 1990, Inorganic Material (Engl. Transl.).
[28] E. Dervishi, Z. Li, F. Watanabe, A. Biswas, Y. Xu, A.R. Biris, V. Saini, A.S. Biris, Large-scale graphene production by RF-cCVD method, Chem. Commun. (2009) 4061–4063, http://dx.doi.org/10.1039/B906323D.

Supplementary Material

In situ X-ray powder diffraction studies of the synthesis of graphene oxide and formation of reduced graphene oxide

Mie Møller Storm, Rune E. Johnsen and Poul Norby
Department of Energy Conversion and Storage, Technical University of Denmark, Frederiksborgvej 399, 4000 Roskilde, Denmark

Figure S1: Pictures of the capilary set-up for the modified Hummer's synthesis.Left: The XRD set-up, (the kapton cone is a safety precausion due to the use of conc. H_2SO_4). Rigth: A close up of the synthesis capillary.

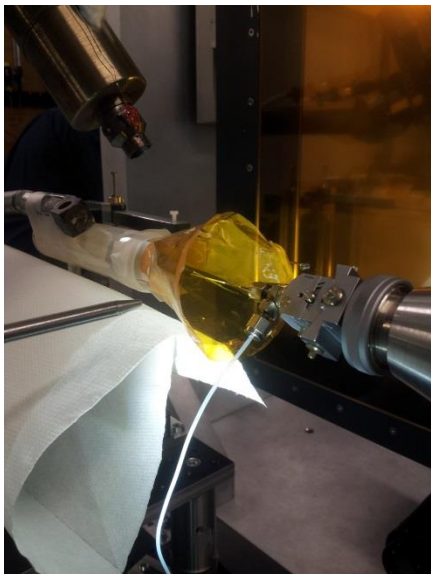

The modified Hummers method

Angle / ° 2θ	*d*-value/ Å	Assignment
5.048	7.970	GO (001)
10.186	3.954	graphite-hydrogensulphate
10.49	3.840	Shoulder, possibly GO
11.797	3.415	Graphite (002)
15.333	2.631	graphite-hydrogensulphate
16.878	2.392	
19.073	2.119	

Table S1: Stage II of the GO synthesis and the related diffraction peaks.

Graphite-hydrogensulphate:

Graphite-hydrogensulphate has been synthesized by mixing graphite and sulfuric acid, and adding hydrogen peroxide. [1, 2] Hydrogen peroxide is an oxidizing agent, as permanganate, which makes it reasonable to believe that graphite-hydrogensulphate could be an intermediate phase during the modified Hummers synthesis. Graphite-hydrogensulphate can also be produced with potassium dichromate[2] or by anodic polarization of graphite in sulfuric acid[3]. The peak at 15.33° in 2θ could also be assigned as the 003 GO diffraction peak. However, as the diffraction peak disappears during stage II and then reappears at stage III (in a less sharp profile and with a slightly shifted *d*-value), it is likely that it is the diffraction peak from graphite-hydrogensulphate during stage II, and then grows as the GO diffraction peak in stage III.

Table S2: The *in situ* Stage III of the GO synthesis and the related diffraction peaks.

Angle/ ° 2θ	*d*-value/ Å	Assignment
5.05	7.967	GO (001)
9.893	4.071	GO’ (002)
10.312	3.906	GO* (002)
11.84	3.403	Graphitic (002)
15.255	2.644	GO (003)
16.645	2.425	
16.927	2.385	Cubic (110)
17.671	2.285	
18.952	2.132	GO (100)
19.737	2.048	GO’ (004) and graphite (101)
20.708	1.953	GO* (004)
21.305	1.899	
23.831	1.7	Graphite (004)
26.026	1.559	Graphite (103)
26.855	1.512	Cubic (210)
29.507	1.378	Cubic (211)
29.943	1.359	
30.755	1.324	GO (006)
34.209	1.193	Cubic (220)
36.333	1.126	Cubic (300)
38.251	1.071	
40.328	1.018	
45.785	0.902	Cubic (321)

Graphite in stage III of the modified Hummers synthesis: It was observed that the synchrotron sample in the capillary dried with time, as the sulfuric acid was drawn from the reaction zone by the glass wool. This could mean that not all of the graphite was converted to GO as concentrated H_2SO_4 in the capillary is essential for the modified Hummers reaction thus is many of the peaks assigned to graphite. The diffraction peak assigned as the 002 reflection of graphite is however also observed for the GO-intermediate sample, even though no liquid was removed from the sample. This peak was not observed in the final GO product of the synthesis. This could either indicate that the graphite is not complete converted until the addition of H_2O_2 or it could point to additional interpretation of the crystalline phase in stage III

Figure S2: A fit of the triclinic unit cell structure to diffractions of Stage III for an *ex situ* sample.

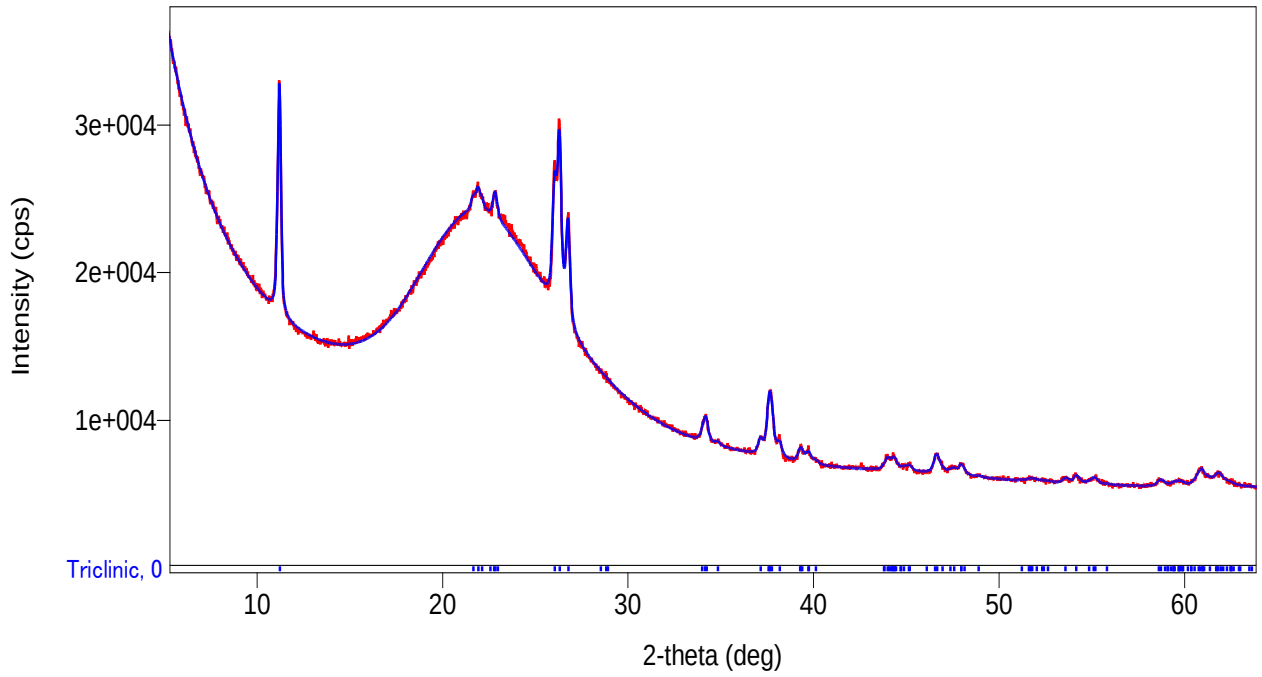

Thermal reduction of GO

The GO diffractions: The GO starting material has the 001 diffraction peak at 4.9° in 2θ (*d*=8.20 Å). Additional GO diffraction peak are observed; the 100 diffraction peak at 18.94° in 2θ (*d*=2.13 Å) and the 110 diffraction peak at 33.10° in 2θ (*d*=1.23 Å). A small graphite impurity is indicated by the 002 diffraction peak at 12° in 2θ (*d*=3.37 Å).

Table S3: The rGO stage of the GO thermal reduction and the related diffraction peaks.

Angle/ 2θ °	*d*-value/ Å	Assignment
11.499	3.504	rGO (001)
11.957	3.370	graphite (002)
19.114	2.114	rGO (100)
19.735	2.048	rGO (101) + Stacking disorder
23.179	1.747	rGO (004)
33.273	1.226	rGO (110)
35.312	1.157	rGO (112)

Figure S3: X-ray powder diffraction surface plot of the rGO synthesis, here illustrated with the heating rate of 5 °C/min.

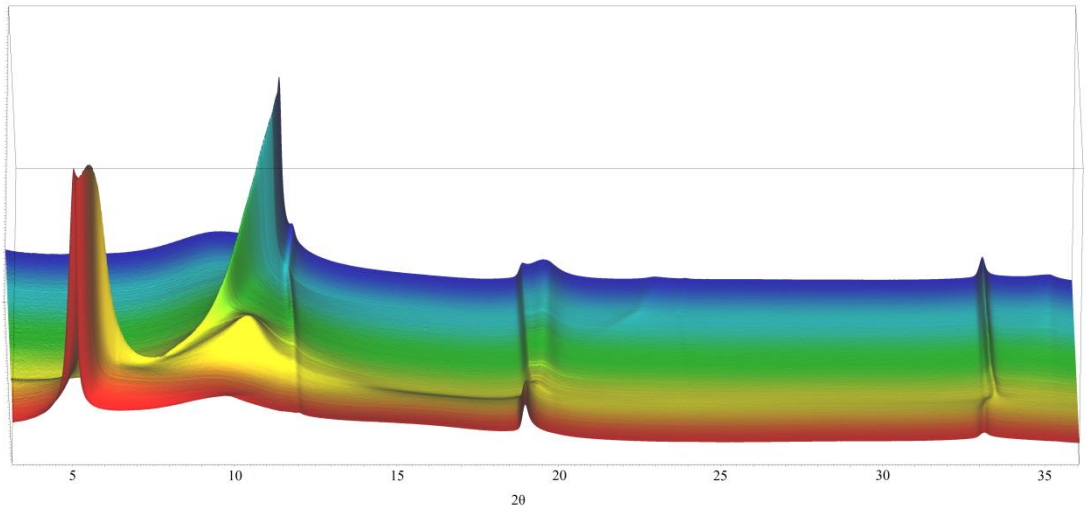

Effect of oxidation time

To investigate the effect of the GO synthesis, thermal reduction of two different oxidized samples of GO, one oxidized 3 hrs (GO3H) and one oxidized 3days (GO3D), were studied *in situ*. The two samples go through the similar stages during the thermal reduction at the temperature ramp of 5 °C/min. The GO stage, the disordered stage and the rGO stage were observed, see Figure S5. The development of the peaks at approximately 19° and 33° in 2θ were similar indicating the formation of rGO. However, the peak at 24.1° in 2θ for GO3H observed in Figure 5 is not observed for the GO3D experiment. As the GO3D sample does not have a graphite impurity, as seen for GO3H, this could indicate that the diffraction peak at 24.1° is the 004 graphite diffraction peak. The disordered stage for the GO3D sample started at 210 °C which was similar to the initiating temperature of the GO3H samples. However, it terminated at 240 °C which was below the termination temperature of the GO3H disordered stage at approx. 285 °C. This is probably due to the difference in sample synthesis, either in regards to intercalated water or functional groups. The result shows how differences in the modified Hummers method can affect the thermal reduction of GO.

Figure S4: Overview of the GO3D thermal reduction at 5° C/min. Inset: A zoom in between 20.7-25° showing the absence of the peak at 24.2° in 2θ.

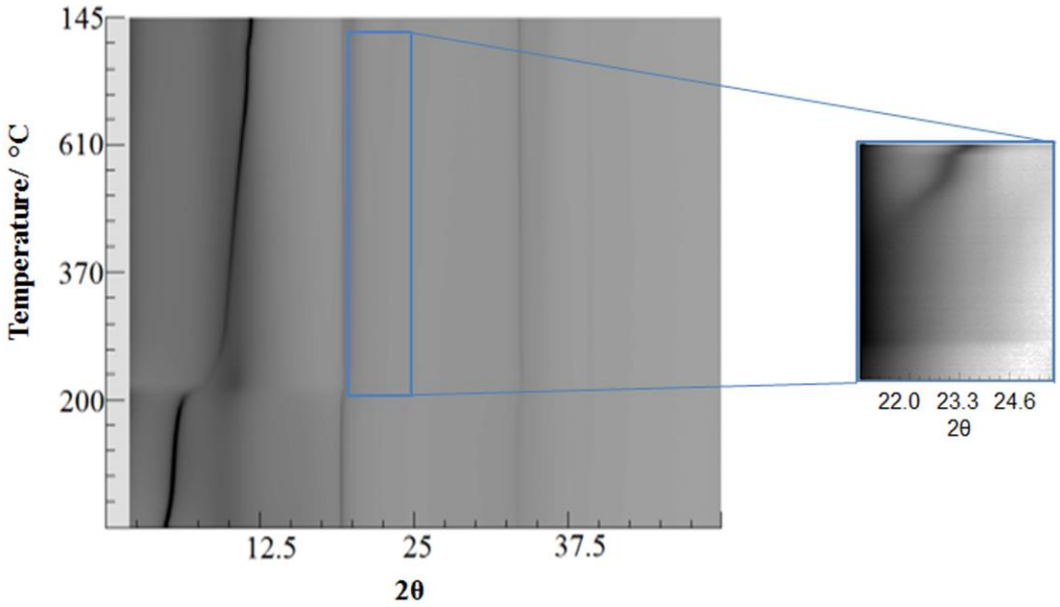

References

1. Hirschvogel, A.; Wagner, F., Graphite particles, sulfuric acid, hydrogen peroxide, agitation. **1978,** US Pat. 4091083 A, (US 05/767,775).
2. Monyakina, L.; Avdeev, V.; Nikol'skaya, I.; Litvinenko, A.; Fadeeva, N., *Inorg. Mater. (Engl. Transl.)* 1990; Vol. 26.
3. Jansen, R.; Beck, F., Graphite hydrogen sulphate as an electrode material for inorganic anodic oxidations. *J. Electroanal. Chem.* **1991,** 302, (1–2), 103-114.

Paper II

CARBON 85 (2015) 233–244

Available at www.sciencedirect.com

ScienceDirect

journal homepage: www.elsevier.com/locate/carbon

Reduced graphene oxide for Li–air batteries: The effect of oxidation time and reduction conditions for graphene oxide

Mie Møller Storm [a,1], Marc Overgaard [a,1], Reza Younesi [a], Nini Elisabeth Abildgaard Reeler [b,c], Tom Vosch [b], Ulla Gro Nielsen [d], Kristina Edström [e], Poul Norby [a,*]

[a] Department of Energy Conversion and Storage, Technical University of Denmark, Frederiksborgvej 399, 4000 Roskilde, Denmark
[b] Department of Chemistry, University of Copenhagen, Universitetsparken 5, 2100 Copenhagen Ø, Denmark
[c] Sino-Danish Centre for Education and Research (SDC), Niels Jensens Vej 2, 8000 Aarhus C, Denmark
[d] Department of Physics, Chemistry and Pharmacy, University of Southern Denmark, Campusvej 55, 5230 Odense M, Denmark
[e] Department of Chemistry-Ångström Laboratory, Uppsala University, Box 538, SE-75121 Uppsala, Sweden

ARTICLE INFO

Article history:
Received 26 June 2014
Accepted 30 December 2014
Available online 6 January 2015

ABSTRACT

Reduced graphene oxide (rGO) has shown great promise as an air-cathode for Li–air batteries with high capacity. In this article we demonstrate how the oxidation time of graphene oxide (GO) affects the ratio of different functional groups and how trends of these in GO are extended to chemically and thermally reduced GO. We investigate how differences in functional groups and synthesis may affect the performance of Li–O_2 batteries. The oxidation timescale of the GO was varied between 30 min and 3 days before reduction. Powder X-ray diffraction, micro-Raman, FE-SEM, BET analysis, and XPS were used to characterize the GO's and rGO's. Selected samples of GO and rGO were analyzed by solid state ^{13}C MAS NMR. These methods highlighted the difference between the two types of rGO's, and XPS indicated how the chemical trends in GO are extended to rGO. A comparison between XPS and ^{13}C MAS NMR showed that both techniques can enhance the structural understanding of rGO. Different rGO cathodes were tested in Li–O_2 batteries which revealed a difference in overpotentials and discharge capacities for the different rGO's. We report the highest Li–O_2 battery discharge capacity recorded of approximately 60,000 mAh/g_{carbon} achieved with a thermally reduced GO cathode.

1. Introduction

Lithium-air (Li–O_2) batteries hold the promise for a future generation of rechargeable batteries with very high specific capacities. The development of such batteries is important for the future of green technologies. However, promising as these batteries are, much research is still needed, and many challenges must be overcome [1,2]. Some of the issues in

* Corresponding author.
E-mail address: pnor@dtu.dk (P. Norby).
[1] These authors contributed equally.
http://dx.doi.org/10.1016/j.carbon.2014.12.104
0008-6223/

the future development of Li–air batteries are: exploration of stable electrolytes suited for the highly reactive environment [3–8], lowering of the significant overpotential on charging the battery [9,10] and improving cyclability [1]. In addition to these challenges the effects of possible contamination from the air should also be considered [11,12]. Development of a stable and lightweight air–cathode for Li–air batteries is important to achieve its potential. Ottakam et al. [13] tested isotope labeled ^{13}C as cathode material and found that not only the electrolyte decomposes upon cycling. Carbon may react as well, and the degree of reaction depends on the hydrophobicity of the carbon material. A capacity retention above 98% upon cycling in 0.5 M $LiClO_4$ in DMSO has been reached with TiC [14], electrodes made by vertical aligned N-doped coral-like carbon fibers has shoved high cyclability combined with a high discharge capacity [15], and cathodes of woven carbon nanotubes also displayed high cyclability, both in regards to capacity limited cycles but also for deep discharged cycles [16].

Reduced graphene oxide (rGO) has shown great promise as an air–cathode with high capacity [17,18] and the material has many of the abilities desired for the Li–air cathode; it has a high specific surface area and a good conductivity [19]. rGO may be prepared with a unique 3D morphology of interconnected pores with sizes on the nano- and mesoscale as well as a structure which is believed to lead to high capacities for graphene cathodes [17]. Several different types of related rGO have been tested as the Li–air battery cathode material, such as "normal" rGO [17,18], doped rGO [20,21], and metal containing rGO [22–25]. rGO cathodes have been tested for both the aprotic [17,18] and hybrid [26] Li–air battery systems with promising results.

Even though rGO has been investigated [19,27,28], the difference of the functional groups in the graphene oxide (GO) and their relation with the functional groups in rGO has not been explored in detail. Gaining a deeper insight into these properties is important since they may have an influence on the use of rGO as a Li–air cathode material. We have investigated the effect of oxidation time on the structure and properties of GO as well as related thermally and chemically reduced GO. Different rGO's were tested as cathode materials for an aprotic Li–O_2 battery.

GO was prepared by a modified Hummers method [29] and the oxidation time for the GO synthesis varied between 30 min and 3 days. Chemically and thermally reduced GO was synthesized from the GO samples. Samples were characterized by Field Emission Scanning Electron Microscopy (FE-SEM), Brunauer–Emmett–Teller surface area analysis (BET), coupled Thermogravimetric Analysis and mass spectrometry (TGA–MS), X-ray powder diffraction (XRD), micro-Raman spectroscopy, X-ray photoelectron spectroscopy (XPS), and solid state ^{13}C nuclear magnetic resonance spectroscopy (^{13}C MAS NMR). Cathodes of selected rGO materials and cathodes of conductive carbon black Super C65 were tested and compared in Li–O_2 cells.

This study shows how some of the functional groups in GO relate to the functional groups of the synthesized rGO, and how the differences in rGO cathodes affects both discharge capacity and the overpotential for time limited discharge/charge cycling in a Li–air battery.

2. Experimental

2.1. GO and rGO preparation

GO was synthesized according to the modified Hummer's method [29]. In an Erlenmeyer flask placed in an ice bath 3 g natural flake graphite, 325 mesh, with 99.8% metals basis (Alfa Aesar) and 1.5 g $NaNO_3$ was mixed under stirring in 100 ml concentrated H_2SO_4. 12 g $KMnO_4$ was added very slowly and cooling was continued for 2 h after addition. The solution was then heated in a water bath to 35 °C for the desired and variable time range (30 min, 1 h, 3 h, 1 day, and 3 days). After heating, the solution was placed on ice and 100 ml ice-cooled water was added followed by slow addition of 25 ml 30% H_2O_2. The precipitate was isolated by centrifugation, washed with 0.1 M H_2SO_4 and left to vacuum dry at 25 °C overnight. GO was washed by centrifugation, four times with 1 M HCl followed by drying, and four times with acetone and drying in a vacuum furnace at 25 °C. The GO materials were named GOX (X = 30min, 1H, 3H, 1D, or 3D, denoting the oxidation time).

HyrGO synthesis, following [30]: 0.2 g GO was delaminated in 200 ml water by sonication for at least 1 h and the solution was filtered on a Büchner funnel with filter paper. To a round bottom flask containing the delaminated GO 2 ml of hydrazinium hydroxide was added. The solution was then heated under reflux at 100 °C for 24 h, causing precipitation of rGO. The solution was filtered and the rGO was washed with 5*100 ml milliQ water and 5*100 ml MeOH. The rGO was dried in air overnight and furthermore dried in an oven at 90 °C overnight.

TrGO synthesis, slightly modified from [31]: 0.2 g GO was placed in an alumina boat and inserted into 1 m long quartz tube with an inner diameter of 50 mm, which was flushed with argon. Hereafter the tube was inserted into a tube furnace pre-heated to 1100 °C and shock-heated for 2 min. The quartz tube was extracted, cooled, and the TrGO powder was washed out with acetone. The rGO samples was named TrGOX or HyrGOX (X = 30min, 1H, 3H, 1D, or 3D, denoting the oxidation time of the GO).

2.2. GO and rGO characterization

FE-SEM was carried out on a Carl Zeiss Supra-35 instrument, 2 kV was used for GO and 3–10 kV for imaging rGO. BET Surface area was measured on a Quantachrome Autosorb-1 instrument and a Micromeritics ASAP 2020 with degassing times from 15 to 30 h at 120 °C (TrGO 300 °C).

TGA–MS was performed using a NETZSCH, STA 409CD TGA system coupled with a NETZSCH, QMS 403D MS system with approximately 15–20 mg of GO, inert argon flow and 0.5 C/min. XRD spectra were measured on a BrukerD8 between 5° and 80° in 2θ with a step size of 0.014° in 2θ and a step time of 1.9 s. The Li–air cathodes were cleaned and dried in a glovebox and measured in an air tight dome containing an Ar atmosphere. Micro-Raman spectroscopy was performed on a home build micro-Raman set-up described in supplementary information. Raman data were fitted to a Lorenz function to the D and the G peak [32], see supplementary information. The areas under the curves were used to calculate $I(D)/I(G)$.

XPS spectra were recorded on a commercial in-house PHI 5500 spectrometer with monochromatic Al K radiation. Scans were made with a step size of 0.1 eV and 50–80 repeated cycles. Igor Pro [33] was used for spectral analysis. XPS on the cathodes was performed after cleaning with dried DME followed by drying in a glovebox. A single cathode was removed from the battery and soaked in electrolyte for four days and cleaned prior to XPS measurement. Solid-state ^{13}C MAS NMR was performed at 11.7 T (125.6 MHz) using a 3.2 mm MAS NMR probe. Single pulse ^{13}C MAS NMR spectra (quantitative) were recorded using 15 kHz spinning speed. ^{13}C NMR spectra are referenced to TMS using the CH resonance in adamantane ($\delta(^{13}C)$ = 38.3 ppm) [34]. Four samples (GO30min, GO3D, TrGO30min, and TrGO3D) were investigated by solid-state NMR (SSNMR) spectroscopy. MestreNova software was used for the analysis of the data and the assignment of the ^{13}C resonances is based on earlier published $\delta(^{13}C)$ in GO [35] and liquid state NMR shifts [36].

2.3. Battery tests

Reference and HyrGO cathodes were prepared by mixing samples of conductive carbon black (Super C65 from Timcal) or HyrGO (30min and 3D) with polyvinylidene fluoride (PVDF) in a 9:1 weight ratio in N-methyl-2-pyrrolidone (NMP). The slurry was drop-casted on cleaned stainless steel (SS) mesh (cleaned by 1 h sonication in 2 M H_2SO_4, followed by washing in water and acetone). TrGO (30min and 3D) was mixed with PVDF in a 1:1 ratio and drop-casted on cleaned SS-mesh. Different binder to carbon material ratios were used as the TrGO samples required more binder to work as cathode in the battery. The cathodes had an average weight of 1.4 mg for HyrGO, 0.9 mg for TrGO cathodes (the cathode of the highest measured specific capacity weighed only 0.37 mg) and 0.9 mg for the Super C65 cathodes. They were dried in a vacuum oven placed in a glovebox at 80 °C for 12 h. The size of the square-like drop-casted cathodes was 4 × 4 mm. Paint-casted cathodes of TrGO samples were made by painting a thick slurry on a cleaned SS mesh. The cathodes were dried in a vacuum oven in the glovebox at 80 °C for 12 h. The paint-casted cathodes had an average size of 50 mm^2 and an average weight of 0.7 mg. Li–O_2 batteries were assembled in a glovebox using a custom built Swagelok cell with gas volume of 10 ml. The batteries consist of a 10 mm Li-disk as the anode followed by two, EtOH cleaned and dried, Cellgaard membranes, 70 μl 1 M LiTSFI in DME electrolyte [37], the cathode on the stainless steel mesh and additional 140 μl electrolyte. The Swagelok cell was activated with oxygen by flushing 4 × 20 s at a flow of approx. 2 ml/s and an overpressure of 0.8 bar. The battery was disassembled, after flushing with argon, in the glovebox and the cathodes were carefully washed with dried DME. At least 3 drop-casted cathode batteries were tested with a current of 0.1 mA/cm^2 for capacity calculations. The cell test consisted of 3 h OCV, 5 min discharge, an impedance measurement (EIS), 9 h and 55 min (or 2 V discharge), 10 h (or 4.65 V) charge, EIS, 2 cycles (10 h or 2–4.65 V), followed by a deep discharge to 2 V. Cycled batteries were charged and discharged between 2 and 4.65 V at 0.1 mA/cm^2 for 10 cycles.

3. Results and discussion

This section describes the characterization of the GO and rGO samples by SEM, BET, TGA–MS, XRD, and micro-Raman spectroscopy, followed by the XPS and ^{13}C MAS NMR results, as both techniques give insight into the functional groups in the samples. After GO and rGO characterizations selected rGO samples are evaluated as cathode materials for Li–O_2 batteries together with cathodes of Super C65 carbon black.

3.1. Characterization of GO and rGO

The different GO's in this article are denoted GOX (X denotes the GO oxidation time as being 30 min, 1H, 3H, 1D, or 3D, H = hour(s) and D = day(s)). The notation for the chemically reduced rGO, reduced by the hydrazine hydrate method [30], is HyrGOX and for the thermally reduced rGO [31] it is TrGOX (X = 30min, 1H, 3H, 1D, or 3D).

Fig. 1 shows selected SEM micrographs of GO and rGO. Fig. 1a is a SEM micrograph of GO30min. SEM micrographs of the other GO samples showed very similar morphology c.f. Fig. S1.

The SEM micrographs of GO reveal a flat crumbled surface with very few or no penetrating cavities. SEM images of HyrGO3D (Fig. 1b) and TrGO3D (Fig. 1c, 30 s reductive heating and Fig. 1d, 2 min reductive heating) indicate that two different morphologies are present. The HyrGO morphology resembles small aggregates, which may be formed by aggregation in the solution during the reduction process. During the hydrazine reduction GO changes from hydrophilic to hydrophobic HyrGO which leads to an observable large scale aggregation. These aggregated structures have cavities and a number of crumpled layers. TrGO3D in Fig. 1c shows small flat particles with a surface resembling "folded sheets". However, Fig. 1d points to a slightly more crumbled structure, but somewhat similar to the aggregate morphology seen for the HyrGO3D. Both TrGO and HyrGO SEM pictures show indications of morphologies with a porous network. No great difference in morphology was observed for the different time dependent oxidized samples.

The BET surface areas of the HyrGO samples ranged from 353 to 497 m^2/g with no observable correlation with the oxidation time. The surface areas of TrGO were of similar size ranging from 343 to 484 m^2/g. However, the surface area of the TrGO's followed a trend where increased oxidation time led to a larger surface area. (Table S1 reports the BET values of HyrGO and TrGO, supplementary information). These increased surface areas might be explained by an increasing amount of edges and defect formations in the graphene induced by the prolonged oxidation time and the subsequent reduction method.

TGA–MS was measured for GOX (X = 30min, 1H, 1D, and 3D), with similar results for the different oxidized samples. An initial small loss of mass was observed from 25 to 110 °C followed by a substantial 48%, 52%, 52%, and 58% loss of mass for GO30min, GO1H, GO1D, and GO3D, respectively in the temperature range 110–210 °C. This was again followed by a small loss of mass up to 1050 °C. The loss of CO_2 is caused by the thermal reduction of GO. The dramatic loss of mass

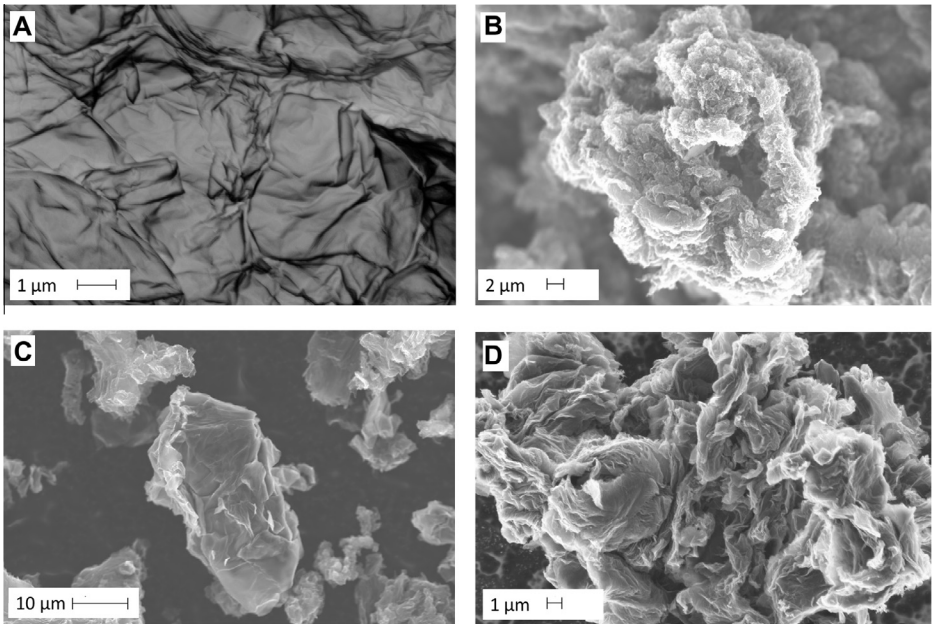

Fig. 1 – SEM micrographs of (A) GO30min, (B) HyrGO3D, (C) and (D) TrGO3D. SEM micrographs reveal different morphologies with an interconnected porous network for the rGO samples.

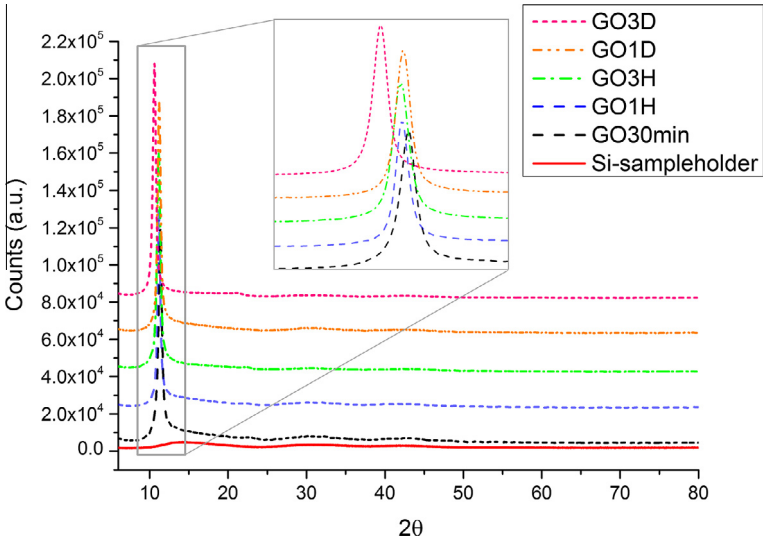

Fig. 2 – XRD of GO30min-GO3D showing an increasing d-spacing of the graphene layers as a function of oxidation time. The inset shows an expansion for the region of the first reflection. (For interpretation of the references to color in this figure legend, the reader is referred to the web version of this article.)

corresponded to loss of H_2O and CO_2. At 1050 °C the total remaining mass was 34%, 29%, 28%, and 22% of the initial mass for GO30min, GO1H, GO1D, and GO3D, respectively, indicating an increase in functional groups or/and more intercalated water molecules as the oxidation time is increased. See the TGA–MS measurements in Fig. S2.

The five different GO powders has the well-known GO XRD patterns (Fig. 2) and Raman spectra (selected spectra are shown in Fig. 3).

The GO diffraction patterns of oxidation time GO1H to GO1D have their interlayer distance ((001) reflection)[2] between 11.19° and 11.22° ($d \cong 7.9$ Å), whereas the GO30min showed a somewhat smaller distance between the graphene layers with the (001) reflection at 11.36° in 2θ ($d = 7.78$ Å). GO3D has a greater interlayer distance, $d = 8.44$ Å, which may be explained by a higher degree of water absorption and/or functionalization. TGA–MS supports this as GO3D has the highest loss of mass. Ref. [38] shows that intercalation

[2] For the GO and GO derived materials we have indexed the patterns based on a hexagonal unit cell where the c-axis is equal to the interlayer distance.

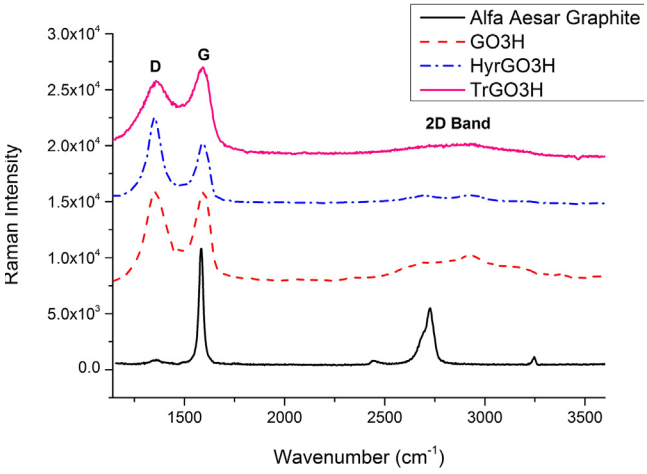

Fig. 3 – Raman spectra of graphite, GO3H, HyrGO3H, and TrGO3H demonstrate distinct differences between GO, HyrGO and TrGO. The D, G, and 2D bands are indicated in the figure on the spectra. (For interpretation of the references to color in this figure legend, the reader is referred to the web version of this article.)

of water in GO has an influence on the d-spacing, as an approximately 6% change in the relative humidity in air can downshift the main peak with 0.5°. This indicates that intercalated water could have a similar effect on the d-spacing. Furthermore, the GO3D diffractogram shows a weak second order reflection at 20.82° (d = 4.26 Å). The chemically reduced rGO (HyrGO) XRD diffractions show a broad (001) reflection around 24° ($d \cong 3.7$ Å) whereas the thermally reduced rGOs (TrGO) have the (001) reflection at 24° (d = 3.7 Å) for TrGO30-min and 26.1–26.4° ($d \cong 3.4$ Å) for TrGOX (X = 1H, 3H, 1D, and 3D). XRD diffractions of TrGO and HyrGO can be seen in Fig. S3. These reflections resemble the (002) reflection of graphite but with larger interlayer distances. The distance between the graphene layers are slightly greater for the HyrGOs compared to the TrGO. Both the HyrGO and the TrGO diffraction patterns display the (100) reflection around 43°. The HyrGO diffraction peaks are narrower than those of TrGO which indicates a higher crystallinity.

Fig. 3 shows a representative Raman spectra of graphite, GO, HyrGO, and TrGO (Additional Raman spectra and data of TrGO and HyrGO can be found in supplementary information; Table S2, Figs. S4 and S5).

Micro-Raman spectroscopy showed a definitive and clear difference between graphite, GO, as well as the two different HyrGO and TrGO samples. The D band at approximately at 1350 cm^{-1} and the G band around 1590 cm^{-1} are of a very similar intensity for the GO samples. Previously Hiramitsu et al. [39] observed a peak around 1750–1850 cm^{-1} related to C=O vibrations [32]. The Raman spectra of our GO samples display a tendency to a very small shoulder in the area of 1840 cm^{-1}, although the signal is too weak to make any definitive conclusion. The Raman spectra of HyrGO have a lower but broader G peak compared to the D peak and a larger I(D)/I(G) ratio as compared to the GO samples. The ratio of I(D)/I(G) is often reported as a measure of the disorder in the carbon material [19,40], thus the D peak represents the lack of order in the initial graphitic sp^2 plane (G peak). We would expect a decrease in the I(D)/I(G) ratio upon reduction if we restore the graphene sheet, however this is not observed. Similar results have been reported earlier [41] and were explained by creation of graphitic domains in rGO, of which there are more domains but of smaller domain size than in GO. The TrGO's spectra show a high G peak compared to the HyrGO spectra and has an I(D)/I(G) ratio larger than for both HyrGO and GO. The TrGO Raman spectra display features also seen in amorphous carbon, but this tendency is not observed in HyrGO. Micro-Raman could not detect large differences between the HyrGO or TrGO samples which had been made from GO using different oxidation times, see supporting information Tables S2 and S5.

XPS measurements of the GO samples demonstrated the presence of carbon and oxygen on the surface as well as minor impurities of chlorine and sulfur from the synthesis method. The impurities were not detected in any of the rGO samples. Somewhat similar relative surface concentrations of carbon and oxygen (C/O ratio) for the GO samples were observed indicating that an oxygen saturation of the graphene framework is quickly reached. The C1s spectra of GO had different shapes depending on the oxidation time and were deconvoluted with the expected binding types being C–C, C–O, C=O, and C(O)O, as in ref [42]. A variation of ±0.1 eV for the binding energies were accepted for the XPS deconvolution for all samples. The relative contribution of each bond to the C1s spectra of GO are shown in Fig. 4 (these results are also presented in Table S3). More GO spectra and the relative areas of deconvoluted peaks can be found in supplementary information, Table S3 and Fig. S6. The C-C graphitic backbone is clearly affected by the oxidation time. As the oxidation time increases the relative amounts of pure C–C bonds decreases from a ratio of 69% (GO30min) to 51% (GO3D). The relative amount of C–O bindings increase from GO30min (25%) to GO3D (36%) as does the relative amounts of C=O and C(O)O bonds. The increase of C=O and C(O)O could indicate a destruction of the carbon backbone as these functional groups are expected to be situated at the edges of the graphene sheet. The C1s spectra of TrGO were deconvoluted with the expected binding types of C–C, C–O, C=O, and C(O)O and the HyrGO spectra were deconvoluted with expected binding types of C–C, C–N, C–O, C=O, and C(O)O following results reported earlier by Stankovich et al. [30].

The survey scans of HyrGO revealed the presence of nitrogen from attached hydrazine as well as a much higher C/O ratio compared to GO between 19.8 and 11.8. Both results were in agreement with previous studies [30]. Deconvolution of the C1s spectra for the HyrGO samples (Fig. S6) were performed with a set of chemical guidelines to achieve a high chemical accuracy in the result, see supplementary information. The relative contribution of each bond type to the C1s spectra of HyrGOs are seen in Fig. 4. Similarly as for the GO samples the HyrGO C1s spectra show how the C–C bond of the rGO decreases from 74% to 67% as the oxidation time is increased. The percentages of C–C bond are greater for the HyrGO samples than for the GO samples, which can be explained by removal of functional groups. The trend for the C=O and C(O)O groups are similar as for the GO samples, but this is sensitive to by the deconvolution guidelines. The

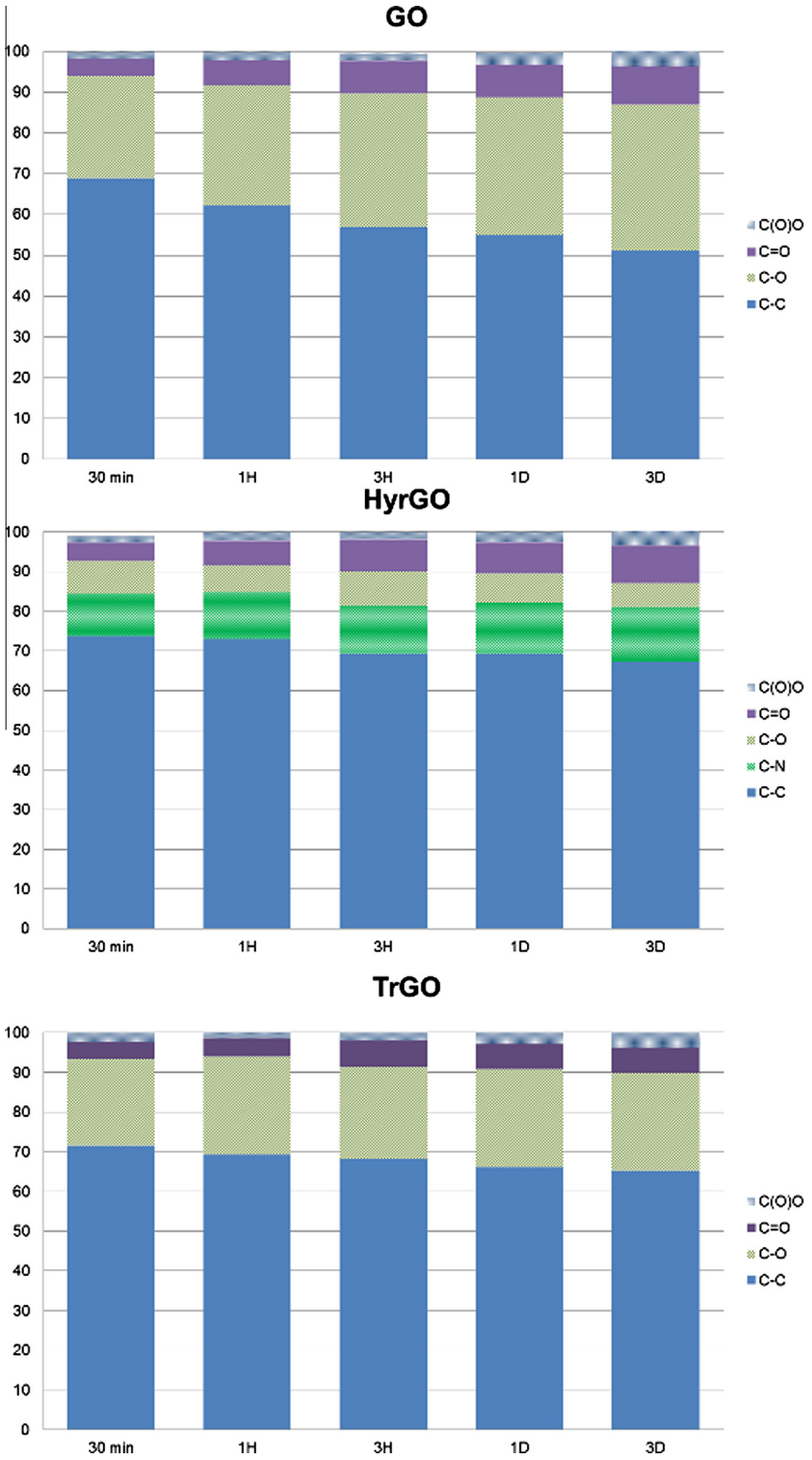

Fig. 4 – The relative contribution of each bond calculated based on the deconvoluted C1s spectra illustrating the evolution of the functional groups for GO, HyrGO, and TrGO. XPS results indicate that selected functional group trends from GO are inherited by HyrGO and TrGO. (For interpretation of the references to color in this figure legend, the reader is referred to the web version of this article.)

amount of C–N bonds in the HyrGO samples grow with increased oxidation time from 11% to 14%. This increase in nitrogen is also observed when the elemental quantities from the survey scans are compared. The elemental quantities show a small amount of nitrogen (approx. 2.5–4%). The increase in hydrazine bonding to the graphene plane can be explained by an increase in epoxy groups (C–O–C) of the GO as the oxidation time is increased [30,43]. This effect demon-

strates that the increasing amounts of C–O groups in GO is carried through to HyrGO. The trends seen for the C–C and C–O bonds in GO seems to be transferred to the HyrGO samples.

The C1s spectra of TrGO (Fig. S5) were fitted with the peaks of C–C, C–O, C=O, C(O)O, and π–π*. The relative contributions of each bond to the deconvoluted spectra of TrGO are summarized in Fig. 4. The ratio of C–C bonds decreases with increased oxidation time from 72% to 65%, as are also observed for HyrGO and GO. There is a higher ratio of C–C in the TrGO compared to the GO samples. The ratio of C–O bonds after thermal reduction does not seem to depend on the GO functionality as the ratio is similar for all five samples. The ratios of C=O are slightly decreased and the C(O)O functional groups are similar as compared to those of GO, and the TrGO samples seem to adopt the GO trend where increased oxidation time leads to increased amounts of C(O)O bonds. The C=O is increasing up to TrGO3H. The trends seen in GO for C–C, C=O, and C(O)O seems to be extended to the TrGO samples.

Comparison of the HyrGO and TrGO measurements reveals that the ratio of C–C bond is in the same range with a slightly higher ratio of C–C bond in the HyrGO samples. There is a much higher ratio of C–O in the TrGO, but the HyrGO samples contain C–N bonds. The ratio of the edge bonded groups C=O and C(O)O are similar.

Solid state ^{13}C MAS NMR was performed on four samples of GOX and TrGOX (X = 30min and 3D), see Fig. 5. They show a slightly different result than XPS in terms of functional groups. However, it is important to note that SSNMR reflects the average composition of the sample, whereas XPS is a surface sensitive technique. Furthermore, regions near paramagnetic centers may be invisible due to fast relaxation such centers have recently been identified in GO [44].

^{13}C MAS NMR of the GO samples showed the presence of C(O)O, C–C, C–OH, C–O–C, and CH_3 groups. If the methyl group is ascribed to the washing solvent, acetone, the identification is very similar to the XPS results for GO. The NMR results for the GO samples are very similar, see Table 1, the major resonances are aromatic C from the graphene sheet, denoted graphitic in the table, hydroxyl (C–OH) and ether/alkoxy (C–O–C) groups, which together constitute 90% of the sample. There are different graphitic signals in the table originating from slightly different environments. In addition, smaller components are C(O)O (from an ester or acid group) and CH_3, assigned to acetone (residual solvent). The concentrations of the different functional groups calculated from XPS and ^{13}C SSNMR are not identical, but as both measurements resulted in broad spectra this is not unexpected. However, both XPS and ^{13}CSSNMR show a decrease in the amount of aliphatic C–C bonds upon oxidation and an increasing amount of C–OH and C(O)O. However, according to the XPS C–O increases with oxidation time whereas the ^{13}C NMR displays the opposite tendency. The ^{13}C NMR does not detect any C=O bonds, with an expected chemical shift around 190 ppm, but these may be below the detection limit (3–5%). The sample composition significantly changes upon reduction. The aliphatic C–O–C and C–OH groups disappear and the regions for C=C, aromatic C and carbonyls at 100–180 ppm becomes more complicated implying the presence of many different local

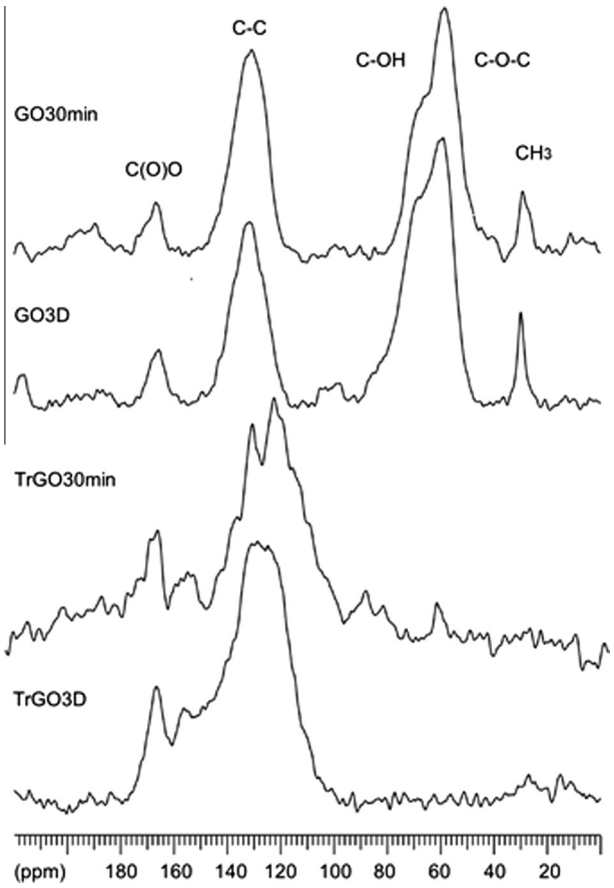

Fig. 5 – Solid state ^{13}C MAS NMR spectra of selected GO and TrGO samples showing the isotropic chemical shift regions with the different functional groups indicated.

environments. These have been assigned in Table 1. ^{13}C NMR of the TrGO samples did only reveal small or zero traces of C–OH and C–O–C groups. These groups were clearly visible, as C–O in the XPS spectra. A similar disagreement between XPS and ^{13}C NMR has been seen for GO and rGO synthesised by Lawsons reagent by Liu et al. [45]. However, the ^{13}C NMR spectra of rGO show the formation of two new functional groups compared to the GO: A sp^2 carbon single-bonded to an oxygen atom and a lactol group. The table for TrGO3D does not have the C_{sp2}-O listed, but the broad O=C–O signal at 156.3 ppm may be split into O=C–O and the C_{sp2}–O functionality, with the concentration being split roughly in half. The lactol group was detected by Ayajan et al. [35] in GO and is a heavily substituted 5 or 6 membered-ring formation. If these types of structures are formed during the heating, they can explain the presence of C–O groups in XPS as well as the formation of the new groups in ^{13}C NMR. ^{13}C NMR shows a decrease in the amount of graphitic signals from TrGO30min to TrGO3D agreeing with the XPS result. With the splitting of the 156.3 ppm peak in TrGO3D, under the assumption of the formation of lactol groups, the amounts of the C–O functionalities are comparable to the XPS results. The amount of C(O)O groups detected with ^{13}C NMR is much greater than those detected with XPS, but these signals were difficult to assign precisely both in the XPS and NMR spectra.

Table 1 – NMR results from analysis of the ^{13}C NMR spectra of GO30min, GO3D, TrGO30min, and TrGO3D.

Sample	Assignment	δ_{iso} (ppm) ±1 ppm	Conc. (%) ±3%	Comment
GO30min	O=C–O	166.5	5.3	Ester or acid-derivative
	"Graphitic"	131.2	41.3	
	C–OH	70.1	11.1	
	C–O–C	59.0	38.7	
	$-CH_3$	29.1	3.5	
GO3D	O=C–O	167.5	4.8	
	"Graphitic"	133.0	32.6	
	C–OH	67.9	33.0	
	C–O–C	58.2	25.3	
	$-CH_3$	29.9	4.3	
TrGO30min	O=C–O	166.9	12.2	Ester or acid-derivative
	O=C–O	156.2	3.7	
	C_{sp2}–O–	147.6	10.3	Aromatic C with O-substituent
	"Graphitic"	130.1	36.0	
	"Graphitic"	119	22.7	
	–C=C–	109.2	2.8	
	Lactol O–C–O	104.6	12.3	
TrGO3D	O=C–O	167.6	4.5	
	O=C–O	156.3	19.7	
	"Graphitic"	138.2	11.0	
	"Graphitic"	132.4	8.9	
	"Graphitic"	125.8	17.3	
	"Graphitic"–C=C–	119.8	17.0	
	–C=C–	112.3	11.0	
	Lactol O–C–O	104.4	1.8	
		92.6	6.3	
	C–OH	66.1	1.5	

3.2. *rGO Li–air batteries*

Fig. 6 shows a battery test for one of the TrGO3D cathodes. The battery test consisted of three limited cycles (limited by 10 h or 2–4.6 V) followed by a deep discharge. The three cycles, limited by time, were made to ensure that the cathodes could both be charged and discharged. The battery tests showed that all tested materials could be cycled within the limits of the test.

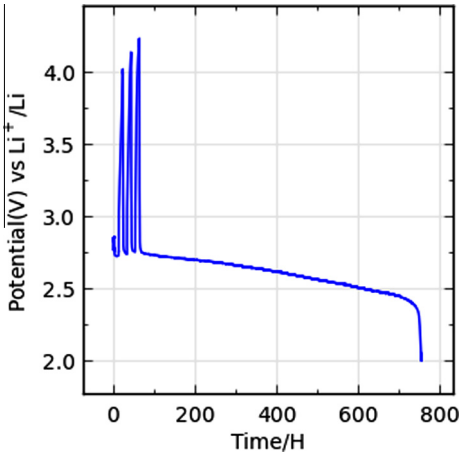

Fig. 6 – Battery test of a TrGO3D cathode tested at 0.1 mA/cm^2. (For interpretation of the references to color in this figure legend, the reader is referred to the web version of this article.)

A TrGO30min cathode was characterized by XRD in Ar atmosphere after deep discharge, see Fig. 7. The presence of Li_2O_2 in the diffraction pattern confirmed that the desired Li–O_2 reaction had taken place. No crystalline carbonate species were detected showing that under these conditions there is no evidence of crystalline decomposition products of either electrolyte or cathode. XPS on a tested and cleaned cathode showed the formation of Li_2O_2 (Fig. S7). A similar XPS result was obtained on a cathode which after battery test termination had been stored in electrolyte for several days. No lithium carbonate was detected on the cathodes. However, after repeated charge/discharge cycles formation of crystalline and non-crystalline carbonate species must be expected as observed from other cathode materials [46].

The TrGO3D battery tested in Fig. 6 has a capacity of 59,792 mAh/g_{carbon} (total cathode weight 0.37 mg), which is the largest capacity currently measured for a porous air–cathode for Li–air. Under the assumption that the cathode has a surface area of 300 m^2/g and is completely covered with a uniform layer of Li_2O_2 the thickness of the layers is calculated to approximately 72 nm. This large capacity was only measured once. However, the other tested cathodes of this material had the highest average capacity of all the tested cathodes in this study. It was possible to cycle this battery but only with considerable loss of capacity as the first cycle was discharged for

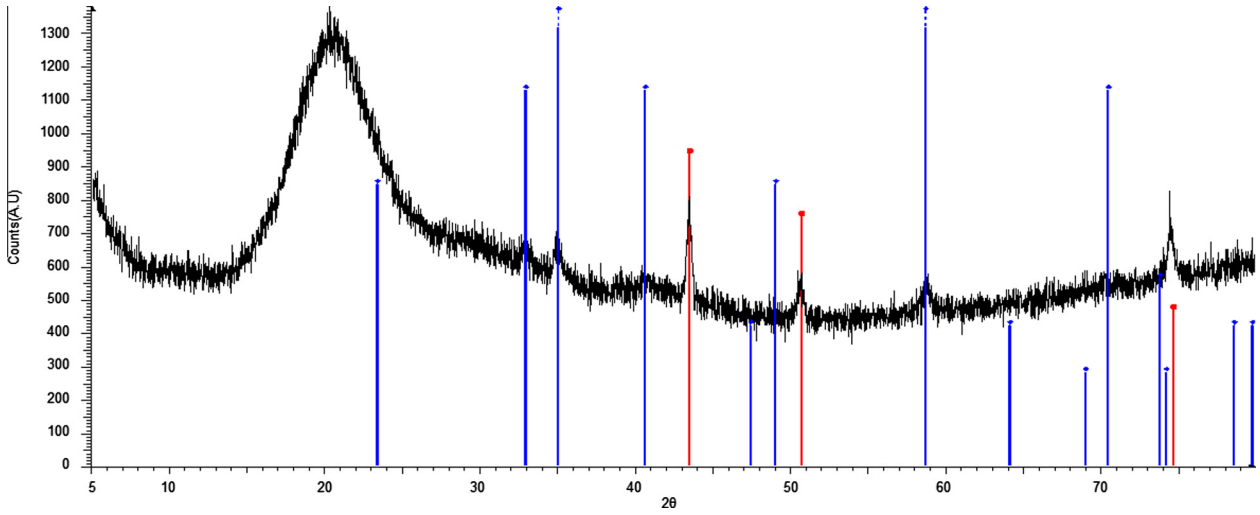

Fig. 7 – XRD of deep discharged TrGO30min battery cathode with peak assignment: blue = Li_2O_2 and red = SS mesh, FeNi. The XRD diffractogram shows only reflections from crystalline Li_2O_2 and no carbonate formation is observed. (For interpretation of the references to color in this figure legend, the reader is referred to the web version of this article.)

approximately 59,792 mAh/g, 692 h, then recharged to ~15500 mAh/g (180 h). The following cycles were deep discharged to an approximate specific capacity of 5931, 2414, 1491, 970, and 631 mAh/g_{carbon} (60, 28, 17, 10, and 5 h). It was also possible to cycle the HyrGO3D cathodes, which resulted in four complete deep discharge cycles with a final capacity retention of 11% of the original capacity (Fig. S8).

The battery capacity varied rather much but the average specific capacity measured at 0.1 mA/cm^2 (excluding the large capacity cathode for TrGO3D) is reported in Table 2.

This study shows that the TrGO cathodes have greater capacities than HyrGO cathodes, and that the HyrGO3D cathodes have an even lower capacity than the Super C65 cathodes. TrGO cathodes results in the highest capacity in the Li–O_2 battery of the tested cathode materials.

The difference in capacity between HyrGO and TrGO may be explained by general morphology difference or surface effects, since both TrGO samples are superior compared to the HyrGO cathodes. However, as HyrGO3D are of an even lower capacity than Super C65 cathodes, it may be that the C–N group leads to this decrease in capacity compared to TrGO cathodes. This would also be in agreement with HyrGO30min having a three times the capacity of HyrGO3D, even though the difference in C–N content is small. A comparison of the XPS results for TrGO30min and TrGO3D shows a decrease in the amount of C–C bonds and an increased ratio of edge groups, C(O)O and C=O. The decreased C–C ratio is not expected to be important and the C/O ratio do not seem to be of importance as no trend is observed. However, an increase in the ratio of C=O and C(O)O groups as well as an increased edge formation may serve as Li_2O_2 nucleation sites and introduce an increased Li_2O_2 coverage of the cathode. Since the highest capacity within the different reduced samples is reached by TrGO3D and HyrGO30min, respectively, it is possible that C=O, C(O)O and edge formation are less important for the capacity, and that something else is affecting it altogether. TrGO3D (484 m^2/g) has a larger surface area than to TrGO30min (342 m^2/g) and this might be the simple explanation for the difference in capacity. However, BET results for the HyrGO samples are rather similar: HyrGO30min 383 m^2/g and HyrGO3D of 399 m^2/g. If surface area was the defining capacity factor we would expect similar capacities for samples with similar surface area. All these assumptions are based on a capacity calculated from the amount of carbon material. However, if the capacity is calculated on cathode weight the results of TrGO30min would be similar to the HyrGO30min. More definitive studies are needed but it is clear that the synthesis procedures of rGO and the initial GO samples are of immense importance for battery capacity.

Fig. 8 shows the time limited cycling from specific battery tests of the five different cathodes. This figure shows how the difference in cathode material results in significant differences in charging behavior and a possible smaller difference on discharge. It is clear that the charging voltage at a constant

Table 2 – The average specific capacity obtained in the Li–O_2 battery test for Super C65, HyrGO and TrGO cathodes (excluding the TrGO3D cathode of approximately 60,000 mAh/g_{carbon}).

Cathode	Binder content (%)	Average specific capacity/mAh/g_{carbon}
Super C65	10	2922
HyrGO30min	10	4063
HyrGO3D	10	1457
TrGO30min	50	6947
TrGO3D	50	11,038

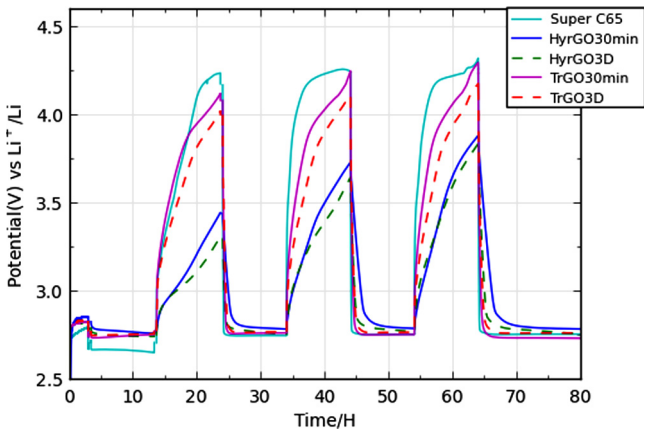

Fig. 8 – Limited battery test cycling curves for the five different cathodes displaying a difference in the potential reached for the time limited cycles dependent on material. (For interpretation of the references to color in this figure legend, the reader is referred to the web version of this article.)

current has a more linear development for the HyrGO cathodes as compared to the more steep curves of Super C65 and TrGO. The time dependent cycling of the battery shows that the HyrGO cathodes reach the time limit at a lower voltage. The TrGO cathodes result in a battery cycling which is more similar to super C65. However, the TrGO cathodes demonstrate a lower end potential and a 2nd and 3rd cycle which are not rising as steeply as the super C65 cathodes. The HyrGO cathodes showed the lowest overpotential with HyrGO30min and HyrGO3D being almost indistinguishable from one another. TrGO3D gives the lowest end potential of the TrGO cathodes. The lower end potential for the HyrGO samples might be related to the C-N bonds on the surface, as this seems to be a definitive difference between the TrGO and HyrGO cathodes. However, other surface effects and morphology could also explain this. The small difference between TrGO30min and TrGO3D could be due to edge formation and edge functional groups. These results demonstrate that the time limited overpotential depends heavily on the cathode material. The cause of this difference might be that the functional groups make charge-transfer easier as well as surface and morphology effects may have a currently unknown influence. Conductivity of the cathodes might also affect the overpotentials, however in the review by Pei et al. [19] the conductivity for a HyrGO material is 2 S/cm and the conductivity of TrGO in Schniepp et al. [31] is between 10 and 23 S/cm. A low overpotential is important in Li–air batteries and much research is aimed toward optimizing this. If the battery material could be tailored to have a more efficient overpotential, the energy efficiency of the Li–air battery would be improved.

Another type of paint-casted cathode with an average area of 50 mm^2 was made and tested at 0.03 mA/cm^2 for the TrGO30min and TrGO3D materials (50% PVDF). The cathodes had an average weight of 0.75 (30 min) and 0.6 mg (3D) for the larger cathode area compared to the other type of cathodes, thus they were tested at a lower current per area but at a higher rate per mass materials. Three batteries of each type of material resulted in an average specific capacity of 3734 mAh/g_{carbon} for TrGO30min and 23,757 mAh/g_{carbon} for TrGO3D. TrGO3D had the larger capacity for both types of cathodes. However, where the TrGO3D paint-casted cathode was superior in capacity compared to that of the drop-casted cathodes, the drop-casted cathodes were superior to the paint-casted for the TrGO30min samples. This signifies that the testing conditions and preparation methods of cathodes as well as the material have to be considered in order to optimize the battery.

4. Conclusions

The effect of oxidation time during synthesis of GO and the following chemically and thermally reduced GO was investigated. XRD of the GO sample showed an increased layer distance induced by oxidation time. XPS showed that the oxidation time of GO affects the ratio of functional groups on the graphene sheets. Part of these functional groups seemed to be extended to thermally and chemically rGO making the initial GO synthesis an important step before further reduction. ^{13}C MAS-NMR showed a small difference in the composition of GO30min and GO3D. In addition, the effect from the thermal reduction of GO to rGO clearly affects the ratio of the functional groups.

Cathodes of TrGOX and HyrGOX (X = 30min and 3D) were tested, and the highest capacity for a Li–O_2 battery today was reached with a TrGO3D cathode. It was furthermore possible to cycle batteries of TrGO3D and HyrGO3D, but only with significant capacity losses.

The high capacity combined with the ability to cycle is a very promising result for rGO based cathodes in Li–air batteries. However, challenges regarding capacity loss, probably due to electrolyte/carbon decomposition during repeated cycling, still remain. The battery tests showed that the composition or the morphology of the rGO samples may have affecting the capacity, and that the different synthesis of the rGO resulted in very different batteries. The rGO synthesis method also affects time limited cycling yielding different shaped charging curves with different overpotentials for different cathodes. This study proved that rGO may be a promising candidate for Li–air batteries of high capacity especially with a tailored rGO composition/functionalization.

Acknowledgments

The authors acknowledge support the ReLiable project funded by the Danish Council for Strategic Research–Programme Commission on Sustainable Energy and Environment (project no. 11-116792). StandUp for Energy is also gratefully acknowledged for support with funding.

Appendix A. Supplementary data

Supplementary data associated with this article can be found, in the online version, at http://dx.doi.org/10.1016/j.carbon.2014.12.104.

REFERENCES

[1] Girishkumar G, McCloskey B, Luntz AC, Swanson S, Wilcke W. Lithium–air battery: promise and challenges. J Phys Chem Lett 2010;1(14):2193–203.

[2] Christensen J, Albertus P, Sanchez-Carrera RS, Lohmann T, Kozinsky B, Liedtke R, et al. A critical review of Li/Air batteries. J Electrochem Soc 2011;159(2):R1–R30.

[3] McCloskey BD, Bethune DS, Shelby RM, Girishkumar G, Luntz AC. Solvents' critical role in nonaqueous lithium–oxygen battery electrochemistry. J Phys Chem Lett 2011;2(10):1161–6.

[4] Younesi R, Norby P, Vegge T. A new look at the stability of dimethyl sulfoxide and acetonitrile in Li–O_2 batteries. ECS Electrochem Lett 2014;3(3):A15–8.

[5] Younesi R. Characterization of reaction products in the Li–O_2 battery using photoelectron spectroscopy. University of Uppsala [PhD thesis]. 2012: Characterization of Reaction Products in the Li–O_2 Battery Using Photoelectron Spectroscopy.

[6] Balaish M, Kraytsberg A, Ein-Eli Y. A critical review on lithium–air battery electrolytes. Phys Chem Chem Phys 2014;16(7):2801–22.

[7] Garcia-Araez N, Novák P. Critical aspects in the development of lithium–air batteries. J Solid State Electrochem 2013;17(7):1793–807.

[8] Lu Y-C, Gallant BM, Kwabi DG, Harding JR, Mitchell RR, Whittingham MS, et al. Lithium–oxygen batteries: bridging mechanistic understanding and battery performance. Energy Environ Sci 2013;6(3):750–68.

[9] Hummelshøj JS, Blomqvist J, Datta S, Vegge T, Rossmeisl J, Thygesen KS, et al. Communications: elementary oxygen electrode reactions in the aprotic Li–air battery. J Chem Phys 2010;132(7):071101.

[10] Chen J, Hummelshøj JS, Thygesen KS, Myrdal JSG, Nørskov JK, Vegge T. The role of transition metal interfaces on the electronic transport in lithium–air batteries. Catal Today 2011;165(1):2–9.

[11] Mekonnen YS, Knudsen KB, Mýrdal JSG, Younesi R, Højberg J, Hjelm J, et al. Communication: the influence of CO_2 poisoning on overvoltages and discharge capacity in non-aqueous Li–air batteries. J Chem Phys 2014;140(12). -.

[12] Gowda SR, Brunet A, Wallraff GM, McCloskey BD. Implications of CO_2 contamination in rechargeable nonaqueous Li–O_2 batteries. J Phys Chem Lett 2013;4(2):276–9.

[13] Thotiyl MMO, Freunberger SA, Peng ZQ, Bruce PG. The carbon electrode in nonaqueous Li-O-2 cells. J Am Chem Soc 2013;135(1):494–500.

[14] Ottakam Thotiyl MM, Freunberger SA, Peng Z, Chen Y, Liu Z, Bruce PG. A stable cathode for the aprotic Li–O_2 battery. Nat Mater 2013;12(11):1050–6.

[15] Shui J, Du F, Xue C, Li Q, Dai L. Vertically aligned N-doped coral-like carbon fiber arrays as efficient air electrodes for high-performance nonaqueous Li–O_2 batteries. ACS Nano 2014;8(3):3015–22.

[16] Lim H-D, Park K-Y, Song H, Jang EY, Gwon H, Kim J, et al. Enhanced power and rechargeability of a Li–O_2 battery based on a hierarchical-fibril CNT electrode. Adv Mater 2013;25(9):1348–52.

[17] Xiao J, Mei D, Li X, Xu W, Wang D, Graff GL, et al. Hierarchically porous graphene as a lithium–air battery electrode. Nano Lett 2011;11(11):5071–8.

[18] Li Y, Wang J, Li X, Geng D, Li R, Sun X. Superior energy capacity of graphene nanosheets for a nonaqueous lithium–oxygen battery. Chem Commun 2011;47(33):9438–40.

[19] Pei S, Cheng H-M. The reduction of graphene oxide. Carbon 2012;50(9):3210–28.

[20] Li Y, Wang J, Li X, Geng D, Banis MN, Li R, et al. Nitrogen-doped graphene nanosheets as cathode materials with excellent electrocatalytic activity for high capacity lithium–oxygen batteries. Electrochem Commun 2012;18:12–5.

[21] Li Y, Wang J, Li X, Geng D, Banis MN, Tang Y, et al. Discharge product morphology and increased charge performance of lithium–oxygen batteries with graphene nanosheet electrodes: the effect of sulphur doping. J Mater Chem 2012;22(38):20170–4.

[22] Yang Y, Shi M, Zhou Q-F, Li Y-S, Fu Z-W. Platinum nanoparticle–graphene hybrids synthesized by liquid phase pulsed laser ablation as cathode catalysts for Li–air batteries. Electrochem Commun 2012;20:11–4.

[23] Dong S, Chen X, Zhang K, Gu L, Zhang L, Zhou X, et al. Molybdenum nitride based hybrid cathode for rechargeable lithium–O_2 batteries. Chem Commun 2011;47(40):11291–3.

[24] Zhang W, Zeng Y, Xu C, Tan H, Liu W, Zhu J, et al. Fe_2O_3 nanocluster-decorated graphene as O_2 electrode for high energy Li–O_2 batteries. RSC Adv 2012;2(22):8508–14.

[25] Wang LX, Ara M, Wadumesthrige K, Salley S, Ng KYS. Graphene nanosheet supported bifunctional catalyst for high cycle life Li–air batteries. J Power Sources 2013;234:8–15.

[26] Yoo E, Zhou H. Li–air rechargeable battery based on metal-free graphene nanosheet catalysts. ACS Nano 2011;5(4):3020–6.

[27] Mao S, Pu H, Chen J. Graphene oxide and its reduction: modeling and experimental progress. RSC Adv 2012;2(7):2643–62.

[28] Zhu Y, Murali S, Cai W, Li X, Suk JW, Potts JR, et al. Graphene and graphene oxide: synthesis, properties, and applications. Adv Mater 2010;22(35):3906–24.

[29] Park S, An J, Piner RD, Jung I, Yang D, Velamakanni A, et al. Aqueous suspension and characterization of chemically modified graphene sheets. Chem Mater 2008;20(21):6592–4.

[30] Stankovich S, Dikin DA, Piner RD, Kohlhaas KA, Kleinhammes A, Jia Y, et al. Synthesis of graphene-based nanosheets via chemical reduction of exfoliated graphite oxide. Carbon 2007;45(7):1558–65.

[31] Schniepp HC, Li J-L, McAllister MJ, Sai H, Herrera-Alonso M, Adamson DH, et al. Functionalized single graphene sheets derived from splitting graphite oxide. J Phys Chem B 2006;110(17):8535–9.

[32] Zana A, Speder J, Reeler NEA, Vosch T, Arenz M. Investigating the corrosion of high surface area carbons during start/stop fuel cell conditions: a Raman study. Electrochim Acta 2013;114:455–61.

[33] IGORPro. WaveMetric.Version 4.0.

[34] Morcombe CR, Zilm KW. Chemical shift referencing in MAS solid state NMR. J Magn Reson 2003;162(2):479–86.

[35] Gao W, Alemany LB, Ci L, Ajayan PM. New insights into the structure and reduction of graphite oxide. Nat Chem 2009;1(5):403–8.

[36] Williams D, Fleming I. Spectroscopic methods in organic chemistry. 5th ed. McGraw Hill; 1995.

[37] McCloskey BD, Bethune DS, Shelby RM, Mori T, Scheffler R, Speidel A, et al. Limitations in rechargeability of Li–O_2 batteries and possible origins. J Phys Chem Lett 2012;3(20):3043–7.

[38] Blanton TN, Majumdar D. X-ray diffraction characterization of polymer intercalated graphite oxide. Powder Diff 2012;27(02):104–7.

[39] Hiramitsu Y, Sato H, Hosomi H, Aoki Y, Harada T, Sakiyama Y, et al. Influence of humidification on deterioration of gas diffusivity in catalyst layer on polymer electrolyte fuel cell. J Power Sources 2010;195(2):435–44.

[40] Tuinstra F, Koenig JL. Raman spectrum of graphite. J Chem Phys 1970;53(3):1126–30.

[41] Ren P-G, Yan D-X, Ji X, Chen T, Li Z-M. Temperature dependence of graphene oxide reduced by hydrazine hydrate. Nanotechnology 2011;22:055705.
[42] Yang D, Velamakanni A, Bozoklu G, Park S, Stoller M, Piner RD, et al. Chemical analysis of graphene oxide films after heat and chemical treatments by X-ray photoelectron and micro-Raman spectroscopy. Carbon 2009;47(1):145–52.
[43] Kim MC, Hwang GS, Ruoff RS. Epoxide reduction with hydrazine on graphene: a first principles study. J Chem Phys 2009;131(6):064704.
[44] Panich AM, Shames AI, Sergeev NA. Paramagnetic impurities in graphene oxide. Appl Magn Reson 2013;44(1–2):107–16.
[45] Liu H, Zhang L, Guo Y, Cheng C, Yang L, Jiang L, et al. Reduction of graphene oxide to highly conductive graphene by Lawesson's reagent and its electrical applications. J Mater Chem C 2013;1(18):3104–9.
[46] Storm MM, Johnsen RE, Younesi R, Norby P. Capillary based Li–air batteries for in situ synchrotron X-ray powder diffraction studies. J Mater Chem A 2014. http://dx.doi.org/10.1039/C4TA04291C.

Supporting information:

Reduced graphene oxide for Li-air batteries:

The effect of oxidation time and reduction conditions for graphene oxide

Mie Møller Storm[a], Marc Overgaard[a], Reza Younesi[a], Nini Elisabeth Abildgaard Reeler[b,c], Tom Vosch[b], Ulla Gro Nielsen[d], Kristina Edström[e] and Poul Norby[a]

[A]Department of Energy Conversion and Storage, Technical University of Denmark, Frederiksborgvej 399, 4000 Roskilde, Denmark, [b] Department of Chemistry, University of Copenhagen, Universitetsparken 5, 2100 Copenhagen Ø, Denmark [c] Sino-Danish Centre for Education and Research (SDC), Niels Jensens Vej 2, 8000 Aarhus C, Denmark, [d]Department of Physics, Chemistry and Pharmacy, University of Southern Denmark, Campusvej 55, 5230 Odense M, Denmark and [e]Department of Chemistry-Ångström Laboratory, Uppsala University, Box 538, SE-75121 Uppsala, Sweden

SEM images

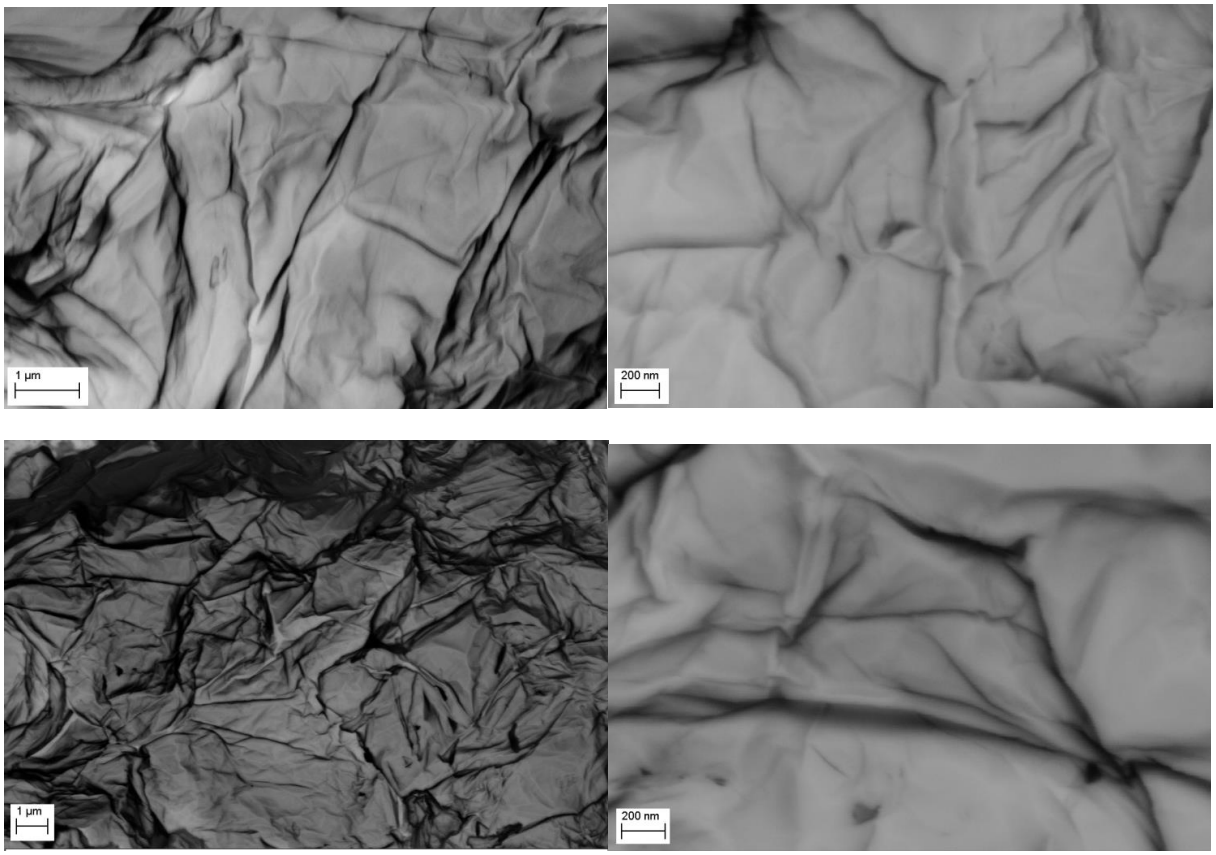

S1: SEM images of the GO samples. GO1H (top left), GO3H (top right), GO1D (bottom left) and GO3D (bottom right).

BET surface area

Table S1: BET surface areas obtained for HyrGO and TrGO.

Sample name	**BET surface area (m^2/g)**	**R^2**
GO3H	35.96	0.99853
HyrGO30min	383	0.99993
HyrGO1H	353	0.99994
HyrGO3H	497	0.99991
HyrGO3D	399	0.9998
TrGO30min	342(1)	0.99996
TrGO1H	370.4(9)	0.99997
TrGO3H	453.3(7)	0.99999
TrGO1D	441.7(5)	0.99999
TrGO3D	483.9(6)	0.99999

TGA-MS

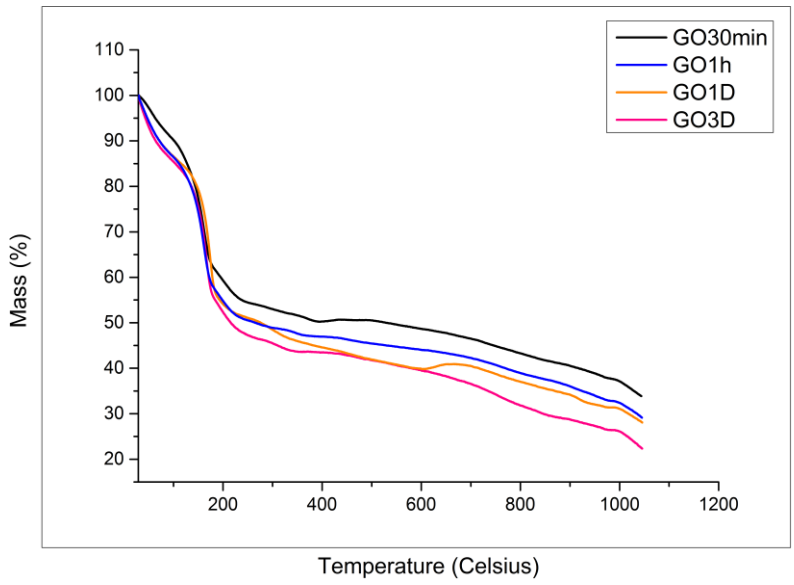

S2: TGA of GO30min, GO1H, GO1D, and GO3D

XRD

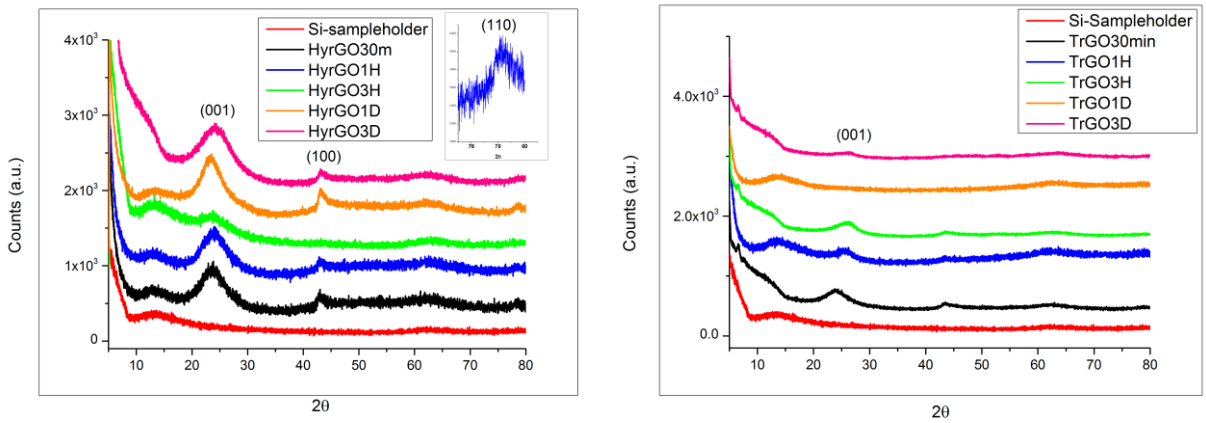

S3: XRD powder diffractograms of HyrGO (left) and TrGO (right) samples. The interlayer graphitic reflection of rGO (marked as (001) is more well defined for the HyrGO samples compared to the TrGO samples. The TrGO samples are less crystalline than the HyrGO which probably can be explained by the synthesis method where the TrGO graphitic layers are blown apart, compared to delamination in water for the HyrGO samples. The HyrGO diffraction patterns also show a more defined (100) reflection at 42°. It is not possible to distinguish the different time dependent samples.

Raman

Micro-Raman spectroscopy was performed by placing a clean cover slip with the pre-deposited dry sample on an Olympus IX71 microscope aligned with a 514 nm CW Argon Ion laser (CVI Melles Griot 35MAP431-200). Two narrow bandpass filter centered at 510 and 514 nm (Semrock FF02-510/20-25 and FF01-514/3-25) were used to spectrally clean the laser source. In the microscope the laser light was reflected on a 70/30 beamsplitter (XF122 from Omega Filters) towards a 100X 1.3 NA immersion oil objective (Olympus UplanFL N) that focused the laser on the sample and collected the Raman signal. A 514 nm longpass filter (Semrock LP02-514RE-25) was used to block the 514 nm laser light in the detection path. The Raman spectrum was recorded using a PI Acton SpectraPro SP-2356 polychromator (600 g mm^{-1} blazed at 500 nm) and a PI Acton SPEC-10:100B/LN_eXcelon Spectroscopy System with a back-illuminated CCD chip (1340×100 pixels). The power of the laser focused at the sample was 123 µW (67 kW/cm^2). X-axis calibration of the spectra was performed after the measurements using a toluene Raman spectrum and a Neon pencil calibration lamp (ORIEL instruments, 6032 neon lamp). Y-axis values of the presented spectra were

modified for representation purposes by adding, subtracting or multiplying the original spectra with a constant value. No other modifications or corrections were performed on the spectra

Table S2: The fitted Raman data, which showed no direct systematic trends regarding the I(D)/I(G) ratio or average distance between defects, $L_{d,}$[1], in regards to GO oxidation time. χ^2 is the chi-squared value.

GO	**GO30min**	**GO1H**	**GO3H**	**GO1D**	**GO3D**
D(cm^{-1})	1355	1355	1349	1352	1355
G(cm^{-1})	1599	1598	1596	1602	1593
I(D)/I(G)	1.6	1.8	1.4	1.6	1.6
L_D (nm)	1.7	1.8	1.6	1.7	1.7
$\chi 2$	9.7	7.9	16.0	18.2	17.2
HyrGO	**HyrGO30min**	**HyrGO1H**	**HyrGO3H**	**HyrGO1D**	**HyrGO3D**
D(cm^{-1})	1352	1353	1350	1350	1355
G(cm^{-1})	1589	1588	1588	1591	1586
I(D)/I(G)	2.2	1.9	2.1	2.6	2.1
L_D (nm)	6.4	6.9	6.5	5.9	6.6
$\chi 2$	1.8	3.3	2.8	2.7	5.3
TrGO	**TrGO30min**	**TrGO1H**	**TrGO3H**	**TrGO1D**	**TRGO3D**
D(cm^{-1})	1357	1353	1357	1357	1359
G(cm^{-1})	1588	1591	1591	1595	1590
I(D)/I(G)	3.9	3.5	3.4	3.3	3.2
L_D (nm)	4.9	5.1	5.2	5.2	5.3
$\chi 2$	1.5	0.9	1.2	1.0	3.5

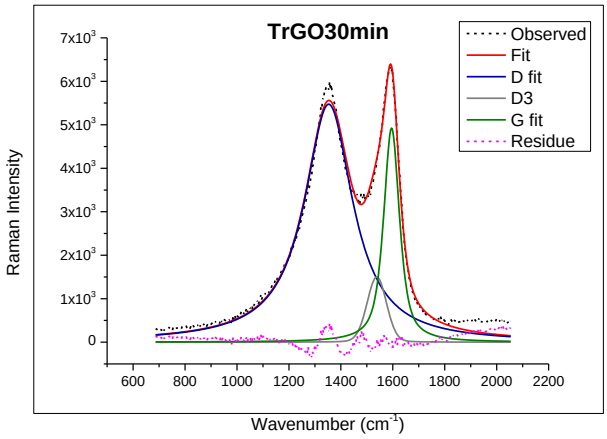

S4: Experimental Raman spectrum of TrGO30min fitted with three Voigt peaks representing the D (blue) and G peak (green) and a fitting supporting peak called D3 (gray).

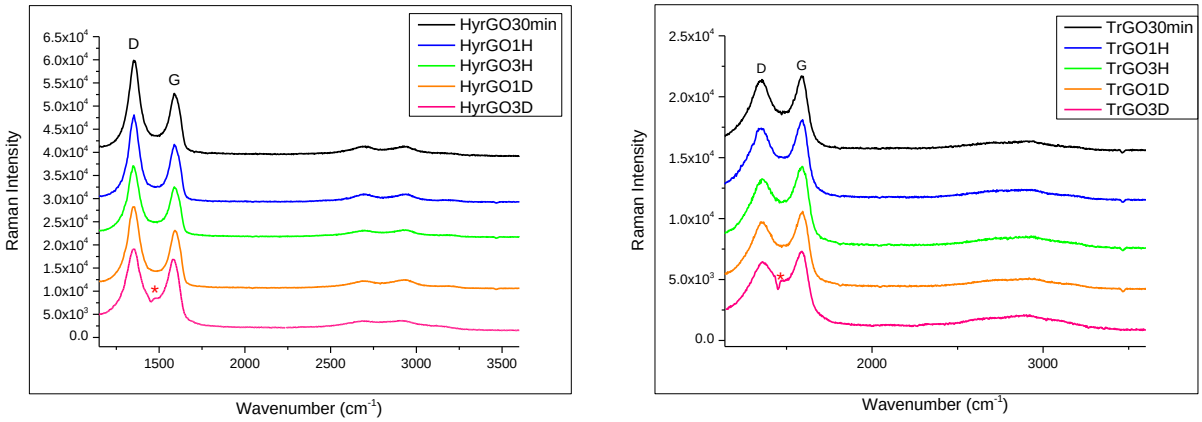

S5: Left: Raman spectra of HyrGO samples, Right: Raman spectra of the TrGO samples.

The Raman spectra are very similar within the HyrGO and TrGO series and no specific trend was observed for the different time dependent samples. The dip (marked with *) in the Raman spectra for TrGO3D and HyrGO3D between the D and the G top is an artifact from the measurements.

XPS:

Table S3: The relative contribution of chemical bonds to the deconvoluted C1s XPS spectra of GO, HyrGO, and TrGO.

XPS GO	**30 min**	**1H**	**3H**	**1D**	**3D**
C-C	69.0	62.2	57.0	55	51.1
C-O	25.0	29.5	32.7	33.7	35.8
C=O	4.3	6.3	8.0	8.1	9.6
CO(O)	1.7	2.0	1.9	2.9	3.6
XPS HyrGO	**30 min**	**1H**	**3H**	**1D**	**3D**
C-C	74	73.1	69.5	69.4	67.3
C-N	10.6	11.9	12	12.9	13.8
C-O	8.2	6.6	8.7	7.2	6.1
C=O	4.5	6.2	8.0	7.9	9.4
COO	1.7	2.2	1.8	2.5	3.5
XPS TrGO	**30 min**	**1H**	**3H**	**1D**	**3D**
C-C	71.6	69.4	68.4	66.3	65.4
C-O	21.8	24.7	23.1	24.6	24.6
C=O	4.4	4.6	6.7	6.4	6.4
COO	2.2	1.9	1.9	2.8	3.6

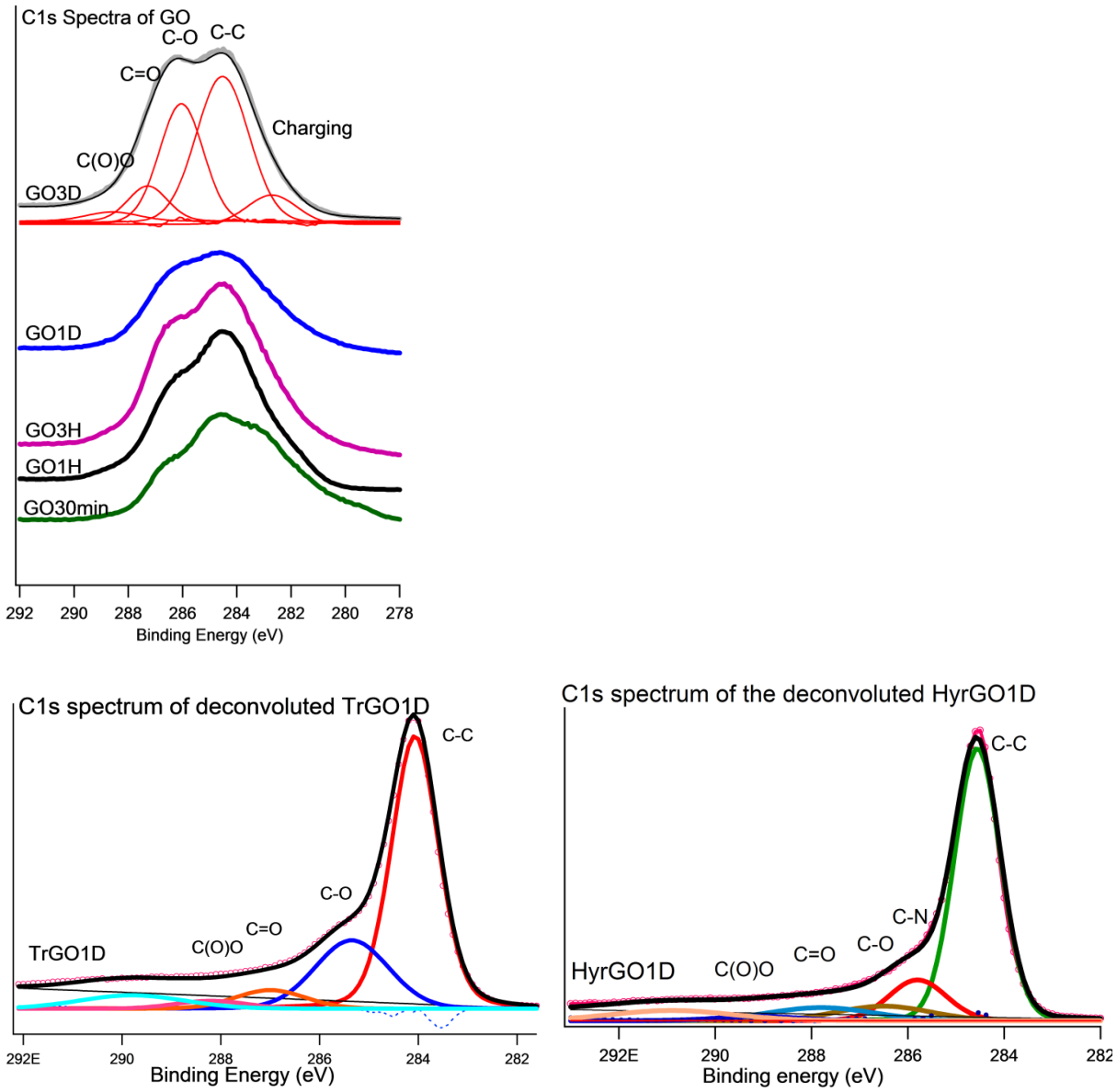

S6: C1s spectrum of the GO (Top), HyrGO (bottom rigth), and TrGO (bottom left) samples.

The XPS measurements of the GO samples were assisted with an electron gun to balance charging due to low conductivity of the samples, but a charging effect was still observed in the GO XPS spectra, as is clearly seen in figure S5.

For the deconvolution of all the C1s spectra we chose not to fit C-H separately, which is usually expected in all XPS data, as it would be difficult to distinguish it from the C-C peak. As mentioned in the article HyrGO was fitted with a set of chemical guideline. The guidelines were inspired from[2] and their results in regards to the reductions methods effect on the different functional

groups. Guidelines: The percentage of pure C-C bonds should be similar or larger than the corresponding GO values, the HyrGO XPS will contain N-C bonds, and the procentage COO and C=O edge groups are assumed to be unaffected or slightly smaller and will thus have rather similar values as the corresponding GO spectra. The last guideline was chosen as the HyrGO spectra had a very large charging effect.

XPS on cathode

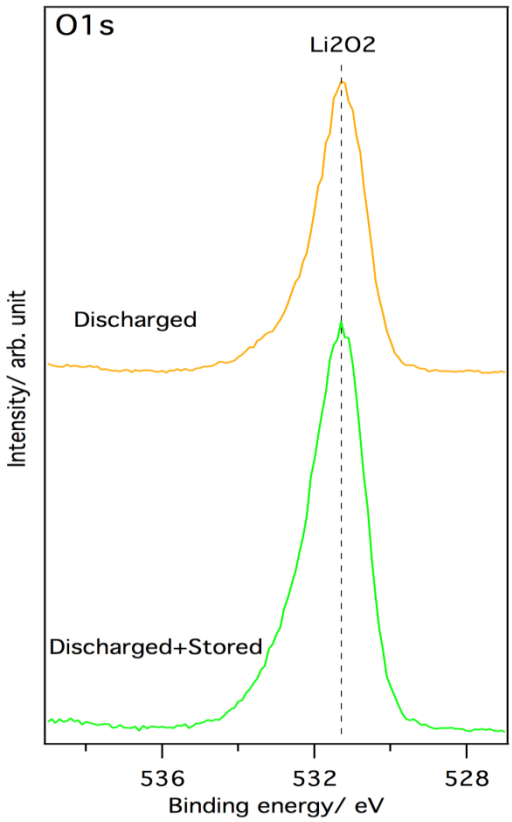

S7: Top: O1s spectrum of a discharged TrGO30min cleaned and dried cathode. Bottom: O1s spectrum of a TrGO30min cathode which was soaked in electrolyte for more than 4 days after battery testing prior to cleaning and drying before XPS measurements. Only Li_2O_2 is detected on these samples.

Battery cycling

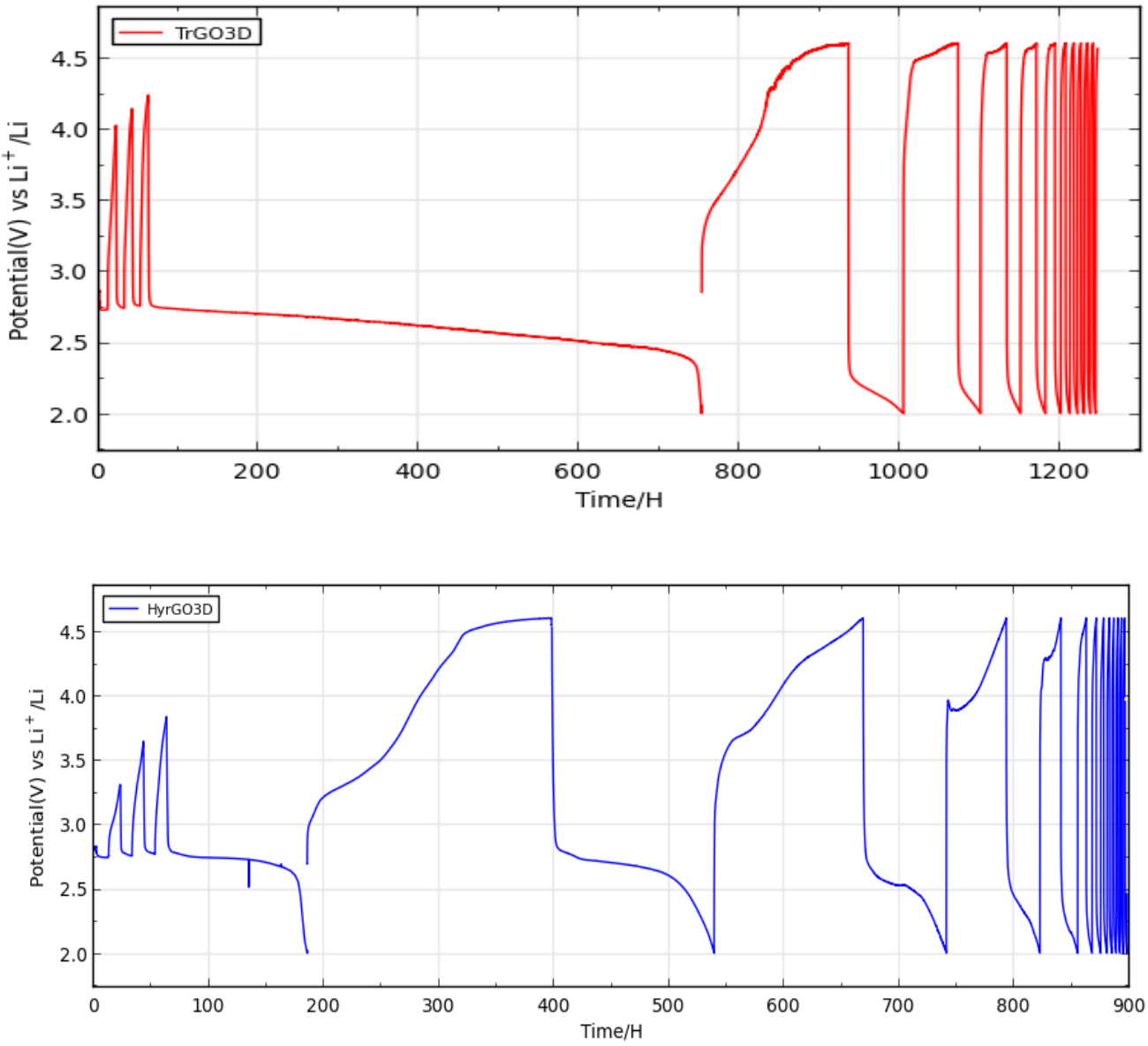

S8: Top: The cycling of a TrGO3D cathode. Bottom: The cycling of a HyrGO3D cathode.

[1] A.C. Ferrari, D.M. Basko, Nat Nano, 8 (2013) 235-246.
[2] S. Pei, H.-M. Cheng, Carbon, 50 (2012) 3210-3228.

Paper III

Journal of Materials Chemistry A

PAPER

View Article Online
View Journal | View Issue

Cite this: J. Mater. Chem. A, 2015, 3, 3113

Capillary based Li–air batteries for *in situ* synchrotron X-ray powder diffraction studies†

Mie Møller Storm, Rune E. Johnsen, Reza Younesi and Poul Norby*

Received 19th August 2014
Accepted 16th December 2014

DOI: 10.1039/c4ta04291c

www.rsc.org/MaterialsA

For Li–air batteries to reach their full potential as energy storage system, a complete understanding of the conditions and reactions in the battery during operation is needed. To follow the reactions *in situ* a capillary-based Li–O_2 battery has been developed for synchrotron-based *in situ* X-ray powder diffraction (XRPD). In this article, we present the results for the analysis of 1st and 2nd deep discharge and charge for a cathode being cycled between 2 and 4.6 V. The crystalline precipitation of Li_2O_2 only is observed in the capillary battery. However, there are indications of side reactions. The Li_2O_2 diffraction peaks grow with the same rate during charge and the development of the full width at half maximum (FWHM) is *hkl* dependent. The difference in the FWHM of the 100 and the 102 reflections indicate anisotropic morphology of the Li_2O_2 crystallites or defects along the *c*-axis. The effect of constant exposure of X-ray radiation to the electrolyte and cathode during charge of the battery was also investigated. X-ray exposure during charge leads to changes in the development of the intensity and the FWHM of the Li_2O_2 diffraction peaks. The X-ray diffraction results are supported by *ex situ* X-ray photoelectron spectroscopy (XPS) of discharged cathodes to illuminate non-crystalline deposited materials.

Introduction

Li–air (Li–O_2) batteries have a theoretical specific energy density comparable to the efficient gravimetric energy density of gasoline, which make them an ideal energy source for battery driven electric vehicles.[1] In the Li–air battery, Li-ions react with oxygen from the air causing precipitation of Li_2O_2 on the air-cathode. The air-cathode is often carbon-based as carbon gives the opportunity to have a light-weight, conducting, and porous cathode. Cathodes based on reduced graphene oxide have demonstrated Li–air batteries with very high capacities.[2–4] However, many challenges are still unsolved for the Li–air battery. Different side reactions take place in the battery and the electrolyte as well as the cathode have been found to decompose in the oxidizing environment.[5–9] It is important to establish the electrochemical and chemical stability window for the electrolyte and investigate the reaction products due to electrolyte decomposition. We are presently investigating the electrolyte reactions using *e.g.* DEMS (Differential Electrochemical Mass Spectrometry) and XPS to identify reaction products and mechanisms. The present *in situ* diffraction study was undertaken to follow formation and decomposition of Li_2O_2 during discharge and charge and to detect crystalline phases from unwanted side reactions. In addition the Li_2O_2 formation/decomposition kinetics is expected to reveal information about unwanted reactions also involving non-crystalline reaction products.

The Li–air battery furthermore has a high overpotential and challenges in regards to cyclability.[1] Several studies show the possibility for a future development of the Li–air battery: Shui *et al.*[10] demonstrated a capacity limited battery cycled 150 times and theoretical studies shows the possibility of lowering the overpotential for the reversible precipitation of Li_2O_2.[11] The many challenges may be overcome if a clear picture of the conditions and reactions in the battery during operation is obtained. *In situ* studies provide an opportunity to explore systems with a minimum of external interference. Investigation of the cathode and anode materials during discharge and charge is of importance, as these components may hold the key to making a rechargeable Li–air battery with high capacity.

Different designs for *in situ* X-ray diffraction (XRD) studies of Li–air batteries have been explored; Lim *et al.*[12] designed a battery setup with Li metal on a stage and a cathode separated by a glass fiber separator assembled within a flow chamber with X-ray transparent windows. Ryan *et al.*[13] performed *in situ* XRD on a Li–O_2 coin cell. The coin cell was set up with Kapton windows within a Kapton sealed flow box. A cell-design based on a Swagelok cell was developed by Shui *et al.*[14] who investigated the capacity limited discharge–charge on a cell containing Li metal, glass micro-fiber filter, and cathode encapsulated in tubular glass.

Capillary-based batteries for *in situ* X-ray powder diffraction (XRPD) analysis have been used for investigation of Li-ion

Department of Energy Conversion and Storage, Technical University of Denmark, Frederiksborgvej 399, DK-4000 Roskilde, Denmark. E-mail: pnor@dtu.dk

† Electronic supplementary information (ESI) available. See DOI: 10.1039/c4ta04291c

batteries,[15] but no Li–air capillary batteries have yet been designed. We have developed a Li–O_2 capillary battery consisting of an electrolyte filled capillary with anode and cathode in each end coated on stainless steel wires. The oxygen in-let is placed on the cathode-side with a flushing system placed above the capillary. In this study, we present a flexible design of a capillary Li–O_2 battery with discharge and charge investigated using synchrotron-based XRPD. Pure oxygen gas was used as even small amount of impurities as for example CO_2 affects the battery performance.[16] The capillary batteries are therefore termed Li–O_2 batteries in this paper.

In situ XRPD during 1st and 2nd discharge–charge (between 2–4.6 V) of different battery cells were performed. The effect of X-ray exposure during charging of Li–O_2 batteries was investigated and cathodes deep discharged 1 and 2 times were analyzed *ex situ* with X-ray photoelectron spectroscopy (XPS) to obtain a complete view of the reactions taking place at the air electrode.

Results and discussion

This section will start with an introduction to the capillary battery set up and general abilities of the capillary batteries. This is followed by a presentation of the *in situ* XRPD tested batteries (battery 1, 2 and 3), and the XRPD results obtained. The *in situ* results will be followed by a presentation of the *ex situ* XPS analysis of the deeply discharged carbon cathodes.

Fig. 1 shows the Li–O_2 capillary cell design, (a picture of the actual Li–O_2 capillary battery is shown in Fig. S1†). The cathode is mounted on a stainless steel (SS) wire in a quartz tube opposite a Li-anode likewise on a SS wire. Quartz tubes were used for XRPD *in situ* measurements and borosilicate capillaries were used for battery tests without X-ray analysis. Both the cathode and the anode were completely covered by electrolyte and the oxygen was flushed through the flushing unit (Swagelok fitting, drawn in black) to fill the battery with gas. OCV was being measured for 2–3 h before the batteries was cycled between 2–4.6 V.

The *ex situ* batteries had the first discharge plateau around 2.5–2.6 V and a second flat discharge plateau at slightly higher voltage, around 2.7–2.8 V, see Fig. 2. The capillary batteries could be cycled between 2 and 4.6 V up to 7 cycles and still maintain a significant capacity, approximately up to 80% of initial discharge capacity.

An *ex situ* XRPD measurement of a discharged cathode showed the presence of Li_2O_2 and confirmed the operation of the Li–O_2 battery. Several other studies have shown that deeply discharged Li–air batteries loose capacity upon cycling and that the electrolyte and/or carbon cathode decomposes to different carbonate species.[17,18] This was confirmed by *ex situ* XRPD measurements of a 5 times discharged cathode which revealed no Li_2O_2 but only other crystalline materials, among those Li_2CO_3, see Fig. S2.†

Battery 1 was discharged and charged, as shown in Fig. 3, at different current rates with XRPD measurements performed every 10 min (30 seconds exposure). The discharge and charge curves displayed a large overpotential (discharge voltage *ca.* 2.5 V *vs.* Li^+/Li), and they were noisy with many spikes, probably due to insufficient connections between the battery and the potentiostat.

Fig. 3 also show a small second discharge plateau for battery 1. No changes were observed in the intensity or the FWHM of the diffraction peaks during this second discharge and it is not included in the analysis of battery 1. Battery 2 was discharged without exposure to X-ray, and charged with XRPD measurements performed every 10 min, followed by charge with constant exposure to X-ray. Battery 3 was discharged and charged without X-ray radiation, which was followed by analysis of the 2nd discharge–charge cycle with X-ray exposure every 10 min. An overview of the test condition for the batteries is presented in Table 1, further description is given in the experimental section.

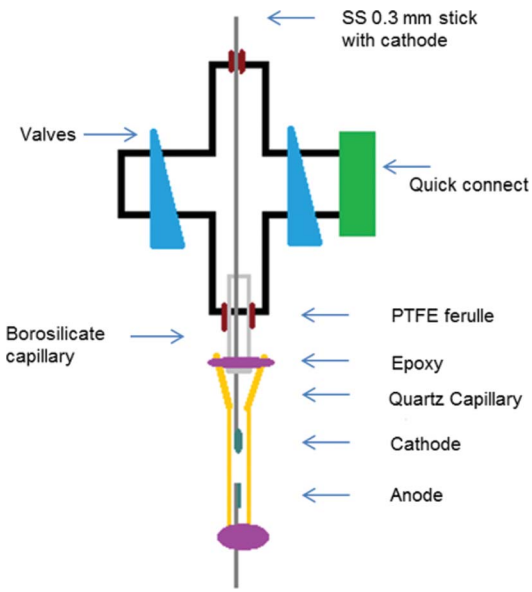

Fig. 1 A schematic drawing of Li–O_2 capillary battery for *in situ* XRPD analysis.

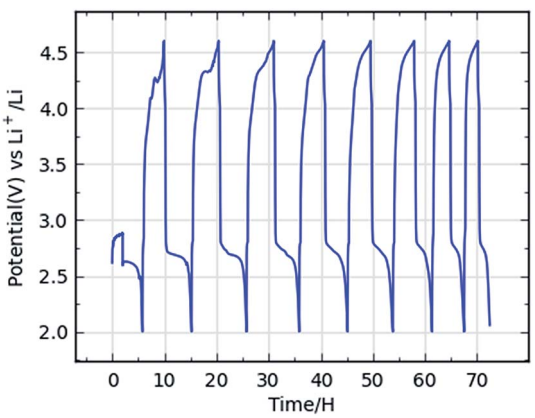

Fig. 2 Cycling curves of a Li–O_2 capillary battery upon deep cycling test.

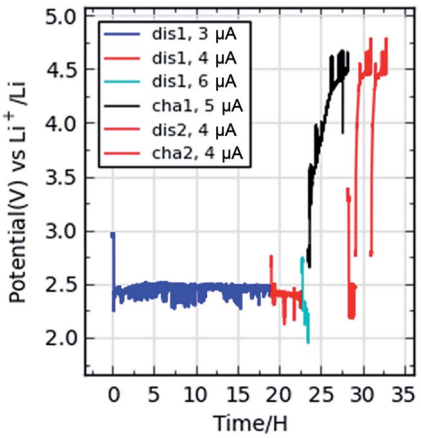

Fig. 3 Discharge–charge curve of Li–O_2 capillary battery number 1 for *in situ* analysis.

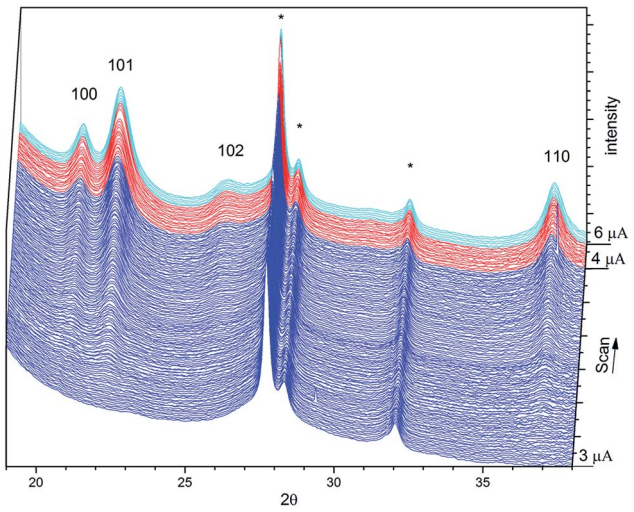

Fig. 4 *In situ* diffraction patterns for the discharge of battery 1 showing the appearance of four diffraction peaks of Li_2O_2 and the ones of the SS wire (*). Blue represent a discharge current of −3 μA, red = −4 μA and light blue = −6 μA.

The *in situ* XRPD patterns collected during the discharge of battery 1 are displayed in Fig. 4. Capillary battery 1 was discharged for a total of approximately 76 μAh and charged for 32 μAh. Four different Li_2O_2 peaks were observed, the 100, 101, 102, and 110 (21.1°, 22.4°, 26.0°, and 37.0°) reflections. The diffraction peaks at 27.8°, 28.4°, and 32.1° were caused by the steel wire. Fig. 5 shows the area (integrated intensity) of Li_2O_2 100 diffraction peak *vs.* capacity. The curve appears linear, as seen in Fig. 5 for the 100 diffraction peak (the data for the other diffraction peaks can be seen in Fig. S3†) which could indicate that no side reactions take place during the first discharge. When the areas of the diffraction peaks are normalized the slopes of the different diffractions are of similar values. However, extrapolation of the curves do not cross the origin (crosses $y = 0$ at 0.013 (100), 0.002 (101), 0.012 (102), and 0.019 mA h (110)), and this indicates that some of the electrons in the battery take part in a different reaction than the Li_2O_2 formation.

The slope of the integrated area *vs.* time (not shown here) of the 100, 101 and 110 Li_2O_2 diffraction peaks increased proportionally with increasing discharge rate as expected, as increased current leads to increased Li_2O_2 deposition, as can be seen from Fig. 5 and S3† no change in the slope is observed in the area *vs.* capacity plot. The increase in discharge rate changed neither the battery voltage plateau nor the type of product being deposited. No other discharge products were observed during the test of battery 1.

The charge of battery 1 revealed a decrease of intensity of the Li_2O_2 diffraction peaks for each of the separate charges. The results of area *vs.* capacity for the first charge are shown in Fig. S4.† The curves showed that the charge of the battery was slower than the discharge, as we for approximately a third of the charged capacity only observed a decrease in Li_2O_2 intensity of approximately 10–20%. This could be caused by possible side reactions probably taking place at the high voltage. It was not possible to charge the battery completely since the connection in the battery was lost due to the formation of gas bubbles between the cathode and anode.

During discharge the FWHM of the growing 100 diffraction peak decreased, as did the FWHM of the 101 diffraction peak. The plots of the FWHM *vs.* capacity can be seen in Fig. S5† for discharge and Fig. S6† for charge. The FWHM of the 102 and 110 diffraction peaks seem to be constant. However, the uncertainty of the parameters was higher as the intensity of these reflections was lower and the FWHM could only be determined in the last part of the discharge. The behavior of the FWHM during charging of battery 1 was more difficult to determine, but if one sees charge 1 and 2, as defined in Fig. 3, as a collected series, the FWHM of 100 diffraction peak increased upon charge as did the FWHM of 101 diffraction peaks. The

Table 1 An overview of the tested batteries

Name	*In situ* battery test	Pretreatment without X-ray
Battery 1	Discharge, charge 1, discharge (negligible) and charge 2	Equilibrated at OCV
Battery 2	Charged with 30 seconds of X-ray exposure every 10 minutes followed by charging at constant X-ray exposure	Equilibrated at OCV and discharged
Battery 3	2nd discharge and charge	Equilibrated at OCV, discharged and charged

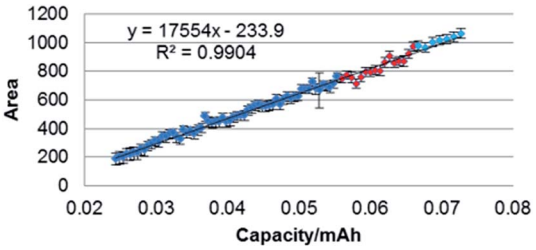

Fig. 5 The development of the peak area of the 100 diffraction peak as a function of capacity. Dark blue equals a current of −3 μA, red = −4 μA and light blue = −6 μA.

FWHM development of the 100 and 101 diffraction peaks indicate crystallite growth in these directions upon discharge. The development of the FWHM of the 102 and 110 diffraction peaks was not conclusive.

The FWHM values of the 101 and 102 diffraction peaks were higher than those of the 100 and 110 diffraction peaks. This could indicate anisotropic morphology of the Li_2O_2 crystallites or defects along the *c*-axis.

Capillary battery 2 was discharged without exposure to X-ray for 5 h/−5 μA yielding two different stages, the first being a plateau at the expected voltage for a Li–O_2 battery with a voltage of 2.54 V and the second stage showing a decrease in voltage from 2.2–2.0 V, see Fig. S7.† The *in situ* charge was initiated by measurements every 10 min and later changed to being at constant X-ray exposure and scans of 30 seconds, see Fig. 6.

The battery reached a voltage plateau around 4.4 V during charge followed by a voltage increase, possibly caused by the depletion of precipitated material. Battery 2 was discharged for approximately 25 μAh and charged for approximately 23.5 μAh before the voltage increase. The results of the *in situ* measurements are shown in Fig. 7, which shows both the 10 min measurements (black and red) and the results for the constant X-ray exposure (purple).

The XRPD of battery 2 showed the presence of two additional unidentified diffraction peaks at 20.7 and 23.1° (Fig. 7), besides the 100, 101 and 110 Li_2O_2 diffraction peaks. These small peaks were not observed in the other *in situ* batteries. Both peaks were very small and had almost constant intensity and FWHM during the charging both with and without constant X-ray exposure. With charging the intensity of all three Li_2O_2 diffraction peaks decreased.

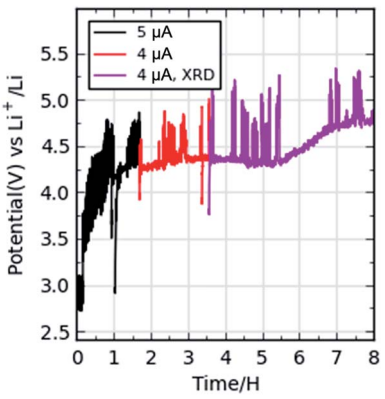

Fig. 6 The charge curve of battery 2 under *in situ* XRPD measurements.

During the 10 min measurements, the rate of the scan was changed from 5 to 4 μa. The *in situ* XRPD measurements during constant X-ray exposure also showed a decomposition of Li_2O_2, see Fig. S8.† If we assume a linear decomposition of Li_2O_2, the decomposition rate increased by a factor of three for the 100 and 101 diffraction peaks when continuously exposed to X-ray. The decomposition rate for the 110 diffraction peak increased only slightly with the constant X-ray exposure. However, care must be taken when making definite conclusion based on this data, since the 110 diffraction peak was of less intensity than the other reflection and thus more difficult to analyze. The 100 and 101 diffraction peaks indicate a large enhanced decomposition upon exposure to X-ray radiation.

The FWHM of the 100 diffraction peak increased with charge as did the FWHM of the 101 diffraction peak. This trend matches the one found for battery 1. The FWHM of the 110 diffraction peak in battery 2 decreased with charge, see Fig. S9.† The broadening of the 100 and 101 increased drastically during the measurements made at constant X-ray exposure, see Fig. 8 for the FWHM of the 101 diffraction peak *vs.* capacity, as did the sharpening for the 110 diffraction peak. This very steep increase only slightly resembles that of the FWHM for the 100 and 101 diffraction peaks in battery 1 and it does not resemble the development of the 110 diffraction peak. This indicate that the constant X-ray exposure alters the FWHM development for all three diffraction peaks. Along with the drastic development of the area *vs.* capacity for the 100 and 101 diffraction peak this display an effect of the constant X-ray exposure on the Li_2O_2. An accelerated electrochemical decomposition of Li_2O_2 by X-ray during charging was observed by Liu *et al.*[19] who detected decomposition of Li_2O_2 in a Li–air battery fabricated with a porous Li_2O_2 electrode in propylene carbonate electrolyte. The capillary battery results support the observation of increased Li_2O_2 decomposition by X-ray for reactions in dimethoxyethane (DME), and make it clear that the enhanced decomposition also is observed for Li_2O_2 which has been precipitated electrochemically during "normal" Li–O_2 battery discharge.

Battery 3 was studied *in situ* during the 2nd discharge–charge cycle, see Fig. S10† for the discharge–charge plots of battery 3. The diffraction peaks of this battery had much lower intensity compared to those of battery 1 and 2. However, the appearance and disappearance of a small 101 Li_2O_2 diffraction peak upon discharge was observed. No other diffraction peaks were observed for this battery. Whether the lack of intensity for the Li_2O_2 was due to the beam placement in the battery combined with the slightly smaller slit size or the formation of less Li_2O_2 cannot be determined by diffraction alone, and *ex situ* XPS was performed on discharged cathodes. As the diffraction patterns are of low intensity no further analysis have been performed.

Ex situ XPS analysis was performed on cathodes deep discharged 1 or 2 times to investigate possible changes in the Li_2O_2 precipitation upon battery cycling. The O1s spectra of the

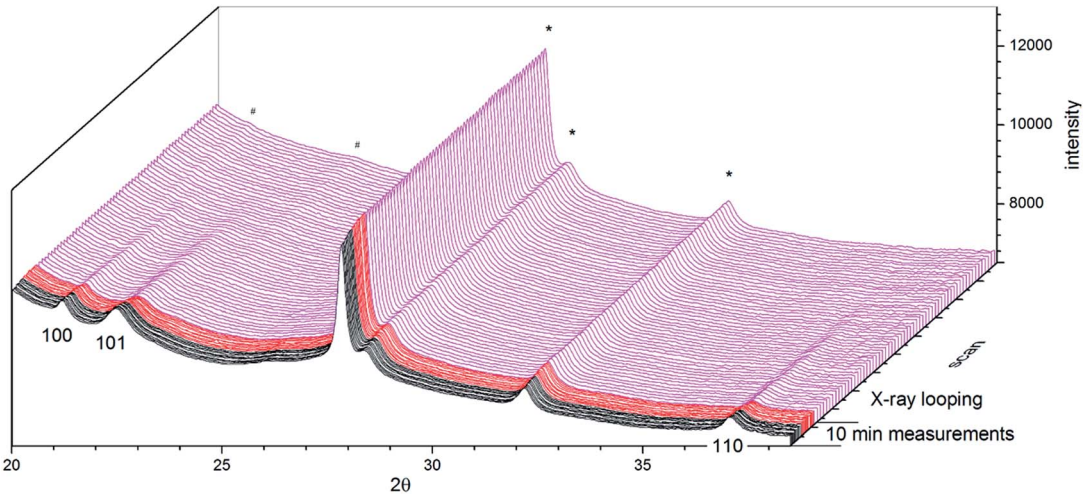

Fig. 7 The *in situ* results for the charge of battery 2, showing the decomposition of the three Li_2O_2 diffraction peaks and the SS wire (*). Two unidentified very weak peaks are observed (#). Black = measurements (30 s X-ray exposure) performed every 10 minutes at 5 μA, red = measurements (30 s X-ray exposure) performed every 10 minutes at 4 μA, purple = continuous data collection during X-ray exposure at 4 μA. Only the first 80 constant exposure X-ray scans (2.7 mA h) are displayed in the figure to make it visually easier to read, even though the decomposition of the peaks was observed for longer time.

discharged and stored cathodes, together with the peak assignments according to the ref. 20–23, are displayed in Fig. 9. The spectra indicate contributions from different oxygen-containing compounds such as Li_2O_2, carbonates, lithium bis(trifluoromethanesulfonyl)imide (LiTFSI) salt, and ethers/alkoxides at binding energies of 531.6, 532.3, 533, and 533.8 eV, respectively (there is also a small peak at very high binding at about 534.7 eV suggesting O bonded to highly electronegative elements such as F). For the "1st discharge" sample, the shoulder at the lower binding energies reveals the presence of Li_2O_2 after 1 discharge, which is in agreement with the *in situ* XRPD results. The relative contribution of Li_2O_2 peak to the O1s spectra decreases from 14% to 4% from the 1st to the 2nd discharge samples. This implies that less Li_2O_2 formed on the 2nd discharge sample. The O1s spectrum of "2nd discharge" sample also shows increased contributions from single- and double-bonded oxygen to carbon indicating increased side products formed by decomposition of the electrolyte. The C1 spectra of the discharge samples (see Fig. S11†) confirm increased contribution from decomposition products when discharging the electrodes for the 2nd time.

The XPS result, which is disclosing smaller amount of Li_2O_2 while higher amount of side products on the 2nd discharge sample compared to the 1st discharge sample, could explain the low intensity of the diffraction peaks of Li_2O_2 observed for the *in situ* XRPD of the 2nd discharge–charge for battery 3.

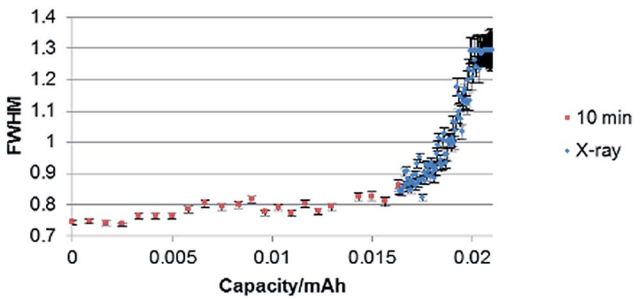

Fig. 8 The development of the FWHM for the 101 diffraction peak during charge for battery 2 with and without constant X-ray exposure.

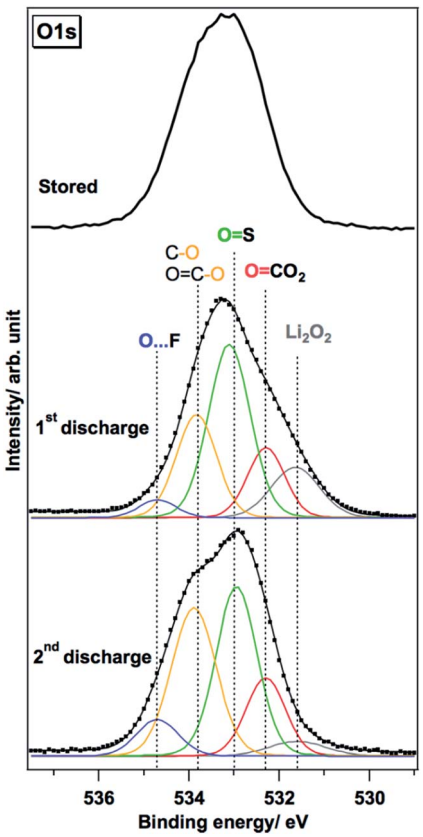

Fig. 9 O1s spectra of *ex situ* analyzed cathodes after 1 or 2 discharge together with stored cathode.

Experimental

Battery assembly

Fig. 1 shows The Li–O_2 capillary cell design. The cathode was made by dip-coating hollow stainless steel (SS) wires (outer diameter 0.3 mm), in a slurry of Super C65 (carbon black from TIMCAL Graphite and Carbon) and 20 wt% polyvinylidene fluoride (PVDF) in *N*-methyl-2-pyrrolidome (NMP) for *in situ* studies and 15–20 wt% PVDF for *ex situ* studies. The slurry used for the cathode in battery 3 contained trace amount of diamond powder to facilitate easy alignment of the battery in the X-ray beam. The small carbon cathode was coated at the end of the SS-wire (which had been slightly sanded and cleaned in acetone before use) by dipping the SS-wire in the slurry and drying the slurry with a heating gun at 100–110 °C. This process was repeated until a cathode of a sufficient size was made. The cathode stick was dried in vacuum oven inside a glovebox at 80 °C for 12 h. The carbon cathodes for the *in situ* study had an average weight of 0.2 mg and the cathodes for the studies of batteries without X-ray and the cathodes for the XPS analysis had an average weight between 0.1–0.2 mg. The Li-anode was prepared by smearing Li onto a 0.4 mm SS-wire which then was glued into a capillary using two-component epoxy. Borosilicate capillaries with an outer diameter of 1.05 mm were used for the *ex situ* XRPD tests, whereas 1 mm quartz capillaries were used for *in situ* XRPD measurements. The quartz capillaries were prepared with a Li-anode in one end and a piece of borosilicate capillary (1.05 mm diameter) in the other end in order to attach it easily to the Li–O_2 flushing unit. The flushing unit had two valves with a quick connector in one end for the inlet of oxygen. The carbon cathode was attached to the unit with a Teflon ferrule and the capillary was filled with 1 M LiTSFI in DME electrolyte and attached to the unit with a Teflon ferrule. Both the anode and cathode were covered by the electrolyte. The two Teflon ferrules hinder short circuiting the battery. The Li–O_2 capillary batteries were assembled inside a glovebox and were tightly sealed before removal from the glovebox. The batteries were flushed several times with oxygen gas (grade 5.0) which resulted in an overpressure of approximately 1.5–2 bars inside the batteries. The valves ensured that the capillary unit could be moved around with the flushing unit working as an oxygen reservoir. The air-exposed end of the capillary coated SS-wire was carefully sealed with two component epoxy glue before the oxygen activation process. Small additional wires were attached to the anode and cathode side of the battery for attaching the potentiostat to the *in situ* setup.

Battery tests

Several capillary-based batteries were electrochemically tested using a Biologic potentiostat and EC-lab software. To analyze formation and decomposition of Li_2O_2 in Li–O_2 cells, three different cells were used in the *in situ* synchrotron-based XRPD experiments. The batteries for *ex situ* XRPD and XPS analysis were left after oxygen filling for 2–3 h. at OCV before being discharge–charged at ±3 μA to 2 V/4.6 V. The *in situ* battery 1 was activated for approx. 5 h, followed by a discharge at −3 μA for 18 h 48 min, a discharge at −4 μA for 3 h. 45 min, and a final discharge at −6 μA. The battery was charged at 5 μA and discharged for a second time at 4 μA for 1 h, before being recharged at 4 μA (as seen in Fig. 2). The XRPD patterns of the cathode were collected every 10 min with an exposure time of 30 s. The voltage of the first discharge at 3 μA have been smoothed using Origin Pro 8.6, using the Adjacent-Average signal process. The second discharge of battery 1 was short, 1 h, and no changes in the area of the diffraction peaks or FWHM were observed probably due to the short duration of the discharge, and the data is not presented in this paper.

After 3 h of resting time at OCV battery 2 was discharged without being exposed to X-ray radiation at 5 μA to 2 V. It was then charged *in situ* with XRPD measurements every 10 min and 30 s exposure time, at 5 μA for 100 min and at 4 μA for 110 min. The battery was charged at 4 μA with continuous exposure to X-ray for approximately 6.6 h. Similar to battery 1, battery 2 gave a noisy battery test curve, which was restarted three times due to voltage spikes.

Battery 3 was kept at OCV for 3 h before battery discharge and charge without X-ray exposure at 4 μA, *i.e.* the first cycle was performed *ex situ*. The 2nd discharge–charge was performed *in situ* with XRPD patterns being collected every 10 min with an exposure time of 60 s. The battery was discharged at −5 μA for 100 min followed by a discharge and charge at ±6 μA.

XRPD

Beamline I711 at MAX-lab was used for the XRPD measurements for battery 1 and 2 with a wavelength of 0.9940 Å, a detector distance of approximately 96 mm and a slit size of 0.2 × 0.2 for the batteries. Between the XRPD measurements the shutter was closed in order to minimize any radiation-induced degradation of the sample. The data were integrated by Fit2D,[24] normalized to the background and fitted in Topas3 [25] as single pseudo-Voigt peaks and a background described by a 5th order Chesbyschev function. Battery 3 was measured at the ESRF at the Swiss Norwegian beamline with a wavelength of 0.7735 Å, a distance to the detector of approximately 194 mm and a slit size of 0.15 × 0.15. *Ex situ* XRPD was measured with a BrukerD8 using CuKα radiation.

XPS

Before *ex situ* analysis by XPS, the capillary batteries discharged one and two times, respectively were carefully disassembled in the glovebox, and the cathodes were washed with dried DME and left for drying. A background sample was stored in electrolyte overnight inside the glovebox before being washed and sealed under similar conditions as the discharged cathodes. The XPS samples were prepared in glovebox on Cu-tape and transported to the XPS machine inside an airtight transfer chamber. XPS measurements were performed on a commercial in-house PHI 5500 spectrometer with monochromatic Al Kα radiation. Scans were made with a step size of 0.1 eV and 35 to 50 repeated cycles. Igor Pro[26] was used for spectral analysis.

Conclusion

The *in situ* XRPD analysis of the cathodes of Li–O_2 capillary batteries revealed precipitation of Li_2O_2 by the growth of the 100, 101, 102 and 110 diffraction peaks upon discharge. Only the Li_2O_2 diffraction peaks were affected by the discharge–charge of the *in situ* analyzed batteries. The development in the FWHM indicated growth in the crystallite size, as seen by narrowing of the 100 and 101 diffraction peaks upon discharge. A constant exposure to X-ray during charge, increased the decomposition rate of the 100 and 101 diffraction peaks remarkable, compared to a small increase for the 110 diffraction peak. The development of the FWHM upon constant X-ray exposure was dramatically and could indicate that X-ray exposure affects the general Li_2O_2 decomposition. Upon charging of the battery a complete decomposition of Li_2O_2 was observed. The 2nd discharge–charge showed a single very low intensity Li_2O_2 diffraction peak which together with the XPS results indicated a decrease in Li_2O_2 precipitation upon deep discharged cycling.

Acknowledgements

The authors acknowledge support from University of Uppsala, Department of Chemistry – Ångström Laboratory, Structural Chemistry, Prof. Kristina Edström and the MAX-lab staff at beam-line I711. Further acknowledgement is given to the ESRF staff at the Swiss-Norwegian beam-line, the ReLiable project funded by the Danish Council for Strategic Research-Programme Commission on Sustainable Energy and Environment (project no. 11-116792), and The Danish Research Council for the financial support of synchrotron measurements (DANSCATT).

References

1 G. Girishkumar, B. McCloskey, A. C. Luntz, S. Swanson and W. Wilcke, *J. Phys. Chem. Lett.*, 2010, **1**, 2193–2203.
2 J. Xiao, D. Mei, X. Li, W. Xu, D. Wang, G. L. Graff, W. D. Bennett, Z. Nie, L. V. Saraf, I. A. Aksay, J. Liu and J.-G. Zhang, *Nano Lett.*, 2011, **11**, 5071–5078.
3 Y. Li, J. Wang, X. Li, D. Geng, R. Li and X. Sun, *Chem. Commun.*, 2011, **47**, 9438–9440.
4 M. M. Storm, M. Overgaard, R. Younesi, N. E. A. Reeler, T. Vosch, U. G. Nielsen, K. Edström and P. Norby, *Carbon*, 2014, DOI: 10.1016/j.carbon.2014.12.104.
5 B. D. McCloskey, D. S. Bethune, R. M. Shelby, T. Mori, R. Scheffler, A. Speidel, M. Sherwood and A. C. Luntz, *J. Phys. Chem. Lett.*, 2012, **3**, 3043–3047.
6 M. M. Ottakam Thotiyl, S. A. Freunberger, Z. Peng and P. G. Bruce, *J. Am. Chem. Soc.*, 2013, **135**, 494–500.
7 M. Balaish, A. Kraytsberg and Y. Ein-Eli, *Phys. Chem. Chem. Phys.*, 2014, **16**, 2801–2822.
8 R. Younesi, P. Norby and T. Vegge, *ECS Electrochem. Lett.*, 2014, **3**, A15–A18.
9 R. Younesi, Characterization of Reaction Products in the Li–O_2 Battery Using Photoelectron Spectroscopy, Ph.D. thesis, University of Uppsala, 2012.
10 J. Shui, F. Du, C. Xue, Q. Li and L. Dai, *ACS Nano*, 2014, **8**, 3015–3022.
11 J. S. Hummelshøj, J. Blomqvist, S. Datta, T. Vegge, J. Rossmeisl, K. S. Thygesen, A. C. Luntz, K. W. Jacobsen and J. K. Nørskov, *J. Chem. Phys.*, 2010, **132**, 071101.
12 H. Lim, E. Yilmaz and H. R. Byon, *J. Phys. Chem. Lett.*, 2012, **3**, 3210–3215.
13 K. R. Ryan, L. Trahey, J. S. Okasinski, A. K. Burrell and B. J. Ingram, *J. Mater. Chem. A*, 2013, **1**, 6915–6919.
14 J.-L. Shui, J. S. Okasinski, P. Kenesei, H. A. Dobbs, D. Zhao, J. D. Almer and D.-J. Liu, *Nat. Commun.*, 2013, **4**, 2255.
15 R. E. Johnsen and P. Norby, *J. Appl. Crystallogr.*, 2013, **46**, 1537–1543.
16 Y. S. Mekonnen, K. B. Knudsen, J. S. G. Mýrdal, R. Younesi, J. Højberg, J. Hjelm, P. Norby and T. Vegge, *J. Chem. Phys.*, 2014, **140**, 121101.
17 M. M. O. Thotiyl, S. A. Freunberger, Z. Q. Peng and P. G. Bruce, *J. Am. Chem. Soc.*, 2013, **135**, 494–500.
18 B. D. McCloskey, D. S. Bethune, R. M. Shelby, G. Girishkumar and A. C. Luntz, *J. Phys. Chem. Lett.*, 2011, **2**, 1161–1166.
19 J. Liu, M. Roberts, R. Younesi, M. Dahbi, K. Edström, T. Gustafsson and J. Zhu, *J. Phys. Chem. Lett.*, 2013, **4**, 4045–4050.
20 R. Younesi, M. Hahlin, M. Roberts and K. Edström, *J. Power Sources*, 2013, **225**, 40–45.
21 R. Younesi, M. Hahlin, F. Björefors, P. Johansson and K. Edström, *Chem. Mater.*, 2012, **25**, 77–84.
22 Y.-C. Lu, A. N. Mansour, N. Yabuuchi and Y. Shao-Horn, *Chem. Mater.*, 2009, **21**, 4408–4424.
23 S. Leroy, H. Martinez, R. Dedryvère, D. Lemordant and D. Gonbeau, *Appl. Surf. Sci.*, 2007, **253**, 4895–4905.
24 A. P. Hammersley, ESRF Internal Report, ESRF97HA02T, 1997.
25 Topas3, *BRUKER-AXS*, 2000.
26 IGORPro, *WaveMetric, Version 4.0*.

Supporting information

Capillary based Li-air batteries for *in situ* synchrotron X-ray powder diffraction studies

Mie Møller Storm, Rune E. Johnsen, Reza Younesi and Poul Norby
Department of Energy Conversion and Storage, Technical University of Denmark, Frederiksborgvej 399, DK-4000 Roskilde, Denmark

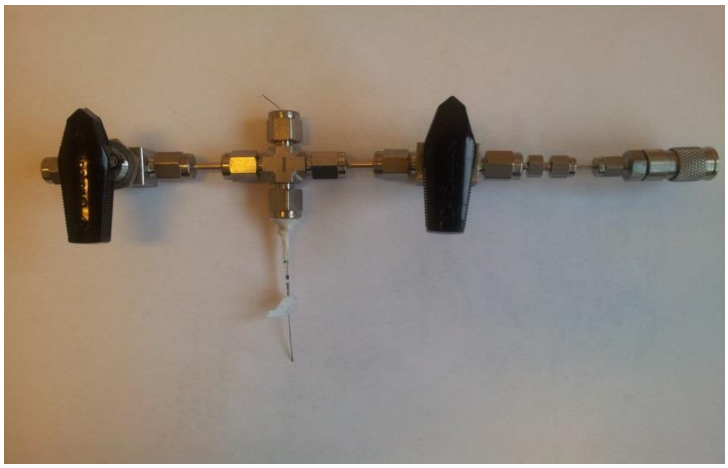

Figure S1: A photo of the capillary battery.

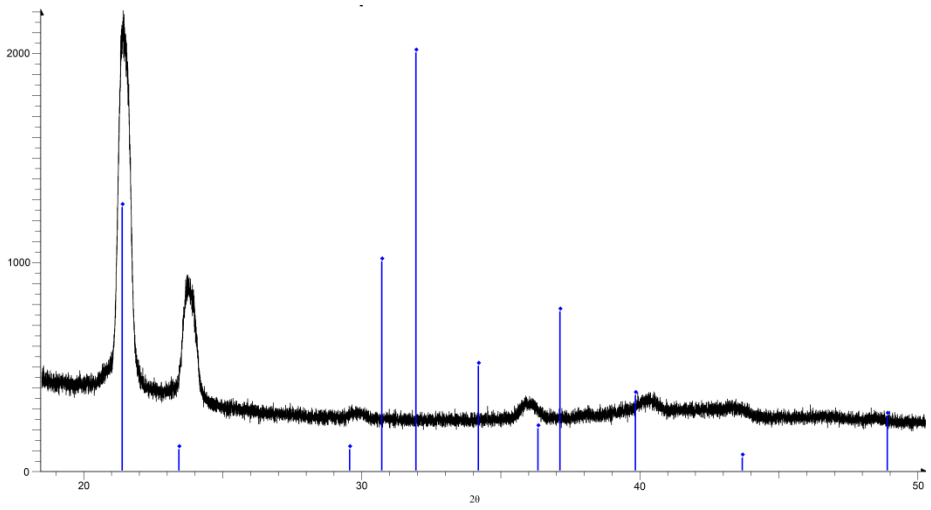

Figure S2: A 5 times discharged cathode. Blue lines: diffraction pattern of Li_2CO_3.

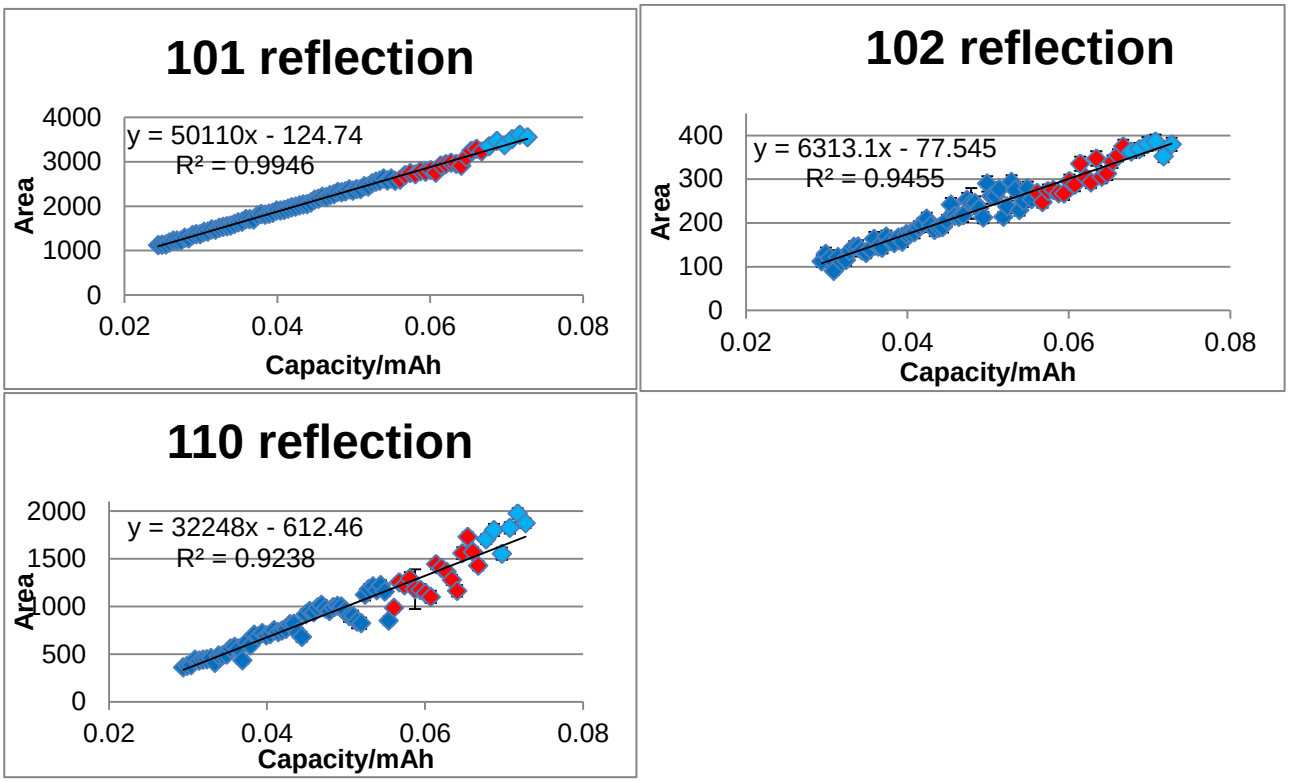

Figure S3: The development of the areas of the reflections as a function of capacity during discharge for the 101, 102 and 110 reflections for battery 1.

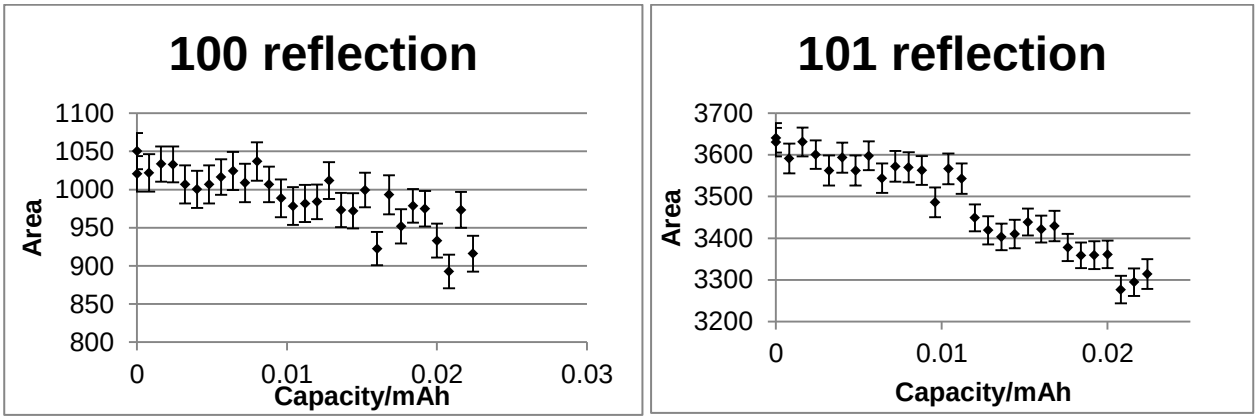

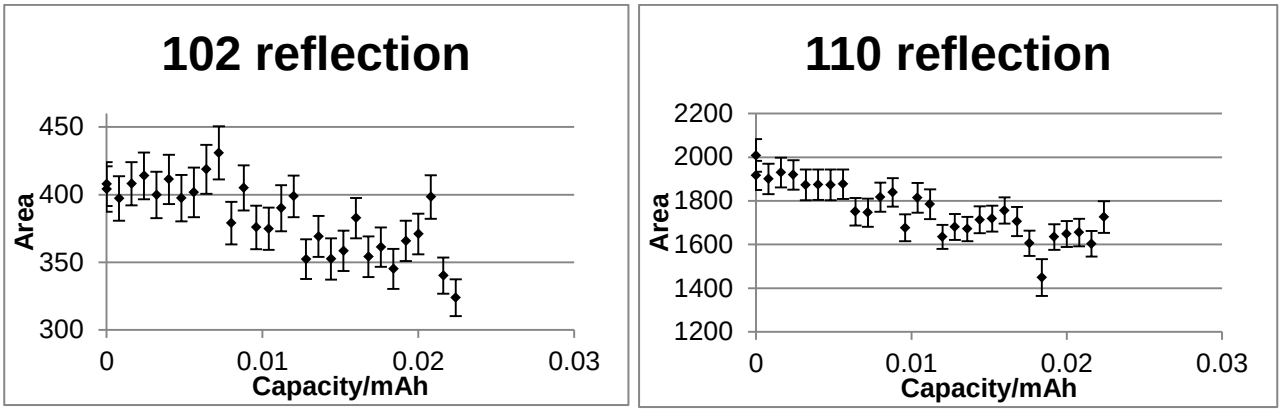

Figure S4: The development of the areas of the reflections for the first charge of battery 1 for the 100, 101, 102 and 110 reflections.

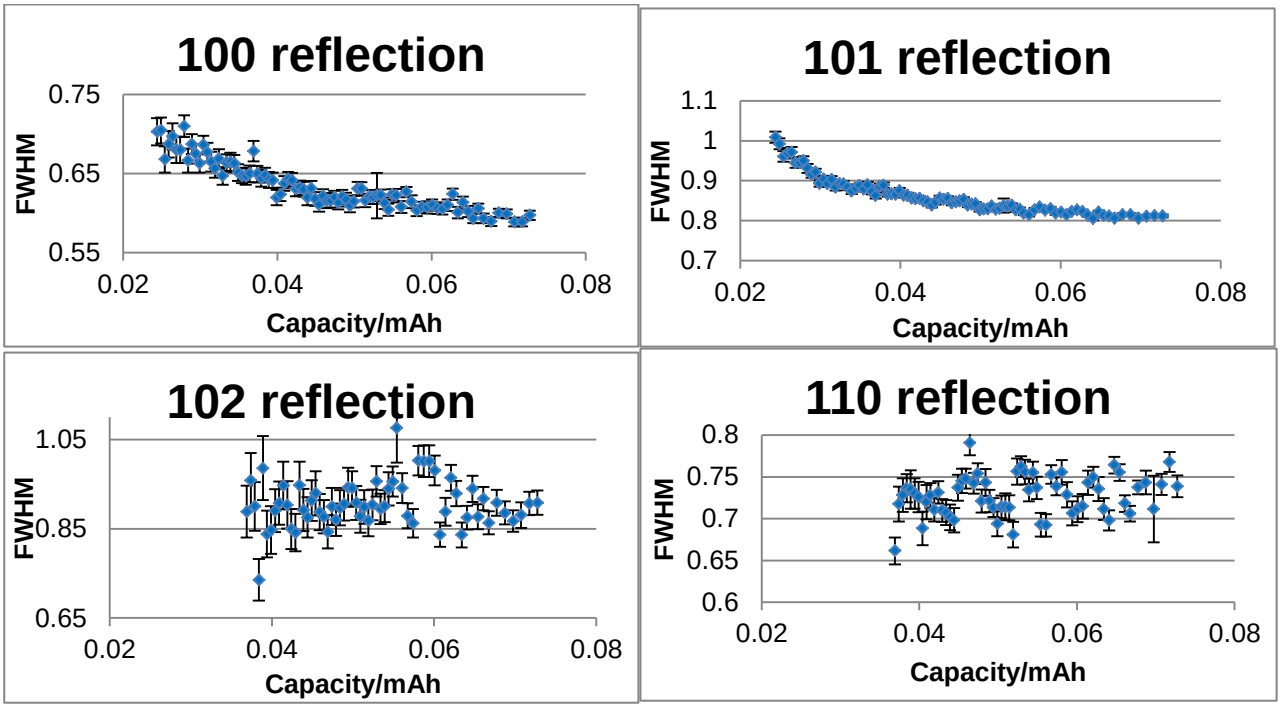

Figure S5: The development of the FWHM during discharge of battery 1 for the 100, 101, 102 and 110 reflections.

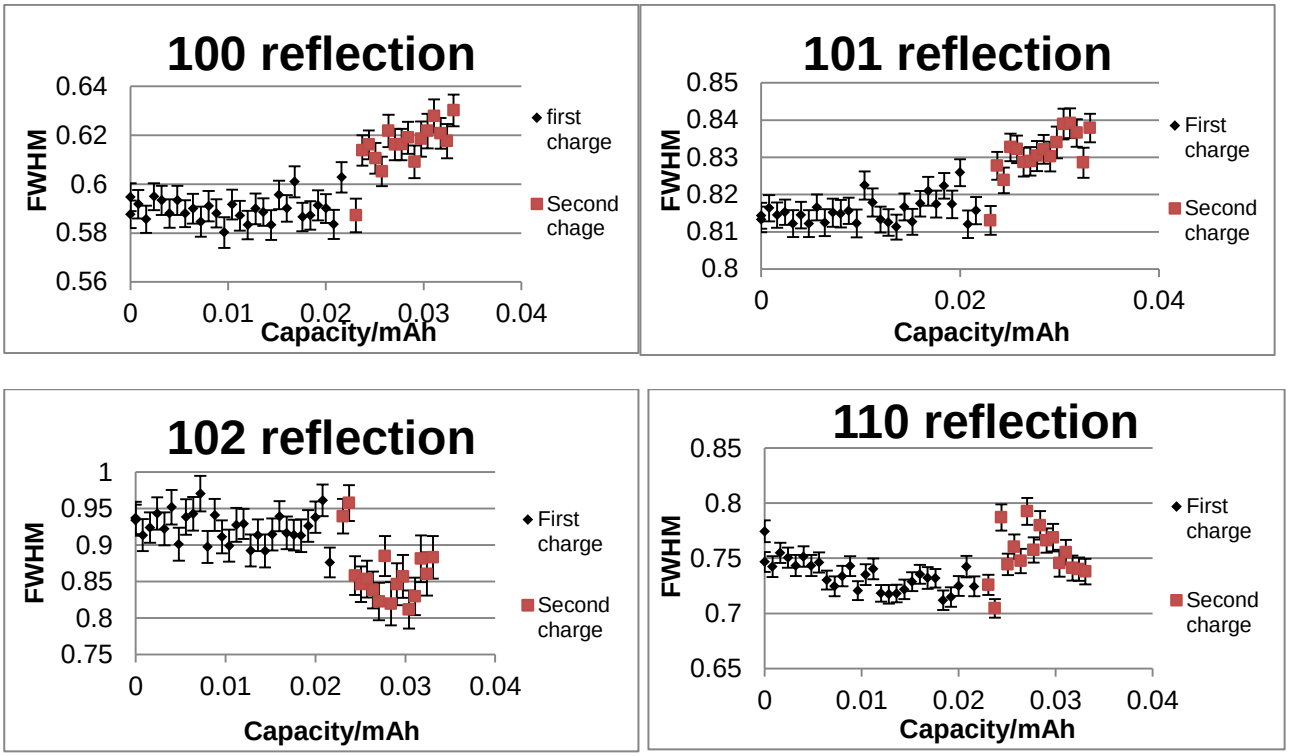

Figure S6: The development of the FWHM during charging of battery 1 for the 100, 101, 102 and 110 reflections.

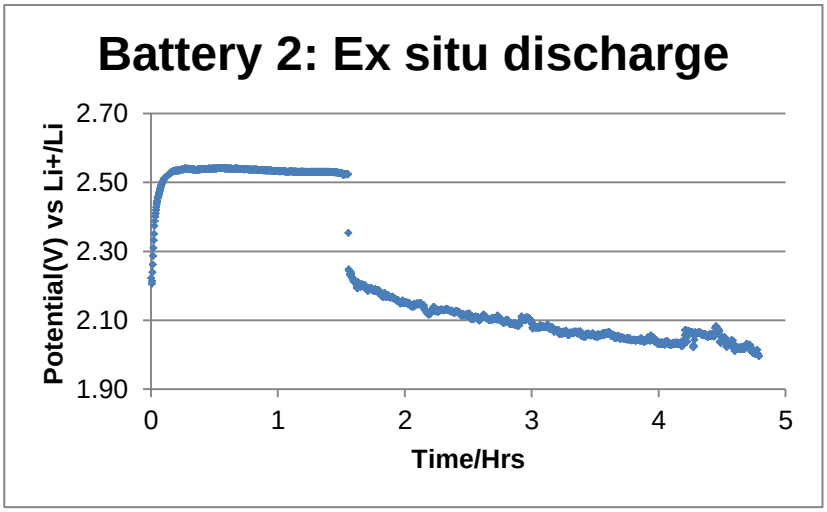

Figure S7: The discharge curve of battery 2

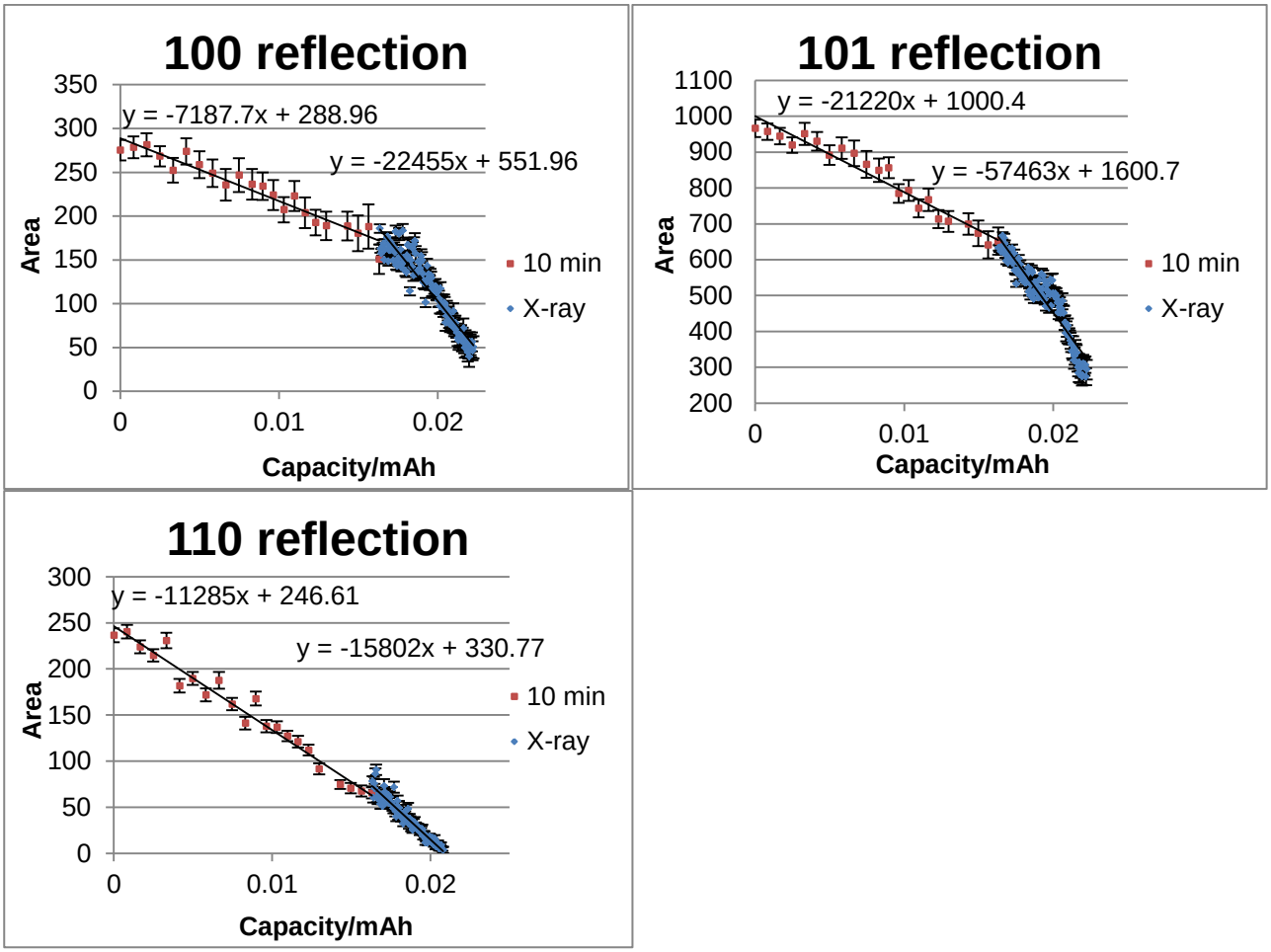

Figure S8: The decomposition of the Li_2O_2 reflections in battery 2 as a function of capacity, depending on a 10 minutes exposure to X-ray or constant X-ray exposure. The left equation is for the 10 minutes measurements and the right equation is for the constant X-ray exposure.

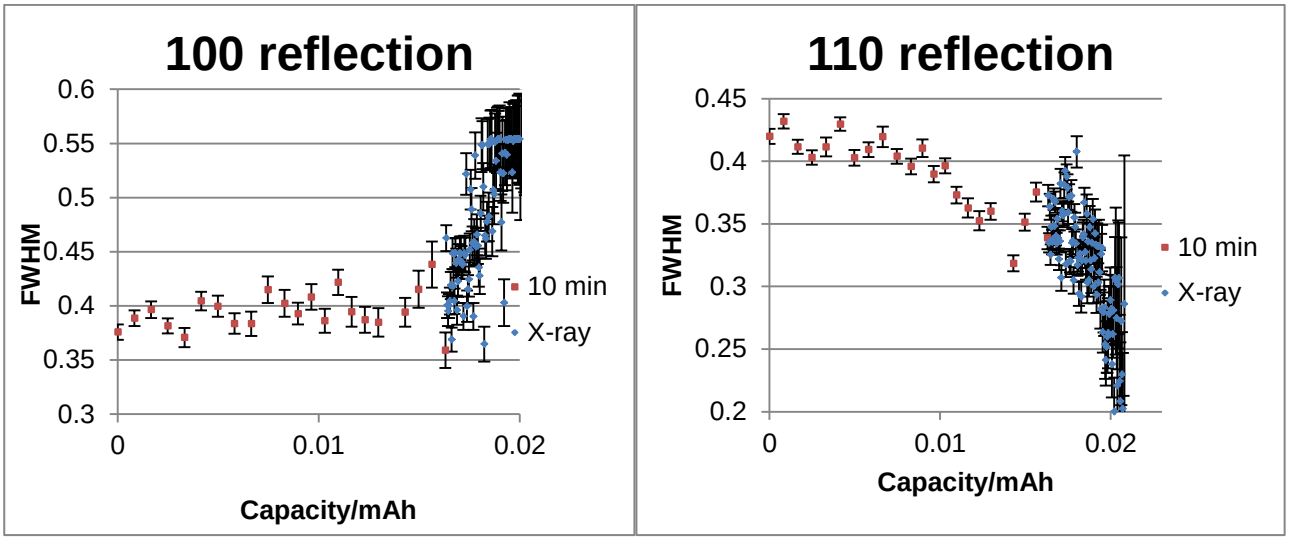

Figure S9: The development of the FWHM for battery 2, both with and without constant X-ray exposure. The upper limit reached for the 100 reflections is due to the fitting procedure for the data.

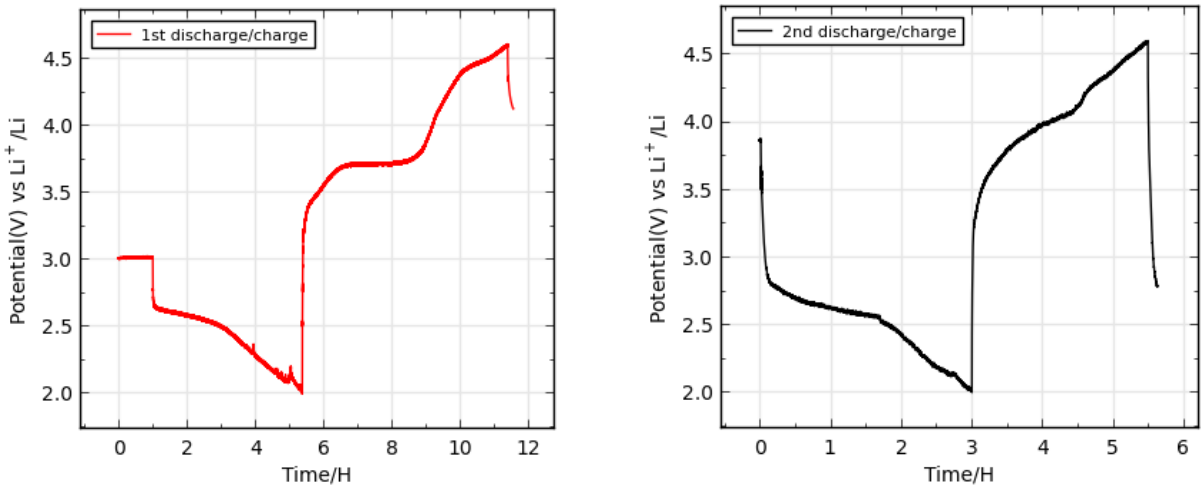

Figure S10: Left: The 1st discharge/charge curves of battery 3 measured at 4 µa. Right: The 2nd discharge/charge curves of battery 3 measured at 5 and 6 µa.

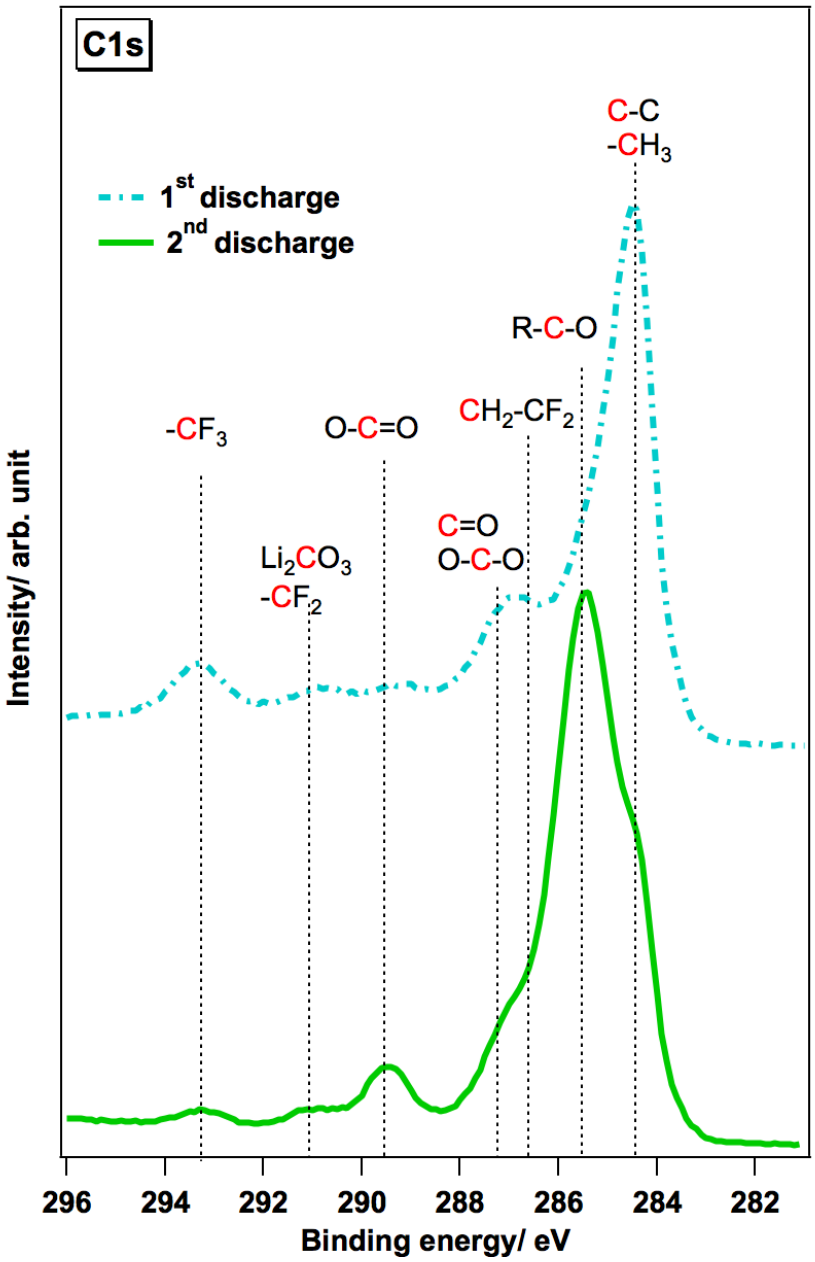

Figure S11: The C1s spectra of *ex situ* analyzed cathodes after 1st discharge (blue/-·-·) or 2nd discharge (green/—) in the capillary Li-O_2 battery.

Paper IV

In situ analysis of the Li-O_2 battery with thermally reduced graphene oxide cathode: influence of water addition

Mie Møller Storm[1], Mathias Kjærgård Christensen[1], Reza Younesi[2] and Poul Norby[1*]

[1]Technical University of Denmark, DTU Energy, Frederiksborgvej 399, 4000 Roskilde, Denmark

[2]Department of Chemistry - Ångström Laboratory, Uppsala University, Box 538, SE-751 21 Uppsala, Sweden

*corresponding author, phone: 0045 21124450, e-mail: pnor@dtu.dk

Abstract

The Li-air technology holds the promise to deliver a battery with increased gravimetric capacities compared to today Li-ion batteries. Reduced graphene oxide has received increasing attention in the Li-air community as a cathode support material with the possibilities to increase the discharge capacity, increase battery cycleability and decrease the charging overpotential. In this article we investigate the effect of water on a thermally reduced graphene oxide cathode in a Li-O_2 battery. Differential electrochemical mass spectroscopy reveals a decreased electron count for batteries with 1000 ppm water in comparison to dry batteries, indicating additional parasitic electrochemical or chemical processes. A similar capacity of the wet and dry batteries indicate that the mechanism in the Li-O_2 battery also depends on the surface of the cathode and not only on addition to the electrolyte as explored by the solution based mechanism. *In situ* XRD of a new design of a capillary based Li-O_2 cell with a thermally reduced graphene oxide cathode shows the formation of LiOH along with Li_2O_2.

Introduction

The high theoretical Li-air battery capacity is only reached for Li-air batteries with an open system with oxygen being drawn from the air. However, the use of oxygen from the air is a challenge in regards to both water and CO_2[1–6].

Since 2011 graphene based cathodes have been studied for non-aqueous Li-air batteries[7,8], where they were found increase the discharge capacity compared to carbon black cathodes, a feature which was assigned to the morphology and surface of graphene. Furthermore graphene-based cathodes hold the promise of lowering of the overpotential on charge of the Li-air battery[9], a crucial challenge which has to be overcome in order to enhance the energy efficiency. Recently graphene-based cathodes have been the theme for many new publications in the Li-air battery community showing an increasing interest in tailored morphology of cathodes materials: Liu *et al.*[10] observed formation of Li_2O_2 and LiOH on graphene based cathode with a DMSO based electrolyte and a discharge capacity of 90.000 mAh/$g_{graphene}$. Lu *et al*[11] showed formation of LiO_2 on a graphene surface with iridium nanoparticles when discharged to 1000 mAh/g without formation of Li_2O_2. Gray *et al.*[12] tested a reduced graphene oxide (rGO) cathode with a LiI redox mediator and found that the use of the redox mediator lowered the overpotential upon charging to 0.2 V and changed the decomposition product to LiOH.

Usually when graphene-like materials are investigated as cathode materials for Li-O_2 batteries the main discharge product, at least on the first cycle, is Li_2O_2[7,13,14]. Lu *et al.*[11] observed LiOH on the 9th cycle of an rGO cathode in 1 M $LiCF_3SO_3$ in tetraethylene glycol dimethyl ether (TEGDME) and aside from Li_2O_2 observations of Li_2O and Li_2CO_3 has also been reported [15]. Liu *et al.*[10] has recently observed LiOH as a discharge product on a binder-free graphene based cathode on aluminum support, where they ascribe the formation on LiOH as a result of reaction with the DMSO based electrolyte.

Li_2O_2 alone reacts chemically with water to form LiOH, however it has been found that the main discharge product in cells with carbon black based cathodes and water is Li_2O_2. Water enhances the discharge capacity of the cell which is explained by the solution based mechanism, where water enables formation of toroidal shaped Li_2O_2[3,5,6,16]. During the formation of Li_2O_2 by the solution based mechanism species formed on the surface of the cathode may become soluble by stabilization of species in the electrolyte, leading to formations of larger toroidal Li_2O_2.

Since decomposition of carbonate based electrolytes in the Li-O_2 battery was observed[17–19] it has been noted several times in the Li-air community that careful characterization, both *ex* and *in situ*, is the key to understanding the Li-air battery[20]. Differential Electrochemical Mass Spectrometry (DEMS) was introduced to the Li-air community by McCloskey *et al.*[18], and has since resulted in knowledge on decomposition of both electrolyte and cathode in Li-air batteries[21–23]. The DEMS analyses the pressure or exhaust gasses of the battery as the battery is running, giving a real time picture of the reactions and the decomposition taking place in the battery. *In situ* X-ray diffraction (XRD) has been used to investigate the formation and decomposition of Li_2O_2 on a carbon cathode[24–27] and the changes in the Li-metal anode[28]. For *in situ* XRD analysis of the Li-air battery we have previously developed a capillary based *in situ* battery cell design[27], which was further optimized for this study, to ensure a known position of the oxygen in-let and better performance results.

With rGO being an upcoming material in Li-air batteries a better understanding of surface reactions and discharge products for rGO cathodes are needed. In this study, we investigate the effect of addition of water to a 1,2dimethoxyethane (DME) electrolyte for a cell with a thermally reduced graphene oxide (TrGO) cathode analyzed by DEMS measurements. We furthermore present a new capillary based battery designed for *in situ* XRD revealing the appearance of LiOH diffraction peaks observed during discharge for a TrGO cathode.

Experimental

Cathode materials

TrGO was synthesized and characterized as described in [14] from GO made by the modified Hummers method: In an Erlenmeyer flask on ice 3 g of graphite (325 mesh, with 99.8% metals basis, Alfa Aesar), 1.5 g of $NaNO_3$ and 100 ml conc. H_2SO_4 were mixed for 10 minutes, followed by a 30 minutes of slow addition of 12 g $KMnO_4$. The solution was cooled for 2 hrs before being heated to 35 °C. After 3 hrs the reaction was terminated by slow addition of 100 ml ice cooled H_2O and 25 ml 30% H_2O_2. The GO was separated from the solution by centrifugation (10 min, 4500 rpm) and washed with 0.1 M H_2SO_4 followed by overnight drying in vacuum furnace at room temperature. The GO was rinsed twice, first four times with 0.1 M HCl and centrifugation followed by overnight drying in vacuum furnace at 25 °C and then by a similar washing procedure with acetone. The thermal reduction of GO was performed in a tube furnace at 1100 °C, in a closed glass tube containing Ar. 250-300 mg GO was reduced at the time for 2 min, yielding approx. 100 mg TrGO, which was washed in acetone.

The SuperC65 (carbon black from TIMCAL Graphite and Carbon) was used directly as delivered

DEMS

The DEMS set-up and procedures are described in further in [29,30]. The DEMS cathodes were spray coated with a 3:1 mixture of TrGO and PTFE in a 1:4 isopropanol:water mixture onto a cleaned SS mesh. The cathodes were punched to 10 mm size, with a weight of 0.3-0.5 mg, and dried in a vacuum furnace at 180 C° for 12 hrs before use. The batteries were assembled in a Swagelok based battery for the DEMS with a 10 mm Li-anode, 2 Whatman separators, 80 µl 1 M Lithium bis(trifluoromethylsulfonyl)imide (LiTFSI) in DME with or without addition of 1000 ppm H_2O, the cathode and a SS mesh current collector. 1 M LiTFSI in DME electrolyte was made by drying

LiTSFI at 180 °C for 12 hrs and DME was dried overnight with molecular sieves heated to 275 °C for 12 hrs before the mixing of the electrolyte. The batteries were discharge-charged at 120 µA between 2 - 4.5 V and 2.7 - 4.5 V. Only the first discharge-charge cycle was investigated. Four batteries were tested with a dry electrolyte and four batteries were investigated with a wet (1000 ppm H_2O) electrolyte. The DEMS volume was calibrated for O_2 and CO_2 gas, resulting in quantitative data. However, the DEMS volume was not calibrated for H_2 thus the data shown in the article are qualitative analyses of the H_2 development during charge. The batteries were leak tested with Ar after the battery test. The standard DEMS test consisted of pressure measurement upon discharge and gas analysis during charge. A dry battery was tested with pressure measurements on both discharge and charge from 2.7-4.3V at 120 µA, and a wet battery was pressure tested at 78.5 µA from 2.7-4.2V, both pressure measurements showed a linear increase of pressure. Batteries for *ex situ* analysis and the DEMS were tested with oxygen grade 6.0 (AGA). Cathodes for *ex situ* analysis were collected for deep discharged cathodes to 2 V. The batteries were disassembled in a glovebox and the cathodes were cleaned with dried DME.

Capillary battery assembly:

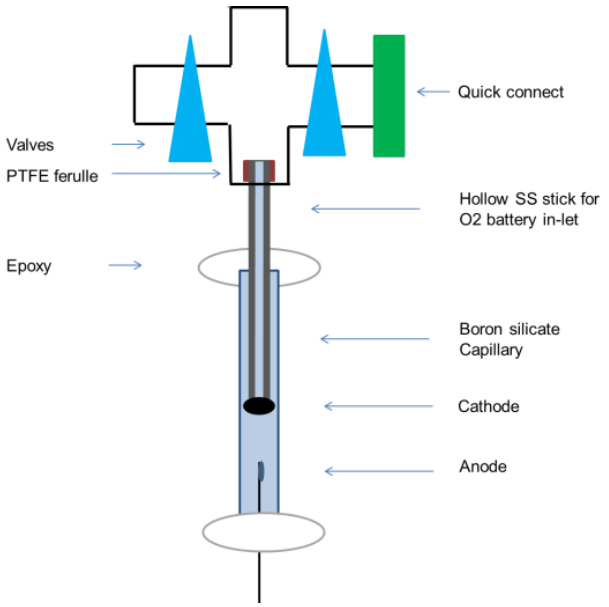

Figure 1: The capillary battery with single point oxygen in-let

A Li-O_2 capillary battery design was first published in [27], but has been optimized to get a single-point oxygen in-let, as shown by the drawing in Figure 1. A picture of the set-up is seen in Figure S1 in supporting information (SI). The anode is Li-metal smeared onto 0.4 mm stainless steel (SS) wire. The cathode was formed on a hollow 0.7 mm SS wire, which has been honed in one end and cleaned in ethanol. The cathode was dip-coated onto the SS wire in a 1:1 carbon material:PVDF slurry with NMP. In between the coatings of the cathode, the cathode was dried with a heating gun at a temperature of 120-130 °C. The cathode was dried at 120 °C and further dried in a vacuum furnace in a glovebox at 180 °C for 12 hrs. The battery was assembled in a glovebox. The anode was glued into an empty flat square borosilicate capillary (outer diameter 4.2*1.25 mm, Hilgenberg) with two-component epoxy glue and the capillary was filled with the dry electrolyte (a water containing electrolyte was not investigated by *in situ* XRD). The cathode was placed in the filled capillary, the top of the capillary was covered with vacuum grease and the cathode wire was then glued to the capillary. The battery was attached via the open end of the SS wire to the oxygen in-let

system by a teflon ferrule and the battery was removed from the glovebox. The oxygen in-let was flushed with oxygen and the battery test was initiated. The batteries were investigated at 3 μa discharged and charged from 1.95-4.65 V. The battery was tested with oxygen grade 3.5 (AGA). As the point of the oxygen in-let for the capillary Li-O_2 battery design is known for this design, two different positions on the cathode were measured during the battery *in situ* test. Position 1 was in the bottom of the hollow SS wire, and was thus assumed to be closest to the oxygen in-let point. For the second position the X-ray beam was moved in the horizontal plane, to a spot with a high carbon diffraction signal and little SS diffraction. Position 2 is assumed to be further from the oxygen in-let. The positions were at least 0.3 mm apart.

Characterization

Synchrotron XRD on the capillary battery was performed at Maxlab beamline 711 with a wavelength of 0.9941 Å and a beam size of 0.2 mm *0.2 mm. A LaB_6 standard combined with the known *d*-values for the SS-wire was used to calibrate the detector to sample distance. The distance was calibrated for position 1. The X-ray diffraction data collection was performed every 10 min. with a 30 sec collection time. The beam was switched of between data collection in order to avoid X-ray radiation experiment effects.[27] Position 1 was measured before position 2. Scan 58 to 60 for the TrGO battery and scan 56-59 for the Super C65 battery were removed from the analysis as these where measured during beam injection. Fit2D was used for data reduction of the 2D diffraction images and the data were normalized in Powder3D using the intensities in 4-6° in 2θ. The peak deconvolution was performed in PDXL[31] for the peaks observed form 18-23° in 2θ. For *ex situ XRD,* powder from a discharged and cleaned TrGO cathode, from the DEMS cell or similar designed Swagelok cell, was sealed in a 0.5mm capillary and measured on a Rigaku Smartlab diffractometer, and the data were analyzed with PDXL. X-ray photoelectron spectroscopy (XPS) spectra were recorded on a commercial in-house PHI 5500 spectrometer with monochromatic Al

Kα radiation. Scans were made with a step size of 0.1 eV and 50 to 80 repeated cycles. Igor Pro was used for spectral analysis. XPS data was fitted with binding energies from [32–36], a deviation of 0.1 eV was accepted. SEM images were taken on a Carl Zeiss Supra-35 instrument at 15 kV.

Results and Discussion

Characterization of TrGO is described in [14]. SEM images of the TrGO show a surface resembling a crumbled sheet with cavities as seen in Figure 2, indicating a compound with a porous structure and a large surface area. The C 1s spectra of XPS analysis showed the presence of several functional groups such as C-C, C-O, C=O and COO on the surface of TrGO revealing a defect filled surface with oxygen functionalities present both on the carbon-backbone sheet of TrGO and on the edges in agreement with reference [27]. XPS and EDX results indicating impurities in the TrGO powder are discussed in SI (Figures S2, S4 and S5).

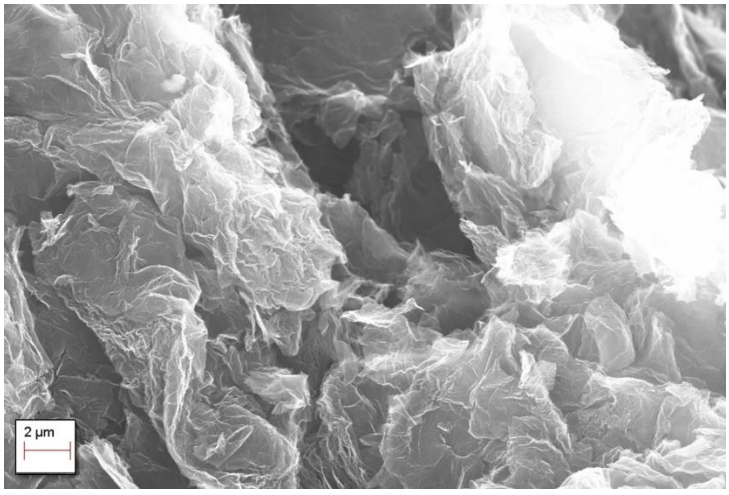

Figure 2: SEM picture of TrGO showing a structure resembling folding sheets with cavities.

Battery	**Discharge (four measurements) / e^-/O_2**	**Charge (1 measurement) / e^-/O_2**
Dry	2.01 ± 0.06	2.2
Wet (1000 ppm water)	1.83 ± 0.10	2.25

Table 1: The electron count of the discharge and charge of the wet and dry batteries.

DEMS analysis was performed on TrGO cathodes using electrolyte with and without added water (1000 ppm) in order to analyse reversibility of ORR and OER. Table 1 shows the electron counts for the wet and dry batteries on charge and discharge obtained from DEMS measurements. The discharge of the dry battery (no additional water) showed a flat curve with a plateau around 2.7 V, which was terminated by a sudden drop in voltage termed sudden death, as described in [29]. The DEMS pressure analysis upon discharge of the dry battery revealed an average electron count of 2.01 ± 0.06 (measured from four batteries). See an example of a fitted pressure measurement in Figure S3. An electron count of 2 e^-/O_2 is expected by ideal formation of Li_2O_2, which was the discharge product observed by *ex situ* XRD on a Swagelok cell with dry electrolyte discharged to 2 V. However, both Li_2O_2 and LiOH were implied by the O 1s XPS spectra on a discharged dry cathode indicating chemical formation of LiOH, which may be caused by reaction between Li_2O_2 and the electrolyte and/or the TrGO surface of graphene. XPS is a surface sensitive technique and formation of a very thin layer or amorphous LiOH on the surface of the cathode would not be detected by XRD. The use of a transfer cup for the XPS measurements ensured air tight transfer from the glovebox, as air exposure results in LiOH formation due to the reaction of Li_2O_2 with water.

Batteries with a TrGO cathode and a wet electrolyte containing 1000 ppm H_2O had similar looking discharge-charge curves as the ones of the dry batteries, see Figure 3 for the charge curve. The discharge consisted of a flat plateau at 2.7 V and the potential of the charge increased to above 4 V where a plateau was formed. Pressure analysis of the wet cell upon discharge resulted in an electron count at 1.83 ± 0.10 e^-/O_2 (measured from four batteries) indicating additional electrochemical or chemical formation of material together with Li_2O_2. *Ex situ* XRD of wet cathodes discharged to 2V showed formation of Li_2O_2. The XPS O1s spectra of a discharged wet cathode surface were similar to the one of the dry cathode showing formation of both Li_2O_2 and LiOH, see Figure S4 and S5. The lowering of the electron count could be caused by water in the electrolyte accelerating the reaction of the Li-anode with oxygen causing an increased consumption of the oxygen (no visible changes in the Li-anode was however observed). It could also be caused by the formation of species with a single electron formation count. As the XPS revealed the presence of no additional side reaction products, formation of soluble decomposition products in the electrolyte or further consumption of oxygen on the Li-metal anode may explain the lowering of oxygen pressure upon discharge.

It has been shown that addition of water to a carbon black cathode based battery increases the discharge capacity compared to a dry battery as explained by the solution based mechanism[3–6]. However, our results showed that the discharge capacities of the wet batteries were not remarkably extended compared to that of dry batteries. This indicates that the solution based mechanism is affected not only by the electrolyte but also by the surface involved in the formation of the discharge product. This can be explained by a surface having a larger or smaller affinity for the surface stabilized species which may affect the reaction mechanism.

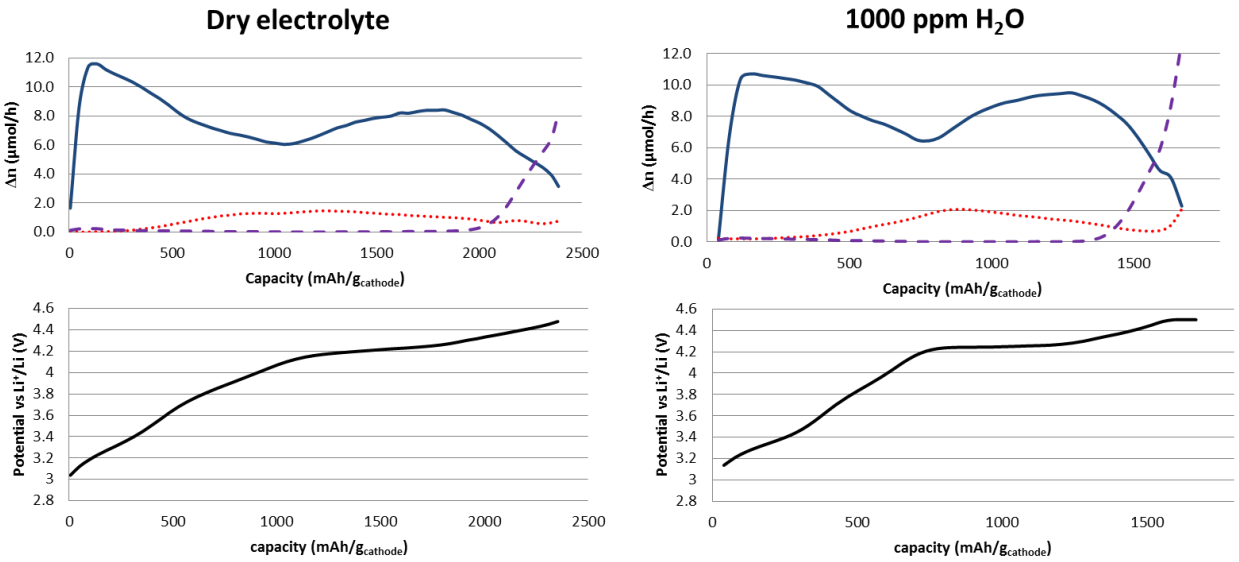

Figure 3: Top: DEMS analysis showing the O_2, H_2 and CO_2 gas evolution for charging of a TrGO cathode in dry and wet electrolyte. Bottom: charge curve for a TrGO cathode in dry and wet electrolyte. DEMS analysis: Blue (full line) = Oxygen, red (….) = Hydrogen (not quantitative) and purple (---) = CO2

The charge of the dry TrGO battery showed an increasing potential with no plateau formation observed below 4.1 V, which could indicate electrolyte decomposition, see Figure 3. The charging of the dry battery was rather similar with plateau formation above 4 V. Charging of the dry TrGO Li-O_2 battery had an average electron count of 2.2 e^-/O_2 (fitted from pressure measurement) and charging of the wet battery was rather similar with an electron count of 2.25 e^-/O_2. The fact that the charge reaction is complicated and leads to decomposition is not unexpected for Li-O_2 batteries. A charge having an increased electron count, as compared to the standard 2 e^-/O_2, may be caused by side reactions e.g. decomposition of electrolyte, especially when tested at these high potentials. During charge for the dry battery different gasses were observed. The DEMS registered O_2 evolution for the entire charge, however, H_2 and CO_2 were furthermore observed (see Figure 3).

CO_2 was observed above 4 V, probably from the decomposition of the electrolyte. However, as the stability of rGO has yet to be examined, decomposition of the cathode is also a possible CO_2 source. The appearance of H_2 can be caused by the decomposition of electrolyte or by decomposition of the TrGO cathode. However, the hydrogen containing groups of TrGO are few and would unlikely cause such levels of H_2.

DEMS analysis of the charge for the wet batteries showed similar tendencies as for the dry batteries: Oxygen evolution is observed for the entire charge and a rise in CO_2 evolution is observed above 4 V. The hydrogen evolution is visible after the initial charge, but seems increased compared to the dry batteries, probably due to the presence of water and possible reactions on the anode. The H_2 levels were increased during the last part of the charge at the highest potentials.

SEM images of discharged cathodes for the wet and dry batteries are presented in Figure S6 and show rather similar morphologies without any observation of toroidal shaped Li_2O_2, maybe due to the discharge rate (0.15 mA/cm^2). This indicates that the discharged products are formed as a film on the cathode surface.

The O 1s XPS spectra were similar for the dry and the wet cathode and no carbonate formation was observed for the cathodes. Small differences in the ratio of materials were detected for the C 1s and F 1s spectra, but further studies have to be performed to understand if this is caused by the addition of water, Figure S5.

In situ XRD performed on a TrGO cathode in a new capillary based battery design with the dry electrolyte had a long 1st discharge with a flat voltage plateau around 2.5 V. A small charge capacity was observed, see Figure 4, with a small decrease of the Li_2O_2 intensity of 19%, the charge of the capillary battery is described in SI. The charging of the capillary battery could be influenced by the *in situ* capillary cell construction as the Swagelok based batteries had better recharge

capacities. A battery with a Super C65 cathode was measured for comparison, and the results are presented in SI and in Figure S7.

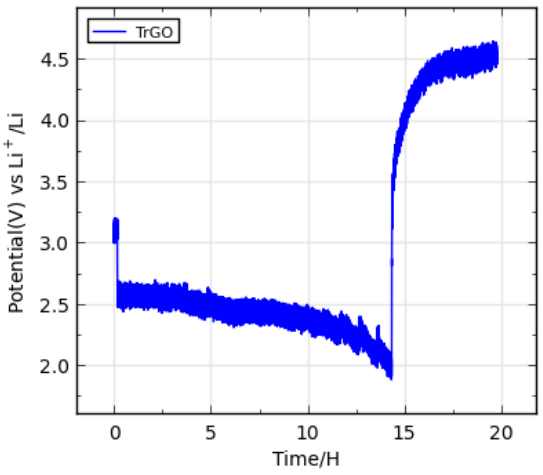

Figure 4: Discharge-Charge profile for capillary batteries with a TrGO cathode and a Super C65 cathode tested at 3 μA.

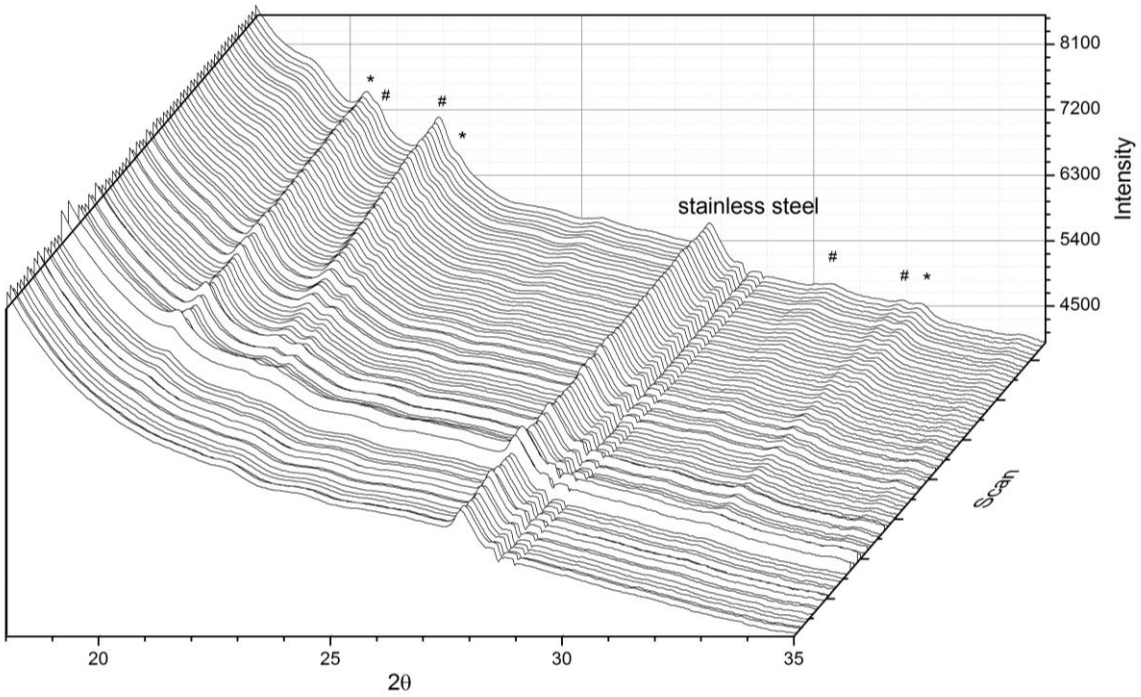

Figure 5: *In situ* XRD in position 1 of a Li-O_2 battery with a dry TrGO cathode. * signify LiOH and # signify Li_2O_2. A X-ray diffraction was taken of the cathode every 10 min.

Several diffraction peaks were observed upon discharge of the TrGO capillary battery, see Figure 5 for the diffraction pattern at position 1. The diffraction peaks at position 2 (XRD measured farther away on the cathode from the oxygen in-let) are similar, however of less intensity. The diffraction peaks are assigned in Figure 5 and Table S1. Diffraction peaks of Li_2O_2 are growing during the discharge as expected, however several other diffraction peaks appeared as well. These diffraction peaks indicate the formation of LiOH. One unassigned peak a *d*=2.964 is observed as well. The diffraction peaks were not observed by *ex situ* XRD of the deep discharged cathode in the Swagelok based battery with a wet or dry electrolyte. The formation of crystalline LiOH in the capillary battery, but not in the Swagelok cells might be caused by several small differences in the set-up, as described in SI, however the formation of LiOH supports the observation of LiOH by XPS.

It was found, for position 1, that the intensity of the LiOH and Li_2O_2 diffraction peaks increased upon discharge and these diffraction peaks also had a decreasing FWHM with discharge. Only the lower angle diffraction peaks were analyzed due to the low intensity of the other diffraction peaks. The decreasing FWHM can indicate crystal growth upon discharge. The peaks at 20.7° and 21.9° were indexed as the 100 and 101 Li_2O_2 diffraction peaks, and their development is in agreement with the development of the 100 and 101 Li_2O_2 diffraction peaks for a carbon black cathode [27]. The two different cathode types have similar trends for intensity and FWHM development of the Li_2O_2 diffraction peak despite the LiOH byproduct.

Conclusion

DEMS analysis of Li-O_2 cells with a wet electrolyte in comparison to a dry electrolyte showed a lower electron count for electrolytes containing additional 1000 ppm water. XPS of discharged cathodes indicated this to be caused by a chemical reaction consuming oxygen taking place in the battery or by formation of soluble species. DEMS analysis of the charge for both wet and dry

batteries showed increased formation of CO_2 during the high potentials, and indicated a slight increase in the levels of hydrogen evolution for the wet batteries. Oxygen evolution was observed for the entire charge. As the wet and the dry electrolyte showed similar discharge capacities this indicate that the surface of the cathode affects the mechanism for Li_2O_2 formation.

An *in situ* XRD study on a TrGO cathode showed formation of both LiOH and Li_2O_2 supporting the XPS measurements. Furthermore, the observed trends for intensity and FWHM during *in situ* crystal growth of Li_2O_2 were similar to a previously studied carbon black cathode, indicating similar Li_2O_2 crystal growth despite formation of additional material.

Supporting information

Supporting information is available free of charge online, and contain additional information on the TrGO cathode material, the DEMS, XPS and data in regards to the capillary battery with a TrGO cathode and the capillary battery with a super C65 cathode.

Acknowledgement

The authors acknowledge Tim Nordh, Uppsala University, for helping with XPS measurements, and the MAX-lab staff at beam-line I711. Further acknowledgement is given to the ReLiable project funded by the Danish Council for Strategic Research-Programme Commission on Sustainable Energy and Environment (project no. 11-116792), and The Danish Research Council for the financial support of synchrotron measurements (DANSCATT).

References

(1) Gowda, S. R.; Brunet, A.; Wallraff, G. M.; McCloskey, B. D. Implications of CO2

Contamination in Rechargeable Nonaqueous Li-O2 Batteries. *J. Phys. Chem. Lett.* **2013**, *4*, 276–279.

(2) Mekonnen, Y. S.; Knudsen, K. B.; Myrdal, J. S. G.; Younesi, R.; Højberg, J.; Hjelm, J.; Norby, P.; Vegge, T. Communication: The Influence of CO2 Poisoning on Overvoltages and Discharge Capacity in Non-Aqueous Li-Air Batteries. *J. Chem. Phys.* **2014**, *140* (12), 2012–2017.

(3) Aetukuri, N. B.; McCloskey, B. D.; García, J. M.; Krupp, L. E.; Viswanathan, V.; Luntz, A. C. Solvating Additives Drive Solution-Mediated Electrochemistry and Enhance Toroid Growth in Non-Aqueous Li–O2 Batteries. *Nat. Chem.* **2014**, *7* (1), 50–56.

(4) Burke, C. M.; Pande, V.; Khetan, A.; Viswanathan, V.; McCloskey, B. D. Enhancing Electrochemical Intermediate Solvation Through Electrolyte Anion Selection to Increase Nonaqueous Li–O2 Battery Capacity. *PNAS* **2015**, *112* (30), 9293–9298.

(5) Abraham, K. M. Electrolyte-Directed Reactions of the Oxygen Electrode in Lithium-Air Batteries. *J. Electrochem. Soc.* **2015**, *162* (2).

(6) Meini, S.; Solchenbach, S.; Piana, M.; Gasteiger, H. a. The Role of Electrolyte Solvent Stability and Electrolyte Impurities in the Electrooxidation of Li2O2 in Li-O2 Batteries. *J. Electrochem. Soc.* **2014**, *161* (9), A1306–A1314.

(7) Xiao, J.; Mei, D.; Li, X.; Xu, W.; Wang, D.; Graff, G. L.; Bennett, W. D.; Nie, Z.; Saraf, L. V.; Aksay, I. A.; et al. Hierarchically Porous Graphene as a Lithium-Air Battery Electrode. *Nano Lett.* **2011**, *11* (11), 5071–5078.

(8) Li, Y.; Wang, J.; Li, X.; Geng, D.; Li, R.; Sun, X. Superior Energy Capacity of Graphene Nanosheets for a Nonaqueous Lithium Oxygen Battery. *Chem. Commun.* **2011**, *47* (33), 9438–9440.

(9) Zhang, W.; Zhu, J.; Ang, H.; Zeng, Y.; Xiao, N.; Gao, Y.; Liu, W.; Hng, H. H.; Yan, Q. Binder-Free Graphene Foams for O2 Electrodes of Li-O2 Batteries. *Nanoscale* **2013**, *5* (20), 9651–9658.

(10) Liu, C.; Younesi, R.; Tai, C.-W.; Valvo, M.; Edström, K.; Gustafsson, T.; Zhu, J. 3-D Binder-Free Graphene Foam as Cathode for High Capacity Li-O2 Batteries. *J. Mater. Chem. A* **2016**.

(11) Lu, J.; Jung Lee, Y.; Luo, X.; Chun Lau, K.; Asadi, M.; Wang, H.-H.; Brombosz, S.; Wen, J.; Zhai, D.; Chen, Z.; et al. A Lithium–Oxygen Battery Based on Lithium Superoxide. *Nature* **2016**, 1–7.

(12) Liu, T.; Leskes, M.; Yu, W.; Moore, A. J.; Zhou, L.; Bayley, P. M.; Kim, G.; Gray, C. P. Cycling Li-O2 Batteries via LiOH Formation and Decomposition. *Science (80-.).* **2015**, No. 350, 530–533.

(13) Wang, Z. L.; Xu, D.; Xu, J. J.; Zhang, L. L.; Zhang, X. B. Graphene Oxide Gel-Derived, Free-Standing, Hierarchically Porous Carbon for High-Capacity and High-Rate Rechargeable Li-O 2 Batteries. *Adv. Funct. Mater.* **2012**, *22* (17), 3699–3705.

(14) Storm, M. M.; Overgaard, M.; Younesi, R.; Reeler, N. E. A.; Vosch, T.; Nielsen, U. G.;

Edström, K.; Norby, P. Reduced Graphene Oxide for Li–air Batteries: The Effect of Oxidation Time and Reduction Conditions for Graphene Oxide. *Carbon N. Y.* **2015**, *85*, 233–244.

(15) Kim, S. Y.; Lee, H.-T.; Kim, K.-B. Electrochemical Properties of Graphene Flakes as an Air Cathode Material for Li-O2 Batteries in an Ether-Based Electrolyte. *Phys. Chem. Chem. Phys.* **2013**, *15* (46), 20262–20271.

(16) McCloskey, B. D.; Burke, C. M.; Nichols, J. E.; Renfrew, S. E. Mechanistic Insights for the Development of Li–O2 Battery Materials: Addressing Li2O2 Conductivity Limitations and Electrolyte and Cathode Instabilities. *Chem. Commun.* **2015**, *51* (64), 12701–12715.

(17) MIZUNO, F.; Nakanishi, S.; Kotani, Y.; YOKOISHI, S.; Iba, H. Rechargeable Li-Air Batteries With Carbonate-Based Liquid Electrolytes. *Electrochemistry* **2010**, *5*, 403–405.

(18) McCloskey, B. D.; Bethune, D. S.; Shelby, R. M.; Girishkumar, G.; Luntz, A. C. Solvents ' Critical Role in Nonaqueous Lithium-Oxygen Battery. *J. Phys. Chem. Lett.* **2011**, *2*, 1161–1166.

(19) Younesi, R.; Veith, G. M.; Johansson, P.; Edstrom, K.; Vegge, T. Lithium Salts for Advanced Lithium Batteries: Li-Metal, Li-O2, and Li-S. *Energy Environ. Sci.* **2015**, *8* (7), 1905–1922.

(20) Luntz, A. C.; Mccloskey, B. D. Nonaqueous Li-Air Batteries: A Status Report. *Chem. Rev.* **2014**, *114*, 11721–11750.

(21) Ottakam Thotiyl, M. M.; Freunberger, S. A.; Peng, Z.; Bruce, P. G. The Carbon Electrode in Nonaqueous Li-O2 Cells. *J. Am. Chem. Soc.* **2013**, *135* (1), 494–500.

(22) McCloskey, B. D.; Speidel, A.; Scheffler, R.; Miller, D.; Viswanathan, V.; Hummelshøj, J. S.; Nørskov, J. K.; Luntz, A. C. Twin Problems of Interfacial Carbonate Formation in Nonaqueous Li-O2 Batteries. *J. Phys. Chem. Lett.* **2012**, *3*, 997–1001.

(23) Das, S.; Højberg, J.; Knudsen, K. B.; Younesi, R.; Johansson, P.; Norby, P.; Vegge, T. Instability of Ionic Liquid-Based Electrolytes in Li–O $_2$ Batteries. *J. Phys. Chem. C* **2015**, *119* (32), 18084–18090.

(24) Shui, J. L.; Okasinski, J. S.; Chen, C.; Almer, J. D.; Liu, D. J. In Operando Spatiotemporal Study of Li2O2 Grain Growth and Its Distribution inside Operating Li-O2 Batteries. *ChemSusChem* **2014**, *7* (2), 543–548.

(25) Ryan, K. R.; Trahey, L.; Okasinski, J. S.; Burrell, A. K.; Ingram, B. J. In Situ Synchrotron X-Ray Diffraction Studies of Lithium Oxygen Batteries. *J. Mater. Chem. A* **2013**, *1* (23), 6915.

(26) Ganapathy, S.; Adams, B. D.; Stenou, G.; Anastasaki, M. S.; Goubitz, K.; Miao, X.-F.; Nazar, L. F.; Wagemaker, M. Nature of Li2O2 Oxidation in a Li–O2 Battery Revealed by Operando X-Ray Diffraction. *J. Am. Chem. Soc.* **2014**, *136* (46), 16335–16344.

(27) Storm, M. M.; Johnsen, R. E.; Younesi, R.; Norby, P. Capillary Based Li–air Batteries for in Situ Synchrotron X-Ray Powder Diffraction Studies. *J. Mater. Chem. A* **2015**, *3* (6), 3113–3119.

(28) Shui, J.-L.; Okasinski, J. S.; Kenesei, P.; Dobbs, H. A.; Zhao, D.; Almer, J. D.; Liu, D.-J. Reversibility of Anodic Lithium in Rechargeable Lithium–oxygen Batteries. *Nat Commun* **2013**, *4*.

(29) Højberg, J.; McCloskey, B. D.; Hjelm, J.; Vegge, T.; Johansen, K.; Norby, P.; Luntz, A. C. An Electrochemical Impedance Spectroscopy Investigation of the Overpotentials in Li-O2 Batteries. *ACS Appl. Mater. Interfaces* **2015**, *7* (7), 4039–4047.

(30) Højberg, J. Fundamental Mechanisms in Li-Air Battery Electrochemistry, Technical University of Denmark, 2015.

(31) Rigaku. Integrated X-Ray Powder Diffraction Software. *Rigaku J.* **2010**, *26* (1), 23–27.

(32) Yang, D.; Velamakanni, A.; Bozoklu, G.; Park, S.; Stoller, M.; Piner, R. D.; Stankovich, S.; Jung, I.; Field, D. A.; Ventrice, C. A.; et al. Chemical Analysis of Graphene Oxide Films after Heat and Chemical Treatments by X-Ray Photoelectron and Micro-Raman Spectroscopy. *Carbon N. Y.* **2009**, *47* (1), 145–152.

(33) Younesi, S. R.; Hahlin, M.; Bjorefors, F.; Johansson, P.; Edstrom, K. Li-O2 Battery Degradation by Lithium Peroxide: A Model Study. *Chem. Mater.* **2013**, *25*, 77–84.

(34) Dedryvère, R.; Laruelle, S.; Grugeon, S.; Poizot, P.; Gonbeau, D.; Tarascon, J. M. Contribution of X-Ray Photoelectron Spectroscopy to the Study of the Electrochemical Reactivity of CoO toward Lithium. *Chem. Mater.* **2004**, *16* (6), 1056–1061.

(35) Younesi, R.; Hahlin, M.; Roberts, M.; Edström, K. The SEI Layer Formed on Lithium Metal in the Presence of Oxygen: A Seldom Considered Component in the Development of the Li-O2 Battery. *J. Power Sources* **2013**, *225*, 40–45.

(36) Leroy, S.; Martinez, H.; Dedryvére, R.; Lemordant, D.; Gonbeau, D. Influence of the Lithium Salt Nature over the Surface Film Formation on a Graphite Electrode in Li-Ion Batteries: An XPS Study. *Appl. Surf. Sci.* **2007**, *253* (11), 4895–4905.

Supporting information

In situ analysis of the Li-O2 battery with thermally reduced graphene oxide cathode: influence of water addition

Mie Møller Storm[1], Mathias Kjærgård Christensen[1], Reza Younesi[2] and Poul Norby[1]

[1]Technical University of Denmark, DTU Energy, Frederiksborgvej 399, 4000 Roskilde, Denmark
[2]Department of Chemistry - Ångström Laboratory, Uppsala University, Box 538, SE-751 21 Uppsala, Sweden

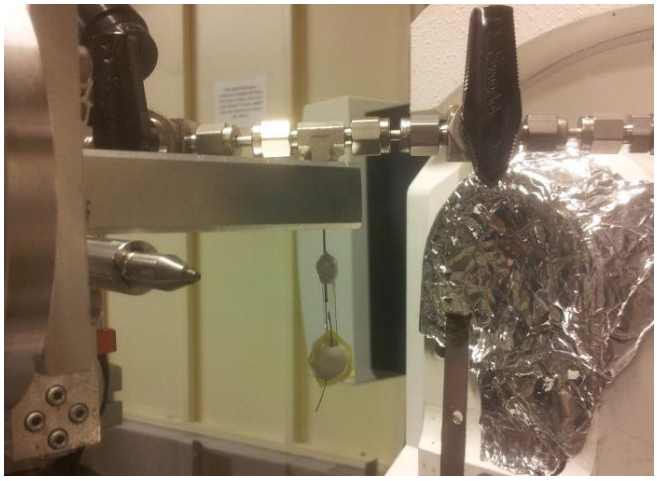

Figure S1: A picture of the capillary battery measured at the Maxlab II, beamline 711.

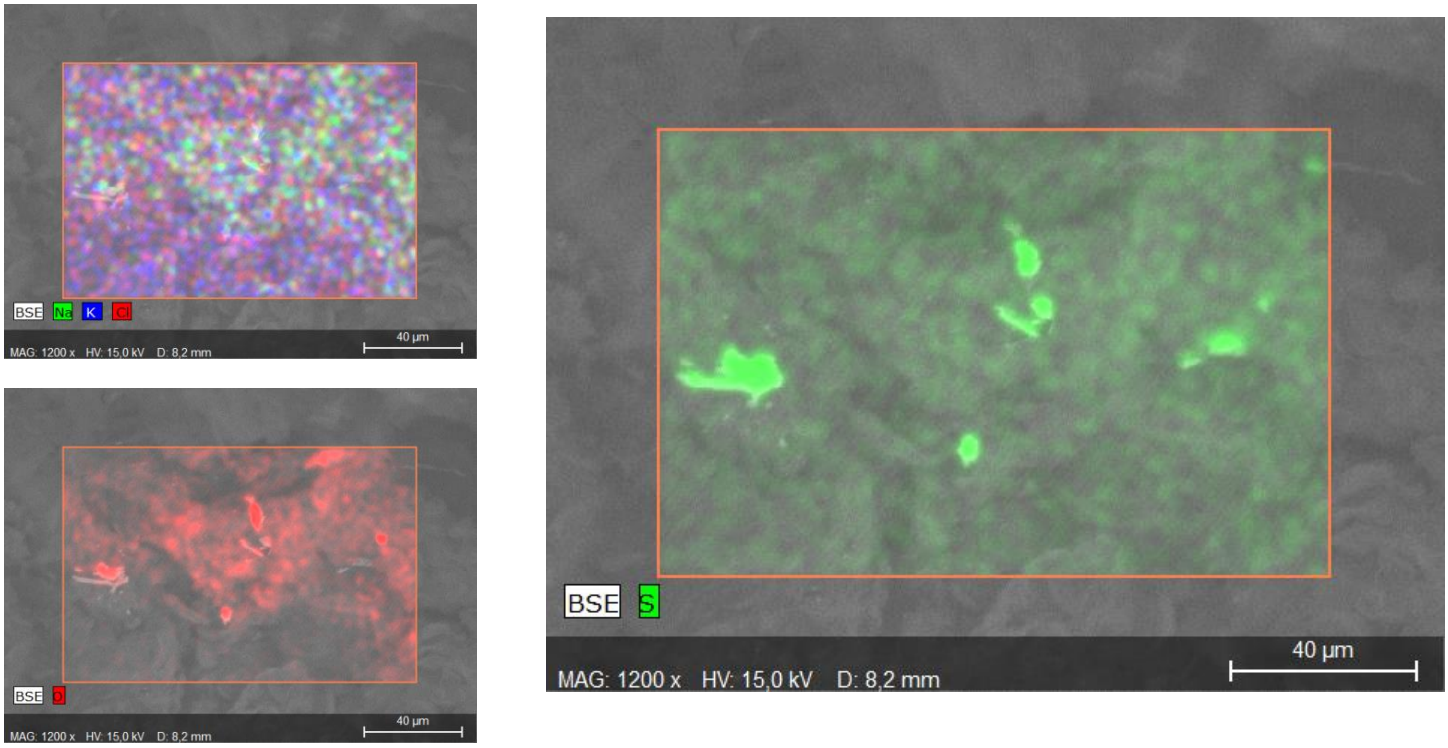

Figure S2: EDX pictures of TrGO of a point in the TrGO sample containing S-rich particles.

EDX

3 different EDX measurements (300 S, 15 KeV, TM3000) revealed the presence of O (67.4-73.5%), S (14.9-11.9 %), K (9.9-7.5%), Cl (6.0-4.0%) and Na(3.9-2.8%) (C could not be measured by EDX). XPS showed the presence of C and O, as expected, and S traces. The sulfur particles observed with SEM-EDX in some areas of the sample are probably created from traces of sulfuric acid in the GO forming particles upon the thermal reduction.

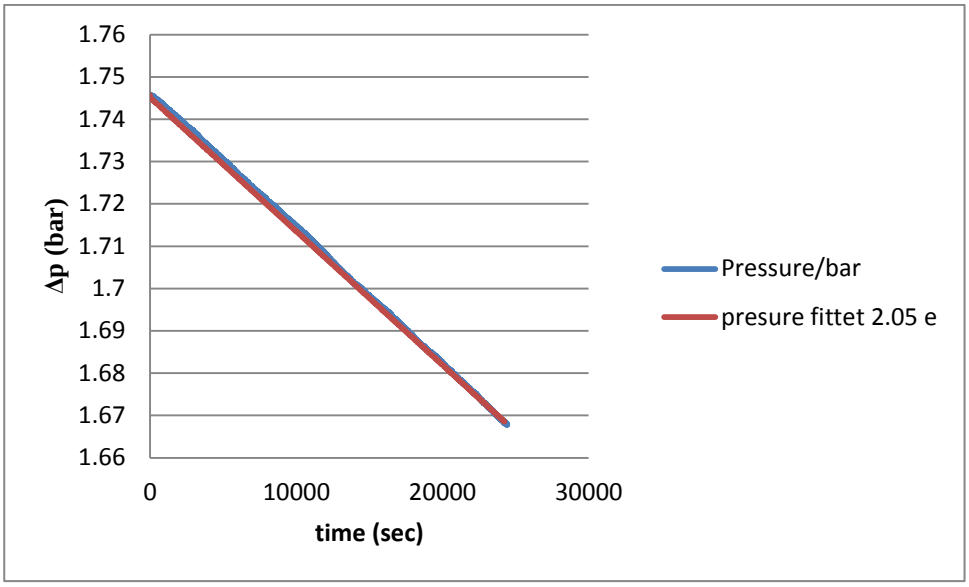

Figure S3: A DEMS discharge pressure measurement of a dry battery with the fitted pressure corresponding to an electron count of 2.05 e^-/O_2.

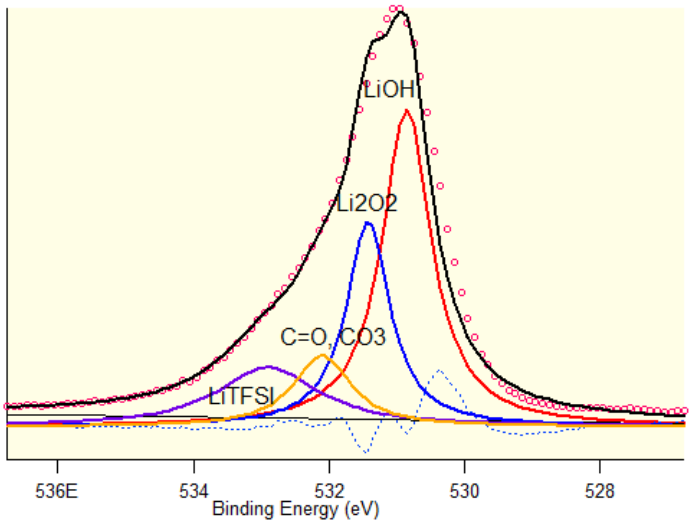

Figure S4: Deconvoluted O 1s XPS spectrum of the dry cathode showing formation of LiOH and Li_2O_2 upon discharge.

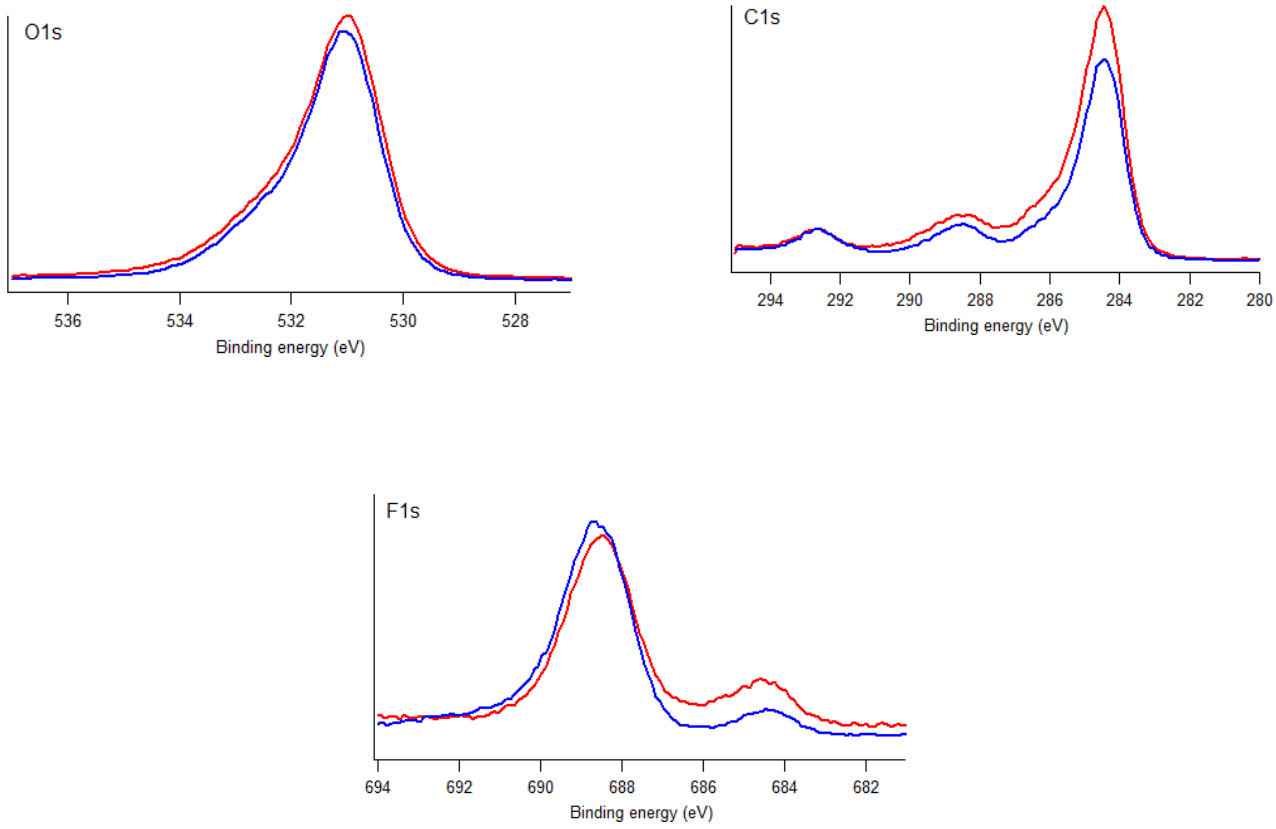

Figure S5: O 1s, C 1s and F 1s spectra of the discharged wet and dry cathode (wet = blue, dry = red)

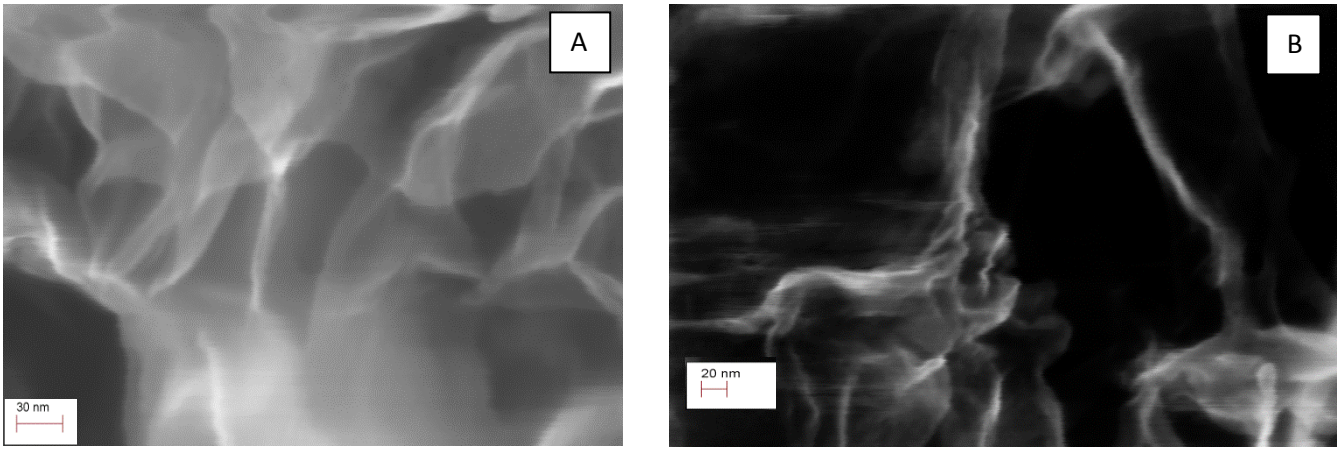

Figure S6: (A) SEM of a discharged dry cathode, (B) SEM of a discharged wet cathode

Super C65 capillary battery

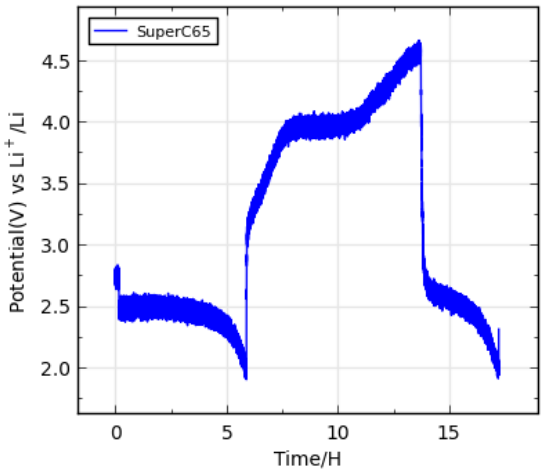

Figure S7: Discharge-charge curve for a Super C65 based capillary battery.

The Super C65 cathode resulted a battery which showed both discharge and charge. It had a smaller discharge capacity than the TrGO cathode, however, it had a charge with a plateau at 4 V indicating Li_2O_2 decomposition. The Super C65 cathodes had a tendency to overcharge, so the first charge is longer than the first discharge, which may be due to electrolyte decomposition, as seen for carbon based cathodes with a DME based electrolyte.[1] The difference in battery discharge-charge profile between the two different cathode materials could be explained by difference in the crystalized discharge product or difference in the electron carrying abilities of the discharge products.

Angle/ ° in 2θ	*d*-value/ Å	Net Intensity	Gross Intensity	Assignment
19.311	2.964	2930	7860	
20.380	2.810	2580	7480	LiOH (101)
20.644	2.774	2410	7290	Li_2O_2 (100)
21.937	2.612	2350	7120	Li_2O_2 (101)
22.386	2.561	1870	6600	LiOH (110)
27.785	2.070	1990	5670	SS
28.381	2.028	1630	5140	SS
30.500	1.890	2010	4830	Li_2O_2 (004)
31.977	1.805	2360	4610	Li_2O_2 (103)
32.394	1.782	2480	4550	LiOH (112)
35.572	1.627	3490	4080	SS
36.099	1.604	3540	3840	Li_2O_2 (104)
36.294	1.596	3670	3870	LiOH (211)

Table S1: The diffraction peaks developed upon discharge of the capillary Li-O_2 battery with the TrGO cathode for position 1.

Charging of the TrGO cathode in a capillary battery

During the charge of the TrGO capillary batteries a plateau was formed at 4.5 V. In position 1 only a 19 % reduction of the 101 Li_2O_2 diffraction peak was observed, as was expected based on the small charge capacity compared to the discharge for the TrGO battery. Even less decomposition was observed for position 2 (6%). See Figure S8 for a comparison between the first and the last diffractogram during discharge.

For position 1 the diffraction peaks at 19, 22.4 and 32° in 2θ was unchanged or decreases slightly upon charge. The diffraction peaks at 20.3, 20.6, 22 and 32.5° in 2θ decreases in intensity with charge. For position 2 the only observed change in the diffraction peaks upon charge were for the diffraction peaks at 20.4, 20.6 and 22° in 2θ. However, as the diffraction peaks of position two are of less intensity they are less conclusive. The decrease of the diffraction peaks at 20.6 and 22° is caused by the small decomposition of Li_2O_2 observed both for position 1 and 2, however it is clear that large amount of Li_2O_2 was unreduced after charge. The LiOH diffraction peaks were also observed to diminish upon charge, but plenty of LiOH intensity was still present at the end of discharge (approx. 80% intensity left).

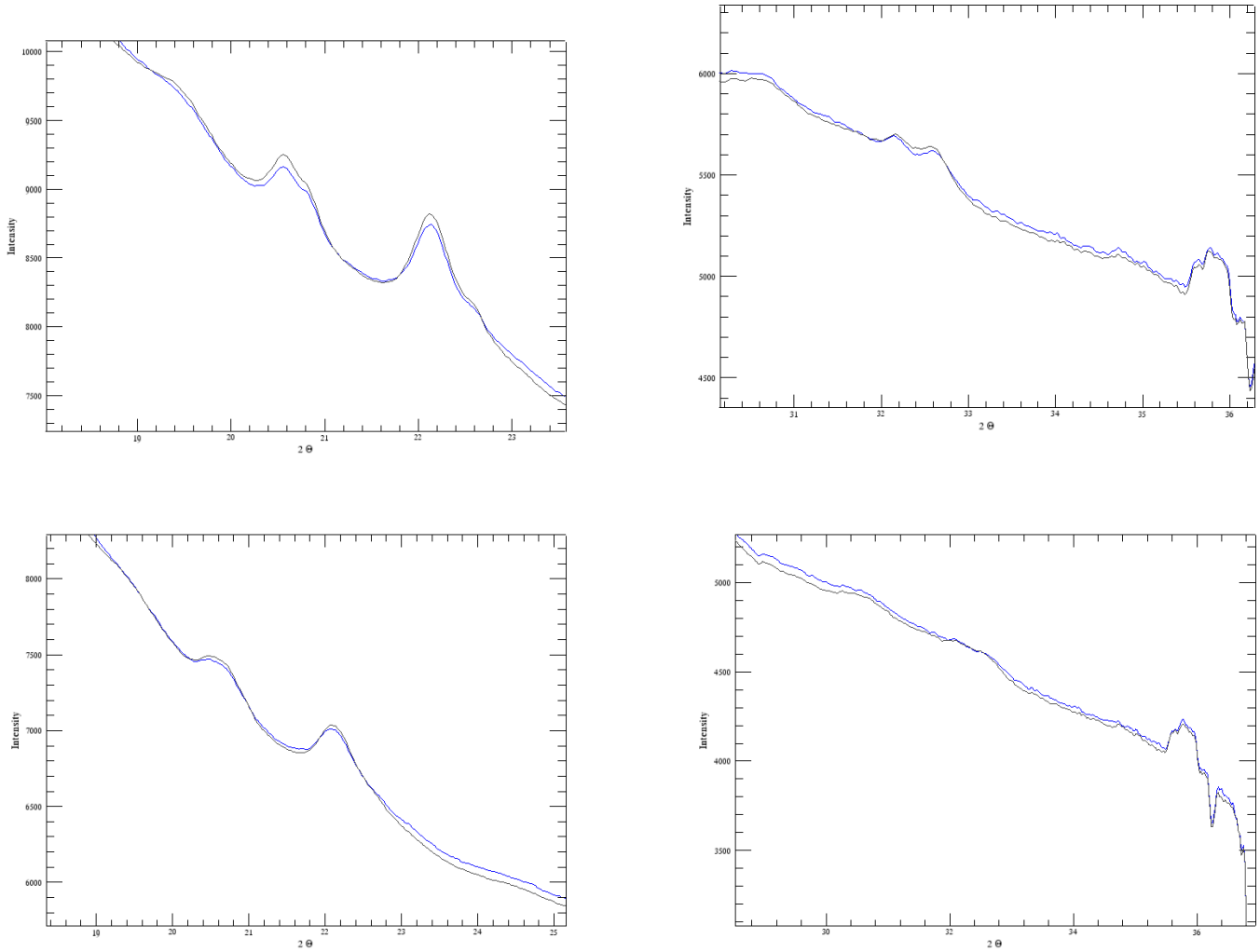

Figure S8: The 1st (gray) and last (blue) X-ray diffractograms from the charge of the TrGO capillary battery. Top: Position 1, Bottom: Position 2.

Difference between Swagelok cells and the capillary battery

The different form of LiOH for the different battery types may be caused by difference in the battery set-up. Different types of binders are used in the batteries, but despite possible decomposition of the binder[2] we do not expect major changes in the chemistry of the composition of the discharge product. The separation of anode and cathode, either by electrolyte or by separator, and the rate of the batteries is another difference between the battery types. We have to remember that the *in situ* capillary battery was exposed to X-ray radiation which may affect the battery by X-ray accelerated decomposition of Li_2O_2 and radiation damage. All these factors could influence the batteries to form different forms of discharge products. Furthermore it was not possible to leak test the capillary batteries and small leaks may be present

References

(1) McCloskey, B. D.; Bethune, D. S.; Shelby, R. M.; Girishkumar, G.; Luntz, A. C. Solvents ' Critical Role in Nonaqueous Lithium-Oxygen Battery. *J. Phys. Chem. Lett.* **2011**, *2*, 1161–1166.

(2) Younesi, S. R.; Hahlin, M.; Bjo, F.; Johansson, P.; Edström, K. Li-O2 Battery Degradation by Lithium Peroxide: A Model Study. *Chem. Mater.* **2013**, *25*, 77–84.